Gianfranco Marra **A NUMERICAL AND EXPERIMENTAL ANALYSIS ON THE MECHANICAL BEHAVIOR OF BOLTED JOINTS BETWEEN PULTRUDED PROFILES AND T-STUBS OF GLASS FIBER REINFORCED POLYMER**

Dottorato di Ricerca
in Ingegneria delle Strutture e del Recupero Edilizio ed Urbano

Università degli Studi di Salerno

Gianfranco Marra

A NUMERICAL AND EXPERIMENTAL ANALYSIS ON THE MECHANICAL BEHAVIOR OF BOLTED JOINTS BETWEEN PULTRUDED PROFILES AND T-STUBS OF GLASS FIBER REINFORCED POLYMER

X Ciclo Nuova Serie (a.a. 2008- 2011)

UNIVERSITÀ DEGLI STUDI DI SALERNO

DIPARTIMENTO DI INGEGNERIA CIVILE

Dottorato di Ricerca in Ingegneria delle Strutture e del Recupero Edilizio ed Urbano

X Ciclo Nuova Serie (a.a. 2008-2011)

A NUMERICAL AND EXPERIMENTAL ANALYSIS ON THE MECHANICAL BEHAVIOR OF BOLTED JOINTS BETWEEN PULTRUDED PROFILES AND T-STUBS OF GLASS FIBER REINFORCED POLYMER

Gianfranco Marra

Il Tutor
Prof. Ing. Luciano Feo

Il Coordinatore
Prof. Ing. Ciro Faella

Il Co-Tutor
Prof. Ayman S. Mosallam

Ringraziamenti

L'esperienza del Dottorato di Ricerca rappresenta un percorso formativo e culturale di notevole interesse dal momento che ha costituito per me un periodo di prezioso arricchimento didattico e professionale, oltre che una vera e propria scuola di vita.

Desidero porgere i miei più sentiti ringraziamenti al Prof. Luigi Ascione e al Prof. Luciano Feo, miei punti di riferimento nel corso di questo triennio.

I miei ringraziamenti vanno al Prof. Luigi Ascione, persona di grande acume intellettuale e morale, docente paterno e carismatico, e al Prof. Luciano Feo, mio tutor, persona a me più vicina, per la sua concretezza nell'affrontare ogni problematica di ricerca e di vita, che ha saputo indirizzarmi, spronandomi, a concludere degnamente il mio cammino di ricerca.

Ringrazio il prof. A.S. Mosallam, emerito professore dell'Università della California di Irvine, per i preziosi consigli ed il materiale a me fornito al fine di ottenere spunti nuovi per il mio percorso di ricerca.

I miei ringraziamenti vanno, inoltre, alle persone che hanno costellato ogni mio giorno lavorativo con i quali ogni legame lavorativo è presto divenuto affettivo e amichevole. In particolare desidero ringraziare tutti i miei colleghi di lavoro.

Non per ultima, ringrazio fortemente la mia famiglia, che mi ha sostenuto assiduamente in questi tre anni credendo in me e convincendomi a non arrendermi mai, ma a superare ogni difficoltà continuando a credere nei miei sogni.

A me,

che ogni giorno ho condotto una vita irreprensibile e corretta verso chi mi ha stimato ed ascoltato, senza arrendermi mai di fronte alle difficoltà quotidiane, ma cercando di dare il meglio che potessi.

"….narrare è resistere…"

Indice

Ringraziamenti

Premessa

CHAPTER I
STRUCTURES OF FIBER-REINFORCED COMPOSITE MATERIAL……..……1

1.1. Examples of applications of innovative material FRP in the world.....6

CHAPTER II
BOLTED JOINTS BETWEEN PULTRUDED PROFILES OF COMPOSITE MATERIAL…….19

2.1. Composite materials: definition and production……..…19

2.2. Bolted joints 22

2.3. Failure modes of bolted joints.....27

CHAPTER III
3D FINITE ELEMENT ANALYSIS OF BOLTED JOINTS
……..45

3.1. Joint J11-J21-J22 50

3.2. Joint J33-J44.....57

3.3. Comparison of results 63

CHAPTER IV
EXPERIMENTAL ANALYSIS OF BOLTED JOINTS ……...67

4.1. Experimental set-up 68
4.2. Joint J22- Test description 72
4.3. Joint J22- Results and discussion 81
4.4. Joint J33 Type 1-Test description..... 88
4.5. Joint J33 Type 1- Results and discussion..... 95
4.6. Overlap zone of Joint J33 Type 1 105
4.7. Joint J33 Type 2-Test description..... 115
4.8. Joint J33 Type 2- Results and discussion..... 129

CHAPTER V
2D FINITE ELEMENT ANALYSIS OF BOLTED JOINTS WITH WASHERS……...…….133

5.1. Results and discussion 136

CHAPTER VI
EXPERIMENTAL ANALYSIS OF BOLTED JOINTS WITH WASHERS……...…….205

6.1. Results and discussion 208

CHAPTER VII
3D NUMERICAL ANALYSIS OF T-STUBS OF GLASS FIBER REINFORCEDPOLYMER……...…….213

7.1. Results and discussion 217

References……...……..……...223

Premessa

Il lavoro oggetto del presente elaborato finale costituisce una dettagliata indagine sui collegamenti bullonati tra profili pultrusi in materiale composito rinforzato con fibre di vetro (GFRP).

In particolare sono stati studiati i parametri che principalmente intervengono nella determinazione del carico ultimo di rifollamento e nella distribuzione degli sforzi di taglio tra i bulloni, assumendo per i collegamenti un comportamento elastico lineare sino a rottura.

I principali fattori che influenzano tale carico sono: la geometria del collegamento, lo spessore degli elementi collegati, il diametro del bullone e delle rondelle, l'angolo di fibratura, il numero di file di bulloni ed il numero di bulloni per fila.

Tale studio è stato condotto sotto la supervisione del Prof. Luciano Feo, in qualità di tutor.

Si presentano dapprima i risultati numerici, condotti su modelli agli elementi finiti realizzati per confermare le indagini sperimentali condotte dal gruppo di ricerca, considerando, inoltre, altri fattori quali la variazione del numero di bulloni per file e del numero di file e la presenza di rondelle rigide.

Infine è stato studiato,mediante analisi numerica agli elementi finiti, il nodo trave-colonna tra elementi in GFRP , ovvero considerando un T-Stub realizzato con due profili a doppio T in GFRP bullonato, al fine di comprendere le modalità di rottura, la diffusione delle tensioni normali e tangenziali, eventuali soluzioni di rinforzo.

I risultati di queste analisi sono riportati nelle seguenti pubblicazioni:

F. Ascione, **V. Cerenza**, **L. Feo**, **G. Marra**: "Analisi delle tensioni in giunzioni bullonate tra profili pultrusi di FRP". In: AIAS XXXVIII Convegno Nazionale, 9-11 settembre 2009, Politecnico di Torino.

F. Ascione, **V. Cerenza**, **L. Feo**, **G. Marra**: "A numerical and experimantalinvestigation on the shear forces distribution among the bolts of GFRP bolted joints". In: XIX Congresso AIMETA, 14-17 settembre 2009, Ancona.

F. Ascione, **V. Cerenza**, **L. Feo**, **G. Marra**: " Stress analysis of bolted joints between FRP pultruded profiles". In: ICCE-17, 26 july – 1 august 2009, Hawaii, USA.

F. Ascione, **V. Cerenza**, **L. Feo**, **G. Marra**: " Influenza della pressione esercitata da rondelle rigide sulla rottura per rifollamento di connessioni bullonate tra laminati compositi fibrorinforzati: primi risultati". In: AIAS XXXIX ConvegnoNazionale, 7-10 settembre 2010, Maratea (PZ).

L. Feo, **G. Marra**, **R. Penna**: "A numerical analysis on the pin-bearing failure load of glass fibre reinforced polymer laminates". In: ICCE-18, 04-10 july, Anchorage, Alaska, USA.

L. Feo, **G. Marra**, **A. S. Mosallam**: "Stress Analysis of Bolted Joints for FRP Pultruded Structures" in press on Composite Engineering: Part B.

G. Marra Thesis: "Analisi sperimentale sulle modalità di rottura di collegamenti bullonati tra profili sottili pultrusi in materiale composito fibrorinforzato (FRP)".

Salerno, 02 gennaio 2012 Gianfranco Marra

CHAPTER I
STRUCTURES OF FIBER-REINFORCED COMPOSITE MATERIAL

Until a few decades ago, the fiber-reinforced composites (FRP - Fiber Reinforced Polymer) were used primarily in the fields of mechanical engineering, aeronautics and aerospace, where their use, compared to conventional materials, has allowed obtaining lighter structures and more technologically advanced, with a significant increase in performance [1].

Variety of manufacturing processes, speed of production, adaptability to complex forms and requirements, ability to obtain products with mechanical properties designed according to the requirements are clear advantages for both the production and the realization of a plane, car, boat, or their components.

In this context, numerous studies have been conducted that have investigated, in particular, the problem of structural connections, performed usually by bolting or bonding technique [1-13].

Bonded joints allow limiting the phenomena of stress concentration, but at the same time, in the design of such joints several factors affect, such as the difficulty of connect elements of a certain thickness, the manufacturing complexity and limited knowledge of failure modes.

In case of higher stresses, and when it is necessary to adopt higher thickness is preferable to use bolted joints, which allow you to get even better ease of assembly and disassembly of components for inspection and repair [1-2].

It is understandable that, despite the reduction of effectiveness of the joint due to the stress concentrations near the holes, using the bolt joints is preferred in the design [3].

The use of FRP materials is growing rapidly in recent times, even in the field of civil engineering, with concrete developments in the operations of consolidation and structural rehabilitation of existing buildings.

In fact, with regard to concrete structures, flexural and shear reinforcement of beams and the confinement of columns allows obtaining effective increases in strength and ductility (**Figure 1.1**).

These issues determine many advantages, especially for the upgrading and seismic design, in an era marked by the tragedy of the earthquake and especially by a strong evolution of the seismic classification of land and related standards [16].

The applications aren't less important are which can be performed for the consolidation of masonry structures, especially those with historical interest, where the use of FRP allows the restoration of low invasiveness and innovative technologies to deal with the problem of vulnerability of centers historic (**Figure 1.2**).

Finally, translucency and low thermal conductivity of composite materials, in particular those ones reinforced with glass fibers, allow integrating the architectural features of the structural components.

Figure 1.1. Interventions with FRP on reinforced concrete structures.

Figure 1.2. Interventions with FRP on masonry structures.

The construction of civil structures, built entirely by the assembly of pultruded FRP, represents a new target.

The extension of the use of FRP in new civil construction is mainly due to accredited advantages they present, such as, for example, light weight, corrosion resistance and high mechanical properties, which ensure rapid assembly of structural elements and, consequently, a significant reduction in labor costs and maintenance.

In the area of new buildings a fundamental problem, which arises from an anisotropic and brittle behavior of composite materials is the design and verification of structural joints, glued and bolted.

In literature, it's possible to find data about connections in composite structures used in the aeronautical, mechanical and naval engineering [1-13].

They are not directly usable in the field of civil engineering, especially because they show different properties from traditional materials normally used.

Moreover, these results mainly refer to mixed connections between components of FRP and metal components, while the study of joints only between elements of FRP is still not sufficiently thorough.

For these materials design and verification relationships, adopted for plastic materials, cannot be applied.

This is due to the orthotropic behavior of composite materials and to the reduced ability to adapt to the plastic behavior than traditional materials.

In the realization of a bolted connection between the profiles of composite material, in fact, it is imperative to take into account the reduced resistance in the direction orthogonal to the fibers and the unknown part where the material failure occurs.

In addition, for example, in the bearing failure, the low adaptive capacity of the pultruded material to a plastic behavior reduces the possibility of a stresses redistribution.

So in the case of bolted connections between pultruded composite profiles, stresses, acting around the hole of a single bolt, cannot be valued using only equilibrium criteria as it occurs in the case of ductile materials..

All of these considerations, arising from the comparison between the use of traditional materials, whose behavior is well known to designers, and the behavior of new materials, for which there are still some unanswered questions, and, at the same time, the charm of the modern buildings with innovative technology, do understand the interest in the issue of joints between profiles made entirely of FRP, which is very timely in view of new market opening and evolution of future structural wealth.

1.1. Examples of applications of innovative material FRP in the world

In the field of structural engineering, the increasing use of composite materials both as a reinforcement of existing structures and as structural elements is due to their characteristics that favor their use.

In particular, their use has spread where it is required a rapid and easy assembling, and a greater resistance to corrosion than traditional materials.

This requirement makes the use of pultruded profiles reinforced both with glass fiber (GFRP - *Glass Fiber Reinforced Polymer*) and carbon fiber (CFRP - *Carbon Fiber Reinforced Polymer*) particularly advantageous for the realization of elements such as grids, temporary structures, bridges and pedestrian bridges, off-shore structures.

A suitable arrangement of the fibers in the matrix of a profile made of FRP allows performances that would require excessively large sections of concrete or steel.

The first achievements using composite materials were made in China in the early ’80, where many pioneering projects were built as bridges, including *Miyun Bridge* (1982), near Beijing, and *Xianyong Bridge*, in Chengdu, made by assembling GFRP and CFRP profiles to realize the structure.

Examples of similar constructions are also found in the United States. In fact the important characteristics of the composite material, as mentioned, including lightness, ease of transportation and installation,

have allowed the creation of structures made entirely of pultruded profiles

In this regard, between different structures, a pedestrian bridge with a single span of 19 m, made by *Creative Pultrusion* for a chemical industry, obtained by using *Pultex* glass fiber profiles and joints with stainless steel bolts, is mentioned.

The peculiarity of this structure is that it has been completely assembled in the factory and then, thanks to much weight content, it was possible to carry and mount it directly *in situ* by using a single crane.

Another relevant example that highlights the qualities of FRP is the pedestrian bridge in glass fiber, made in Washington, at the Olympic National Park.

It has a single span of 24 m that allows the crossing of the river that flows into the park. It was built to substitute the old and preexisting steel bridge, damaged in December 1993 by a flood of the river.

The decision to restore the crossing preferring a structure made of composite materials compared to a traditional metal structure was due to the fact that for the installation of this structure would have been necessary to use a helicopter, incompatible solution with the no-fly zone that exists within the park.

For this reason you had to think of items that could be carried by a certain simplicity and then assembled on site: they opted, therefore, for pultruded profiles that were transported on the backs of mules in order to avoid damaging the natural ecosystem.

Structures of particular value, consisting of profiles made of glass or carbon fibers embedded in a matrix usually made of vinyl ester resins, then bolted or glued together, are following bridges: the *Laurel Lick Bridge* (1997) (**Figure 1.3**a), the *Dickey Creek Bridge* (**Figure 1.3**b) in Virginia, the *Clear Creek Bridge* (1996) (**Figure 1.4**a) in Colorado, the *Bentley Creek Bridge* (1999) (**Figure 1.4**b) in New York State, the *Wickwire Run Bridge* (1997) (**Figure 1.5**a) and the *Tom's Creek Bridge* (1996) (**Figure 1.5**b).

(a) (b)

Figure 1.3. *Laurel Lick Bridge* (a) e *Dickey Creek Bridge* (b).

(a) (b)

Figure 1.4. *Clear Creek Bridge* (a) e *Bentley Creek Bridge* (b).

(a) (b)

Figure 1.5. *Wickwire Run Bridge* (a) e *Tom's Creek Bridge* (b).

The most popular bridges, made of composite material in Europe at early ’90, are the *Aberfeldy Bridge* (1992) (**Figure 1.6**) in Scotland, the *Bonds Mill Lift Bridge* (1992) (**Figure 1.7**a) the *Bromley South Bridge* (1992) (**Figure 1.7**b), the *Halgavor Bridge* (**Figure 1.8**a) in England and the *Parson’s Bridge* (1992) (**Figure 1.8**b) in the Galles.

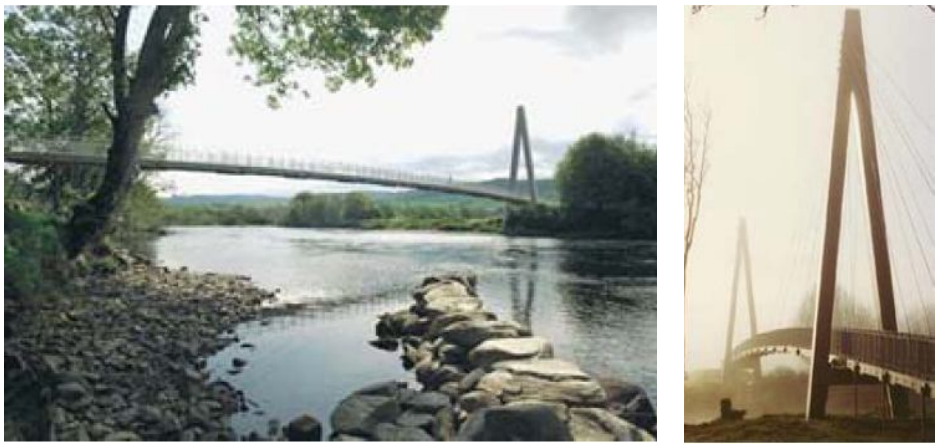

Figure 1.6. *Aberfeldy Bridge*.

(a) (b)

Figure 1.7. *Bonds Mill Lift Bridge* (a) e *Bromley South Bridge* (b).

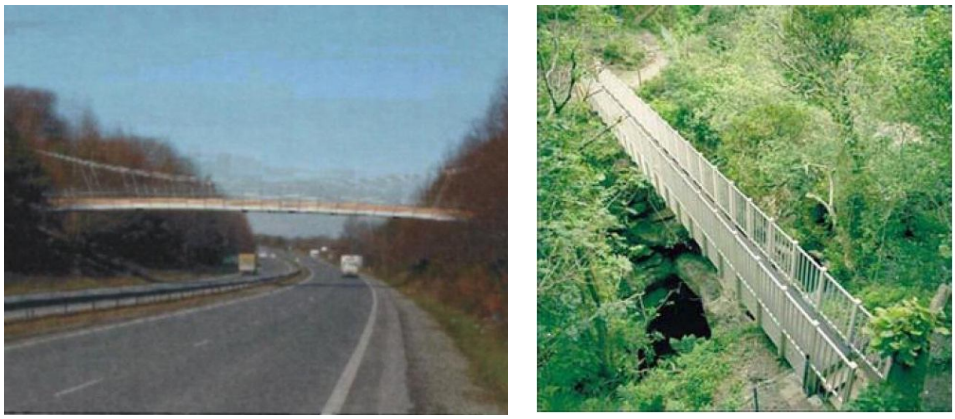

(a) (b)

Figure 1.8. *Halgavor Bridge* (a) e *Parson's Bridge* (b).

The bridge Aberfeldy, in particular, is a pedestrian bridge that crosses the golf club Aberfeldy and it is the first suspension bridge built completely by using composite materials; both the bridge that the two towers are of GFRP, while the rods are reinforced with aramidic fibers.

Once again it is interesting to focus on the lightness of the FRP, which in this case constituted a double advantage: they have been used, in fact, about 14.5 tons of composite material for the realization of such a

structure, but its weight is only 2 kN / m and it was also mounted in ten weeks without the help of a crane.

Finally, worthy of note, are the bridge*Fiberline Bridge* (1997) (**Figure 1.9**) in Denmark, located near a rail crossing, which is a cable-stayed bridge made of bolted GFRP profiles, and the *Pontresina Bridge* (1997) (**Figure 1.10**) in Switzerland.

Figure 1.9. *Fiberline Bridge.*

Figure 1.10. *Pontresina Bridge*.

In particular, the constructive system that distinguishes most of the composite material structures produced in Europe is called ACCS (*Advanced Composite Construction System*), which provides for the assembly of modular panels closed-section of different geometric shapes FRP (**Figure 1.11**) with connector systems, made of FRP, that provide seamless integration between the parties of the structure.

As regards, however, the buildings, the first example made of pultruded fiberglass is an experimental building, the Eycatcher Building, completed in 1998 in Switzerland and presented at the fair in Basel in 1999 (**Figure 1.12**). It is the tallest building made of GFRP in the world: in fact, it is 15 meters high, consists of five levels and is composed of GFRP sandwich panels, placed between the GFRP profiles, that form the structure. The connections were obtained by bolting and epoxy resin.

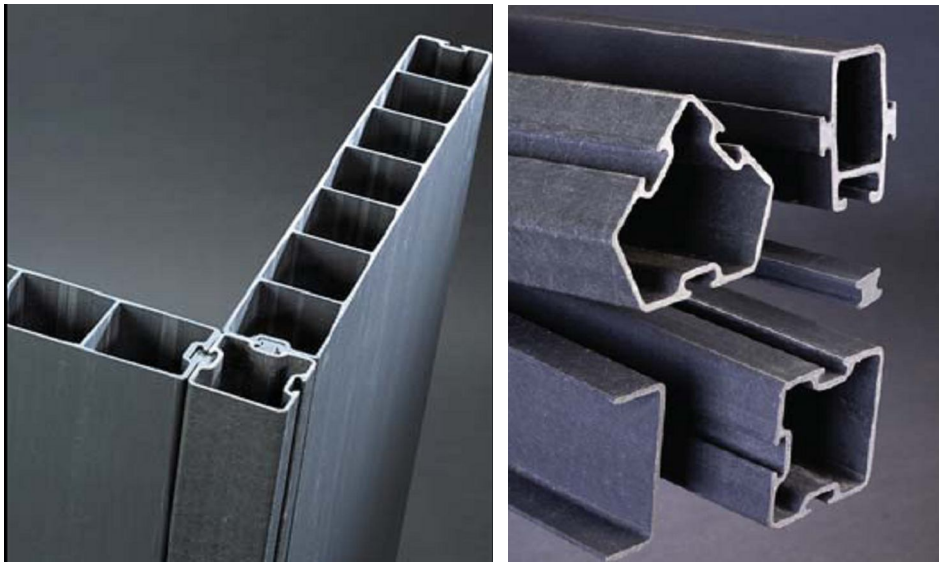

Figure 1.11. Modular panels assembled according to the ACCS system.

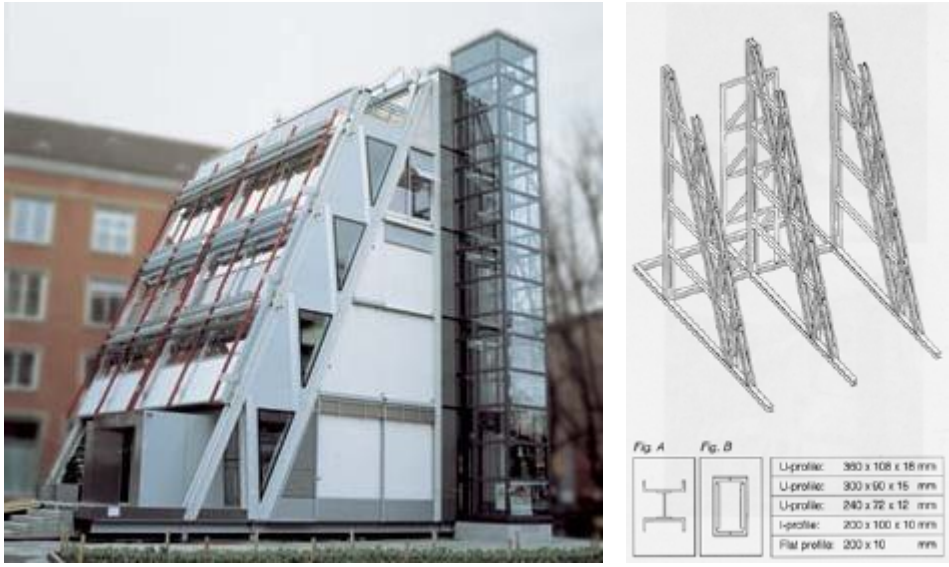

Figure 1.12. *Eycatcher Building.*

The peculiarity of this structure is that at the end of exposure was dismantled and moved to another part of town where it is currently used as office building open to the public.

It should be noted that the facade of the GFRP frames do not form thermal bridges, because the facades made of translucent, highly insulating, are filled with *aerogel*.

Un altro settore in cui si è dimostrato particolarmente idoneo l'impiego di strutture realizzate con materiale composito è quello delle Another area, where the use of composite material structures is very popular, is the realization of platforms *off-shore*.

Some examples are: *Mars Tension Leg* (**Figure 1.13**) built by *Shell Petroli* in the Mexico gulf and the platforms built for the *Dow Chemical* in Texas.

Figure 1.13. *Mars Tension Leg.*

In Italy, the FRP is used primarily for the consolidation and reinforcement, but they are still little used as base material for the construction of whole structures.

Among the few experiences an example is a pedestrian inflatable bridge composed of folding tubes of GFRP , made in Rome during the Jubilee of 2000, and the roof of the courthouse of Pescara (**Figure 1.14**), consisting entirely of pultruded structural shapes glued and bolted.

Figure 1.14. The roof of the courthouse of Pescara.

It is understandable, therefore, that current knowledge in the field of composite materials is still limited at the national level and this is mainly due to the absence of reference standards.

Nevertheless, the successful increasing applications of these materials is arousing the interest of the entire scientific community.

The Italian scientific community, therefore, gathered the results of a great research work, based on numerical analysis and experimental, to provide guidelines for the proper use of composites as a structural material.

The most important document is the CNR-DT 205/2007, prepared by the CNR to provide specific guidelines for the design, execution and control of structures made of thin pultruded profiles of reinforced composite material.

In summary, the composite materials, used primarily for reinforcement of concrete structures and deteriorated or damaged masonry, are not frequently used for the new civil construction.
The main factors that limit its use are:

- the high cost of the material;
- the limited availability of materials;
- the problem of the joints and unions;
- the absence of reference standards;
- the need to develop an appropriate mechanical modeling of the structural behavior of these materials.
- the inadequate characterization of the rheological properties of these materials.

Conversely, in civil structures, madeby assembling pultruded profiles, following advantages have been obtained:

- a reduction of the structural masses up to 70% with respect of those of conventional materials;
- reduced construction time without resorting to excessive use of labor and / or heavy equipment;
- better resistance to corrosion than traditional materials;
- reduced maintenance.

CHAPTER II
BOLTED JOINTS BETWEEN PULTRUDED PROFILES OF COMPOSITE MATERIAL

In this study a discussion of some problems concerning the behavior of bolted joints in civil structures, made entirely of fiber-reinforced composite material, is carried out.

For this purpose a brief description of main features and production techniques of composite materials is exposed.

2.1. Composite materials: definition and production

Composite materials consist of two main phases: *fiber* and *matrix*.

The *fiber*, present in the form of thin filaments of circular cross section, contribute largely to the stiffness and strength of the composite.

The *matrix* is a connecting element that, in addition to transfer the tension to the fibers, at the same time protects them from the outside.

Sometimes other substances (such as fillers) are used in addition to matrices , in order to improve specific properties of the composite, or even to reduce the cost and to improve the workability and dimensional stability.

The mechanical behavior of a composite material is orthotropic because it has different mechanical properties considering three different directions.

In particular it shows the same properties considering, separately, three symmetrical planes that coincide with the natural axes of the

composite, i.e. the direction of the fiber and the two directions orthogonal to these ones.

Another important factor to consider is the *orientation of the fiber*, and their arrangement. In fact the fiber inclination influences the behavior of composite material, as well as the presence of only one direction or two orthogonal direction of the fibers. In the first case the composite is defined *unidirectional*, in the other case *bidirectional*.

The production of a composite laminate can be done by *lamination*, i.e. by bonding successive layers of composite, or *pultrusion*.

Pultrusion is a production technique that consists of an extrusion by dragging fibers in the resin carrying the product in a mold (die) to assign the shape of the section to the profile (**Figure 2.1**).

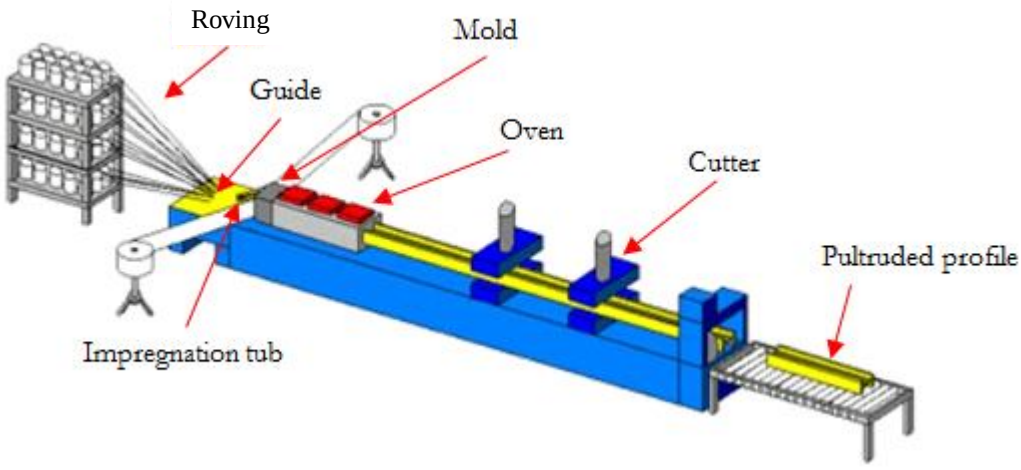

Figure 2.1. Pultrusion process.

The most popular version of this technique with impregnation resin bath, shown in **Figure 2.1**, consists of a closed mold (die) process, divided into three phases:

- forming,
- impregnation,
- consolidation.

The fibers are drawn from a group of coils (roving) and conveyed, through racks that conform the provision, to a tank containing the resin matrix impregnation, the catalyst and any fillers.

Once impregnated, the fibers come in a heated mold (die) in which the material is consolidated under pressure and eliminates all voids between the fibers, giving continuity to the product.

The excess resin is removed while the treated fibers are conducted at the end of the process.

Exit from the mold, the matrix has now solidified and the composite thus obtained is driven at a constant rate through the cylinder, the last unit of the production line, where there is a circular saw that cuts the profile to the desired length .

You can add layers of mat or tissue to reinforce the profiles in directions different from that of pultrusion; furthermore, with special equipment, you can also weaving, winding and interweaving of fibers directly on the production line.

Through this process they are normally produced several artifacts, such as rods for oil wells, prestressing cables, reinforcing bars for ordinary concrete, molds for the production of mechanical equipment used in offshore and chemical plants, transmission trees , pieces of window frames, profiles in thin-walled open or closed, tape reinforcement for concrete structures.

It is understood that the technique of pultrusion has a high flexibility, since it allows to obtain products with different profiles by simply changing the matrix shaped: with this technology can be, in fact, made various types of structural forms, such as bars, tubes, plates, panels, plates and profiles, slim-shaped cross-section corner, "C" double "T", etc.

The pultruded profiles are a very useful application in many areas, because the high mechanical strength that characterizes them, even with very low specific weight,solves a number of problems, such as lightness, strength, corrosion resistance, electrical insulation and thermal related to traditional materials.

2.2. Bolted joints

The most frequently used configurations of bolted joints in engineering practice and which are the subject of research carried out are those with double overlap, obtained by assembling two external profiles and an internal profile of thickness twice that of the external elements (**Figure 2.2**).

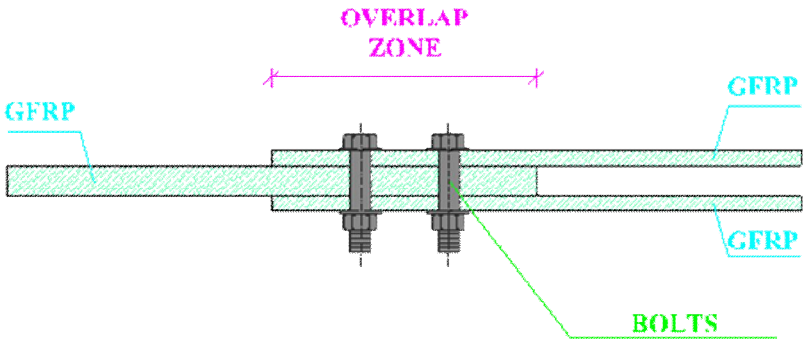

Figure 2.2. Double overlap bolted joint.

Elements that form the joints considered are made of thin pultruded profiles of composite material made of polymeric resins reinforced with glass fibers (*GFRP - Glass Fiber Reinforced Polymer*) and are interconnected through the technique of bolting.

The choice of glass fibers as a reinforcement was dictated primarily by the fact that they, compared to those of carbon and aramid, which are also commercially available, have a higher corrosion resistance and non-reactivity.

The result is essential advantages, especially if you think that the purpose of deepening an issue concerning the structural bolted connections between composite profiles is that their use in new buildings, made entirely of these materials, and these structures, as well as in Chapter I, may range from a simple pedestrian bridge, to the construction of bridges, offshore structures, buildings of great height.

Bolted connections, in the scientific literature, have been studied by many researchers as Starikov and Schön [1], Prabhakaran, Razzaq, Devara [2], Camanho and Matthews [7], which analyzed their main failure modes by varying bolts diameter, distances between the holes, distances of holes from the edges, type of lamination and fiber inclination with respect of load direction.

Considering results reported by mentioned authors, failure modes of bolted joints between pultruded profiles are illustrated in this work

In particular in this study the bearing failure mode of double overlap bolted joint is exposed. This kind of failure is due to high stresses that born at bolt-hole interface under a tensile load applied with respect of bolted joints axis.

An extensive investigation, numerical and experimental, is carried out, to formulate design and verification criteria of some simple types of bolted connections between fiber-reinforced composite material pultruded profiles.

In this regard different types of joints are considered, by varying geometrical parameters, number of rows and number of bolts per row.

Study purposes are:

- a better understanding of the theoretical formulations and mechanical models currently available in national and international scientific literature, with particular reference to the failure modes of the connections and the corresponding bearing resistance by changing geometrical parameters, to the

prediction of tensile strength, to the resistance criteria of bolted joints;

- analyzing the distribution of shear stresses between the different bolts that form the joint, varying the geometry of the connection, the rows number of bolts and the number of bolts per row;
- examining influence of fiber inclination on the bearing resistance.
- observing stress distribution near the holes;
- examining stress distribution to define extinction distance from the hole;
- comparing results of numerical analysis with experimental analysis results and comparing these ones with the values suggested in the specific Guide Lines and to validate criteria in the scientific literature.
- considering, also, the presence of variable diameter washer and their effects on bearing stresses;
- analyzing a beam-column node to understand the failure mode of bolt-joint in the T-Stub, stress distribution and the zone where the failure occurs;
- considering a steel reinforcement placed between the column flanges.

In detail, therefore, the thesis consists of the following parts:

- analyzing all the known failure modes of bolted joints;
- 3D finite element analysis of different configurations of joints, by varying number of rows and number of bolts per row, under tensile load;
- experimental analysis of joint with three bolts per row and three rows (J33) under tensile load, using a system of sensors, placed in the holes, and strain gauges to measure, respectively, bearing stresses and deformation near the holes [14, 15, 21-27];
- comparison numerical results with experimental results and with values suggested in the CNR-DT 205/2007 [20];
- 2D finite element analysis of a GFRP plate with a single bolt considering the variation of fiber inclination, the presence of diameter washer, the effects on the bearing stress, the effect on the extinction distance of stresses, the effects on resistance criterion (Tsai Hill and Maximum Stress) [14-15];
- experimental analysis of a GFRP plate, under tensile load, by varying fiber inclination [14-15], using a system of sensors, placed in the holes, and strain gauges to measure, respectively, bearing stresses and deformation near the holes;
- comparison numerical results with experimental results;

- 3D finite element numerical analysis of a beam-column node with and without steel reinforcement.

2.3. Failure modes of bolted joints

Considering results from many authors, it's possible to resume the following failure modes of a single bolt joint between FRP elements.

In particular it's necessary to distinguish the case where the bolt is subjected to shear stress from the case where it's subjected to tensile stresses.

In the first case, typical failure modes are:

- net-section failure (**Figure 2.3**);
- shear-out failure (**Figure 2.6**);
- bearing failure (**Figure 2.8**);
- fastener shear failure (**Figure 2.11**).

The first mode of failure, *net-section failure* (**Figure 2.3**), occurs when ratio between, hole diameter *d*, and plate width *w*, and the ratio between acting stress and bearing resistance, show high values.

This failure concerns the resistant section of the plate weakened by the presence of the hole, perpendicular to the direction of stress transmitted from the bolt.

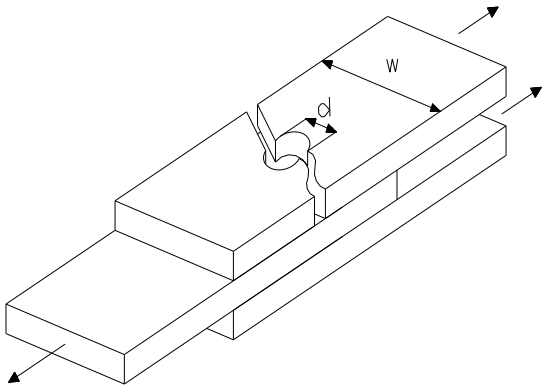

Figure 2.3. Net-section failure.

The verification of normal stresses of the resistant section of the element weakened by the presence of the holes should be carried out in relation to the following limitations [20]:

- traction force parallel to the fibre direction (**Figure 2.4**):

$$V_{Sd} \leq \frac{1}{\gamma_{Rd}} \cdot f_{Lt,Rd} \cdot (w - n \cdot d) \cdot t \,. \qquad \textbf{(2.1)}$$

- traction force orthogonal to the fibre direction (**Figure 2.5**):

$$V_{Sd} \leq \frac{1}{\gamma_{Rd}} \cdot f_{Tt,Rd} \cdot (w - n \cdot d) \cdot t \,. \qquad \textbf{(2.2)}$$

Terms in the equations **(2.1)** and **(2.2)** have following meanings:

- V_{Sd} is the force transmitted by the bolt to the element;
- γ_{Rd} is the partial model coefficient, for perforated sections assumed to be equal to 1.11;
- $f_{Lt,Rd}$ and $f_{Tt,Rd}$ are the design traction resistances of the material along the fibre direction and orthogonal to the fibre direction, respectively;
- n is the number of holes;
- t is the thickness of the FRP element.

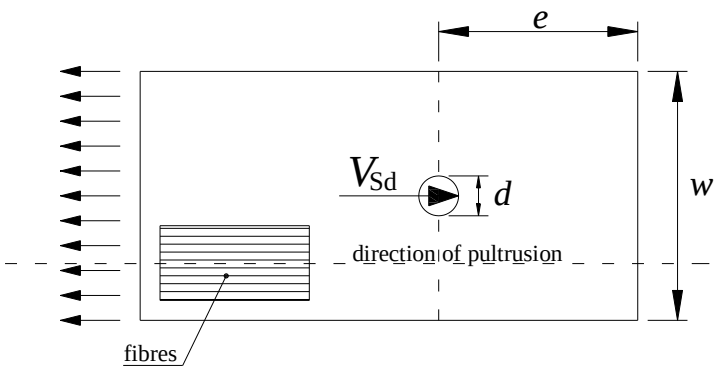

Figure 2.4. Net-section failure mode for traction force parallel to the fibre direction.

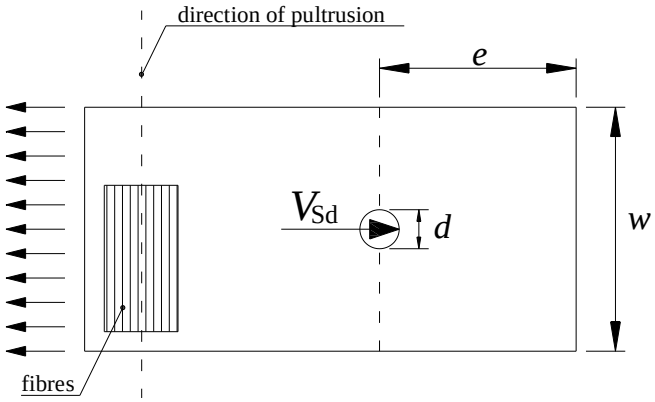

Figure 2.5. Net-section failure mode for traction force orthogonal to the fibre direction.

In the case of mono-axial strengthening, if the force V_{Sd} is inclined with a generic angle α in relation to the fibre direction, $f_{\alpha t,Rd} = f_{Tt,Rd}$ due to $\alpha > 6°$ being assumed [20].

Another failure mode is *shear-out failure* (**Figure 2.6**), which is due to shear stress parallel to shear force in the bolt. It occurs when distance *e* of the hole from the free edge of the plate is small.

The presence of holes causes, as it is well known, a weakening of the plate that can induce the occurrence of this type of failure.

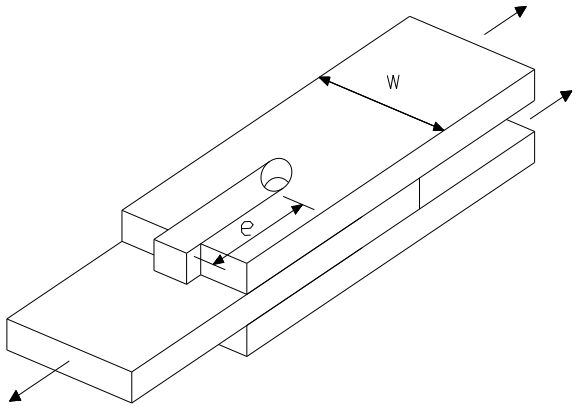

Figure 2.6. Shear-out failure.

The verification of bolt-shear failure should be carried out following (**Figure 2.7**):

$$V_{Sd} \leq f_{V,Rd} \cdot (2\,e - d) \cdot t\,, \qquad \textbf{(2.3)}$$

being $f_{V,Rd}$ the design shear resistance of the FRP element [20].

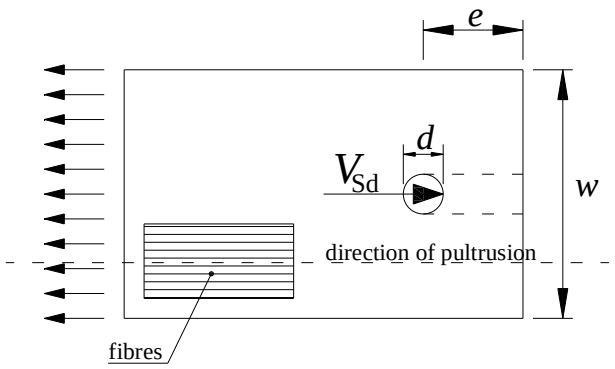

Figure 2.7. Bolt-shear failure mode.

Bearing failure concerns the zone near the hole, at the interface with the bolt (**Figure 2.8**).

It is due to compressive stresses acting on the hole surface and occurs, generally, for small value of ratio between hole diameter *d* ad plate width *w*, or between acting stress and bearing resistance.

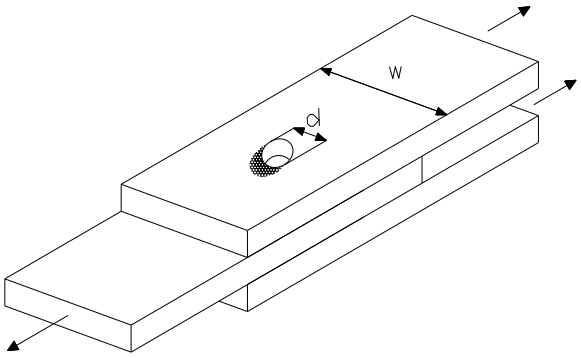

Figure 2.8. Bearing failure.

The bolts, in fact, resisting shear stress, however, can deform the plate holes in which they are, because of the diversity of materials they are made.

This failure mechanism must be opportunely investigated because, for the composite material, the zone where the failure occurs is not known “a priori”.

In verifying bearing failure, the mean value of the pressure on the shank of the bolt on the surface of the hole should satisfy the following limitations

- force parallel to the fibre direction (**Figure 2.9**):

$$V_{Sd} \leq f_{Lr,Rd} \cdot d_b \cdot t \,. \qquad \textbf{(2.4)}$$

- force orthogonal to fibre direction (**Figure 2.10**):

$$V_{Sd} \leq f_{Tr,Rd} \cdot d_b \cdot t \,. \qquad \textbf{(2.5)}$$

where $f_{Lr,Rd}$ and $f_{Tr,Rd}$, are the design resistance to bearing failure of the material in the fibre direction and orthogonal to the fibre direction, respectively [20].

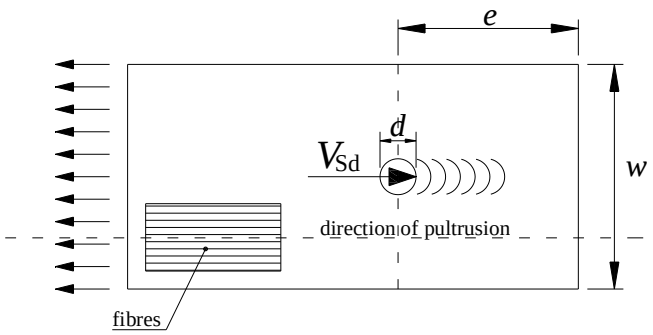

Figure 2.9. Bearing failure.

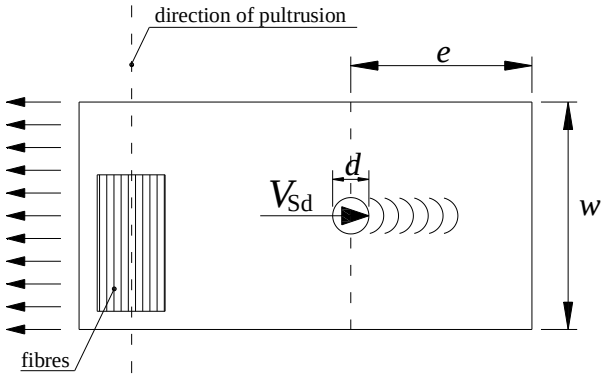

Figure 2.10. Bearing failure.

Fastener shear failure is due to high values of shear stresses in the bolts (**Figure 2.11**).

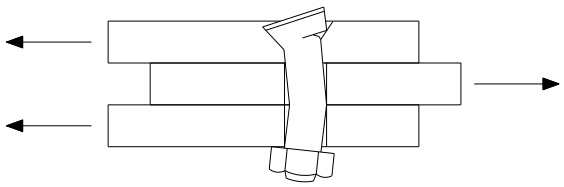

Figure 2.11. Fastener shear failure.

In the verification of shear failure of a steel bolt, the following limitation should be satisfied:

$$V_{Sd} \leq f_{Vb,Rd} \cdot A_b , \qquad \textbf{(2.6)}$$

where $f_{Vb,Rd}$ represents the shear design resistance of the bolt, as defined by the currently adopted regulations and A_b is the resistant area of the section of the bolt [20].

For joints whose bolts are subjected to tensile stress it's necessary to distinguish the failure *pull-out failure* (**Figure 2.12**) mechanism and the *bolt failure* due to strain

The first one occurs for perforation of FRP plate. It should be verified that the following results:

$$N_{Sd} \leq f_{V,Rd} \cdot \pi \cdot d_r \cdot t\,, \qquad \textbf{(2.7)}$$

where d_r is the diameter of the washer.

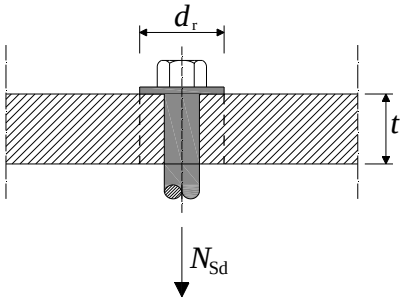

Figure 2.12. Pull-out failure mode.

Verification of steel bolt under tensile force should be carried out according to the following limitation:

$$N_{Sd} \leq F_{tb,Rd}\,, \qquad \textbf{(2.8)}$$

where $F_{tb,Rd}$ is the design strain resistance of the bolt, as defined in the currently adopted rules (**Figure 2.13**).

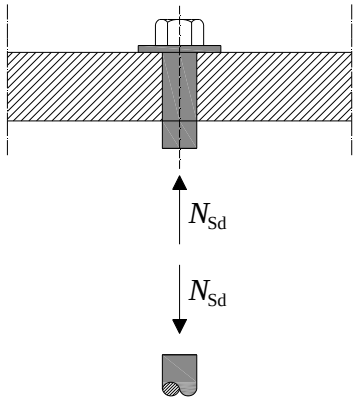

Figure 2.13. Bolt failure due to strain.

For joint with more bolts, it's possible to define one more failure mode, called *block shear* [2].

This failure occurs with the detachment of an irregular shape portion of plate, caused by a combination of normal stresses, acting perpendicular to the cross section of the element connected, and shear stresses, parallel to the shear force direction in the bolts.

This mode of failure, which occurs with a more complex mechanism than other types of failure and less manageable through known verification formulations, can be generated by different causes, or even a coexistence of these, such as distances of the bolt hole from the free edge of the plate in the direction of shear, *e* too small, the distance of the bolt

hole with respect to the free edge of the plate in the direction orthogonal to the shear stress *s*, too low, low distances between the holes .

It's possible to distinguish four different possible mechanisms, defined *Mode 1, Mode 2, Mode 3, Mode 4* (from **Figure 2.14** to **Figura 2.17**).

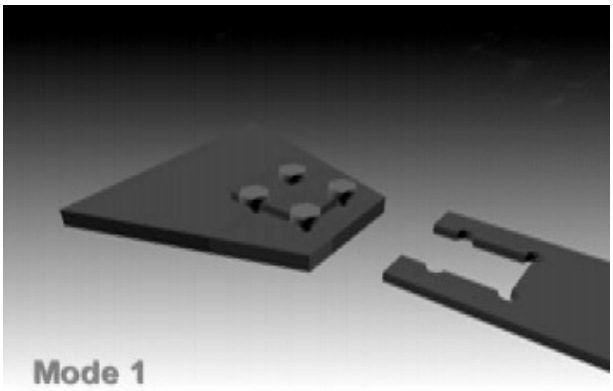

Figure 2.14. Block shear failure *Mode 1*.

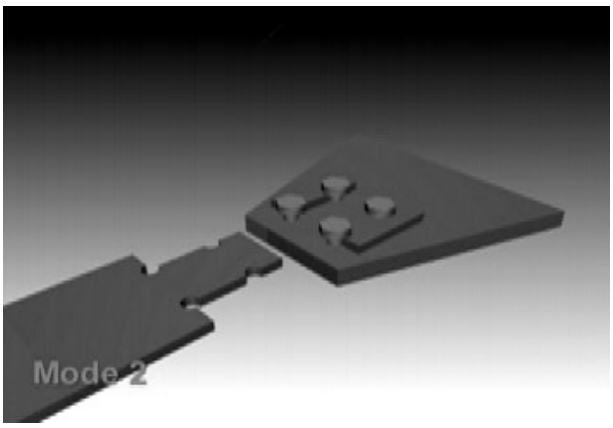

Figure 2.15. Block shear failure *Mode 2*.

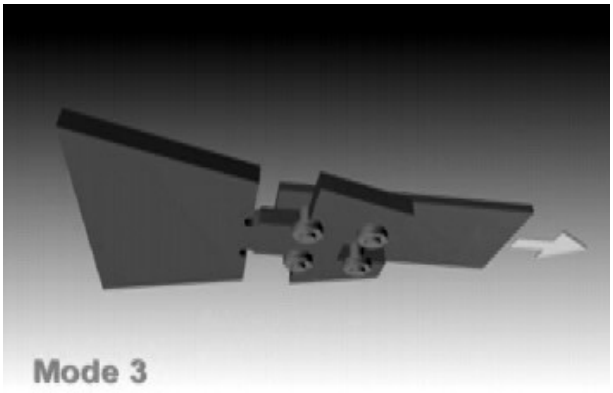

Figure 2.16. Block shear failure *Mode 3*.

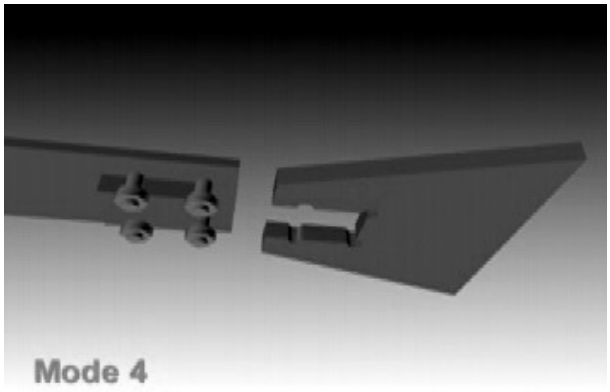

Figura 2.17. Block shear failure *Mode 4*.

Studies have shown, therefore, that the position of the bolts and the size of the specimen influence strongly failure modes of joints between composite elements.

In this regard, it is interesting to report some considerations arising from the analysis conducted by researchers R. Prabhakaran, Z. Razzaq

and S. Devara [2], who have dealt with numerical and experimental study on specimen characterized by different provisions of the bolts suggesting, at the end of this investigation, the design criteria for the two most critical failure modes for bolted joints: *block shear* and *net-section failure.*

For the *block shear* it's possible to write:

$$R_u = \phi_{BS} R_n = \phi_{BS} \left(\tau_u A_{ns} + \sigma_u A_{nt} \right). \qquad \textbf{(2.9)}$$

Nella relazione **(2.9)**:

R_u is the effective resistance of specimen in tensile test;

R_n is the nominal resistance of specimen provided by the manufacturer;

τ_u is the nominal value of shear stress;

σ_u is the nominal value of normal stress;

A_{ns} is the net area of the reagent section under shear stress;

A_{nt} is the net area of the reagent section under normal stress;

ϕ_{BS} is the *block shear* resistance factor.

In order to evaluate the failure resistance it's necessary to make a linear regression of the experimental results, not being known a priori resistant sections of the specimen for both normal and tangential stresses.

The purpose of this procedure is to determinate the resistance factor Φ_{BS}, through which, once you know the nominal resistance R_n, evalued through the equation **(2.9)**, it's possible to know the specimen effective resistance R_u.

To determinate vaules of A_{ns} and of A_{nt} it's possible to measure the portion detached in direction parallel and orthogonal to normal load, respectively.

In pictures from **Figure 2.18** to **Figure 2.21** different deterinations of *Shear area* A_{ns} and *Tension area* A_{nt} are illustrated for different modes of failure.

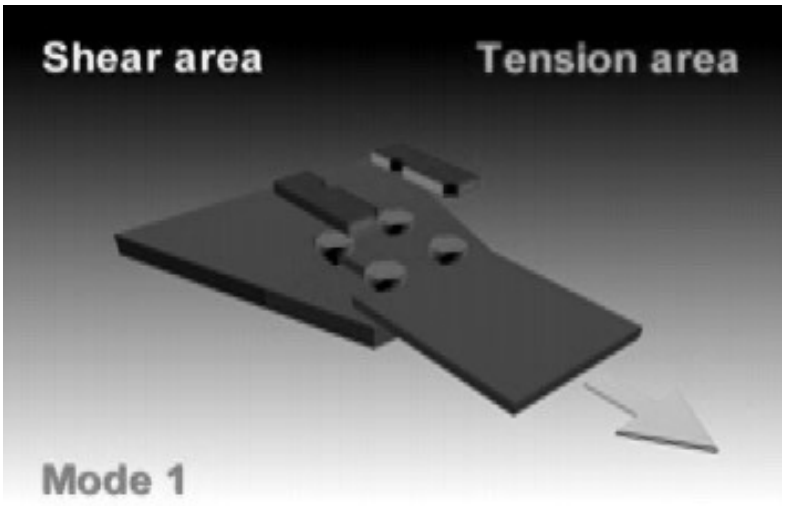

Figure 2.18. A_{ns} and A_{nt} (*block shear failure mode 1*).

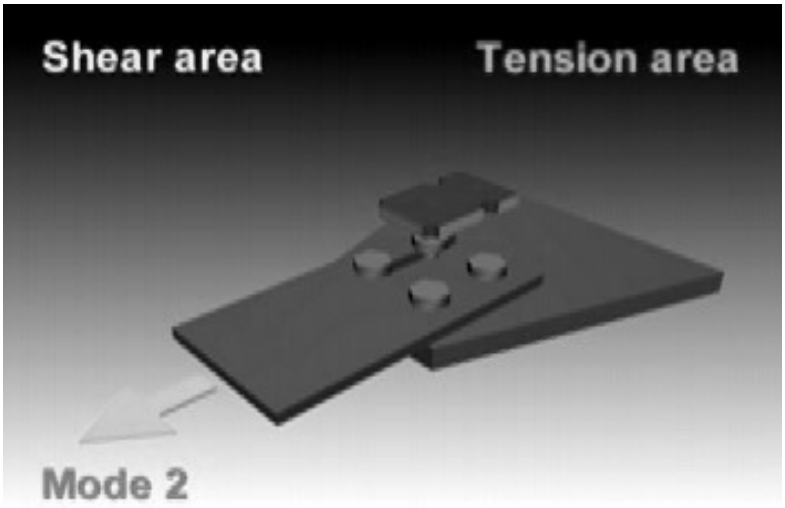

Figure 2.19. A_{ns} and A_{nt} (*block shear failure mode 2*).

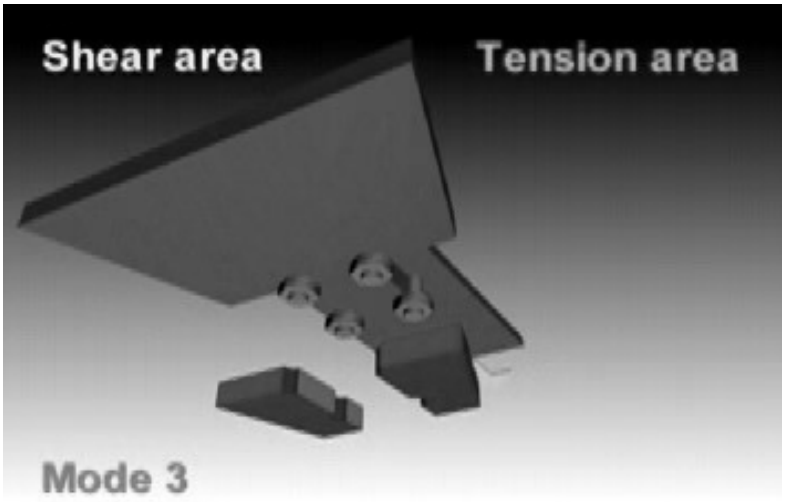

Figure 2.20. A_{ns} and A_{nt} (*block shear failure mode 3*).

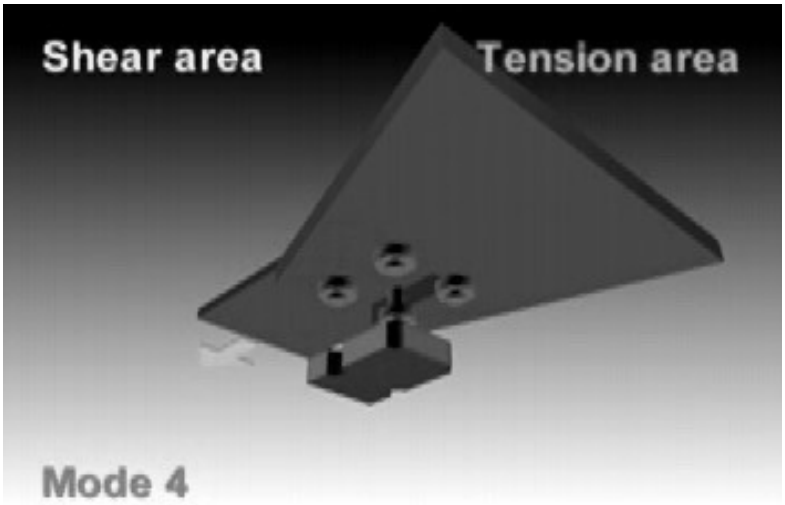

Figure 2.21. A_{ns} and A_{nt} (*block shear failure mode 4*).

It's possible, likewise, to evaluate the resistance for *net-section failure*, making a linear regression in the following equation:

$$T_u = \phi_{NT} T_n = \phi_{NT} \left(\sigma_u A_{nt} \right). \qquad \textbf{(2.10)}$$

where:

T_u is the effective resistance of specimen in tensile test;

T_n is the nominal resistance of specimen provided by the manufacturer;

σ_u is the nominal value of normal stress;

A_{nt} is the net area of the reagent section under normal stress;

ϕ_{NT} is the *net-section failure* resistance factor.

The procedure is the same as the previous case.

The final resistance of the specimen is:

$$R = \min\left(R_{BS} = \phi_{BS} R_n;\ T_{NT} = \phi_{NT} T_n\right). \qquad \textbf{(2.11)}$$

The verification consists of to satisfy the following limitation:

$$P_d \le R. \qquad \textbf{(2.12)}$$

where P_d is the applied load.

This procedure is called ***Load and Resistance Factor Design*** – **LRFD** [2].

CHAPTER III
3D FINITE ELEMENT ANALYSIS OF BOLTED JOINTS

In this chapter a 3D finite element analysis of different configurations of bolted joints is carried out to evaluate shear stress distribution, i.e. bearing stress distribution, between bolts that form the connection.

Every type of joint is obtained by varying several parameters such as:

- number of bolts;
- number of rows;
- number of bolts per row.

Furthermore, this analysis allows, for each case, to observe the extinction distance of compressive stress from the hole.

Bolted joints are analyzed using the software Straus7 of G + D Computing. In particular the following types of FRP joints, all double-overlap, are studied [21-27]:

- **Type J11**: one row of bolts, one bolt per row;
- **Type J21**: two rows of bolts, one bolt per row;
- **Type J22**: two rows of bolts, two bolts per row;
- **Type J33**: three rows of bolts, three bolts per row;
- **Type J44**: four rows of bolts, four bolts per row.

The jointed elements consist of bi-directional multilayer symmetrical composites reinforced with glass fibre (*Glass-Fiber Reinforced Polymer – GFRP*). The bolts used are of stainless steel class 8.8 and their diameter d_b is equal to 14 mm.

This value as well as the distances between the holes, the distances of the holes from the edge and the hole diameter, used for each of the previously mentioned configurations, correspond to the limit values suggested in the Technical Document CNR-DT 205/2007 [20] (**Table 3.1**). These terms are shown in **Figure 3.1**.

Table 3.1. Geometric limitations relative to a bolted joint.

Bolt diameter (recommended)	$t_{min} \leq d_b \leq 1.5 \cdot t_{min}$ $d_b \geq t_{min}$
Hole diameter	$d \leq d_b + 1$ mm
Washer diameter	$d_r \geq 2 \cdot d_b$
Distances between holes	$w_x \geq 4 \cdot d_b$ $w_y \geq 4 \cdot d_b$
Distances from edges	$e/d_b \geq 4$ $s/d_b \geq 1/2 \cdot (w_y/d_b)$

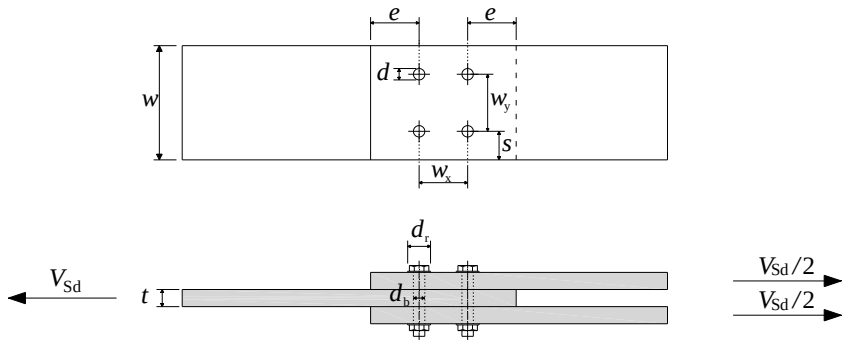

Figure 3.1. Bolted Joint.

In detail, the distance used between the holes is equal to 60 mm, the distance of the holes from the edge is respectively equal to 60 mm in the load direction and equal to 30 mm in the direction orthogonal to the load.

So, once known both the number of bolts and the number of rows, the geometry is fixed for each joint (from **Figure 3.2** to **Figure 3.6**).

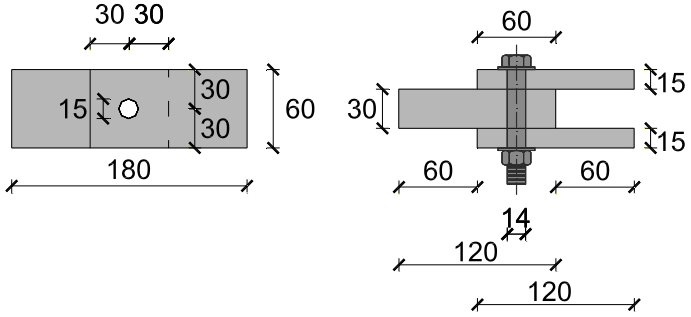

Figure 3.2. Joint J11.

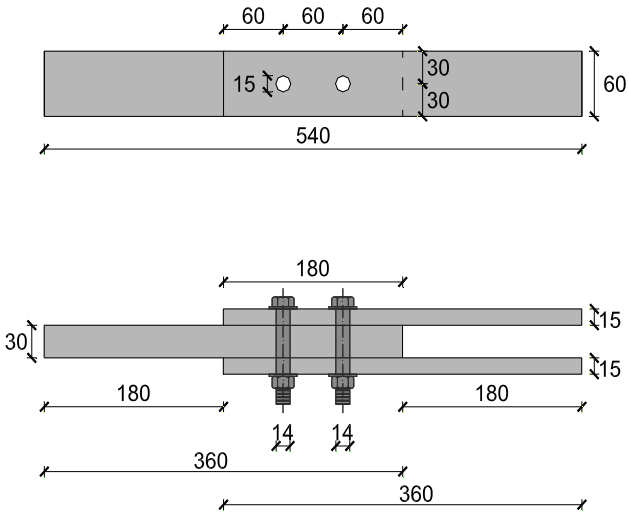

Figure 3.3. Joint J21.

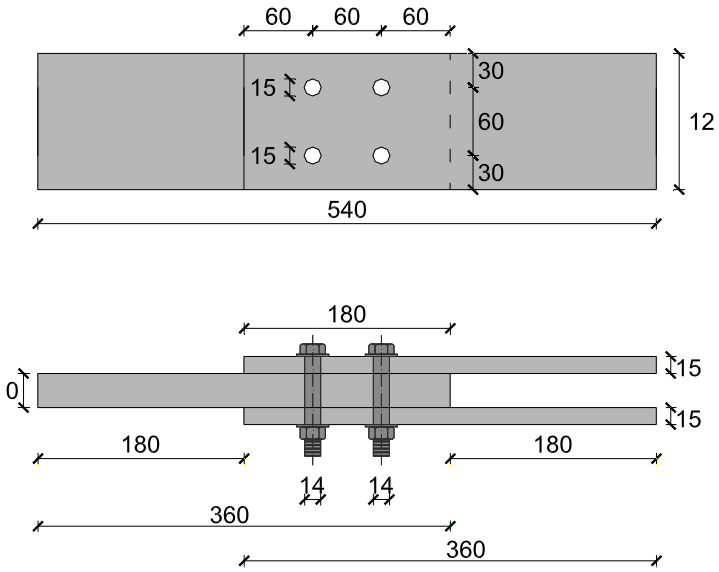

Figure 3.4. Joint J22.

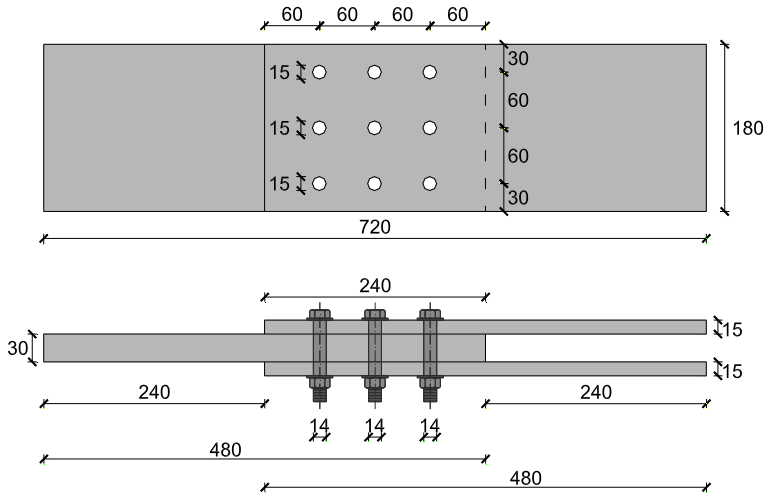

Figure 3.5. Joint J33.

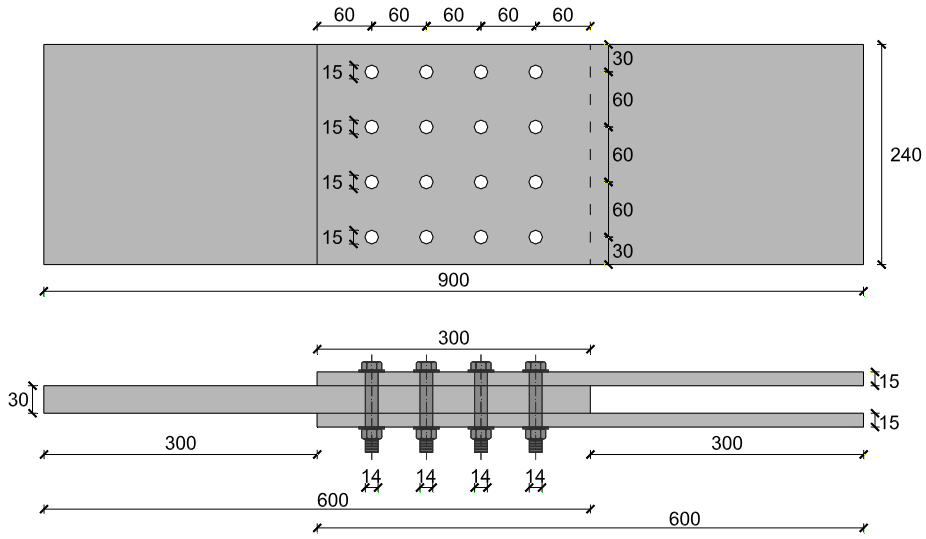

Figure 3.6. Joint J44.

The joints are modelled by using eight-nodes orthotropic finite elements (bricks), while one-dimensional *point-contact elements* are used to simulate the contact between the bolt and the FRP plates. The mechanical properties of the bricks are reported in **Table 3.2**.

Table 3.2. Mechanical properties.

$\mathbf{E_x}$ [MPa]	$\mathbf{E_y}$ [MPa]	$\mathbf{E_z}$ [MPa]	$\mathbf{G_{xy}}$ [MPa]	$\boldsymbol{\nu_{xy}}$
25000	25000	8500	3000	0.23

where:

- $\mathbf{E_x}$ is the Young modulus in fiber direction and orthogonal to tensile load direction;
- $\mathbf{E_y}$ is the Young modulus in fiber direction and parallel to tensile load direction;
- $\mathbf{E_z}$ is the Young modulus and orthogonal to plane x-y;
- $\mathbf{G_{xy}}$ is shear modulus in the plane x-y;
- $\boldsymbol{\nu_{xy}}$ is Poisson modulus in the plane x-y.

3.1. Joint J11 - J21 - J22

Joint J11 (**Figure 3.7**) has two external square plates with a length equal to 60 mm and thickness to 15 mm. The internal plate has a length equal to 120 mm along the *y* axis, a width equal to 60 mm along the *x* axis and a thickness equal to 30 mm.

In the section E-E of both external plates, a tensile load is applied equal to 10 MPa, while the internal plate is locked in the section I-I (**Figure 3.7**). In **Figure 3.8** the finite element mesh is illustrated.

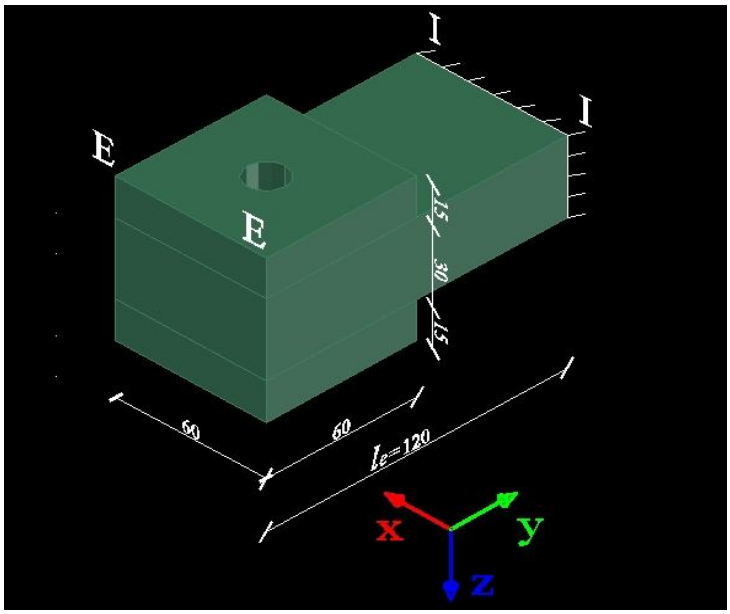

Figure 3.7. Joint J11 (dimensions in mm).

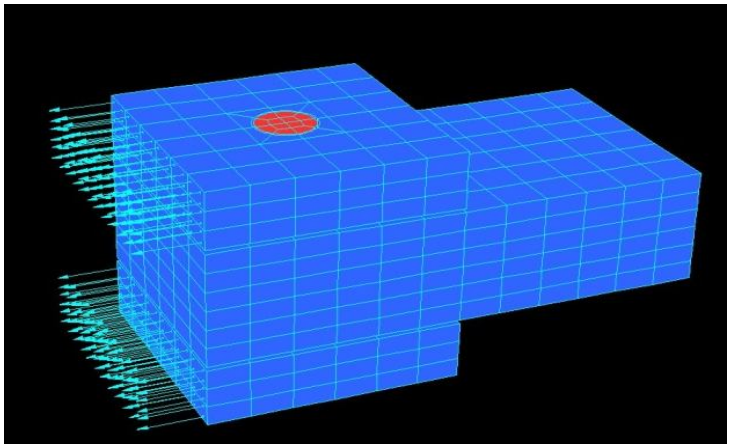

Figure 3.8. Mesh of joint J11.

In **Figure 3.9a)** and **Figure 3.9b)**, the normal stress distribution σ_{yy} is reported at the interface bolt-hole for each plate of joint J11.

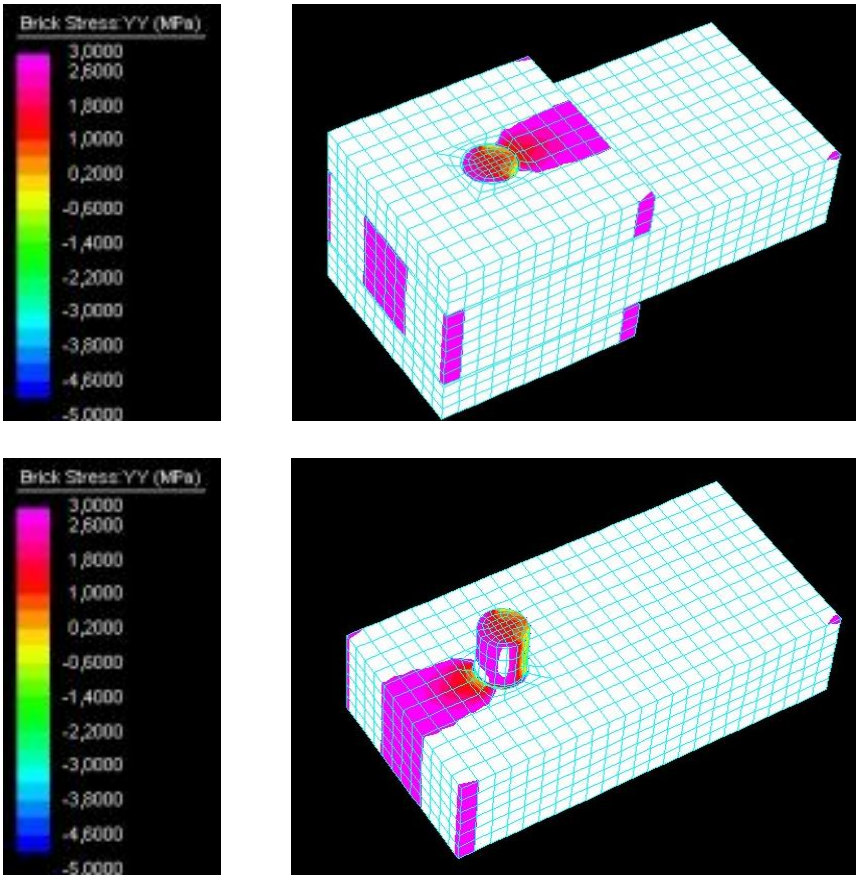

Figure 3.9. Normal stress distribution σ_{yy} around the hole in the joint J11; a) external plates; b) internal plate.

The second joint studied, J21, has two rows of bolts and one bolt per row. The external plates have a length equal to 180 mm, a width equal to 60 mm and thickness equal to 15 mm, while the internal one has a length equal to 360 mm, a width equal to 60 mm and a thickness equal to 30

mm (**Figure 3.10**). The load applied and constraints considered are the same ones adopted for the joint J11. The mesh is reported in **Figure 3.11**.

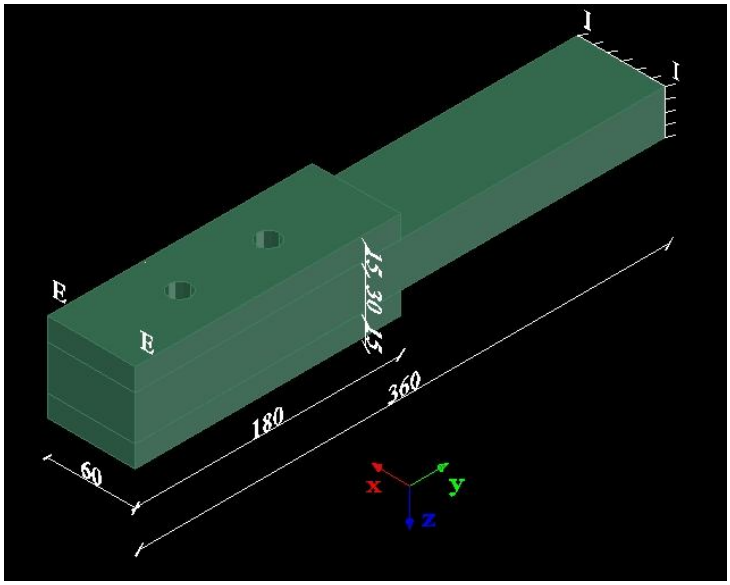

Figure 3.10. Joint J21 (dimensions in mm).

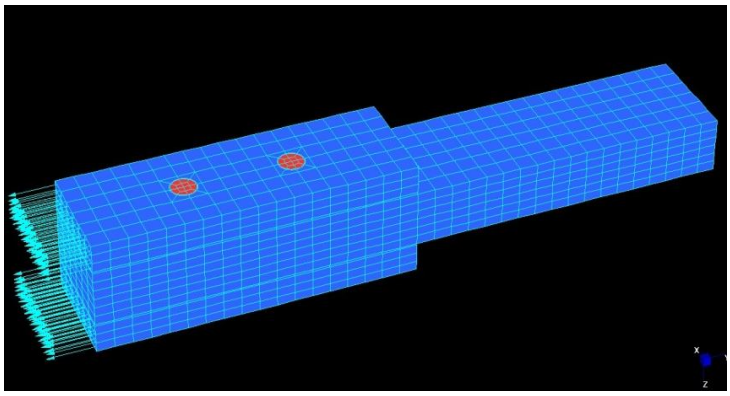

Figure 3.11. Mesh of joint J21.

In **Figure 3.12a)** and **Figure 3.12b)**, the normal stress distribution σ_{yy} is reported at the interface bolt-hole for each plate.

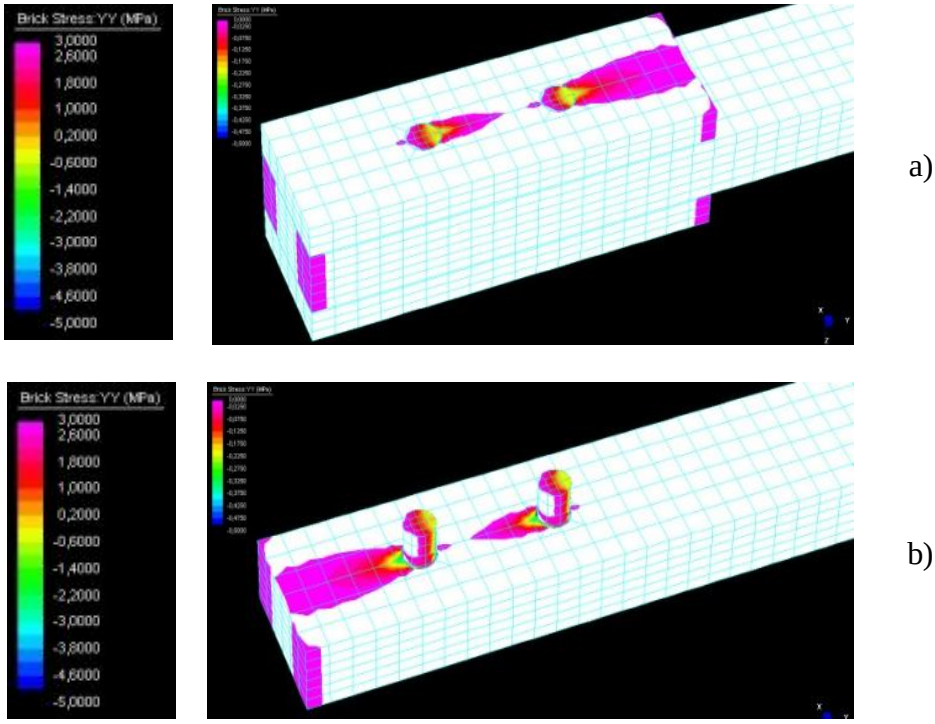

Figure 3.12. Normal stress distribution σ_{yy} around the hole in the joint J21; a) external plates; b) internal plate.

The joint J22, characterized by two rows of bolts and two bolts per row, has a length equal to 180 mm, a width equal to 120 mm and a thickness equal to 15 mm for the external plates, while, for the internal one, the length is the same as for the joint J21, the width is equal to 120 mm and the thickness is equal to 30 mm (**Figure 3.13**). The load applied

and constraints considered are the same as for the joint J11. The mesh is reported in **Figure 3.14**.

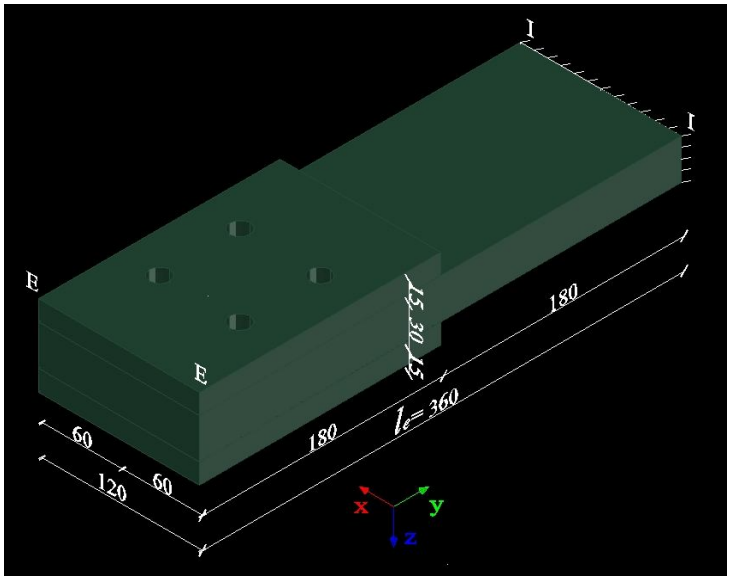

Figure 3.13. Joint J22 (dimensions in mm).

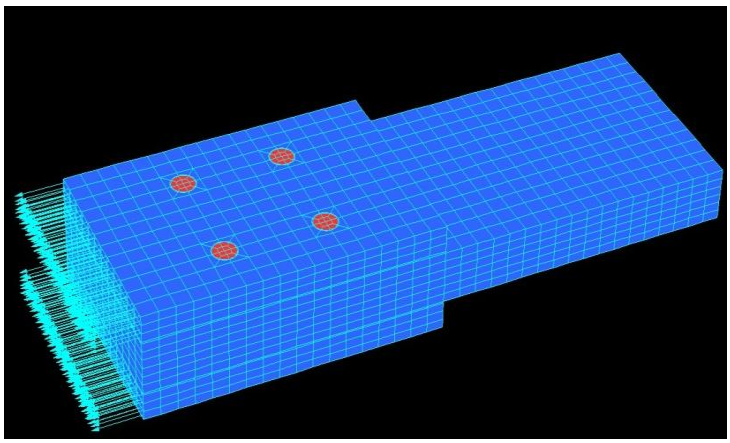

Figure 3.14. Mesh of joint J22.

In **Figure 3.15**, the normal stress state σ_{yy} is presented at the interface bolt-hole for each plate.

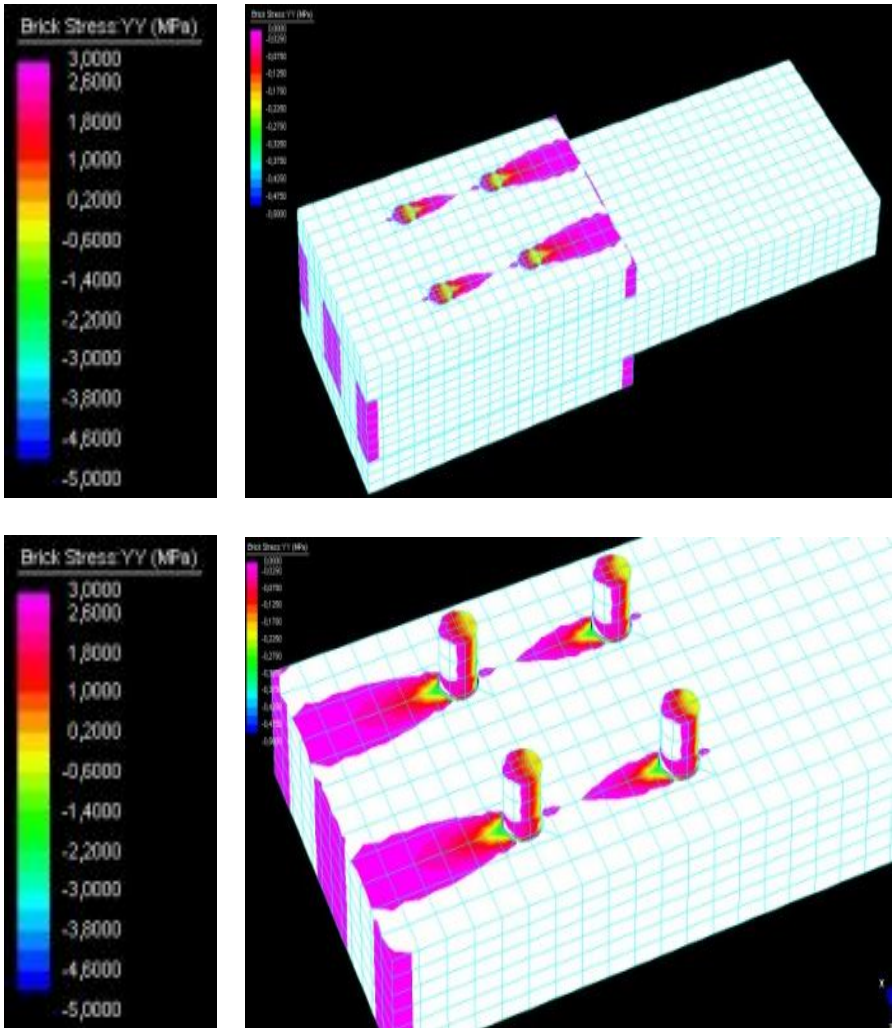

Figure 3.15. Normal stress distribution σ_{yy} around the hole in the joint J22; a) external plates; b) internal plate.

3.2. Joint J33 - J44

Joint J33, characterized by three rows of bolts and three bolts per row, has a length equal to 240 mm, a width equal to 180 mm and a thickness equal to 15 mm for the external plates, while, for the internal one, the length is equal to 480 mm, the width is equal to 180 mm and the thickness is equal to 30 mm (**Figure 3.16**).

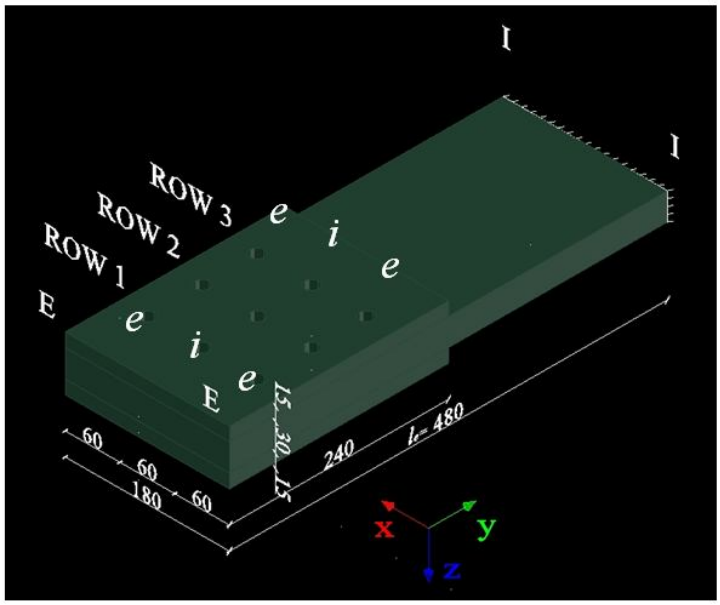

Figure 3.16. Joint J33 (dimensions in mm).

The load applied and constraints considered are the same as for the joint J11. The mesh is reported in **Figure 3.17**.

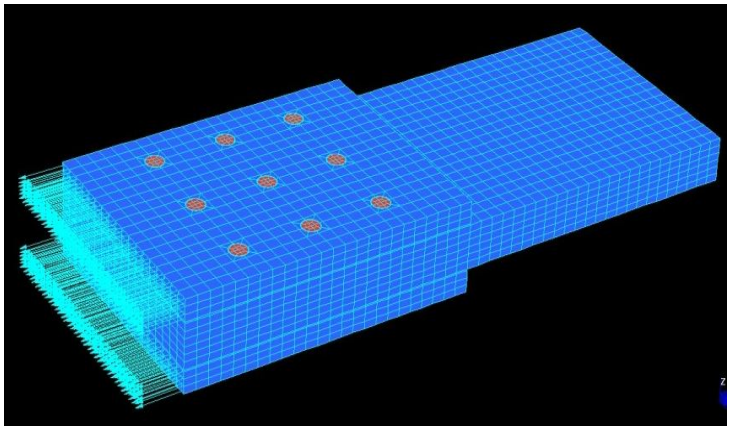

Figure 3.17. Mesh of joint J33.

In **Figure 3.18**, the normal stress state σ_{yy} is presented at the interface bolt-hole for each plate.

In this case, it is interesting to determine, due to it not being as immediate as in the previous cases, the shear stress distribution coefficients for each bolt and each row of bolts (**Table 3.3**).

These coefficients are equal to 28% for central row 2 and 36% for the external rows 1 and 3 (**Figure 3.16**).

In addition, the stress distribution is symmetrical in relation to the central row, with the external bolts (e) of each row resulting more loaded than the internal one (i) (**Figure 3.16**).

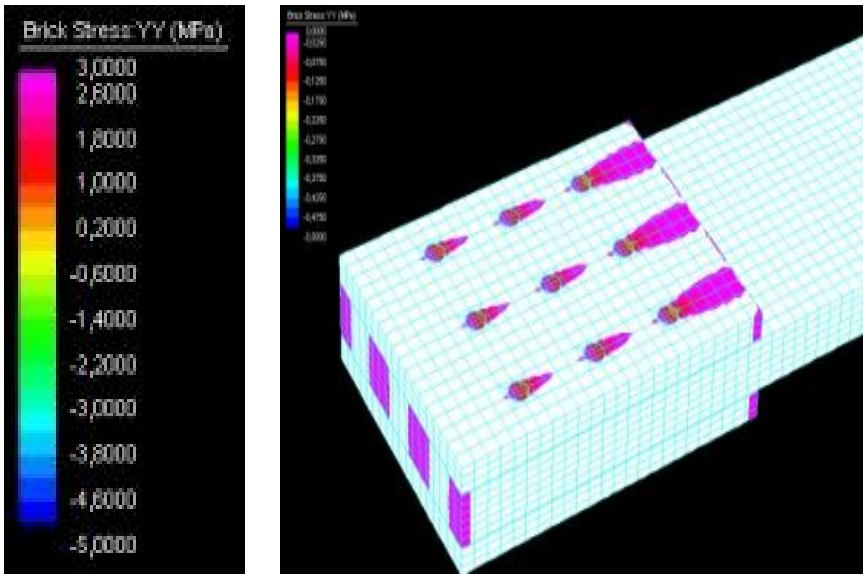

a)

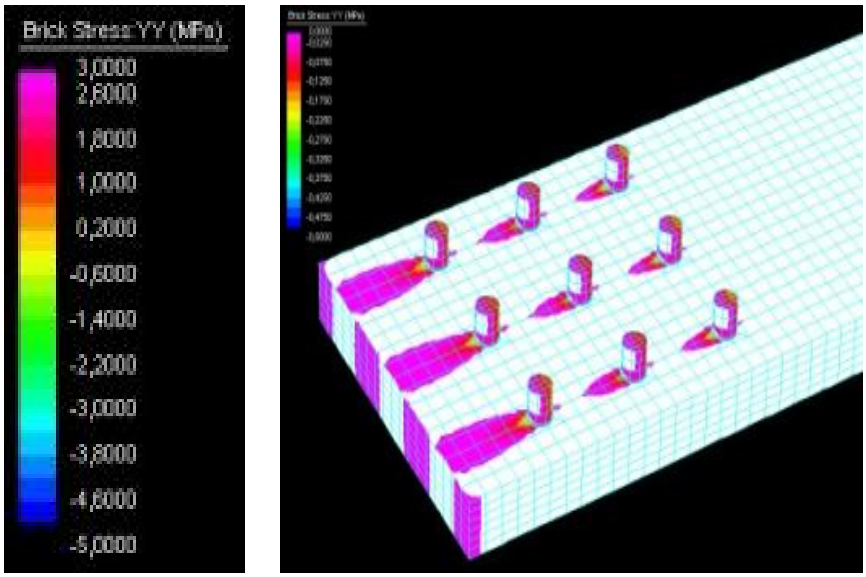

b)

Figure 3.18. Normal stress distribution σ_{yy} around the hole in the joint J33; a) external plates; b) internal plate.

Table 3.3. *Shear stress distribution coefficients* for each bolt and each row of bolts obtained by FEM analysis-J33.

Joint **J33**	**Row 1** **[%]**	**Row 2** **[%]**	**Row 3** **[%]**
e	12.1	9.4	12.1
i	11.8	9.2	11.8
e	12.1	9.4	12.1
Total	**36.0**	**28.0**	**36.0**

The last joint type studied is illustrated in **Figure 3.19**. J44 has four rows of bolts and four bolts per row. The external plates length is equal to 300 mm, the width equal to 240 mm and thickness equal to 15 mm, while the internal one has a different length, equal to 600 mm, and a different thickness equal to 30 mm (**Figure 3.19**).

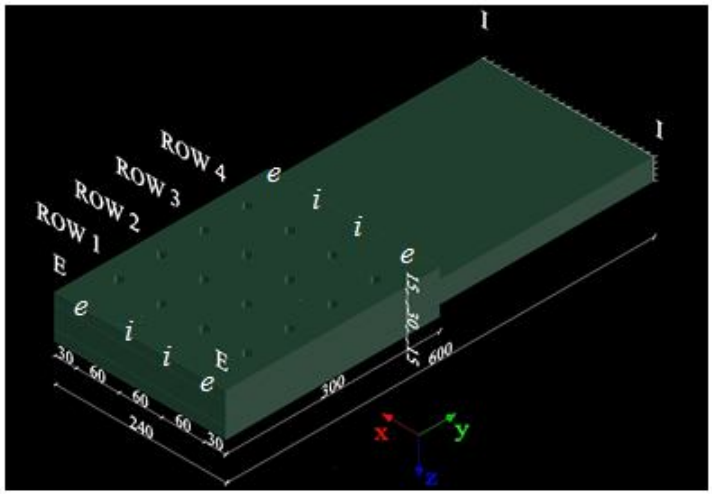

Figure 3.19. Joint J44 (dimensions in mm).

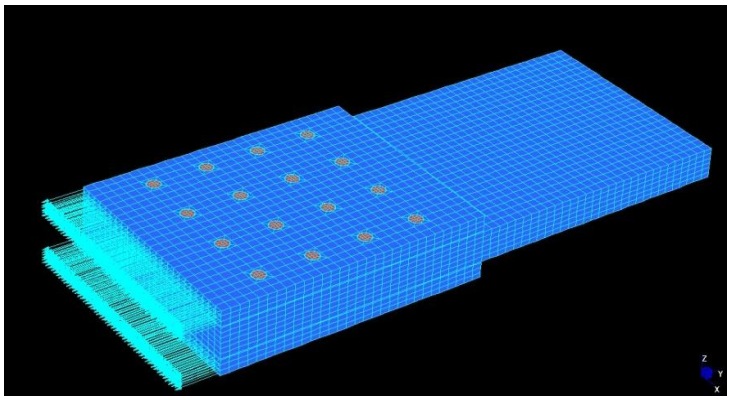

Figure 3.20. Mesh of joint J44.

The load applied and constraints considered are the same as for the joint J11.

Figure 3.21 shows the normal stress distribution σ_{yy} around the sixteen holes of the plates.

In this case, the shear stress distribution coefficients values are determined for each row and each bolt.

They are reported in **Table 3.4**. These coefficients are equal to 31% for the external rows (row 1 and 4) and 19% for the internal ones. In this case, the stress state is also symmetrical, with the external bolts (e) of each row being more loaded than the internal ones (i) (**Figure 3.19**).

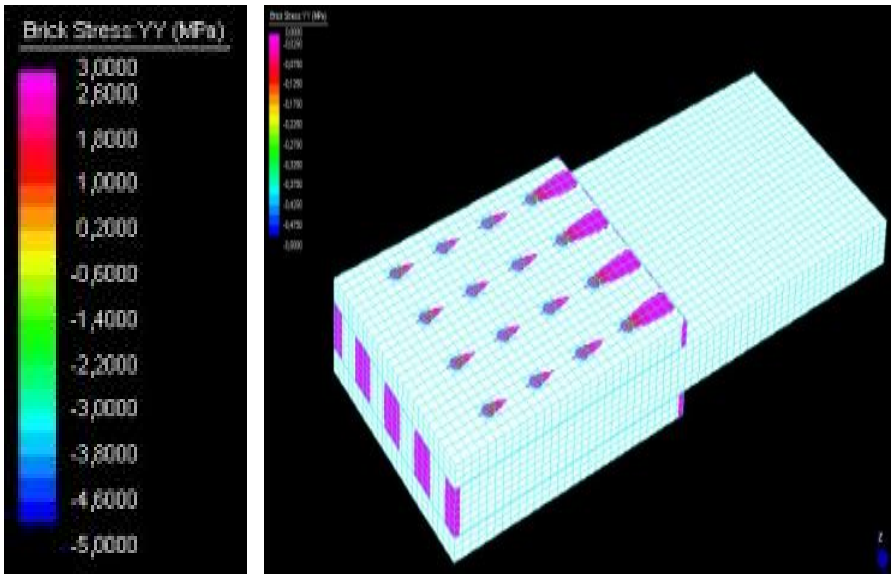

a)

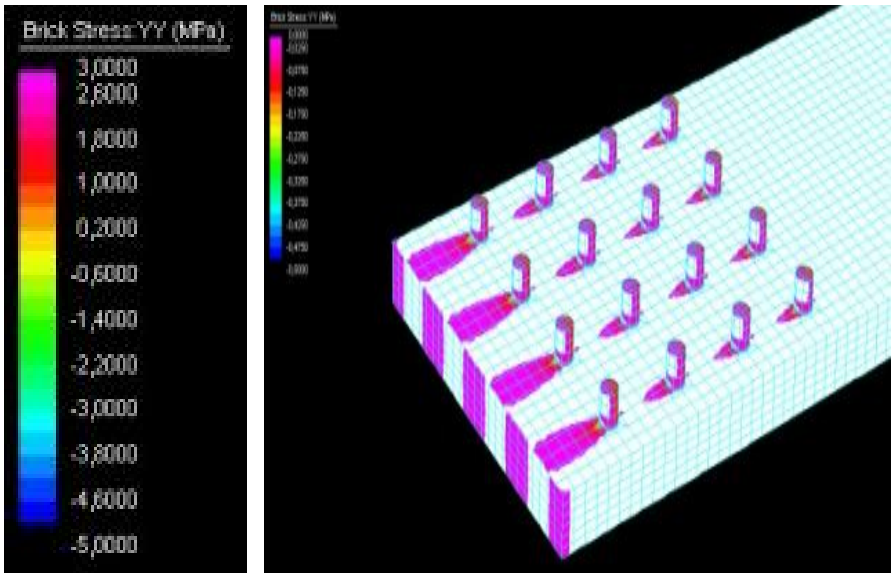

b)

Figure 3.21. Normal stress distribution σ_{yy} around the hole in the joint J44; a) external plates; b) internal plate.

Table 3.4. *Shear stress distribution coefficients* for each bolt and each row of bolts obtained by FEM analysis-J44.

Joint **J44**	**Row 1 [%]**	**Row 2 [%]**	**Row 3 [%]**	**Row 4 [%]**
e	7.9	4.9	4.9	7.9
i	7.6	4.6	4.6	7.6
i	7.6	4.6	4.6	7.6
e	7.9	4.9	4.9	7.9
Total	**31.0**	**19.0**	**19.0**	**31.0**

3.3. Comparison of results

The *shear stress distribution coefficients* values reported in **Table 3.5** are obtained through a finite element numerical analysis, while the values suggested by the Technical Document CNR-DT 205/2007 are reported in following tables.

These values are *normalized with respect of the resulting shear stress*.

Table 3.5. Shear stress distribution coefficients for each row of bolts obtained by FEM analysis.

Joint	**Row 1 [%]**	**Row 2 [%]**	**Row 3 [%]**	**Row 4 [%]**
J11	100	-	-	-
J22	50	50	-	-
J33	**36**	**28**	**36**	-
J44	**31**	**19**	**19**	**31**

Table 3.6. Shear stress distribution coefficients for each row of bolts suggested by CNR-DT 205/2007 and normalized with respect of the shear stress resulting.

Joint	Row 1 [%]	Row 2 [%]	Row 3 [%]	Row 4 [%]
J11	100	-	-	-
J22	50	50	-	-
J33	**41**	**18**	**41**	-
J44	**29**	**21**	**21**	**29**

Comparing the results reported in **Table 3.5** with those in **Table 3.6**, the coefficients obtained for joint J44 are almost coincident, while for joint J33, there are percentage differences respectively equal to **13.8%** for external rows and **55.5%** for the internal one.

Joints with a number of rows greater than four are not recommended.

Summarizing joints J11, J21 and J22 are used to test the meshed model. Contrariwise joints J33 and J44 show, in **Figure 3.22** and in **Figure 3.23** the mentioned percentages of distribution.

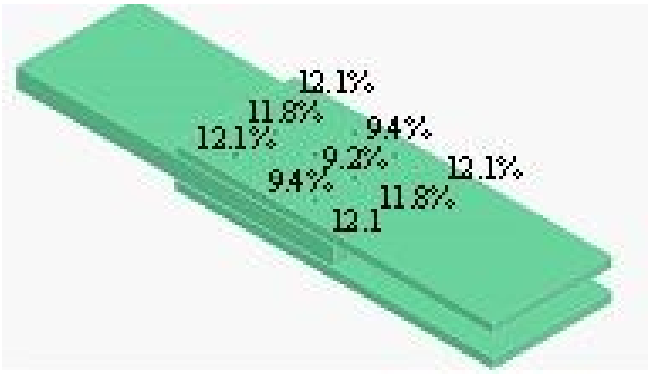

Figure 3.22. Distribution of stresses J33.

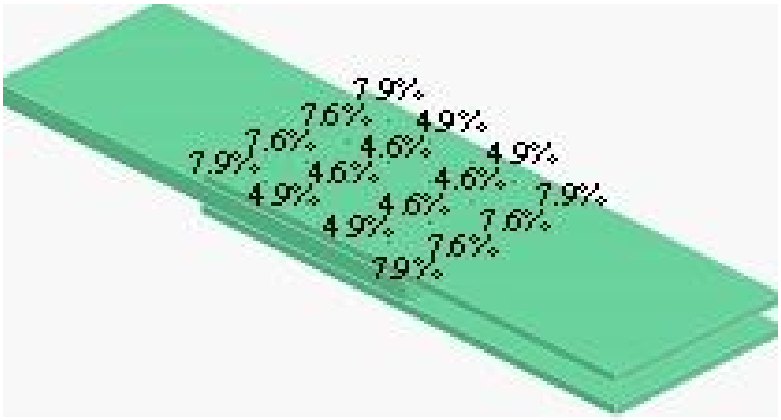

Figure 3.23. Distribution of stresses J44.

CHAPTER IV
EXPERIMENTAL ANALYSIS OF BOLTED JOINTS

At the same, an experimental investigation, carried out at the Material and Structure Laboratory of the Department of Civil Engineering of the University of Salerno, is presented in order to validate the numerical results obtained in the previous chapter.

For this purpose, different types of bidirectional GFRP joints, the same studied in the numerical analysis, are tested. All of them were fabricated by vacuum laminating 24 sheets of bidirectional glass fibre and two plies of chopped strand mat, impregnated with epoxy resin.

The volume fractions of the fibres and matrix respectively are approximately equal to 65% and 35% [21-27].

In detail joint J21 and J33 are tested and results are presented in this chapter. Their geometrical parameters are the same used for the numerical analysis as well as stainless steel bolts, while mechanical parameters of GFRP are shown in **Table 4.1**.

Table 4.1. Mechanical properties of the GFRP.

Property	Value [MPa]
Tensile limit strength, 0°	310
Tensile limit strength, 90°	310
Compressive limit strength, 0°	381
Compressive limit strength, 90°	381
Modulus of elasticity, 0°	25.000
Modulus of elasticity, 90°	25.000

4.1. Experimental set-up

For the experimental tests, an universal machine SCHENCK Hydropolus S56 was used (**Figure 4.1**). This machine consists of a hydraulic piston with a loading capacity of +/- 630 kN, stroke of +/- 125 mm and a self-balanced steel frame used to counteract the axial loadings. The machine works both under displacement and load control.

In order to measure displacements, the testing machine is equipped with an LVDT, while the tension/compression loads are controlled by means of a load cell [21-27].

Figure 4.1. Universal machine SCHENCK Hydropolus S56.

An experimental system was set up in order to carry out all the tests, made up of a test device as well as a sophisticated automatic data acquisition system with three ‘‘System 5100 Vishay MM" switchboards, set out in parallel with 60 extensometric channels (**Figure 4.2**).

Figure 4.2. System 5100 Vishay MM.

Furthermore, a pressure mapping system is used to measure bearing stresses at bolt-hole interface.

In fact this system has flexible sensors , ***GRIP*™ 4255N** of **Tekscan** that have been placed in the holes on the edge where the action of bearing stress is expected (**Figure 4.3**).

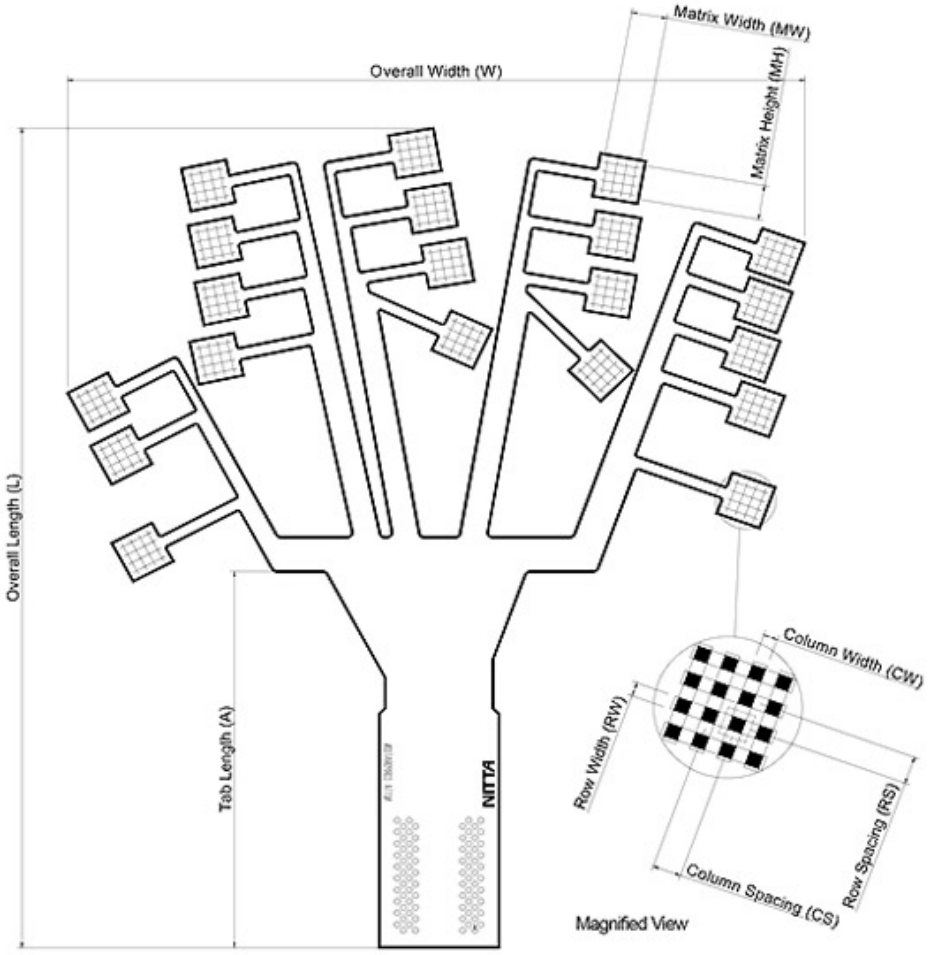

	General Dimensions			Sensing Area Dimensions									
	Overall Length	Overall Width	Tab Length	Matrix Width	Matrix Height	Columns			Rows			Total No.of	Resolution
Model	L	W	A	MW	MH	CW	Pitch CS	Qty.	RW	Pitch RS	Qty.	Sensels	Sensel Density
US	(in.)	(in.)	(in.)	(in.)	(in.)	(in.)	(in.)		(in.)	(in.)			(sensel per sq. in.)
4255N	14.17	12.13	6.5	0.63	0.63	0.079	0.157	4	0.079	0.157	4	320	40.3
Metric	(mm)	(mm)	(mm)	(mm)	(mm)	(mm)	(mm)		(mm)	(mm)			(sensel per sq. cm)
4255N	360.0	308.0	165.0	16.0	16.0	2.0	4.0	4	2.0	4.0	4	320	6.3

Figure 4.3. Sensor ***GRIP*™ 4255N** of **Tekscan**.

The sensors and their arrangement in the holes are illustrated in **Figure 4.4**.

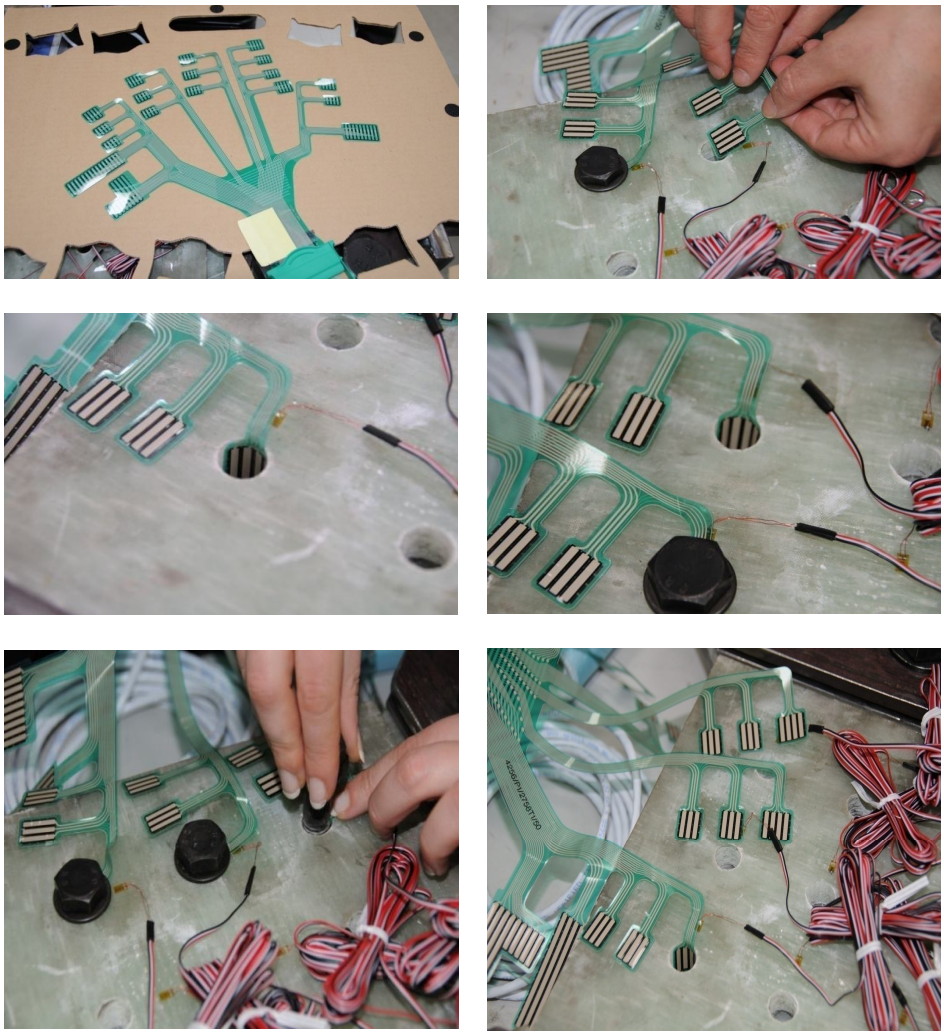

Figure 4.4. Sensors and their arrangement in the holes.

All the FRP specimens are equipped with several pairs of strain gauges, placed on both sides.

The gauges used (C2A-06.062LR-120 Vishay MM) are rectangular (**Figure 4.5**).

They are placed near the hole to measure the deformation of this zone where bearing stresses act.

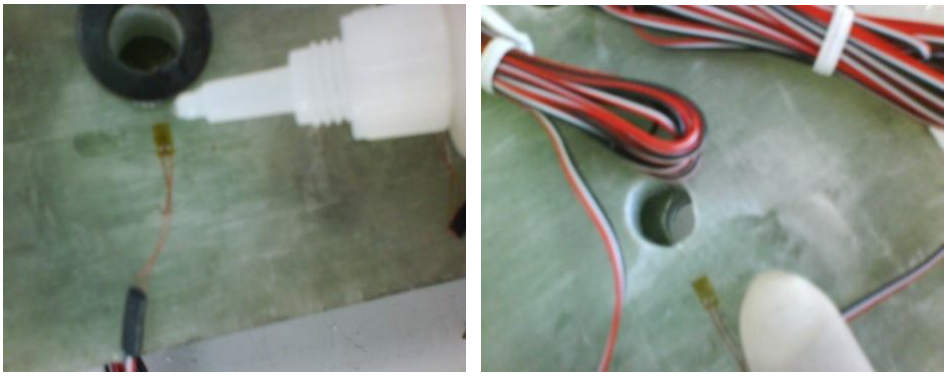

Figure 4.5. Strain gauges C2A-06.062LR-120 Vishay MM.

4.2. Joint J21 – Test description

The joint J21 has only one row with two bolts. It's placed in the machine by using two attack devices made of steel [27].

It consists of five steel plates, two of which are welded on a bracket above, also of steel, and inside the GFRP specimen is housed , while the other three are fixed on another steel support and inside the part of the joint that consists of two plates is housed.

The connection between GFRP plates and steel support is realized by bolting.

In **Figure 4.6** is shown the specimen in the test machine

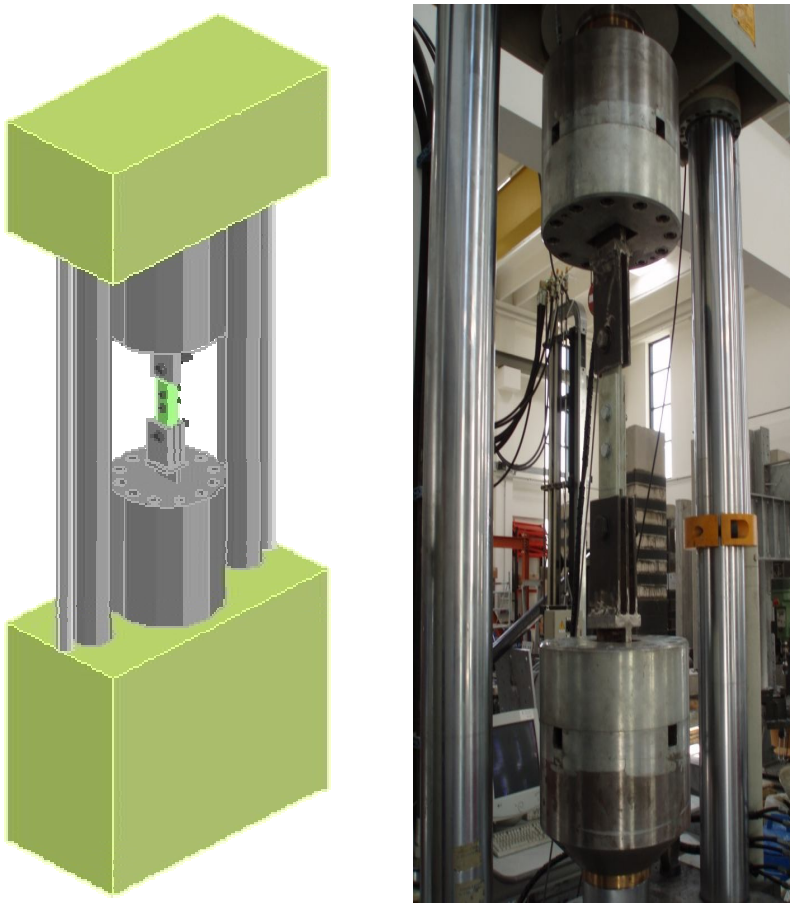

Figure 4.6. Joint J21 in the test machine.

In **Figure 4.7** the geometric characteristics of the specimen size of both the joint J21 and bolts that form the connection under study and that connect GFRP plates to steel support is shown.

In **Figure 4.8** the design of test device is illustrated.

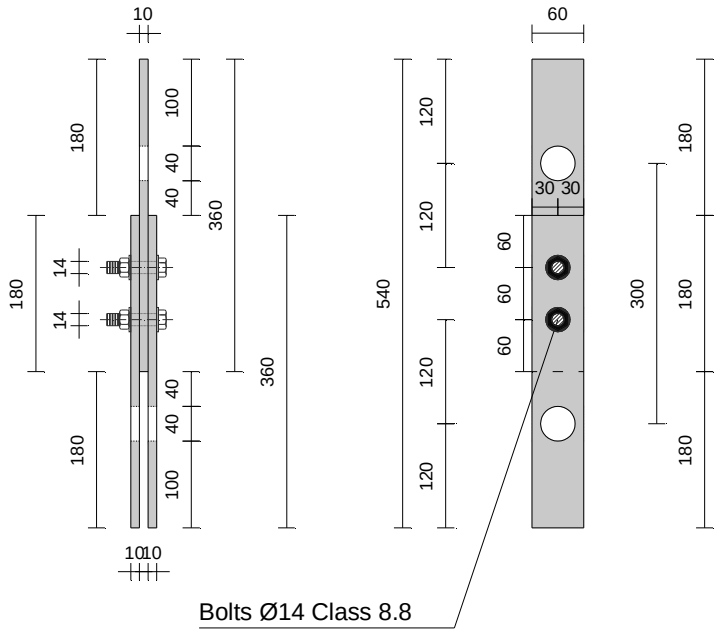

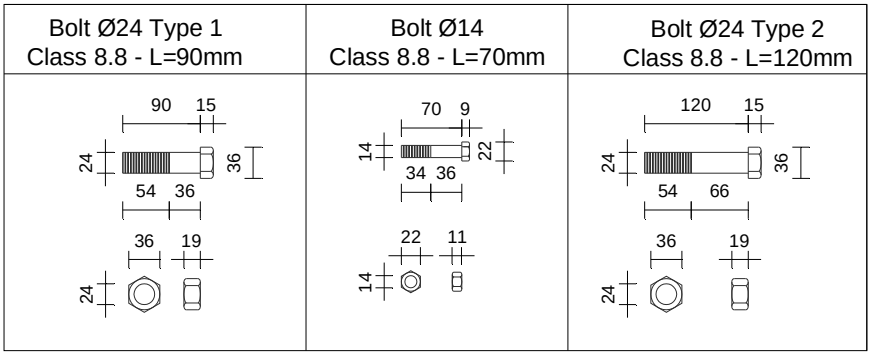

Figure 4.7. Geometry and bolting of joint J21.

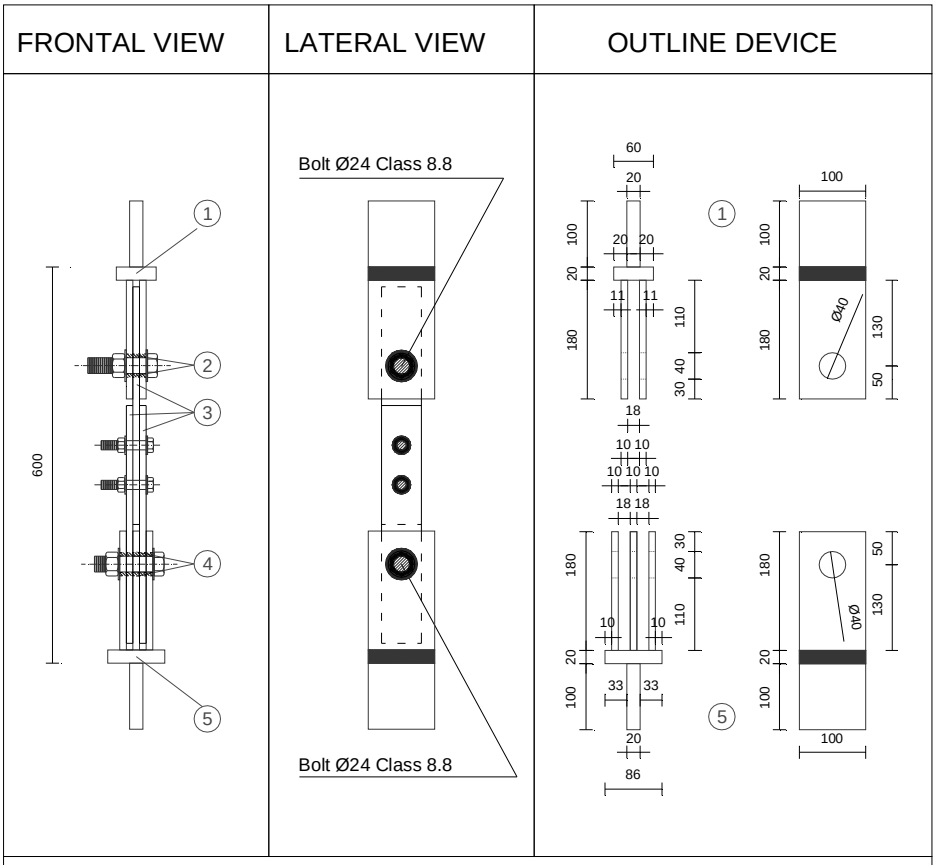

LEGEND
① UPPER STEEL JAW
② UPPER STEEL TUBE ($Ø_i$=25mm ; $Ø_e$=35mm ; L=38mm)
③ GFRP SPECIMENS
④ LOWER STEEL TUBE ($Ø_i$=25mm ; $Ø_e$=35mm ; L=66mm)
⑤ LOWER STEEL JAW

Figure 4.8. Design of test device.

The assembling of joint J21 is shown in **Figure 4.9**.

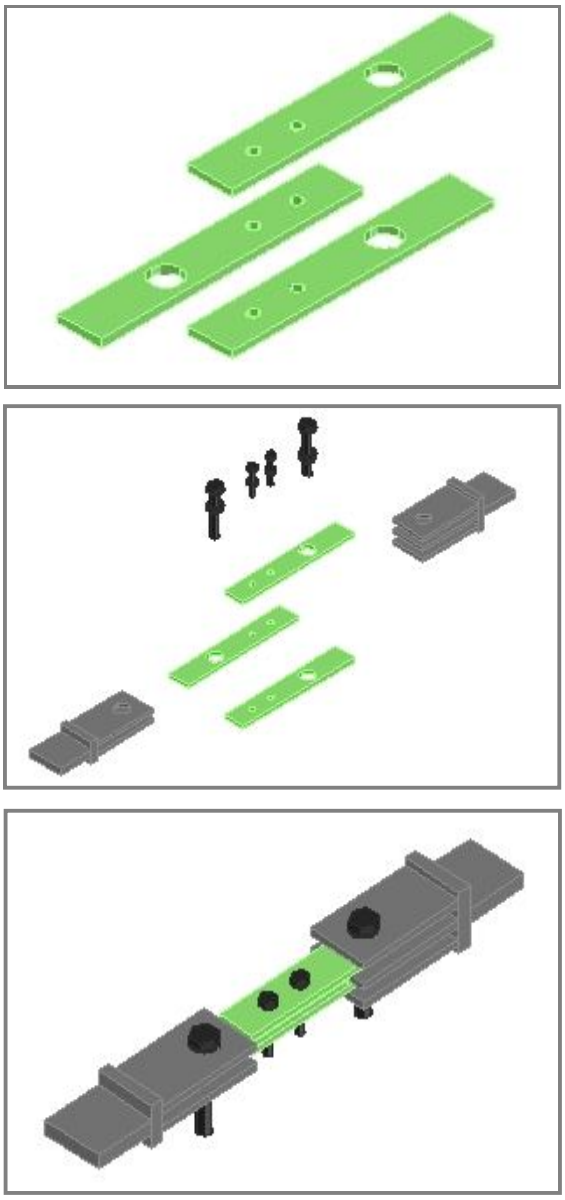

Figure 4.9. Assembling of joint J21.

Steel supports are reported in **Figure 4.10**.

Figure 4.10. Steel supports.

The joint J21, subjected to tensile test, exhibited a peculiar failure mode, very similar to the block shear, showing a delamination in the end section.

It occurred because the ratio between hole diameter *d* and plate width *w* is high.

The delamination occurred in the upper layers of the specimen where there is a change of fiber inclination from 0° to 90° (**Figure 4.11**).

In **Figure 4.12** failure surfaces A1, A2, and A3 are shown.

This failure mode is due to the action of both the normal stresses and shear stresses. But not knowing the real failure mechanism, three hypotheses are assumed.

In the first case *net-section failure* occurs before the *delamination*. In the second *delamination* occurs before *net-section failure* and in the last

hypothesis both *net-section failure* and *delamination* occur at the same time [27].

Figure 4.11. Joint J21 failure.

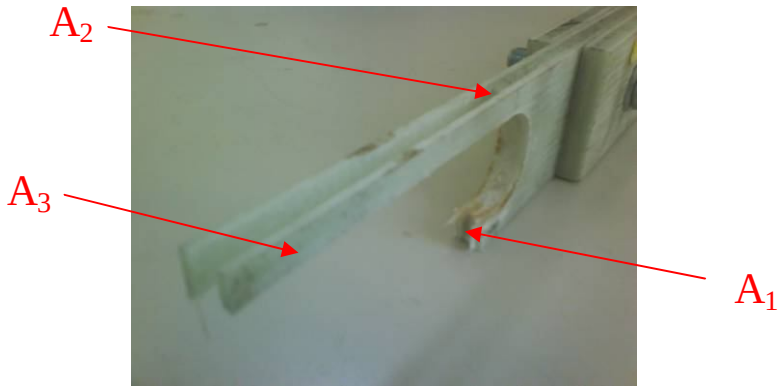

Figure 4.12. Failure surfaces.

In **Figure 4.13** it's possible to observe the global view of the failure of this specimen.

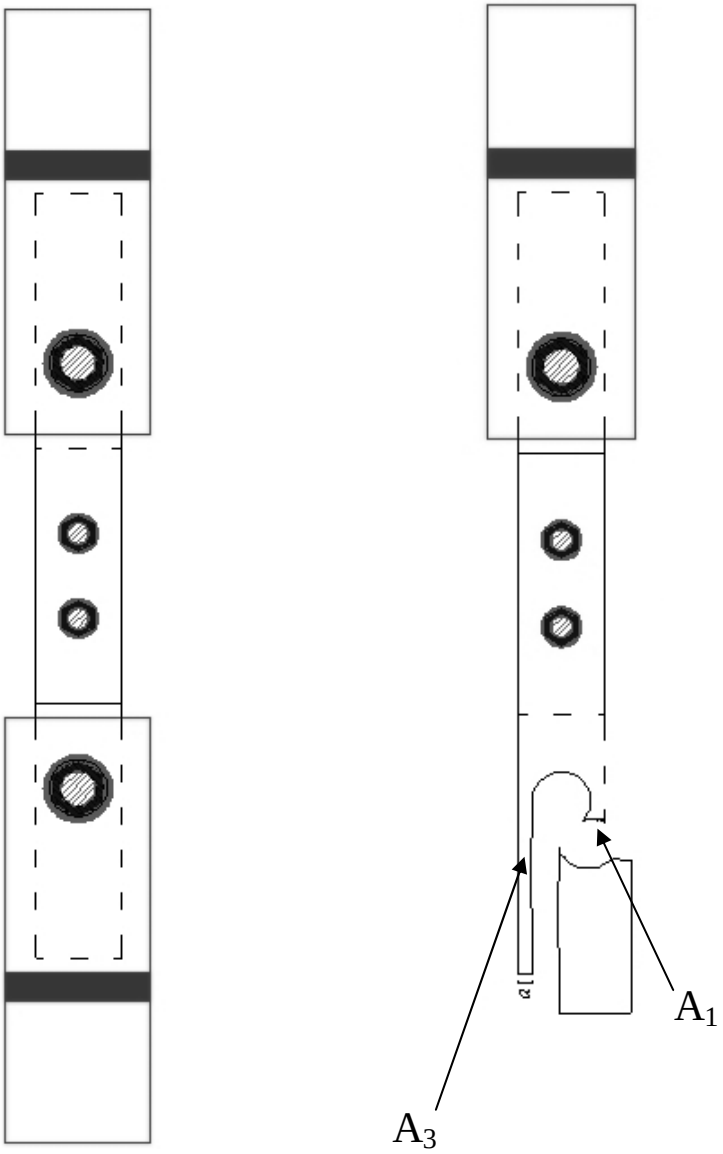

Figure 4.13. Failure of specimen J21.

The test was performed through a deformation of $V = 9.9 \cdot 10^{-3}$ mm/s. The load that caused the specimen failure is equal to **F_u = 78.75 kN**, while the maximum displacement is **δ_u = 1.03 cm**.

It's possible to read these values on the chart of test machine (**Figure 4.14**).

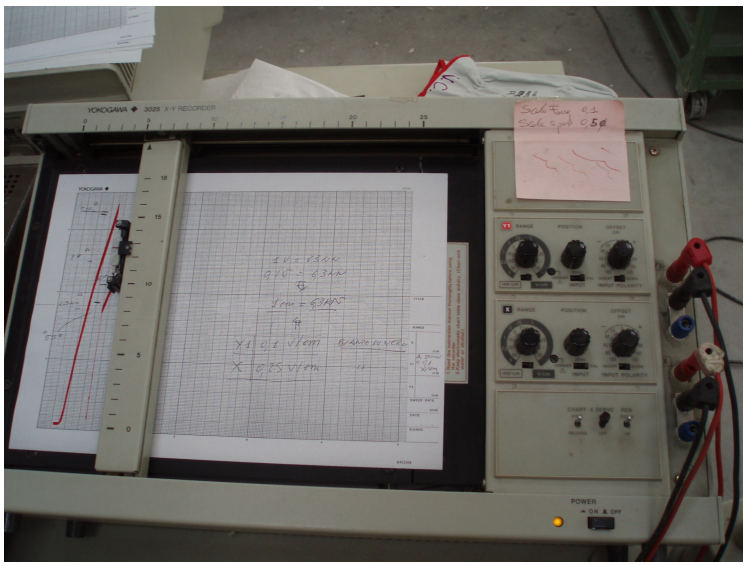

Figure 4.14. Chart of test machine.

In **Figure 4.15** the load curve is shown. The load step form a linear curve that represents the mechanical behavior of GFRP specimen.

The test has been performed in control of displacements, but it would have been the same to perform the test in force control because the mechanical behavior of GFRP is linear elastic

Force Scale [kN/cm]	**Displacement scale [cm/cm]**
6.30	0.31
F [kN]	**δ [cm]**
0.00	0.00
3.78	0.06
10.71	0.16
34.65	0.44
50.40	0.63
78.75	**1.03**

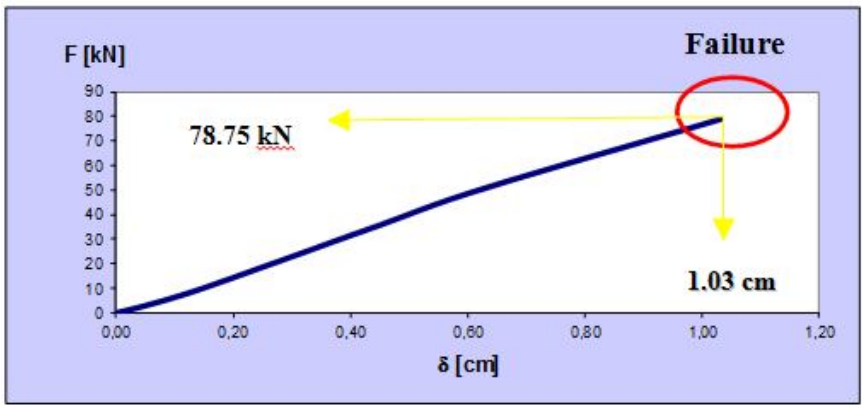

Figure 4.15. Load curve.

4.3. Joint J21 – Results and discussion

To describe the failure mode of joint J21 and the stress state acting on the failure surface, three hypotheses are assumed [27]:

1) *net-section failure* occurs before the *delamination*;
2) *delamination* occurs before *net-section failure*;
3) both *net-section failure* and *delamination* occur at the same time.

Geometrical parameters relevant to the description of the stress state are as follows:

- a = 10 mm;
- b = 12 mm;
- c = 3 mm;
- l = 115 mm.

The meanings of these values is shown in **Figure 4.16** and refer to specimen J21.

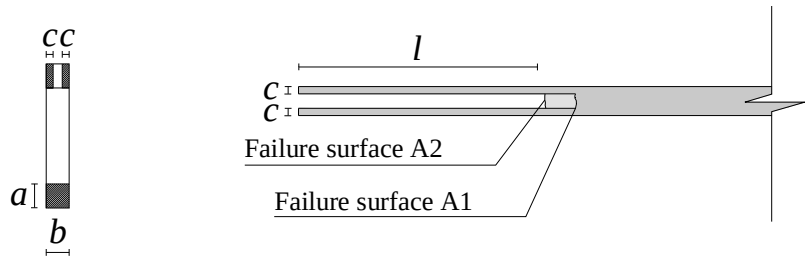

Figure 4.16. Geometrical parameters to determinate A1, A2 and A3.

1) First hypothesis: *net-section failure* occurs before the *delamination* [27];

In this first theoretical modeling it is assumed that *net-section failure* occurs before the *delamination* of the GFRP specimen.

Therefore, in the ultimate conditions, the only resistance mechanism is one where the load is completely absorbed by the surface **A3** subjected to *delamination* (**Figure 4.17**).

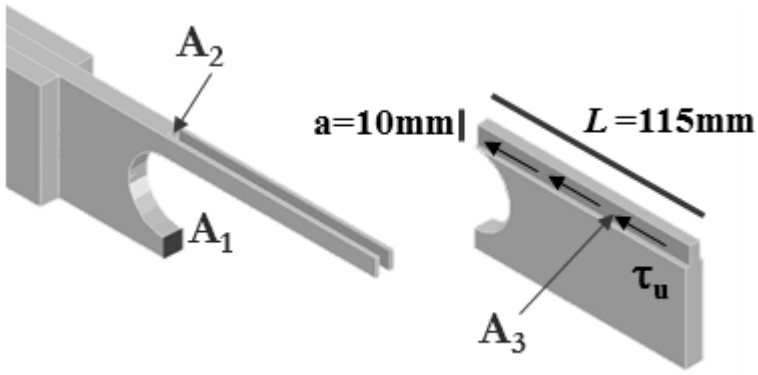

Figure 4.17. Failure mechanism - First hypothesis.

Formalizing the assumptions in the equations can be written as follows:

$$\tau = \frac{F_u}{2A_3} = \frac{78.75\,\text{kN}}{2300\,\text{mm}^2} = 34.2\,\frac{\text{N}}{\text{mm}^2}, \qquad \textbf{(4.1)}$$

$$\sigma = 0\,, \qquad \textbf{(4.2)}$$

where $A_3 = a \cdot l = 1150\,\text{mm}^2$.

The point $\mathbf{P_1}\,(\sigma\,,\tau\,)$, identified through the equations **(4.1**) and **(4.2**), represents one point of failure.

Normal stress is equal to zero because *net-section failure* occurs before the *delamination.*

Furthermore it's assumed that *net-section failure* occurs on the surface **A1** and **A2** at the same time.

2) Second hypothesis: *delamination* occurs before *net-section failure*;

In this second theoretical modeling it is assumed that *delamination* occurs before *net-section failure* of the GFRP specimen.

Therefore, in the ultimate conditions, the only resistance mechanism is one where the load is completely absorbed by the surfaces **A1** and **A2** subjected to *net-section failure* (**Figure 4.18**).

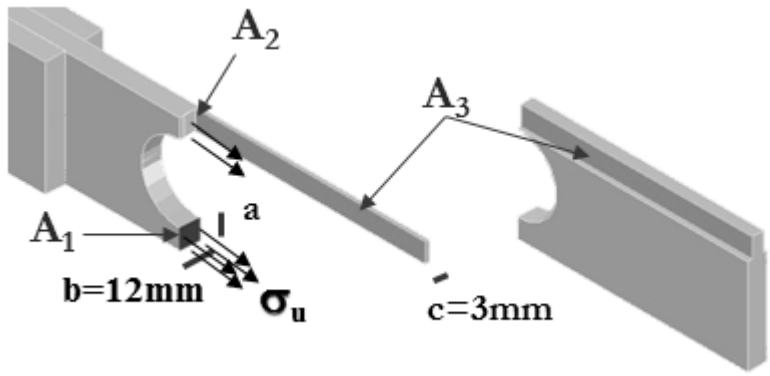

Figure 4.18. Failure mechanism - Second hypothesis.

Formalizing the assumptions in the equations can be written as follows:

$$\sigma = \frac{F_u}{A_1 + A_2} = \frac{78.75\,kN}{180\,mm^2} = 437.5\,\frac{N}{mm^2}, \qquad \textbf{(4.3)}$$

$$\tau = 0\,, \qquad \textbf{(4.4)}$$

where $A_1 = a \cdot b = 120\,\text{mm}^2$ and $A_2 = a \cdot (b - 2c) = 60\,\text{mm}^2$.

The point $\mathbf{P_2}\,(\sigma\,,\tau\,)$, identified through the equations **(4.3**) and **(4.4**), represents one point of failure.

Shear stress is equal to zero because *delamination* occurs before the *net-section failure.*

Furthermore it's assumed that *net-section failure* occurs on the surface **A1** and **A2** at the same time.

3) Third hypothesis: both *net-section failure* and *delamination* occur at the same time.

In this case the load is completely absorbed by the surfaces **A1**, **A2** and **A3**.

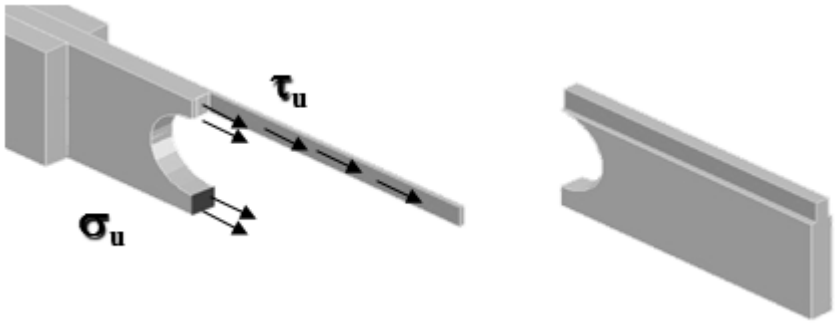

Figure 4.19. Failure mechanism - Third hypothesis.

For the equilibrium, in the ultimate conditions, it can be written:

$$\sigma\left(A_1 + A_2\right) + \tau A_3 = F_u \quad \Rightarrow \quad \tau = -\frac{\left(A_1 + A_2\right)}{A_3}\sigma + \frac{F_u}{A_3}. \qquad \textbf{(4.5)}$$

This equation represents a linear curve that is the *resistance domain* of this joint J21.

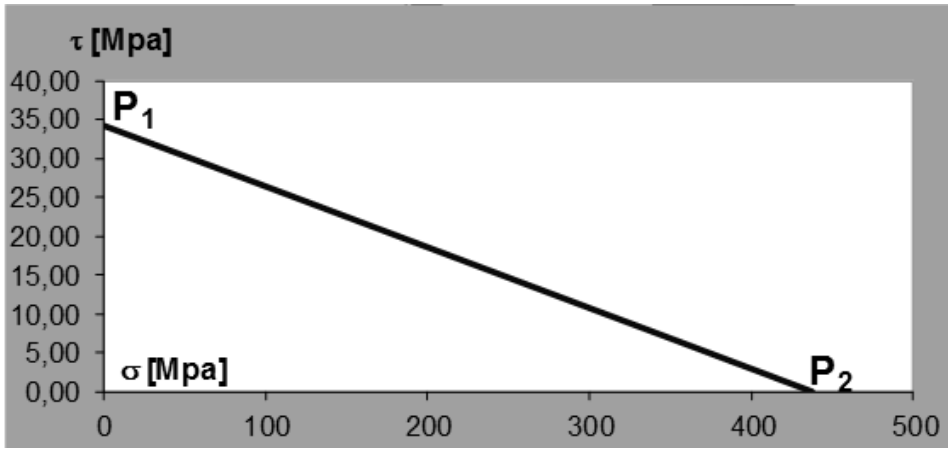

Figure 4.20. Resistance domain of joint J21 for *block shear*.

Summarizing, this linear domain is a prediction of failure, for a single bolt joint, for a mechanism similar to *block shear* with *delamination*.

It's clear that the stress state is assumed plane.

4.4. Joint J33 Type 1 – Test description

The joint J33 Type 1 has three rows with three bolts per row. It's placed in the machine by using two attack devices made of steel.

It consists of five steel plates, two of which are welded on a bracket above, also of steel, and inside the GFRP specimen is housed , while the other three are fixed on another steel support and inside the part of the joint that consists of two plates is housed.

The connection between GFRP plates and steel support is realized by bolting.

In **Figure 4.21** is shown the specimen in the test machine.

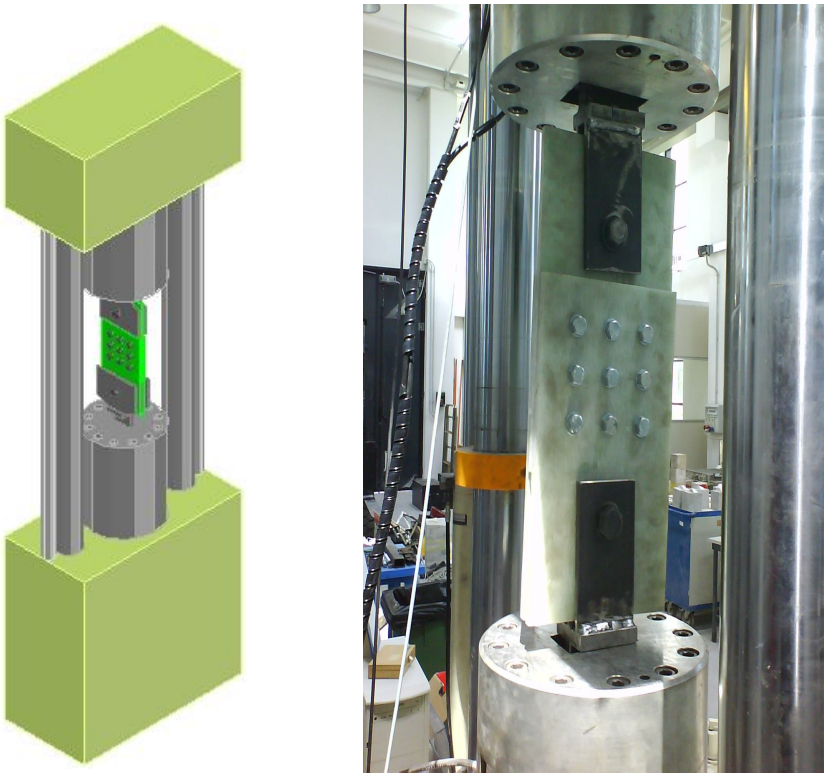

Figure 4.21. Joint J33 Type 1 in the test machine.

In **Figure 4.22** the geometric characteristics of the specimen size of both the joint J33 Type 1 and bolts that form the connection under study and that connect GFRP plates to steel support is shown.

In **Figure 4.23** the design of test device is illustrated.

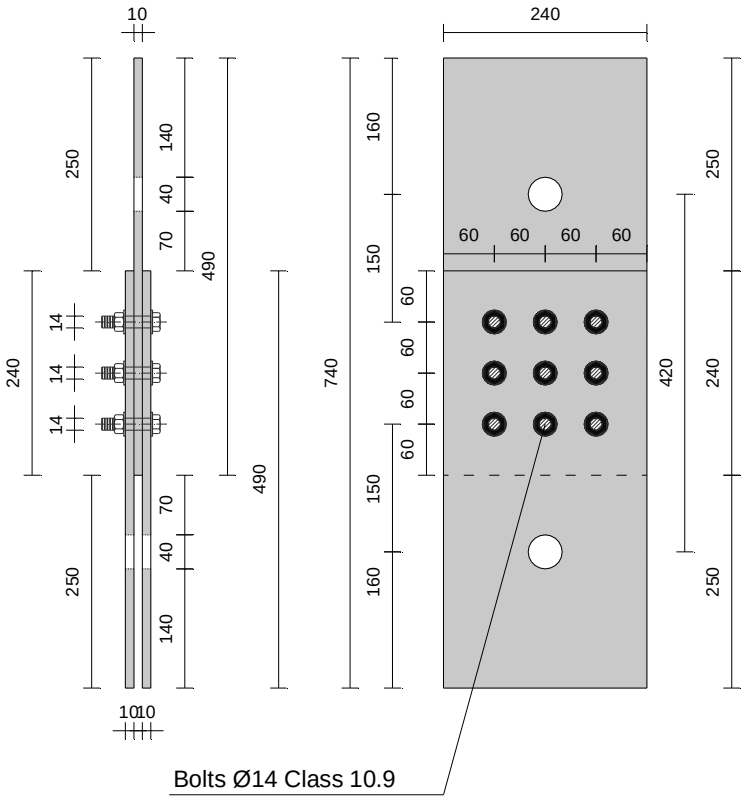

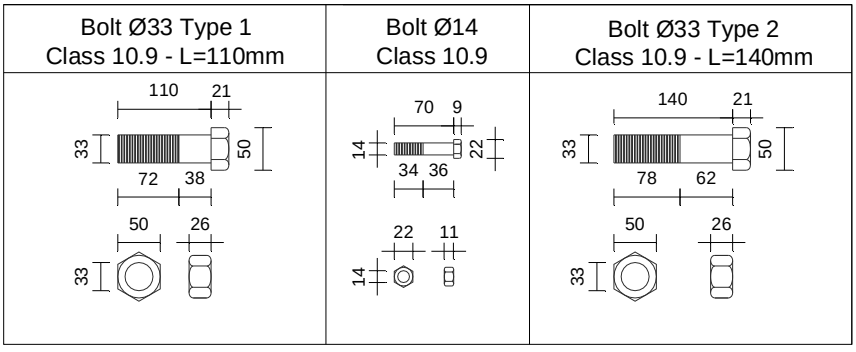

Figure 4.22. Geometry and bolting of joint J33.

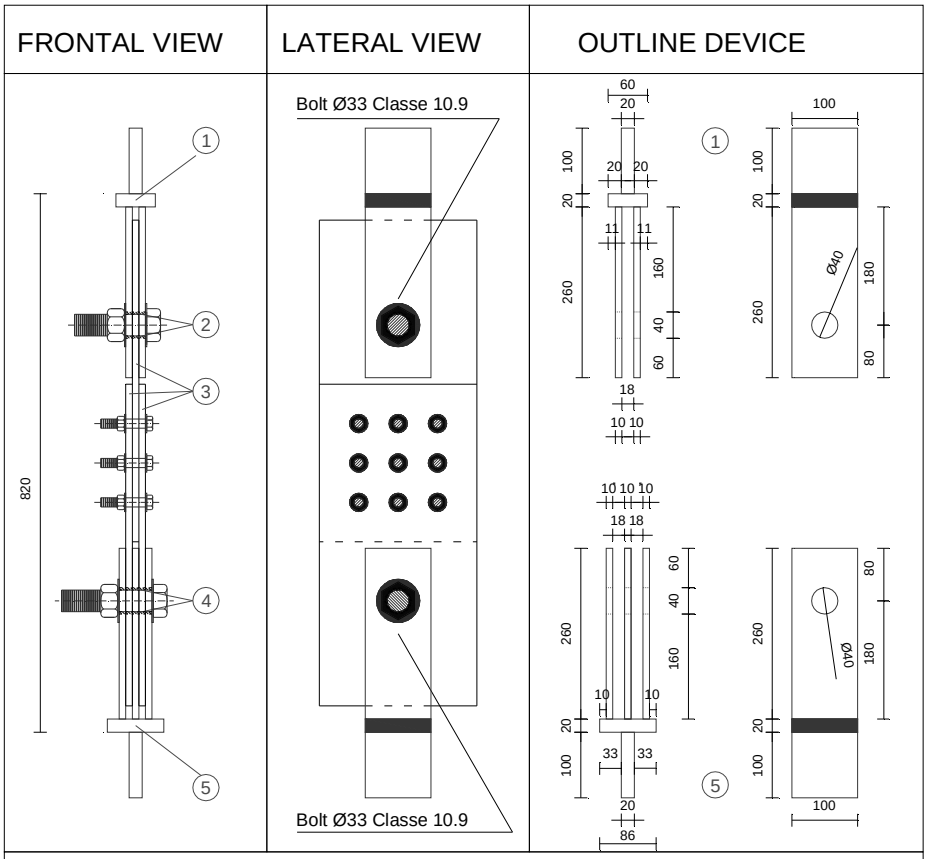

LEGEND

① UPPER STEEL JAW
② UPPER STEEL TUBE ($Ø_i$=33mm ; $Ø_e$=50mm ; L=36mm)
③ GFRP SPECIMENS
④ LOWER STEEL TUBE ($Ø_i$=33mm ; $Ø_e$=50mm ; L=62mm)
⑤ LOWER STEEL JAW

Figure 4.23. Design of test device.

Steel supports are reported in **Figure 4.24**.

Figure 4.24. Steel supports.

In **Figure 4.25** the 3D picture of the joint J33 Type 1 is shown.

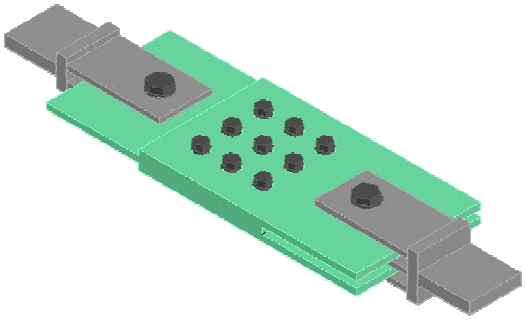

Figure 4.25. 3D picture of J33 Type 1.

The failure of this joint occurred for bearing stresses in the holes $\mathbf{B_1}$ an $\mathbf{B_2}$ (**Figure 4.26**) where bolts, connecting plates to steel supports, are placed (**Figure 4.27**).

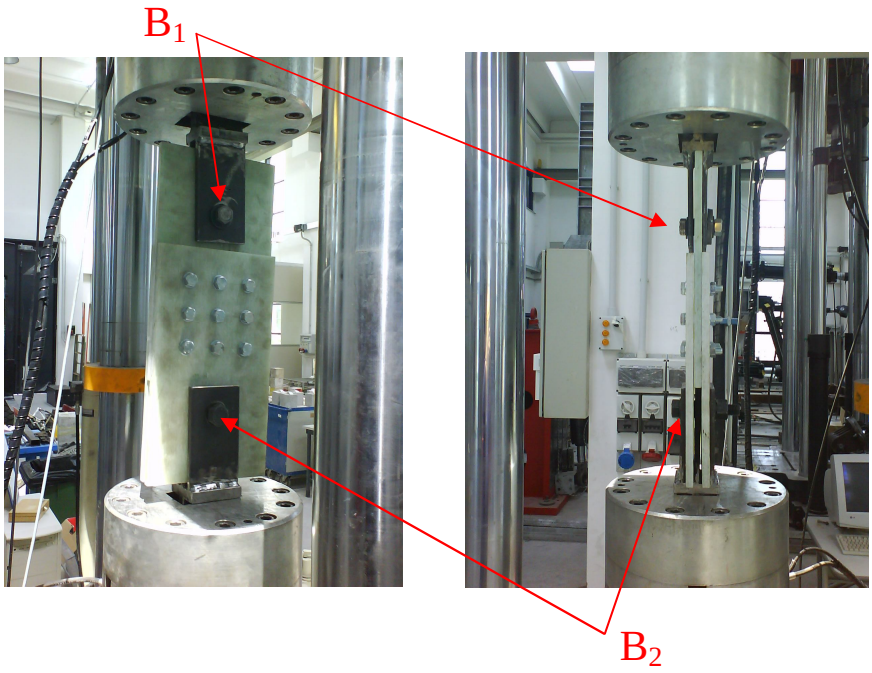

Figure 4.26. Holes $\mathbf{B_1}$ and $\mathbf{B_2}$ in the specimen.

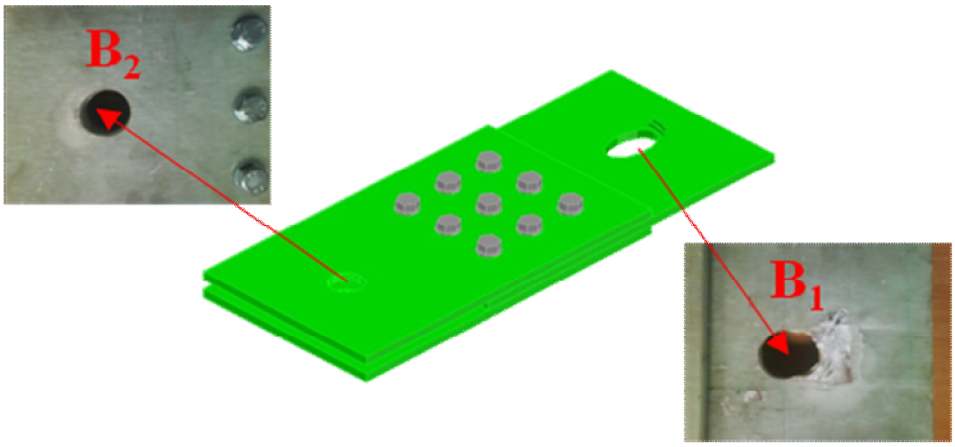

Figure 4.27. Holes $\mathbf{B_1}$ and $\mathbf{B_2}$ where bearing failure occurred.

To describe the failure stress state acting in the GFRP plate, geometrical parameters of holes are illustrated below:

- $t_{plate} = 12\,mm$;
- $D_{hole} = 40\,mm$;
- $A = t \cdot D = 480\,mm^2$.

The load curve is shown in **Figure 4.28** where it's possible to observe bearing failure of holes $\mathbf{B_1}$ and $\mathbf{B_2}$.

Force scale [kN/cm]	**Displacements scale [cm/cm]**	
15.75	0.31	
F [kN]	**δ [cm]**	**ε_{tot}**
0.00	0.000	0.000
15.75	0.092	0.023
31.50	0.185	0.046
47.25	0.277	0.069
63.00	0.354	0.088
78.75	0.431	0.108
94.50	0.507	0.127
100.80	0.554	0.138
63.00	0.554	0.138
78.75	0.707	0.177
67.73	0.738	0.185
88.20	0.984	0.246
78.75	0.984	0.246
91.35	1.076	0.269
83.48	1.076	0.269
113.40	1.476	0.369
102.38	1.507	0.377
129.15	1.937	0.484
122.85	2.060	0.515
135.45	2.460	0.615
97.65	2.460	0.615
0.00	1.999	0.500

Bearing B1

Bearing B2

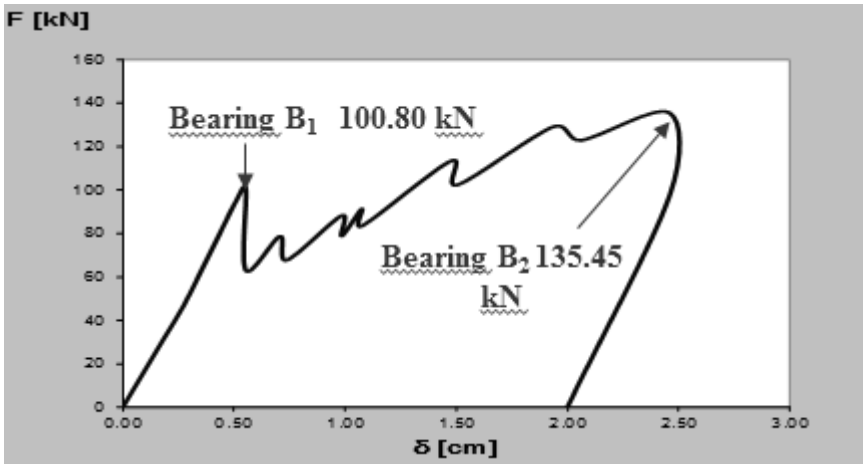

Figure 4.28. Force-displacement diagram for joint J33 Type 1.

4.5. Joint J33 Type 1– Results and discussion

The load curve of **Figure 4.28**, is linear up to the load value of **100.80 kN** where bearing failure of hole $\mathbf{B_1}$ occurs.

After this value of force the curve is non-linear. In fact there are traits decreasing where the damaged fibers were unloaded and increasing traits where fibers, still intact, are loading.

The test was stopped where bearing failure of second hole $\mathbf{B_2}$ occurs, i.e. at force equal to **135.45 kN**.

The meanings of value of ε of **Figure 4.28** is illustrated in the following equation:

$$\varepsilon = \frac{\delta}{D}, \qquad \textbf{(4.6)}$$

where *D* is the hole diameter equal to 40 mm (**Figure 4.29**) and δ is the displacement value read on the graph.

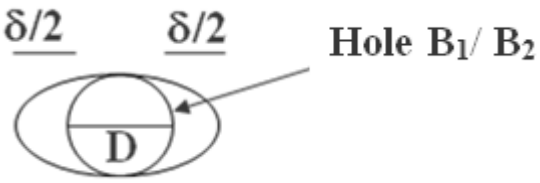

Figure 4.29. Hole deformation.

On the load curve it's possible to observe the *displacement at the elastic limit* which is equal to:

$$\delta_{\text{elast.}} = 0.461\text{cm}, \tag{4.7}$$

which corresponds to an *elastic hole deformation* of:

$$\varepsilon_{\text{elast.}} = \frac{\delta_{\text{elast.}}}{D} = \frac{0.461\text{cm}}{4\text{cm}} = 0.115. \tag{4.8}$$

The *ultimate displacement* of $\mathbf{B_1}$ is:

$$\delta_{u,B1} = 1.7\,\text{cm}, \tag{4.9}$$

which corresponds to deformation of:

$$\varepsilon_{u,B1} = \frac{\delta_{u,B1}}{D} = \frac{1.7\,\text{cm}}{4\,\text{cm}} = 0.425, \tag{4.10}$$

while the *ultimate displacement* of $\mathbf{B_2}$ is:

$$\delta_{u,B2} = \delta_{Rif.B2} = 0.3\,\text{cm}, \tag{4.11}$$

which corresponds to deformation of:

$$\varepsilon_{u,B2} = \varepsilon_{Rif.B2} = \frac{\delta_{Rif.B2}}{D} = \frac{0.3\,\text{cm}}{4\,\text{cm}} = 0.075\,. \tag{4.12}$$

To understand the deformation process, two hypotheses are assumed:

1) in the first case (*HP1*), the deformations of the hole $\mathbf{B_2}$ were not considered in the linear trait, because the reagent section of this hole is twice the reagent section of the hole $\mathbf{B_1}$;
2) in the second case (*HP2*), the deformations of the hole $\mathbf{B_2}$ were considered in the linear trait.

1) First case: Hypothesis 1

In this case, as mentioned, deformations of the hole **B₂** were not considered in the linear trait [27].

After the bearing failure of **B₁** ($\varepsilon = \varepsilon_{B.B1}$), deformations of the hole **B₂** were considered assuming a linear relation between the deformations of **B₁** (ε_{I}) and deformations of **B₂** (ε_{II}).

Summarizing it results:

$$\varepsilon \leq \varepsilon_{B.B1} \quad \Rightarrow \quad \varepsilon_{I} \neq 0, \quad \varepsilon_{II} \square 0; \tag{4.13}$$

$$\varepsilon > \varepsilon_{B.B1} \quad \Rightarrow \quad \varepsilon_{I} \neq 0, \quad \varepsilon_{II} \neq 0. \tag{4.14}$$

where:

$\varepsilon_{B.B1}$ is the failure bearing deformation of **B₁**;

ε is the specimen deformation under tensile load.

Reporting in a diagram $\varepsilon_{I} - \varepsilon_{II}$ points of deformation state, at bearing failure of **B₁ (P₁)** and **B₂ (P₂)**, it's possible to obtain the following relation:

$$\varepsilon_{I} = \varepsilon_{B.Bl} + m \cdot \varepsilon_{II}, \tag{4.15}$$

where:

$$m = \frac{\left(\varepsilon_{\mathrm{u,Bl}} - \varepsilon_{B.\mathrm{Bl}}\right)}{\left(\varepsilon_{\mathrm{u.B2}}\right)}, \qquad \textbf{(4.16)}$$

assuming that $m = \tan(90°)$ for $\varepsilon \le \varepsilon_{B.\mathrm{B1}}$ **(4.13)**, because $\varepsilon_{\mathrm{II}} = \varepsilon_{\mathrm{B2}} = 0$.

In **Figure 4.30** the bilinear is shown where:

for $\varepsilon \le \varepsilon_{B.\mathrm{B1}}$, $\varepsilon_{\mathrm{I}} = \varepsilon_{B.\mathrm{Bl}} = 0.138$ (**Figure 4.28**);

for $\varepsilon > \varepsilon_{B.\mathrm{B1}}$, $\varepsilon_{\mathrm{I}} = \varepsilon_{B.\mathrm{Bl}} + m \cdot \varepsilon_{\mathrm{II}}$,

knowing that $\varepsilon_{\mathrm{u,Bl}}$ and $\varepsilon_{\mathrm{u,B2}}$ are illustrated in the equations **(4.10)** and **(4.12)**, respectively.

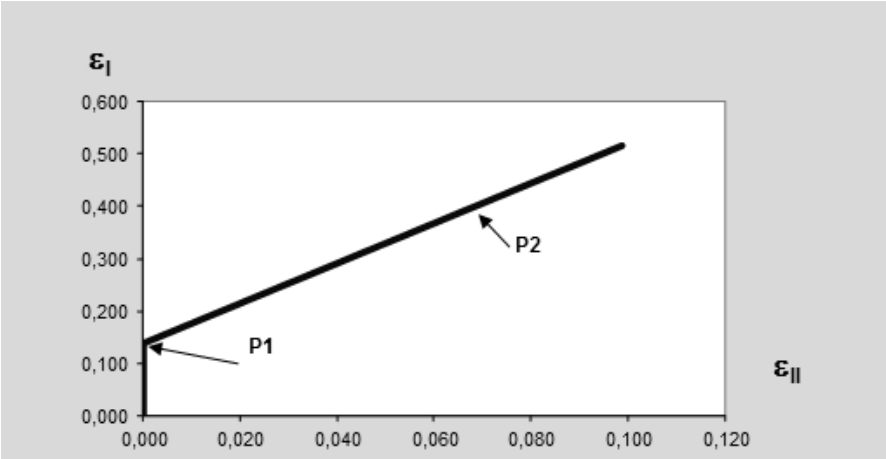

Figure 4.30. Deformation diagram.

Furthermore, the following equation is valid:

$$\varepsilon_{I} + \varepsilon_{II} = \varepsilon \ . \qquad \textbf{(4.17)}$$

Bearing stresses, during tensile test, for $\mathbf{B_1}$ and $\mathbf{B_2}$, respectively, are:

$$\sigma_{I} = \frac{F}{A_1} = \frac{F}{D \cdot t}, \qquad \textbf{(4.18)}$$

$$\sigma_{II} = \frac{F}{A_2} = \frac{F}{2 \cdot D \cdot t}, \qquad \textbf{(4.19)}$$

while, solving the equation system of **(4.15)** and **(4.17)**, it results (**Figure 4.31**):

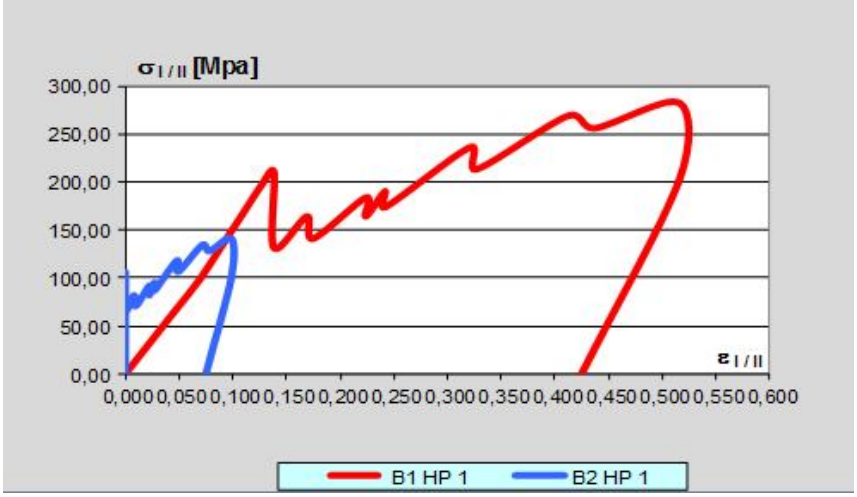

Figure 4.31. Stress-deformation diagram of $\mathbf{B_1}$ and $\mathbf{B_2}$.

Points of the **Figure 4.31** are shown in **Table 4.2**.

Table 4.2. Points of the stress-deformation diagram.

HP1					
B1			**B2**		
σ_I **[Mpa]**	ε_I	δ_I **[cm]**	σ_{II} **[Mpa]**	ε_{II}	δ_{II} **[cm]**
0.00	0.000	0.000	0.00	0.000	0.000
32.81	0.023	0.092	16.41	0.000	0.000
65.63	0.046	0.185	32.81	0.000	0.000
98.44	0.069	0.277	49.22	0.000	0.000
131.25	0.088	0.354	65.63	0.000	0.000
164.06	0.108	0.431	82.03	0.000	0.000
196.88	0.127	0.507	98.44	0.000	0.000
210.00	0.138	0.554	105.00	0.000	0.000
131.25	0.138	0.554	65.63	0.000	0.000
164.06	0.169	0.675	82.03	0.008	0.032
141.09	0.175	0.700	70.55	0.010	0.038
183.75	0.224	0.895	91.88	0.022	0.089
164.06	0.224	0.895	82.03	0.022	0.089
190.31	0.242	0.968	95.16	0.027	0.108
173.91	0.242	0.968	86.95	0.027	0.108
236.25	0.321	1.285	118.13	0.048	0.191
213.28	0.327	1.309	106.64	0.049	0.198
269.06	0.413	1.650	134.53	0.072	0.287
255.94	0.437	1.748	127.97	0.078	0.312
282.19	0.516	2.065	141.09	0.099	0.395
203.44	0.516	2.065	101.72	0.099	0.395
0.00	0.425	1.699	0.00	0.075	0.300

2) Second case: Hypothesis 2

In this second case deformations of **B_2** were considered also on the linear trait for $\varepsilon \le \varepsilon_{B.B1}$ [27].

For the equilibrium it must be:

$$\sigma_{I} \cdot A_1 = F = \sigma_{II} \cdot A_2 , \qquad \textbf{(4.20)}$$

then:

$$\sigma_{I} = \sigma_{II} \cdot \frac{A_2}{A_1} . \qquad \textbf{(4.21)}$$

Being on the linear trait of the load curve it's possible to write:

$$E \cdot \varepsilon_{I} = E \cdot \varepsilon_{II} \cdot \frac{A_2}{A_1} , \qquad \textbf{(4.22)}$$

then:

$$\varepsilon_{I} = 2 \cdot \varepsilon_{II} . \qquad \textbf{(4.23)}$$

Furthermore, observing the equation **(4.17)**, it results:

$$\varepsilon = \varepsilon_{\mathrm{I}} + \varepsilon_{\mathrm{II}} = \varepsilon_{\mathrm{I}} \cdot \left(1 + \frac{1}{2}\right). \tag{4.24}$$

and then:

$$\varepsilon_{\mathrm{I}} = \frac{2}{3}\varepsilon, \tag{4.25}$$

$$\varepsilon_{\mathrm{II}} = \frac{1}{3}\varepsilon. \tag{4.26}$$

Using the equations **(4.18)**, **(4.19)** and **(4.25)**, **(4.26)** you can obtain **Figure 4.32**:

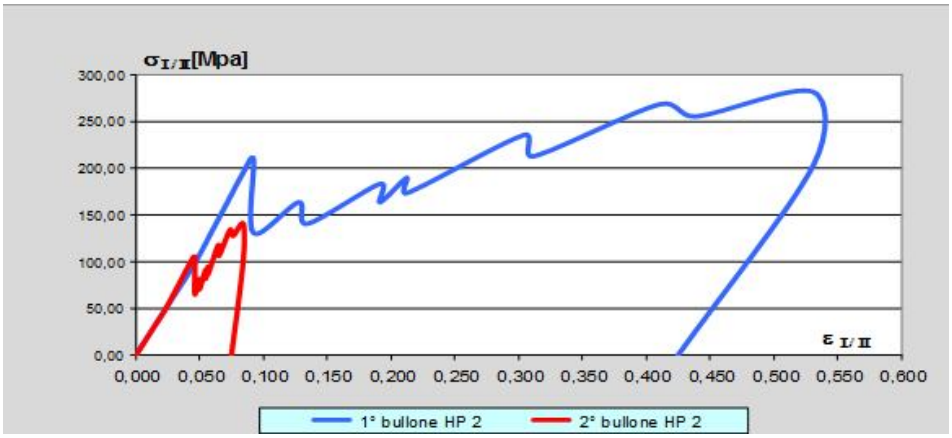

Figure 4.32. Stress-deformation diagram of $\mathbf{B_1}$ and $\mathbf{B_2}$.

Points of this diagram are reported in **Table 4.3**.

Table 4.3. Points of the stress-deformation diagram.

HP2					
B1			B2		
σ_I [MPa]	ε_I	δ_I [cm]	σ_{II} [Mpa]	ε_{II}	δ_{II} [cm]
0.00	0.000	0.000	0.00	0.000	0.000
32.81	0.015	0.062	16.41	0.008	0.031
65.63	0.031	0.123	32.81	0.015	0.062
98.44	0.046	0.185	49.22	0.023	0.092
131.25	0.059	0.236	65.63	0.029	0.118
164.06	0.072	0.287	82.03	0.036	0.144
196.88	0.085	0.338	98.44	0.042	0.169
210.00	0.092	0.369	105.00	0.046	0.185
131.25	0.092	0.369	65.63	0.046	0.185
164.06	0.128	0.510	82.03	0.049	0.197
141.09	0.135	0.539	70.55	0.050	0.199
183.75	0.191	0.765	91.88	0.055	0.219
164.06	0.191	0.765	82.03	0.055	0.219
190.31	0.213	0.850	95.16	0.057	0.226
173.91	0.213	0.850	86.95	0.057	0.226
236.25	0.304	1.218	118.13	0.065	0.258
213.28	0.312	1.246	106.64	0.065	0.261
269.06	0.411	1.642	134.53	0.074	0.295
255.94	0.439	1.755	127.97	0.076	0.305
282.19	0.531	2.123	141.09	0.084	0.337
203.44	0.531	2.123	101.72	0.084	0.337
0.00	0.425	1.699	0.00	0.075	0.300

The relation between ε_I and ε_{II}, in the *first case* (HP1) and in the *second case* (HP2), is illustrated in the **Figure 4.33**.

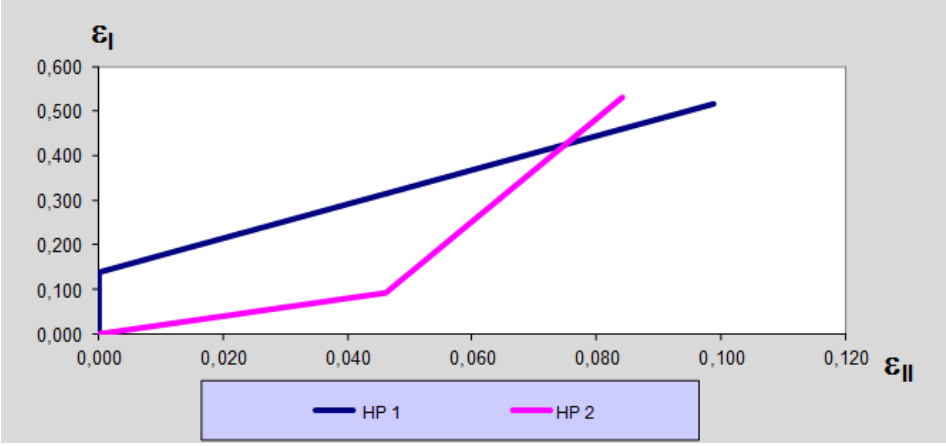

Figure 4.33. Deformation diagram.

4.6. Overlap zone of joint J33 Type 1

In the overlap zone there are three rows of bolts and three bolts for row (**Figure 4.34**).

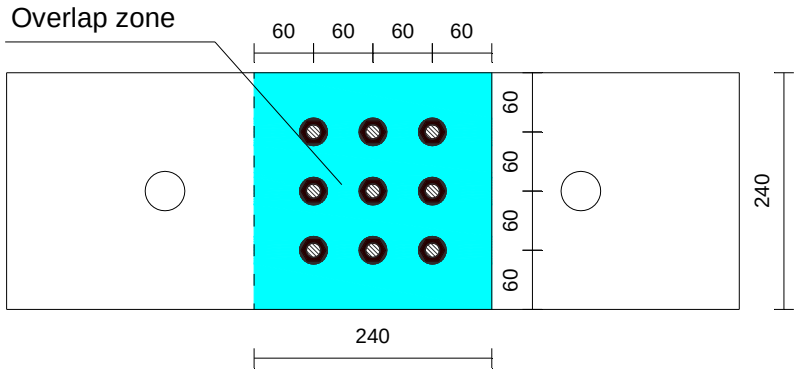

Figure 4.34. Overlap zone.

In this case, also, you can assume two behavior of the joint:

1) rigid plates;
2) deformable plates.

1) Rigid plates

In this first case that the plates have infinite stiffness so you can obtain:

$$\sigma_{Bearing} = \frac{F}{n_b \cdot d_b \cdot t}, \quad \textbf{(4.27)}$$

$$\tau = \frac{F}{n_b \cdot A_b}, \quad \textbf{(4.28)}$$

where n_b is the number of bolts and A_b is its area equal to:

$$A_b = \frac{\pi d_b^2}{4} = 153.94\,\text{mm}^2. \quad \textbf{(4.29)}$$

for a diameter of bolt, in the overlap zone, equal to d_b = 14 mm.

Looking at **Figure 4.28** and considering equations **(4.27)** and **(4.28)**, it's possible to obtain (**Table 4.4**):

Table 4.4. Normal and shear stresses in the overlap zone.

✓ *RIGID PLATES*

$\sigma_{Beaaring.}$	τ
[MPa]	**[Mpa]**
0.00	0.00
9.72	11.37
19.44	22.74
29.17	34.10
38.89	45.47
48.61	56.84
58.33	68.21
62.22	72.76
38.89	45.47
48.61	56.84
41.81	48.88
54.44	63.66
48.61	56.84
56.39	65.94
51.53	60.25
70.00	81.85
63.19	73.89
79.72	93.22
75.83	88.67
83.61	97.77
60.28	70.48
0.00	0.00

2) Deformable plates

It's possible to admit that the deformation of the zone presents a linear diagram (**Figure 4.35**):

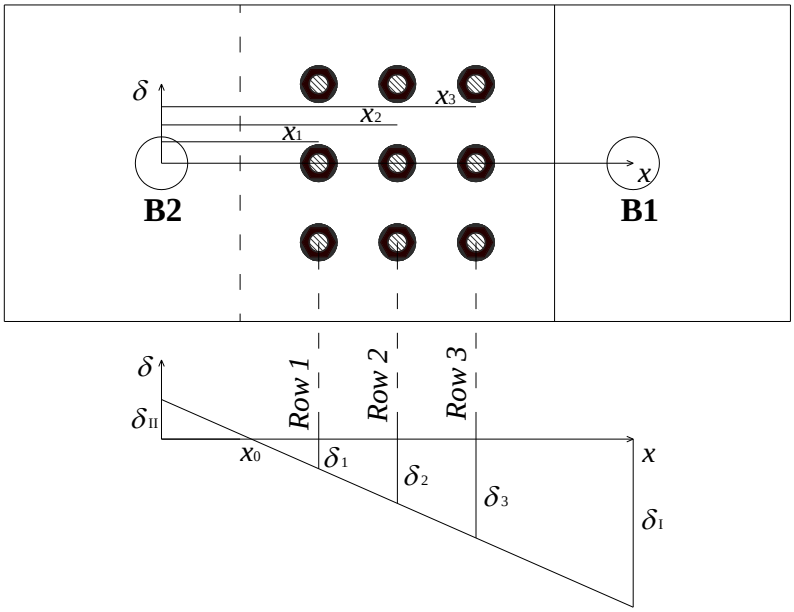

Figure 4.35. Deformation diagram in the overlap zone.

Considering that force resulting of each row is F_1, F_2 and F_3, it must be, for each value of F:

$$F_1 + F_2 + F_3 = F \ . \qquad \textbf{(4.30)}$$

The deformation for each row is:

$$\varepsilon_i = \frac{\delta_i}{D} \qquad (i = 1, 2, 3), \qquad \textbf{(4.31)}$$

and, for the linearity of the diagram, it's true:

$$\varepsilon_i = \frac{\delta_i}{D} = \frac{m'(x_i - x_o)}{D} = m\,(x_i - x_o) \qquad (i = 1, 2, 3), \qquad \textbf{(4.32)}$$

where D is the hole diameter equal to 15 mm. Furthermore, being:

$$F_i = \sigma_i A_i \qquad (i = 1, 2, 3), \qquad \textbf{(4.33)}$$

it must result **(4.30)**:

$$\sigma_1 A_1 + \sigma_2 A_2 + \sigma_3 A_3 = F\,, \qquad \textbf{(4.34)}$$

where A_1, A_2 and A_3 are the net section for each row (1, 2 and 3) (**Figure 4.35**).

The overlap zone shows a linear elastic mechanical behavior. Then it's possible to write:

$$\sigma_i = E\varepsilon_i \qquad (i = 1, 2, 3), \qquad \textbf{(4.35)}$$

and substituting the equation **(4.35)** in the equation **(4.34)**, and considering the equation **(4.32)**, you can write [27]:

$$\sum_{i=1}^{3} m\,E\,A_i\,(x_i - x_0) = F. \qquad \textbf{(4.36)}$$

From equation **(4.36)**, it's possible to obtain the value of E and to calculate bearing stresses for each load step through the equation **(4.35)** using the deformation distribution of HP1 and HP2, as mentioned.

The values of E, σ and ε distributions are reported in **Table 4.5** and **Table 4.6** for deformable plates.

Table 4.5. Stresses and deformations distribution-deformable plates.

HP1						
E HP1 **[MPa]**	$\sigma_{1,Rif.}$ *Row 1* **[MPa]**	$\sigma_{2,Rif.}$ *Row 2* **[MPa]**	$\sigma_{3,Rif.}$ *Row 3* **[MPa]**	ε_1 *Row 1*	ε_2 *Row 1*	ε_3 *Row 1*
0.00	0.00	0.00	0.00	0.000	0.000	0.000
13.98	1.48	2.92	4.35	0.106	0.209	0.311
27.96	2.97	5.83	8.70	0.212	0.417	0.622
41.94	4.45	8.75	13.05	0.318	0.626	0.933
55.92	5.94	11.67	17.40	0.425	0.835	1.245
69.89	7.42	14.58	21.75	0.531	1.043	1.556
83.87	8.90	17.50	26.10	0.637	1.252	1.867
89.46	9.50	18.67	27.84	0.679	1.335	1.991
55.92	5.94	11.67	17.40	0.425	0.835	1.245
69.89	7.42	14.58	21.75	0.531	1.043	1.556
60.11	6.38	12.54	18.70	0.456	0.897	1.338
78.28	8.31	16.33	24.36	0.594	1.168	1.742
69.89	7.42	14.58	21.75	0.531	1.043	1.556
81.08	8.61	16.92	25.23	0.616	1.210	1.805
74.09	7.86	15.46	23.05	0.563	1.106	1.649
100.65	10.68	21.00	31.32	0.764	1.502	2.240
90.86	9.64	18.96	28.27	0.690	1.356	2.022
114.63	12.17	23.92	35.67	0.870	1.711	2.551
109.03	11.57	22.75	33.93	0.828	1.627	2.427
120.22	12.76	25.08	37.41	0.913	1.794	2.676
86.67	9.20	18.08	26.97	0.658	1.294	1.929
0.00	0.00	0.00	0.00	0.000	0.000	0.000

Table 4.6. Stresses and deformations distribution-deformable plates.

			HP2			
E HP2 **[MPa]**	$\sigma_{1,Rif.}$ *Row 1* **[MPa]**	$\sigma_{2,Rif.}$ *Row 2* **[MPa]**	$\sigma_{3,Rif.}$ *Row 3* **[MPa]**	ε_1 *Row 1*	ε_2 *Row 1*	ε_3 *Row 1*
0.00	0.00	0.00	0.00	0.000	0.000	0.000
13.06	1.58	2.92	4.26	0.121	0.223	0.326
26.12	3.16	5.83	8.51	0.242	0.447	0.652
39.18	4.73	8.75	12.77	0.362	0.670	0.977
52.24	6.31	11.67	17.02	0.483	0.893	1.303
65.30	7.89	14.58	21.28	0.604	1.117	1.629
78.36	9.47	17.50	25.53	0.725	1.340	1.955
83.59	10.10	18.67	27.23	0.773	1.429	2.085
52.24	6.31	11.67	17.02	0.483	0.893	1.303
65.30	7.89	14.58	21.28	0.604	1.117	1.629
56.16	6.79	12.54	18.30	0.520	0.960	1.401
73.14	8.84	16.33	23.83	0.677	1.251	1.825
65.30	7.89	14.58	21.28	0.604	1.117	1.629
75.75	9.15	16.92	24.68	0.701	1.295	1.890
69.22	8.36	15.46	22.55	0.640	1.184	1.727
94.04	11.36	21.00	30.64	0.870	1.608	2.346
84.89	10.26	18.96	27.66	0.785	1.452	2.118
107.10	12.94	23.92	34.89	0.991	1.831	2.672
101.87	12.31	22.75	33.19	0.942	1.742	2.541
112.32	13.57	25.08	36.60	1.039	1.921	2.802
80.98	9.78	18.08	26.38	0.749	1.385	2.020
0.00	0.00	0.00	0.00	0.000	0.000	0.000

In **Figure 4.36** and **Figure 4.37** distributions between the case of deformable plates, for each row, and rigid plates, for HP1 and HP2, respectively, are compared.

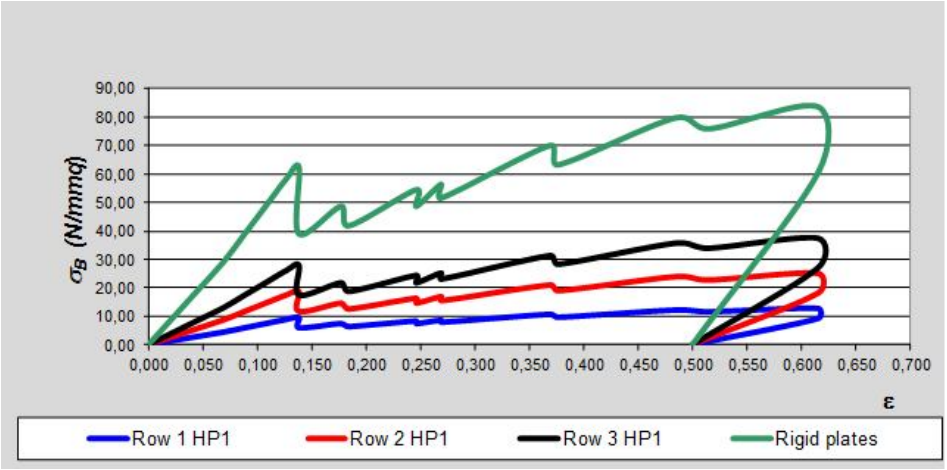

Figure 4.36. Bearing stresses-deformation diagram.

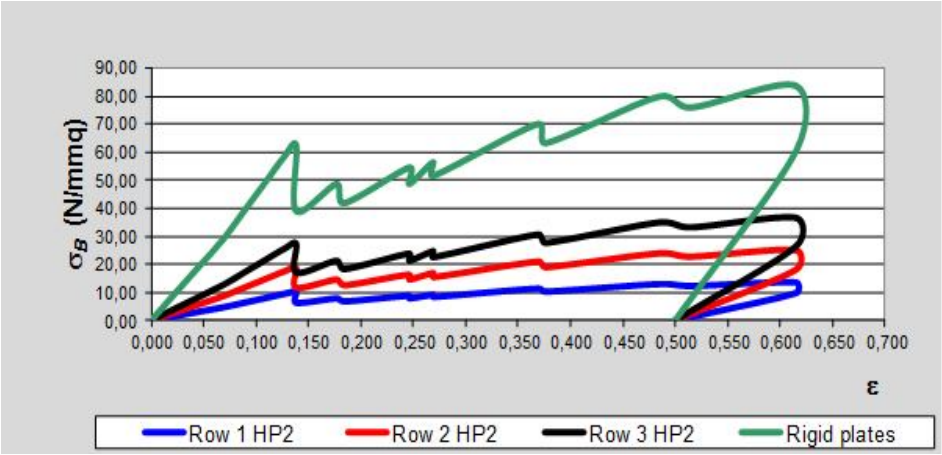

Figure 4.37. Bearing stresses-deformation diagram.

The bearing failure of joint J33 Type 1 occurred in the holes of steel supports. This is due to the use of the same device adopted for joint J21, inefficient for this case.

To facilitate the failure in the overlap zone, a new specimen is designed to ensure that the failure occurs in the zone of bolts rows.

For this purpose, both bearing failure and net-section failure of steel supports zone must occur after the same failures of overlap zone.

In this regard, the following condition must be valid, in the rigid plates hypothesis [27]:

$$\frac{F}{n_F \cdot (t + n \cdot s) \cdot D_s} \leq \frac{F}{n_f \cdot t \cdot D}. \qquad \textbf{(4.37)}$$

where:

- F is the tensile load;
- D_s is the hole in the steel supports zone;
- D is the hole of bolt in the overlap zone;
- n_F is the number of holes needed in the steel supports zone;
- n_f is the number of holes in the overlap zone;
- t is the thickness of the GFRP plate;
- s is the eventual thickness of a reinforcement plate of steel;
- n is the ratio between the Young modulus of GFRP and the Young modulus of steel.

From the equation **(4.37)**, it's possible to obtain:

$$n_F \geq \frac{n_f \cdot t \cdot D}{(t + n \cdot s) \cdot D_s} \qquad \textbf{(4.38)}$$

Furthermore, to ensure that the net-section failure also occurs in the overlap zone (**Figure 4.38**) it must be valid the equation **(4.39)**.

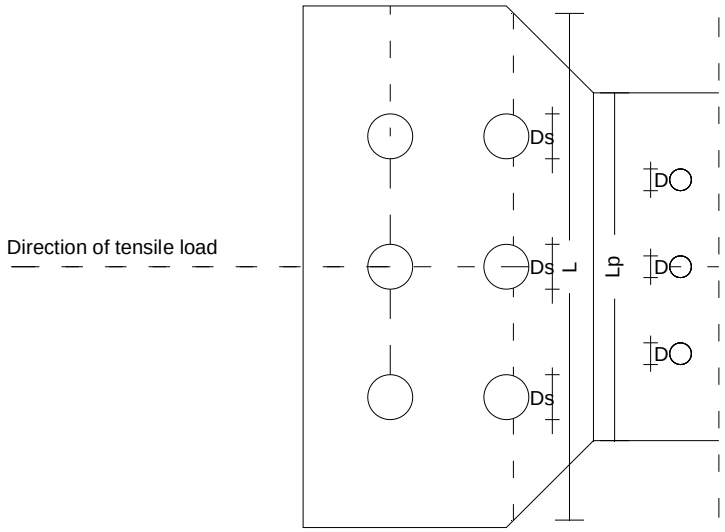

Figure 4.38. New specimen designed.

$$\frac{F}{n_R\left(L-n_F^{'}\cdot D_s\right)\cdot\left(t+2\cdot n\cdot s\right)}\leq\frac{F}{n_r\cdot t\cdot\left(L_p-n_f^{'}\cdot D\right)}, \qquad \textbf{(4.39)}$$

Where n_R and n_r are the number of rows for steel supports zone and overlap zone, respectively.

The number of holes $n_F = n_R\, n'_F$.

When equations **(4.38)** and **(4.39)** are satisfied, the failure occurs in the overlap zone [27].

4.7. Joint J33 Type 2 – Test description

The joint J33 Type 2 is shown in **Figure 4.39** and **Figure 4.40**.

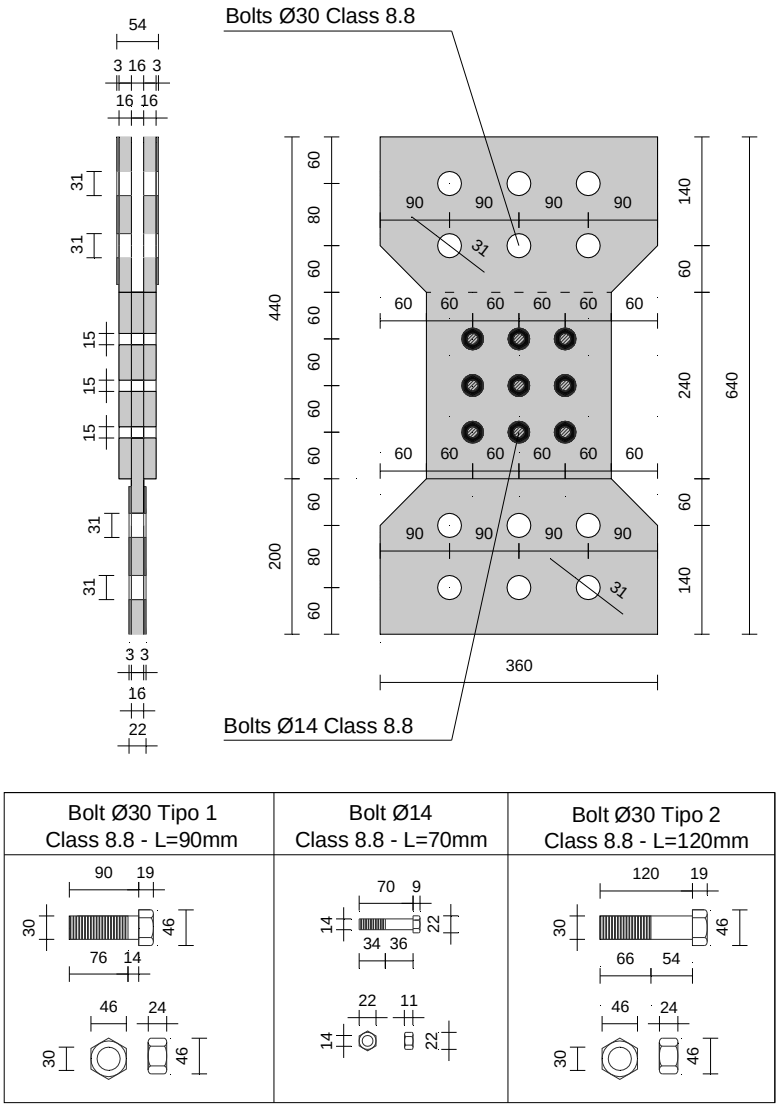

Figure 4.39. The joint J33.

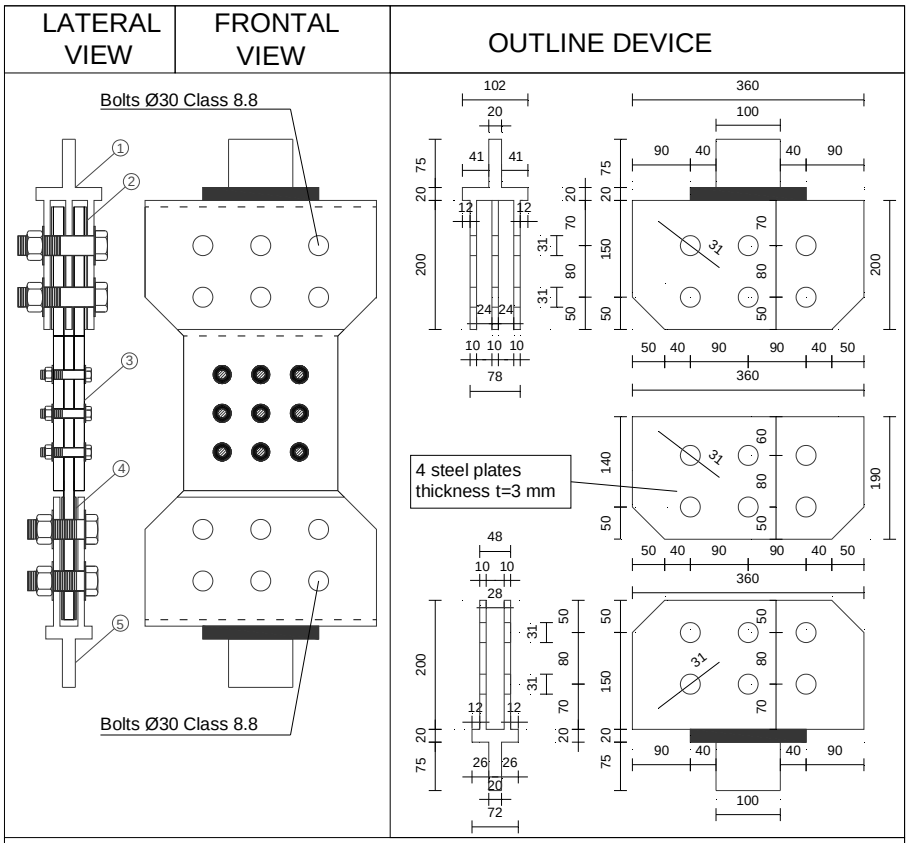

Figure 4.40. The joint J33-outline device.

Increasing the width of terminal sections of the plates, and choosing six holes of diameter equal to 30 mm for the joint J33 Type 2, it's possible to observe the new specimen designed.

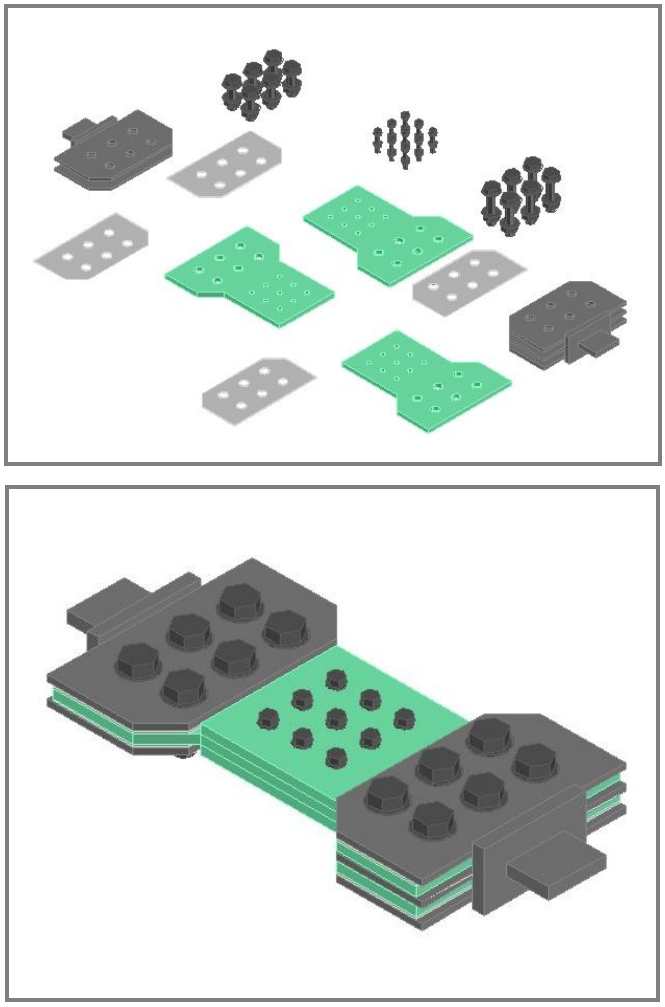

Figure 4.41. The joint J33 assembly.

For the experimental tests, the universal machine SCHENCK Hydropolus S56 was used. This machine consists of a hydraulic piston with a loading capacity of +/- 630 kN, stroke of +/- 125 mm and a self-balanced steel frame used to counteract the axial loadings. The machine works both under displacement and load control.

In order to measure displacements, the testing machine is equipped with an LVDT, while the tension/compression loads are controlled by means of a load cell [21-27].

The experimental system was set up in order to carry out all the tests, made up of a test device as well as a sophisticated automatic data acquisition system with three ‘‘System 5100 Vishay MM" switchboards, set out in parallel with 60 extensometric channels (**Figure 4.42**).

Figure 4.42. System 5100 Vishay MM.

Furthermore, a pressure mapping system is used to measure bearing stresses at bolt-hole interface.

In fact this system has flexible sensors , ***GRIP*™ 4255N** of **Tekscan** that have been placed in the holes on the edge where the action of bearing stress is expected (**Figure 4.43**).

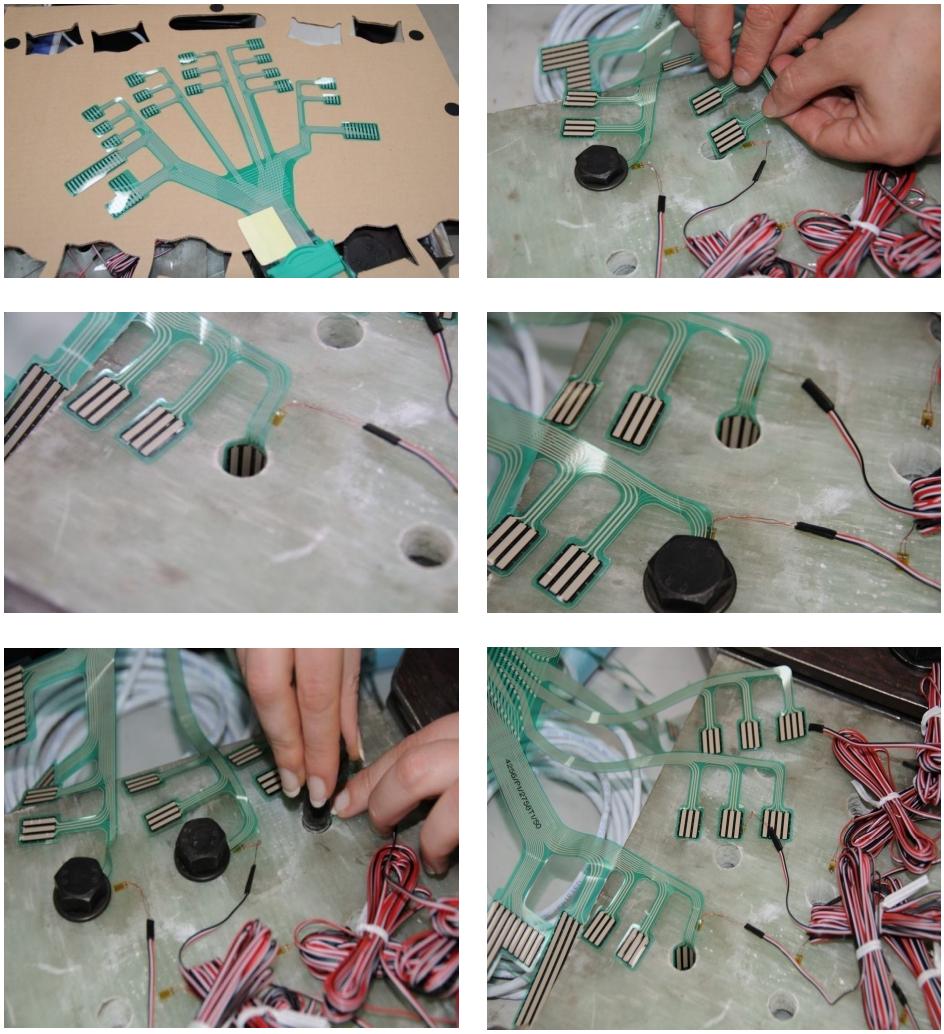

Figure 4.43. Sensors and their arrangement in the holes of J33 Type 2.

The disposition of the sensors is shown in **Figure 4.44** and in **Figure 4.45**.

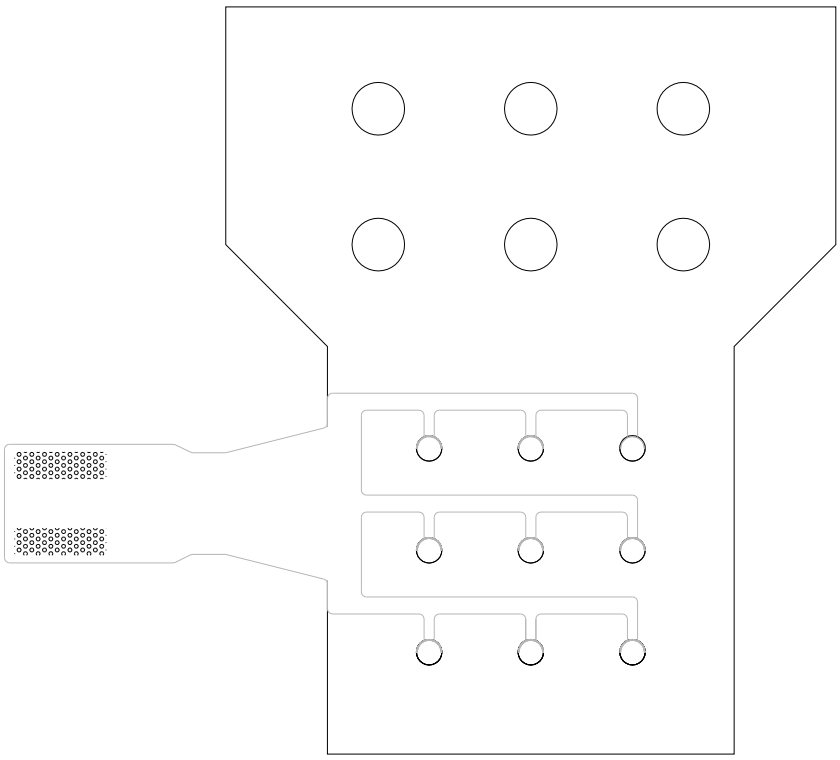

Figure 4.44. Sensors and their arrangement in the holes of J33 Type 2.

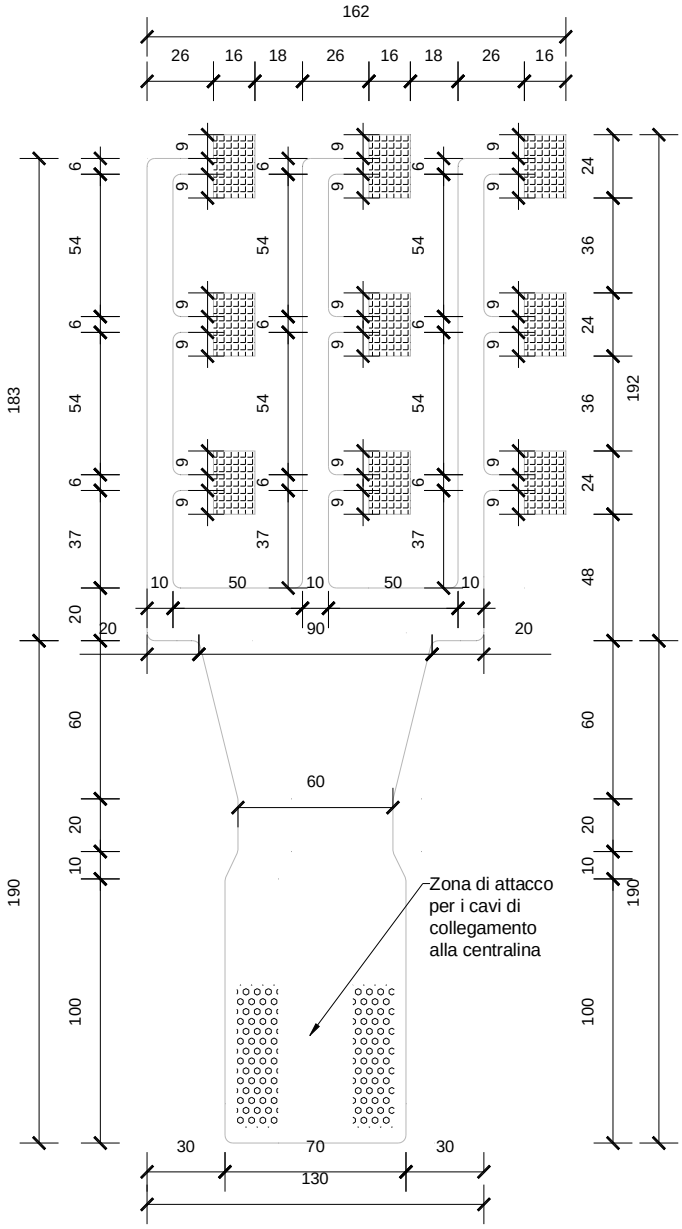

Figure 4.45. Sensors and their arrangement in the holes of J33 Type 2.

The gauges used (C2A-06.062LR-120 Vishay MM) are rectangular.

They are placed near the hole to measure the deformation of this zone where bearing stresses act (**Figure 4.46**).

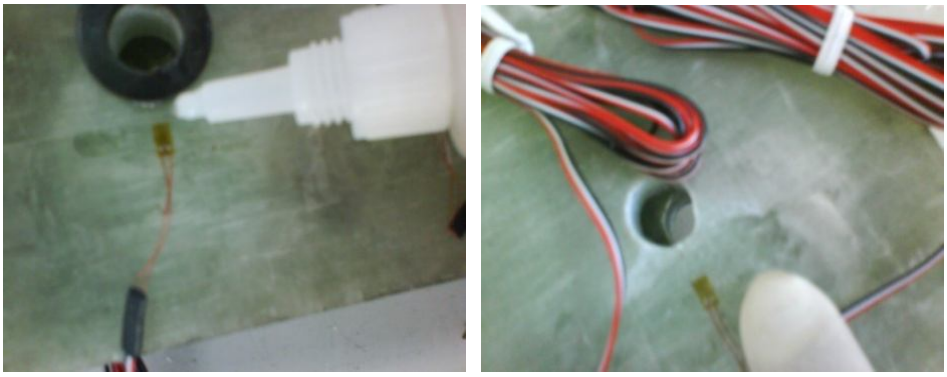

Figure 4.46. Strain gauges C2A-06.062LR-120 Vishay MM.

The specimen, assembled and instrumented, is shown below (**Figure 4.47**)

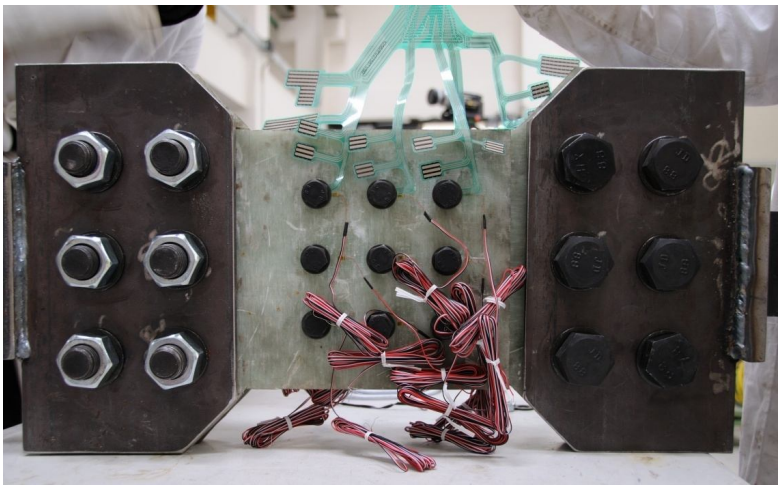

Figure 4.47. Joint J33 Type 2, assembled and instrumented.

The specimen thus prepared is placed in the test machine (**Figure 4.48** and **Figure 4.49**).

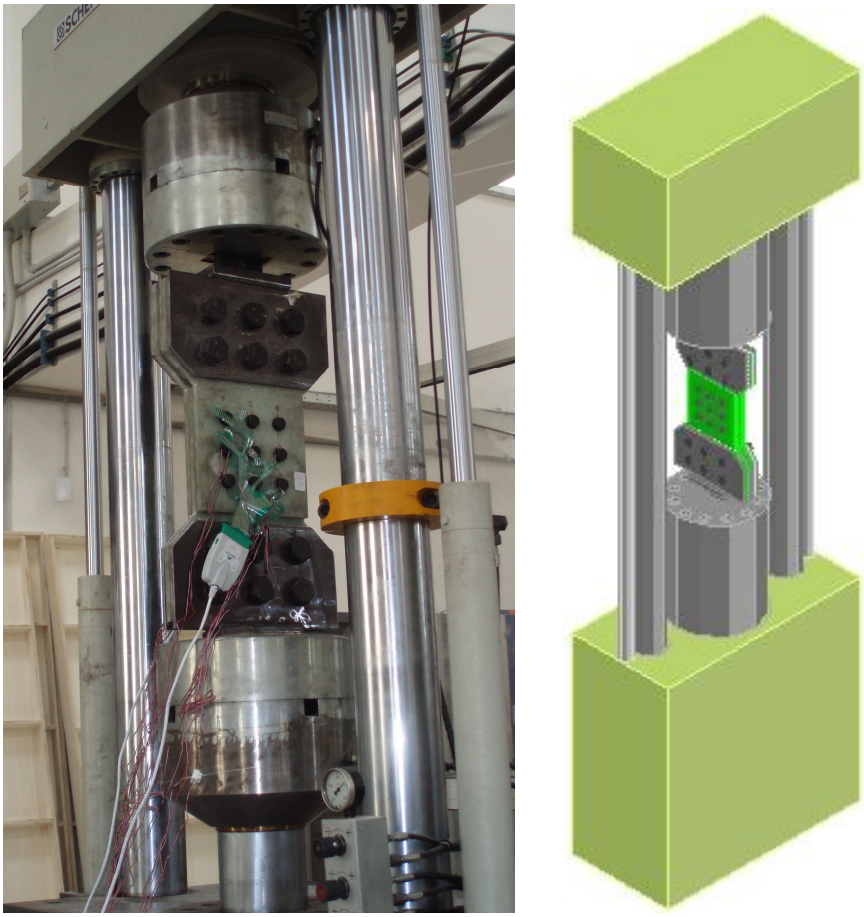

Figure 4.48. Joint J33 Type 2 in the test machine.

Figure 4.49. Joint J33 Type 2 in the test machine.

The sensors system is place on both sides of the specimen, to facilitate the understanding of the results.

These sides are A and B as shown in **Figure 4.50**.

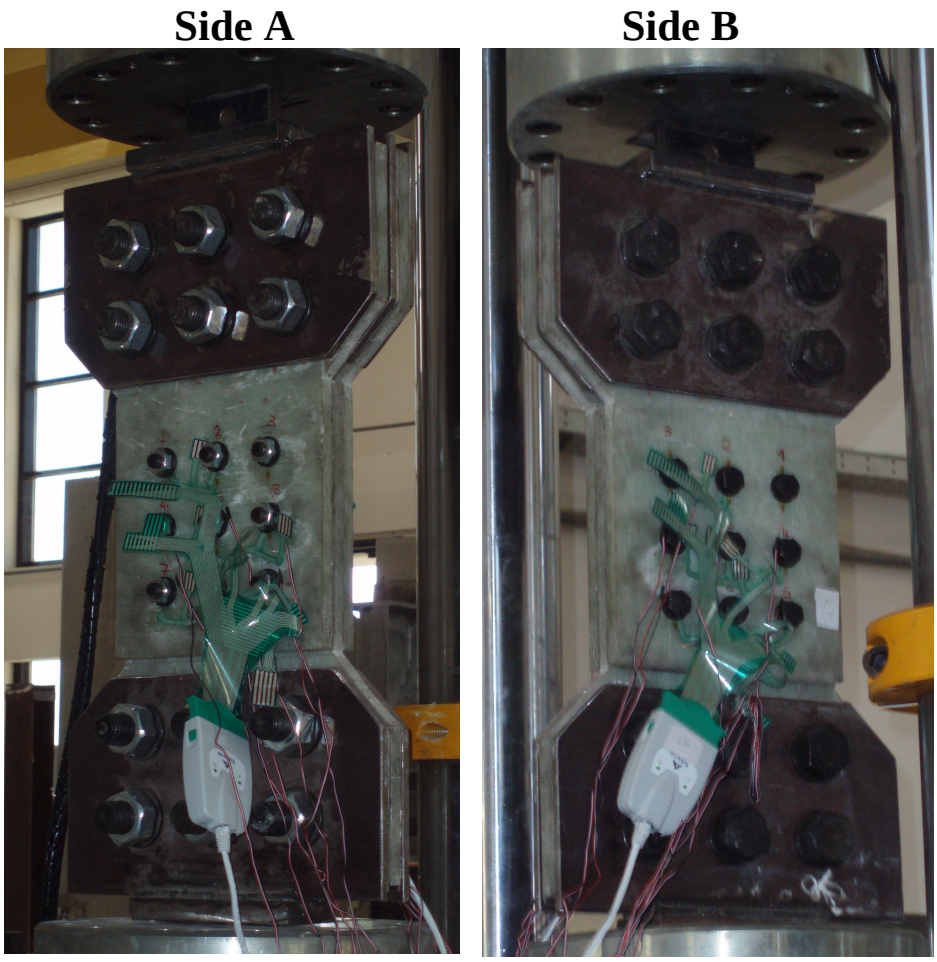

Figure 4.50. Joint J33-Side A and B.

The strain gauges arrangement is illustrated in **Figure 4.51** and **Figure 4.52**.

The strain gauges are placed near the holes, where the bearing stress is expected.

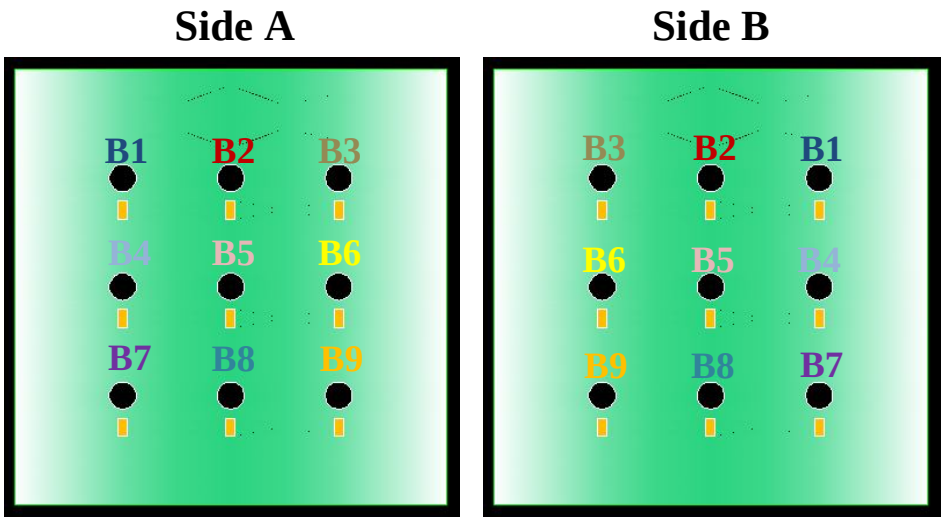

Figure 4.51. Joint J33-Strain gauges arrangement on side A and B.

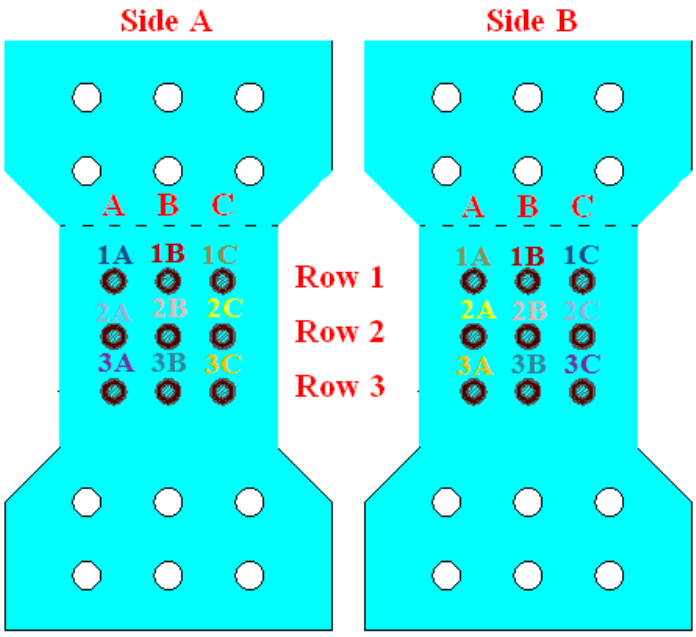

Figure 4.52. Joint J33-Strain gauges arrangement on side A and B.

The correspondence between bolts and sides to detect the measurement, is summarized in **Table 4.7**.

Table 4.7. Bolts and sides.

BOLT		SIDE A		SIDE B
B1	⇔	**1 A**	⇔	**1 C**
B2	⇔	**1 B**	⇔	**1 B**
B3	⇔	**1 C**	⇔	**1 A**
B4	⇔	**2A**	⇔	**2 C**
B5	⇔	**2 B**	⇔	**2 B**
B6	⇔	**2 C**	⇔	**2 A**
B7	⇔	**3 A**	⇔	**3 C**
B8	⇔	**3 B**	⇔	**3 B**
B9	⇔	**3 C**	⇔	**3 A**

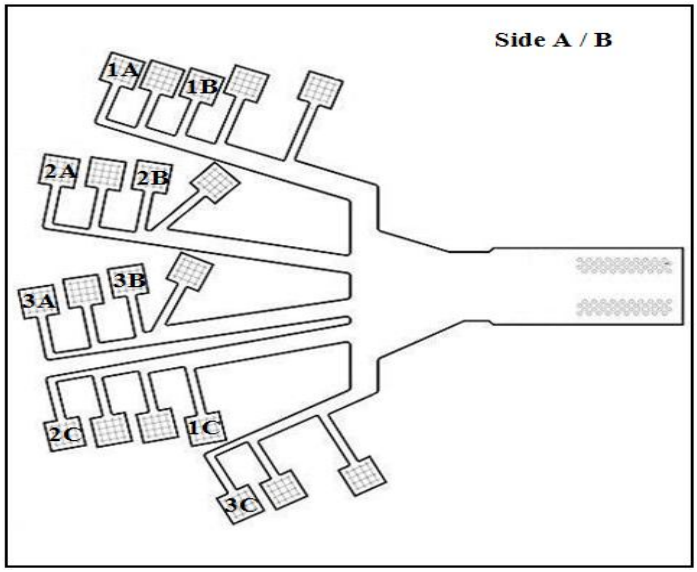

Figure 4.53. Used sensors.

The rectangular sensors [21-27], of twenty present on the system, used to detect the measurement of bearing stresses, are shown in **Figure 4.53**.

The **Iscan** output, to observe the pressure inside each hole, is illustrated in **Figure 4.54**.

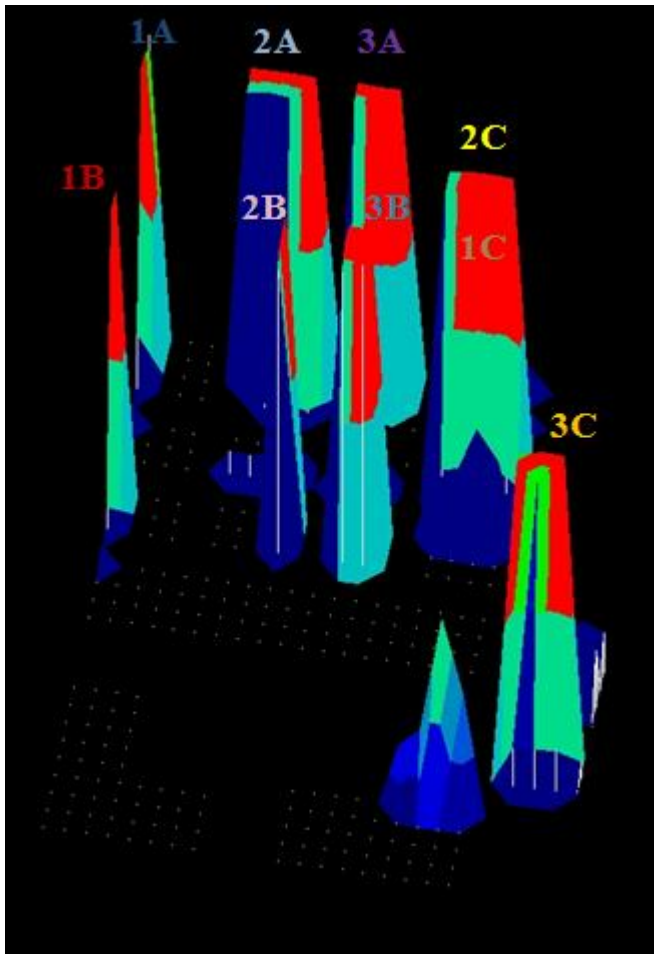

Figure 4.54. Pressure map.

4.8. Joint J33 Type 2 – Results and discussion

A first obvious result of this experimental test performed on the bolted connection J33, in agreement with that found in numerical, is that the bolts of the outer rows are more stressed than those of inner row (**Figure 4.55**).

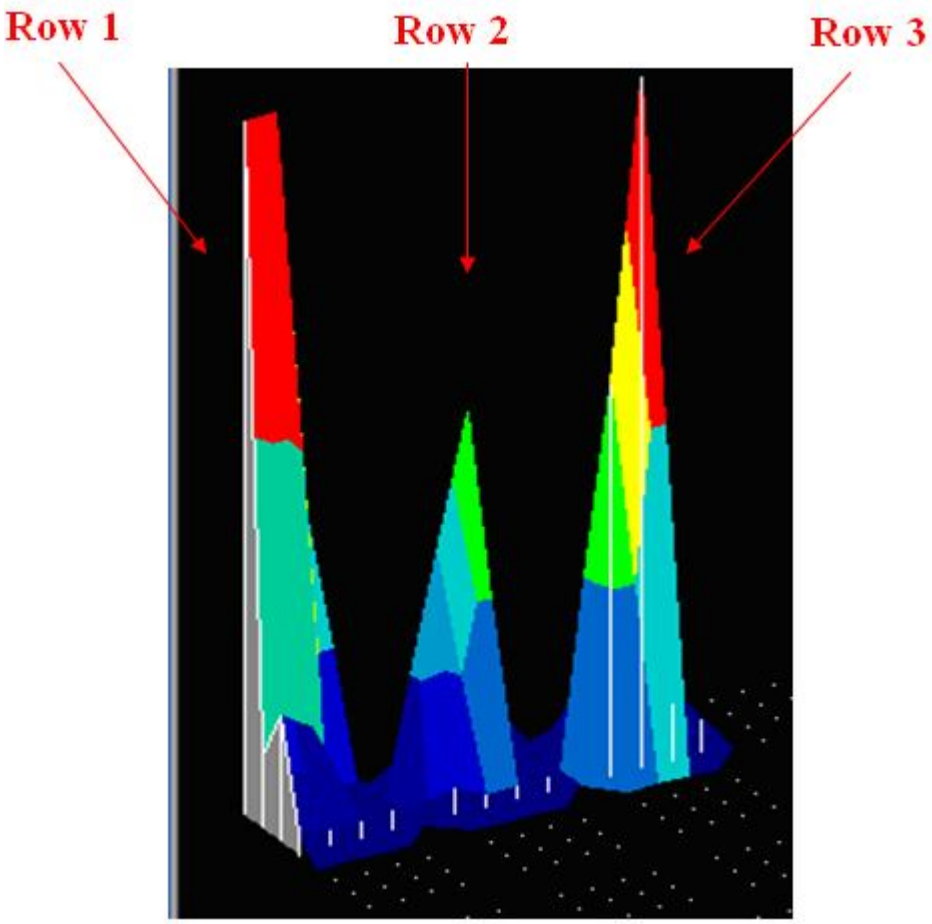

Figure 4.55. Pressure map for each row.

Interpolating data of sensors system, the coefficient of shear stresses distribution are shown in **Figure 4.56** and reported in **Table 4.8**.

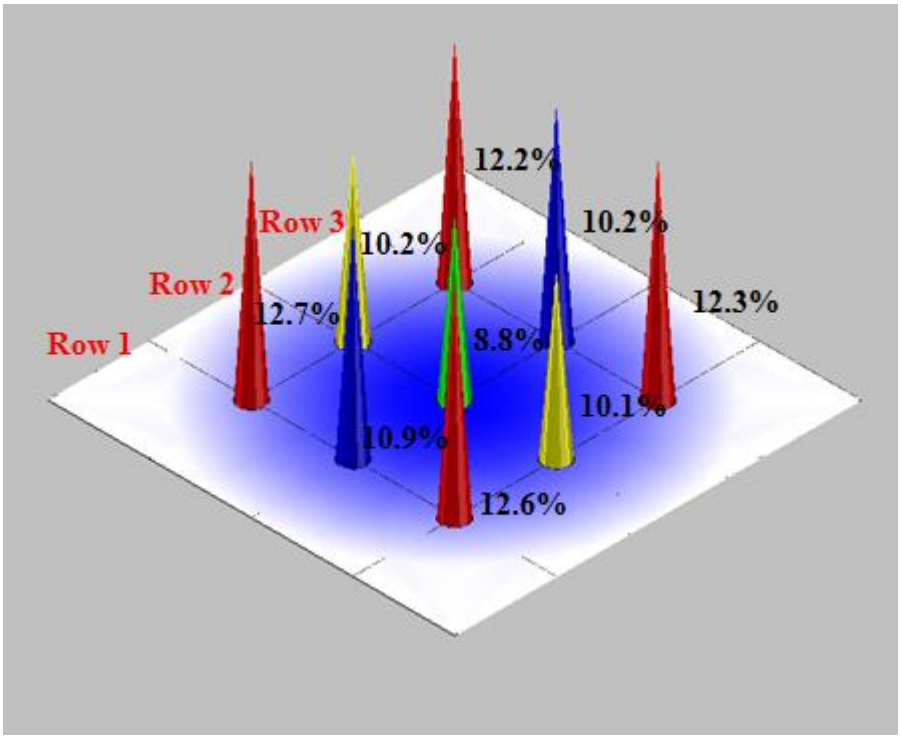

Figure 4.56. Shear stress distribution of J33 Type 2.

Table 4.8. *Shear stress distribution coefficients* for each bolt and each row of bolts obtained by experimental analysis ofJ33.

Joint **J33**	**Row 1** [%]	**Row 2** [%]	**Row 3** [%]
e	12.7	10.2	12.2
i	10.9	8.8	10.2
e	12.6	10.1	12.3
Total	**36.2**	**29.1**	**34.7**

In **Table 4.9** results from 3D finite element numerical analysis of J33 are shown.

Table 4.9. *Shear stress distribution coefficients* for each bolt and each row of bolts obtained by FEM analysis-J33.

Joint **J33**	**Row 1** **[%]**	**Row 2** **[%]**	**Row 3** **[%]**
e	12.1	9.4	12.1
i	11.8	9.2	11.8
e	12.1	9.4	12.1
Total	**36.0**	**28.0**	**36.0**

The maximum percentage error, comparing results of different analyses, is equal to 15.68%.

The values suggested in CNR-DT 205/2007 [20], for each row, and normalized with respect of the shear stress resulting, are equal to 41%, 18% and 41%, respectively.

The maximum percentage error between the experimental analysis and the mentioned values is 55.55% for the internal row [21-27].

CHAPTER V
2D FINITE ELEMENT ANALYSIS OF BOLTED JOINTS WITH WASHERS

A circular plate of GFRP is analyzed using the software Straus7 of G + D Computing.

In the centre of this plate, there is a hole with a diameter d_f equal to 22 mm, to simulate the case of a ***single bolt joint***.

The stainless steel bolt, inside the hole, has a diameter d_b equal to 20 mm, thus the plate diameter is equal to $4d_b$ [21-27].

On the bolt, there is an edge horizontal pressure of 0.00571 MPa that corresponds to a resulting of 1 N.

The mesh was obtained by discretizing the FRP plates using two-dimensional finite element type "composite laminate" consisting of a layer of orthotropic material type "ply .

The analysis is carried out considering a bolted joint with variable diameter washer, with variable applied washer pressure, and considering, also, the different fiber inclination with respect of tensile load direction.

This analysis studies the influence of washer and fiber inclination on the bearing stresses and on the failure due to bearing load (**Figure 5.1**).

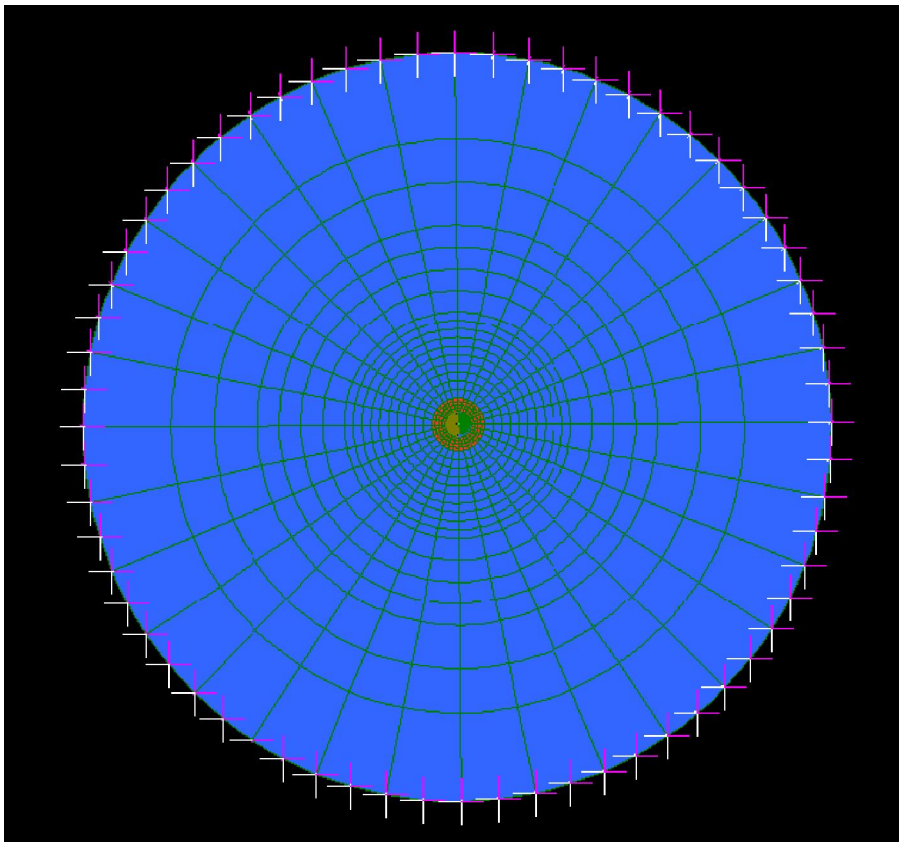

Figure 5.1. Glass composite plate (GFRP) with washer.

The mechanical properties of the GFRP plate and steel bolt are illustrated respectively in **Table 5.1** and **Table 5.2**.

Table 5.1. Mechanical properties of the glass FRP.

Modulus of elasticity in the fibres direction (E_1)	25000 [MPa]
Modulus of elasticity in the direction transverse to the fibres (E_2)	8500 [MPa]
Shear modulus (G_{12})	3000 [MPa]
Poisson ratio (ν_{12})	0.23

Table 5.2. Mechanical properties of the steel bolt.

Modulus of elasticity (E)	210000 [MPa]
Shear Modulus (G)	87500 [MPa]
Poisson ratio (ν)	0.2

The analysis is carried out considering the influence of variable diameter washers (D_w = 30, 40, 50 mm) on the failure modes of the plate and in particular on the bearing stresses around the hole by varying the fibre inclination in the laminate and the washer pressure (p_w) respectively equal to 7.2 MPa (finger-tight) and 216 MPa (**Figure 5.2**). In addition, the fibre angles considered are: 0°, 5°, 15°, 30°, 45°, 60°, 75°, 90°.

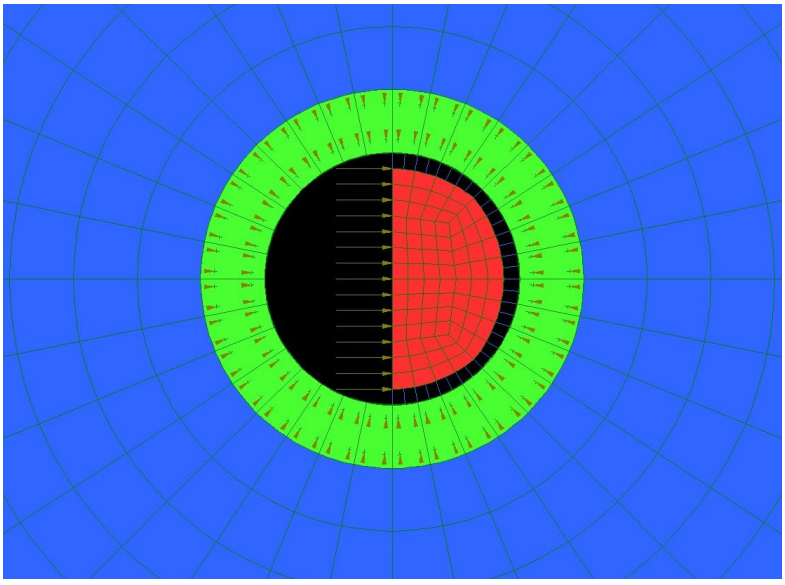

Figure 5.2. Glass composite plate (GFRP) with washer.

The lateral contact bolt/surface is modeled using one-dimensional

finite element, point contact element, with stiffness only in compression.

The plate is modeled **without washers (ww)**.

5.1. Results and discussion

Results of a non-linear analysis, carried on mentioned joints, is presented considering different fiber inclinations and the presence of washer.

In particular, the stress diagram of normal stress in fiber direction (σ_{11}) and orthogonal to this direction (σ_{22}) is illustrated in the figures below (from **Figure 5.3** to **Figure 5.114**).

Furthermore the following figures show the effects of the presence of mentioned variable diameter washers and the fiber inclinations (α) equal to 0°, 5°, 15°, 30°, 45°, 60°, 75°, 90° considering a washer pressure (p_w) equal to 7.2 MPa (finger-tight) and 216 MPa, respectively.

Moreover, the contact surface respectively between the hole and the washer and the plate is modelled, also, through a *point-contact element*, with the ***friction μ*** equal to 0.07 [21-27].

The finite element analysis is carried out by applying an edge compression pressure to the steel bolt in order to evaluate the bearing stress acting around the hole.

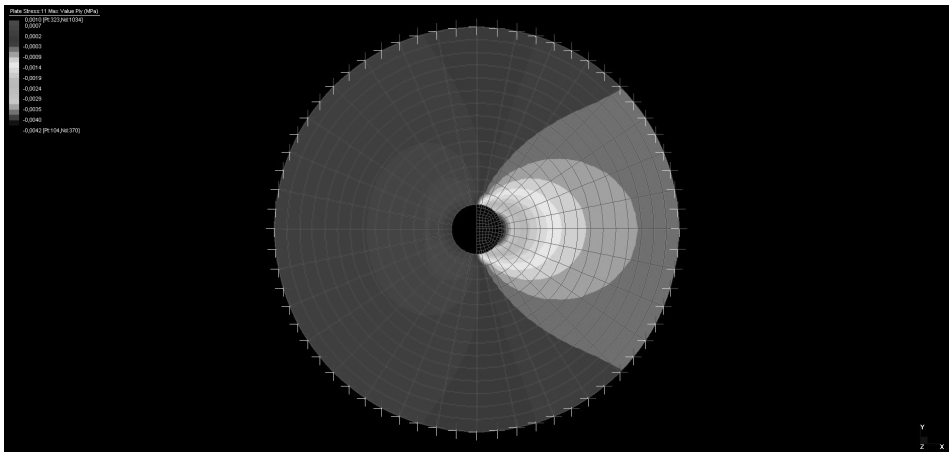

Figure 5.3. Diagram of stress σ_{11} – α = 0°– ww – p_w = 7.2 MPa.

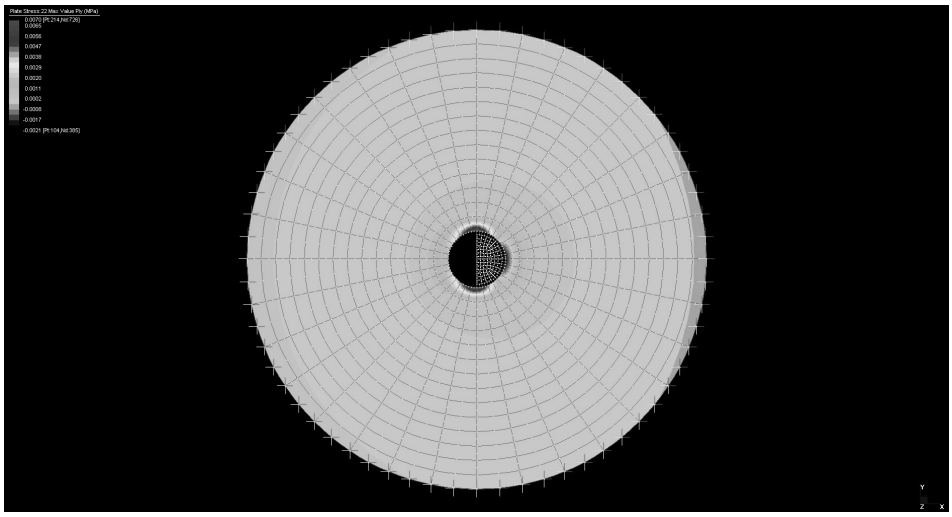

Figure 5.4. Diagram of stress σ_{22} – α = 0°– ww – p_w = 7.2 MPa.

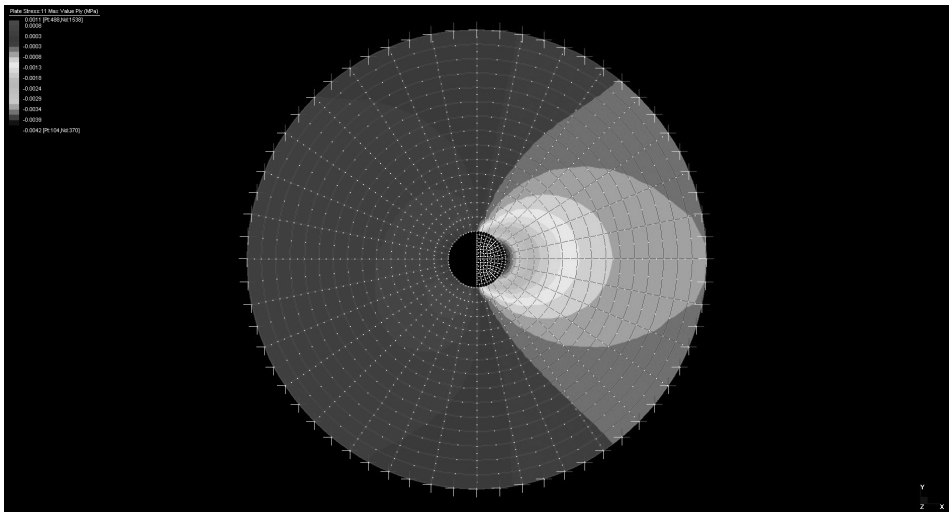

Figure 5.5. Diagram of stress σ_{11} – α = 5°– ww – p_w = 7.2 MPa.

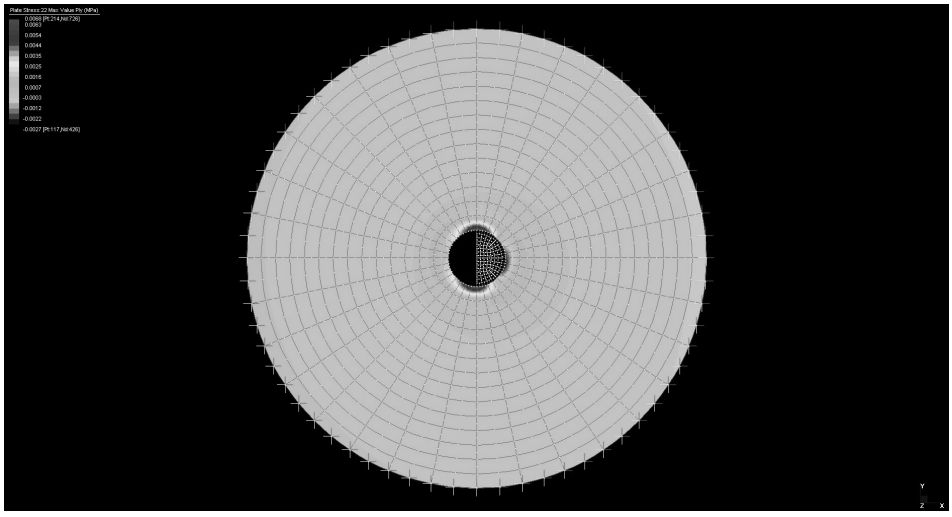

Figure 5.6. Diagram of stress σ_{22} – α = 5°– ww – p_w = 7.2 MPa.

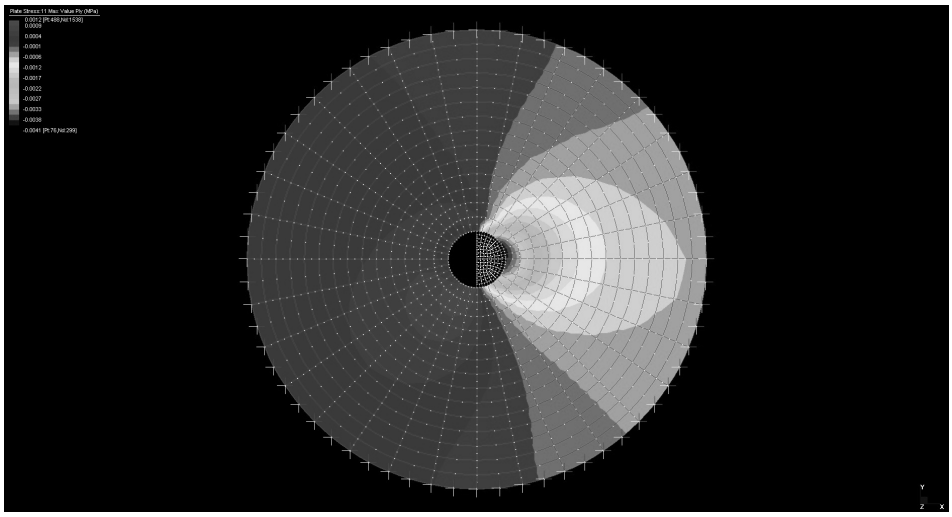

Figure 5.7. Diagram of stress σ_{11} – α = 15°– ww – p_w = 7.2 MPa.

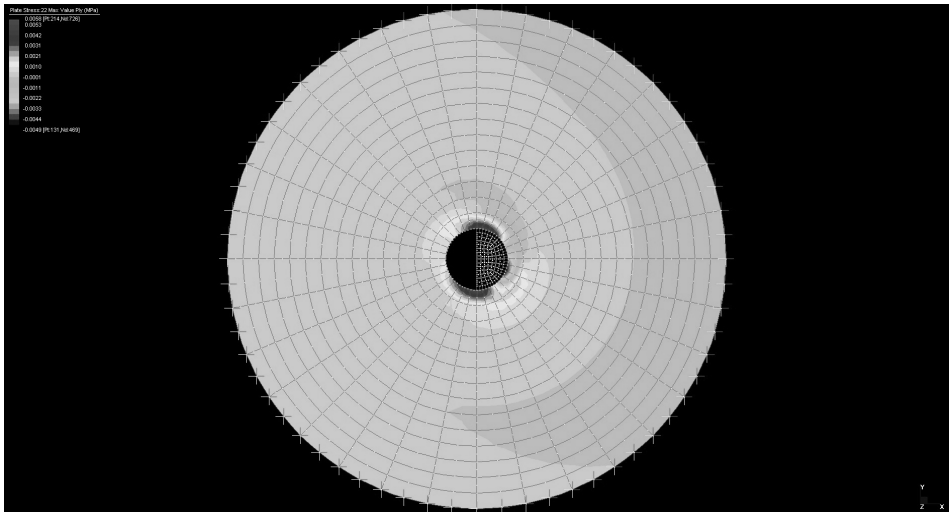

Figure 5.8. Diagram of stress σ_{22} – α = 15°– ww – p_w = 7.2 MPa.

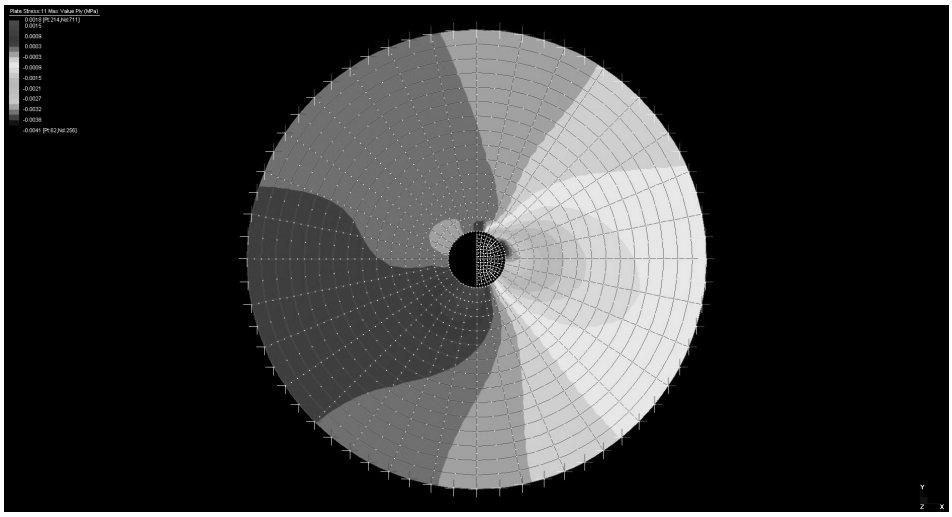

Figure 5.9. Diagram of stress σ_{11} – α = 30°– ww – p_w = 7.2 MPa.

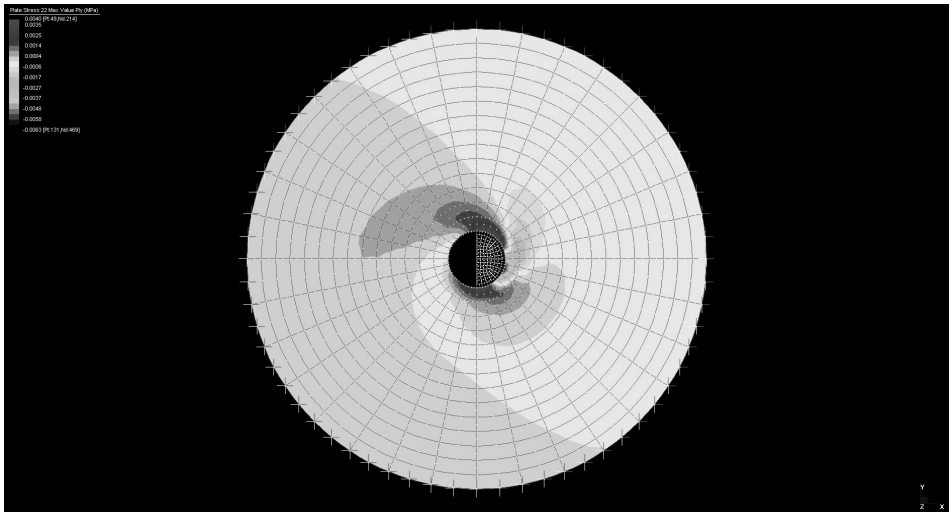

Figure 5.10. Diagram of stress σ_{22} – α = 30°– ww – p_w = 7.2 MPa.

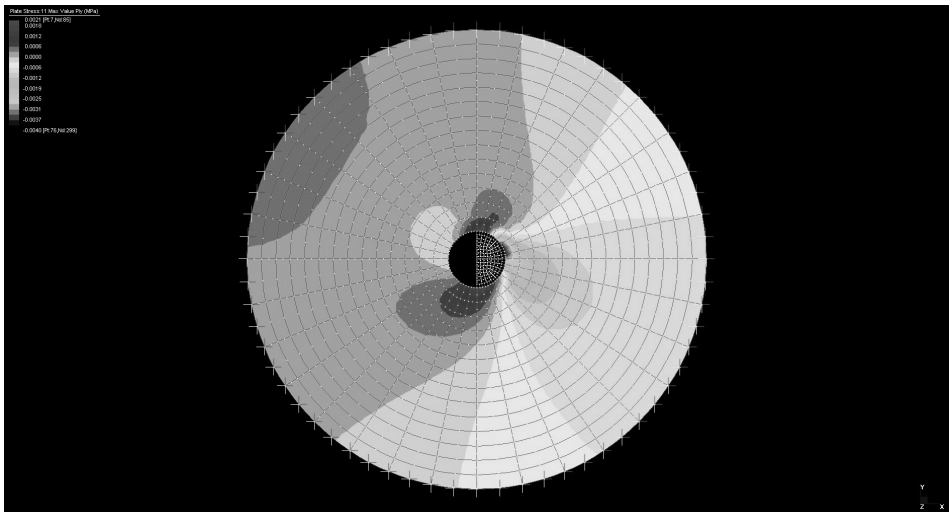

Figure 5.11. Diagram of stress σ_{11} – α = 45°– ww – p_w = 7.2 MPa.

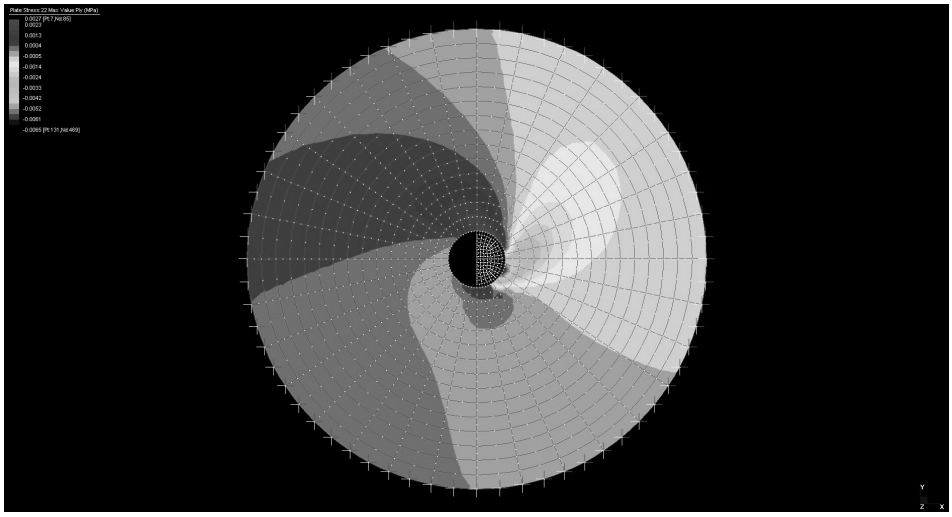

Figure 5.12. Diagram of stress σ_{22} – α = 45°– ww – p_w = 7.2 MPa.

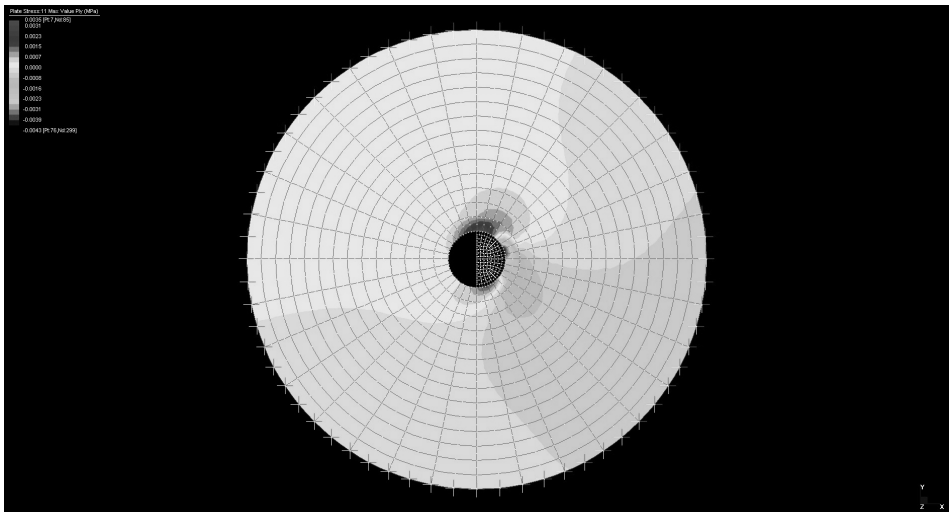

Figure 5.13. Diagram of stress σ_{11} – α = 60°– ww – p_w = 7.2 MPa.

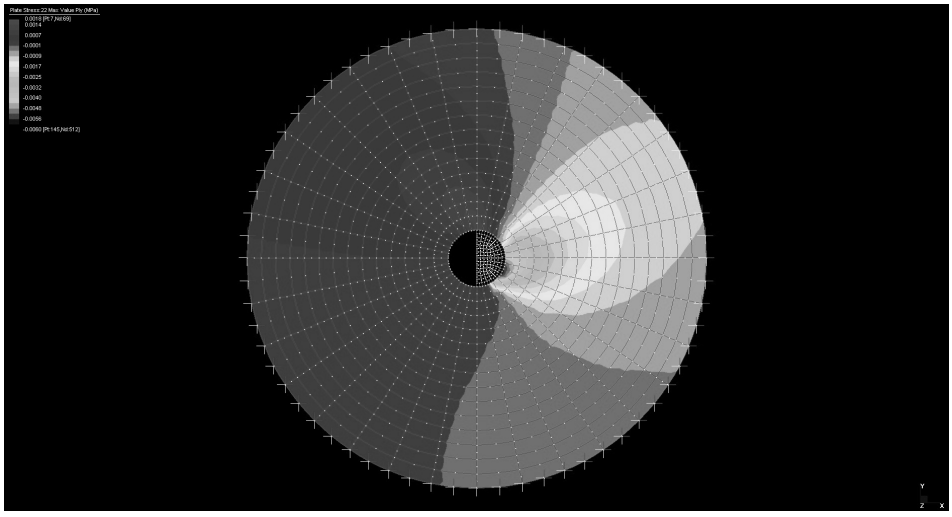

Figure 5.14. Diagram of stress σ_{22} – α = 60°– ww – p_w = 7.2 MPa.

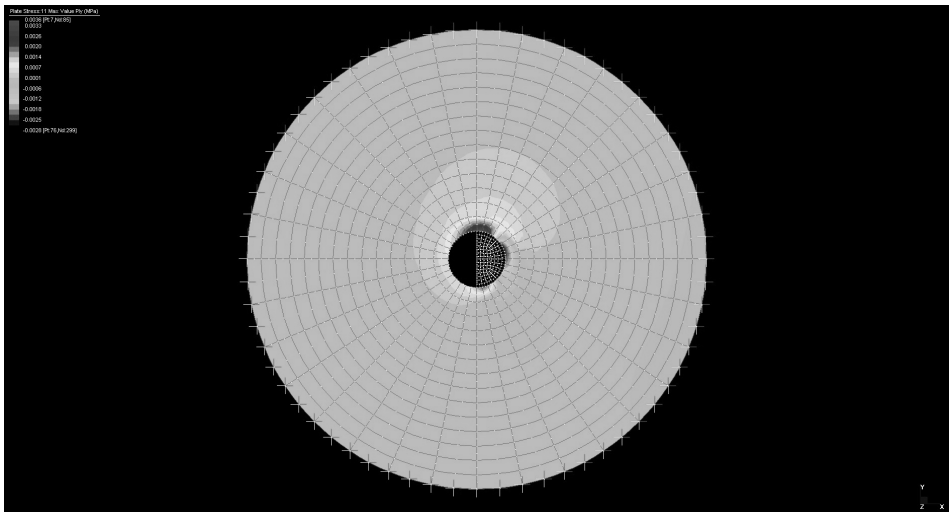

Figure 5.15. Diagram of stress σ_{11} – α = 75°– ww – p_w = 7.2 MPa.

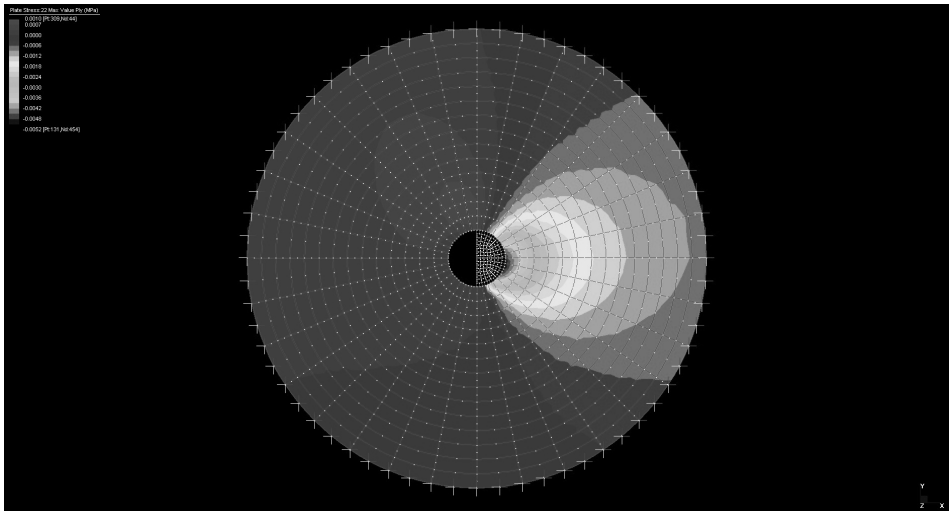

Figure 5.16. Diagram of stress σ_{22} – α = 75°– ww – p_w = 7.2 MPa.

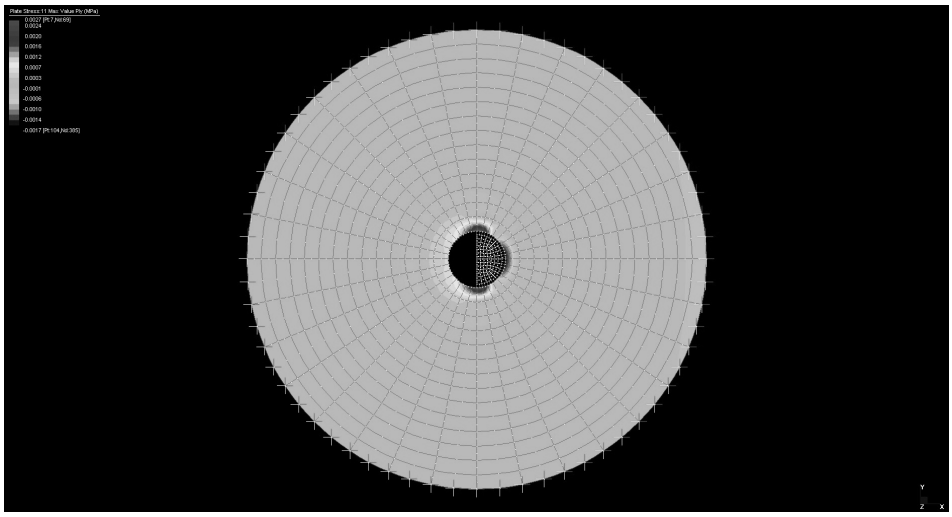

Figure 5.17. Diagram of stress σ_{11} – α = 90°– ww – p_w = 7.2 MPa.

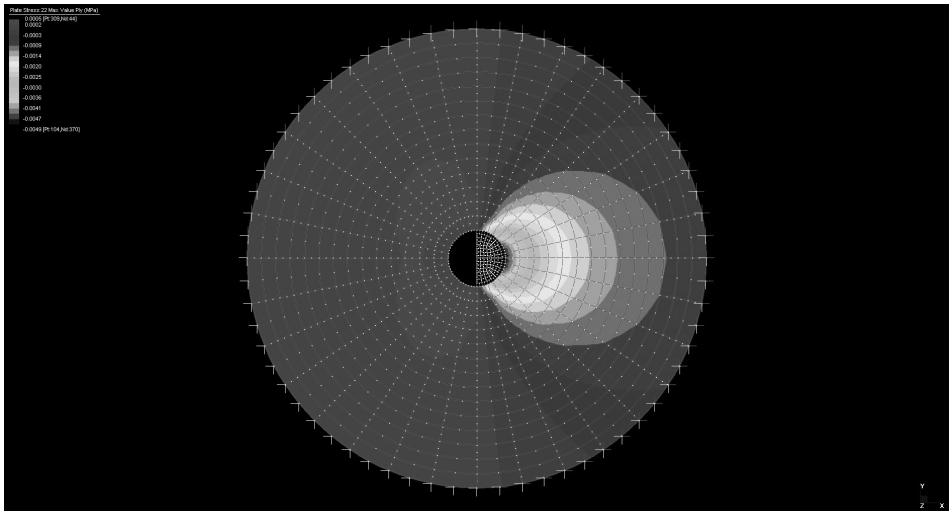

Figure 5.18. Diagram of stress σ_{22} – α = 90°– ww – p_w = 7.2 MPa.

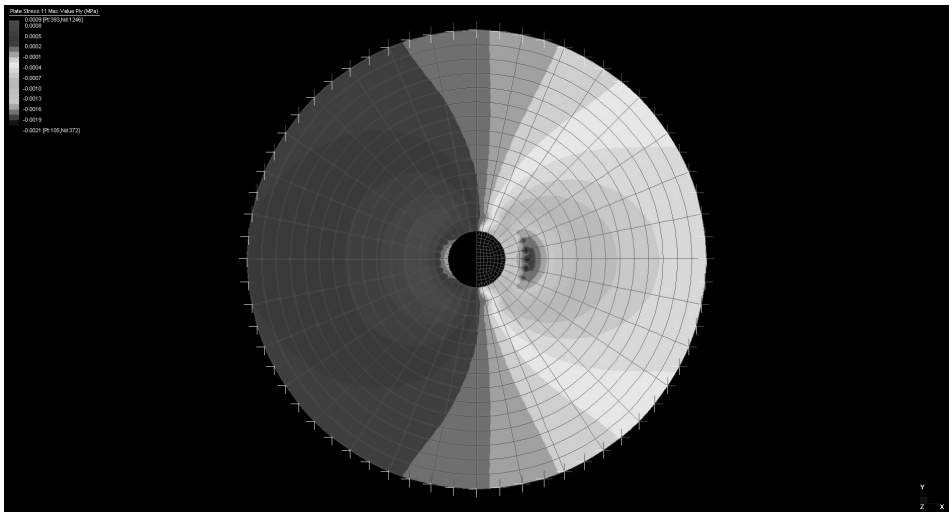

Figure 5.19. Diagram of stress σ_{11} – α = 0°– D_w = 30mm – p_w = 7.2 MPa.

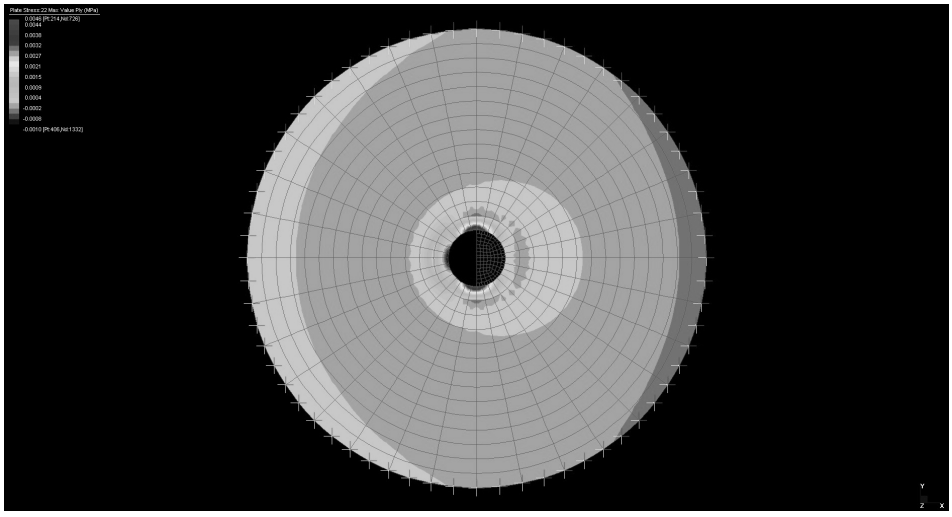

Figure 5.20. Diagram of stress σ_{22} – α = 0°– D_w = 30mm – p_w = 7.2 MPa.

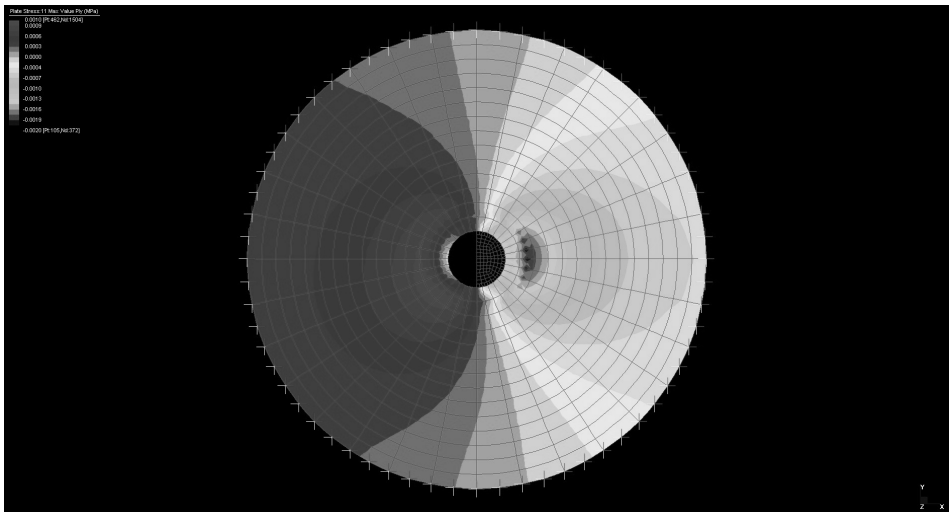

Figure 5.21. Diagram of stress σ_{11} – α = 5°– D_w = 30mm – p_w = 7.2 MPa.

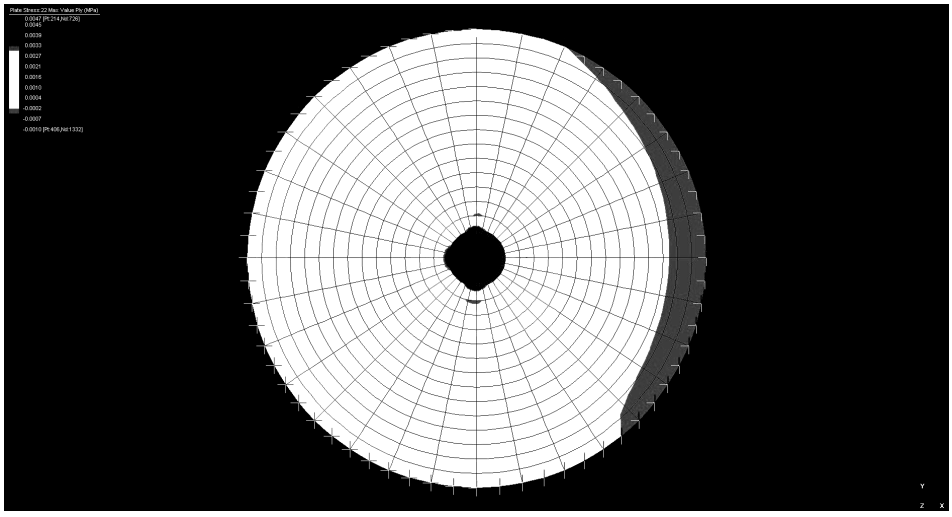

Figure 5.22. Diagram of stress σ_{22} – α = 5°– D_w = 30mm – p_w = 7.2 MPa.

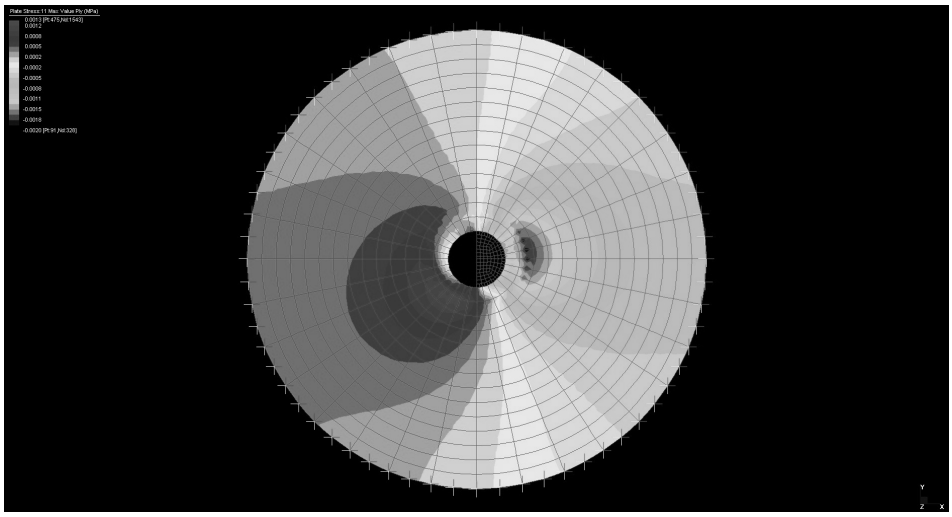

Figure 5.23. Diagram of stress σ_{11} – α = 15°– D_w = 30mm – p_w = 7.2 MPa.

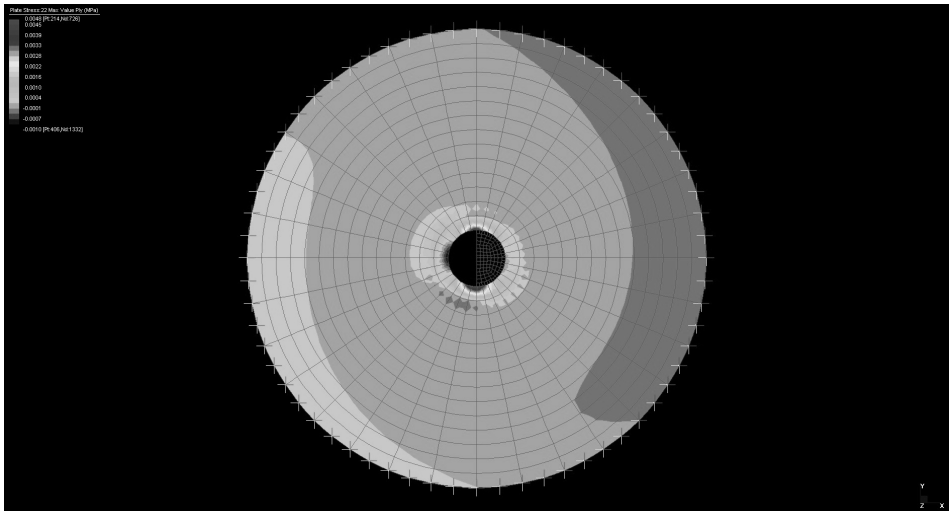

Figure 5.24. Diagram of stress σ_{22} – α = 15°– D_w = 30mm – p_w = 7.2 MPa.

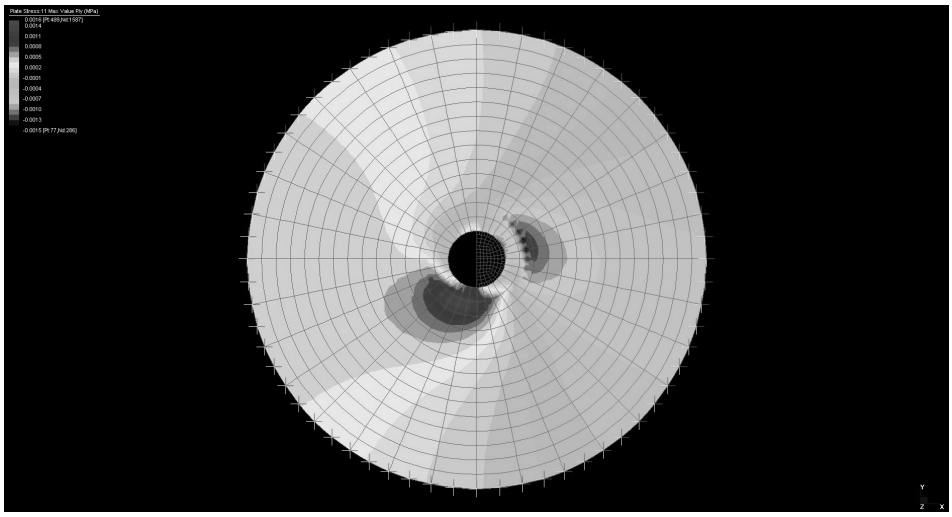

Figure 5.25. Diagram of stress σ_{11} – α = 30°– D_w = 30mm – p_w = 7.2 MPa.

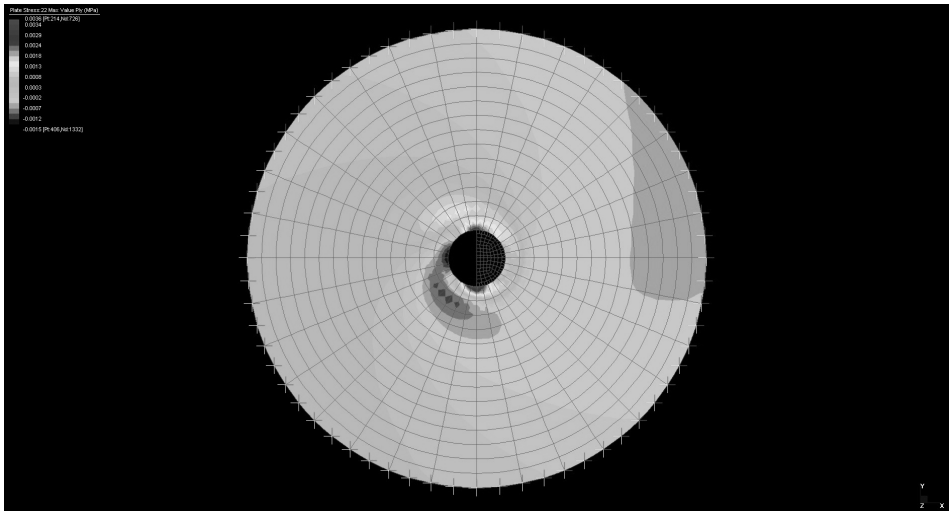

Figure 5.26. Diagram of stress σ_{22} – α = 30°– D_w = 30mm – p_w = 7.2 MPa.

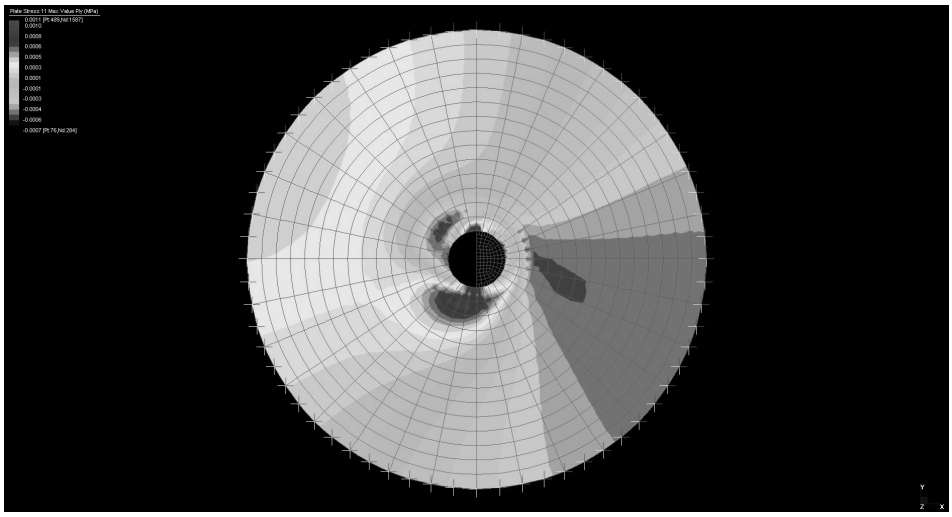

Figure 5.27. Diagram of stress σ_{11} – α = 45°– D_w = 30mm – p_w = 7.2 MPa.

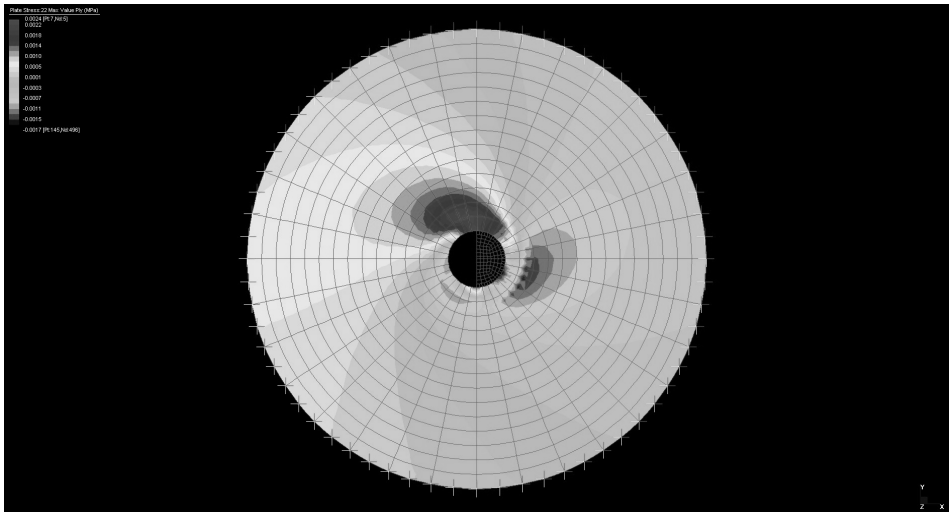

Figure 5.28. Diagram of stress σ_{22} – α = 45°– D_w = 30mm – p_w = 7.2 MPa.

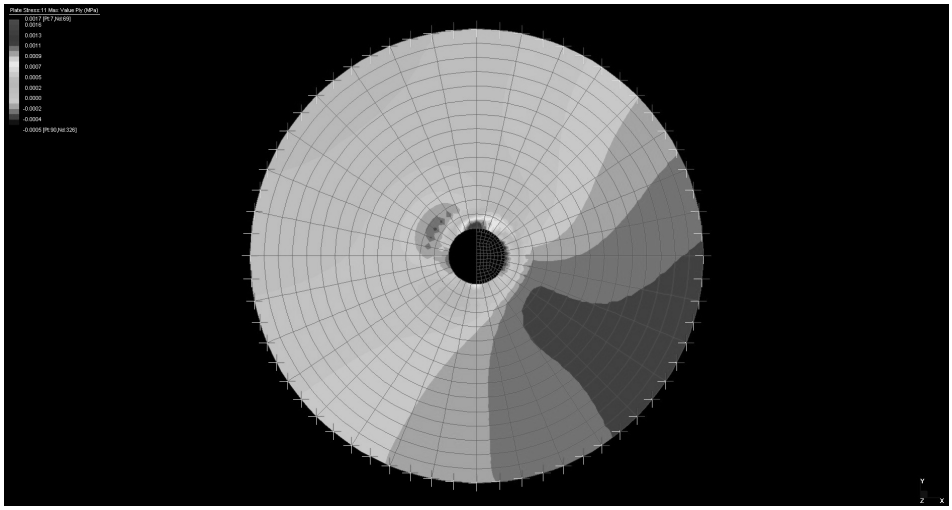

Figure 5.29. Diagram of stress σ_{11} – α = 60°– D_w = 30mm – p_w = 7.2 MPa.

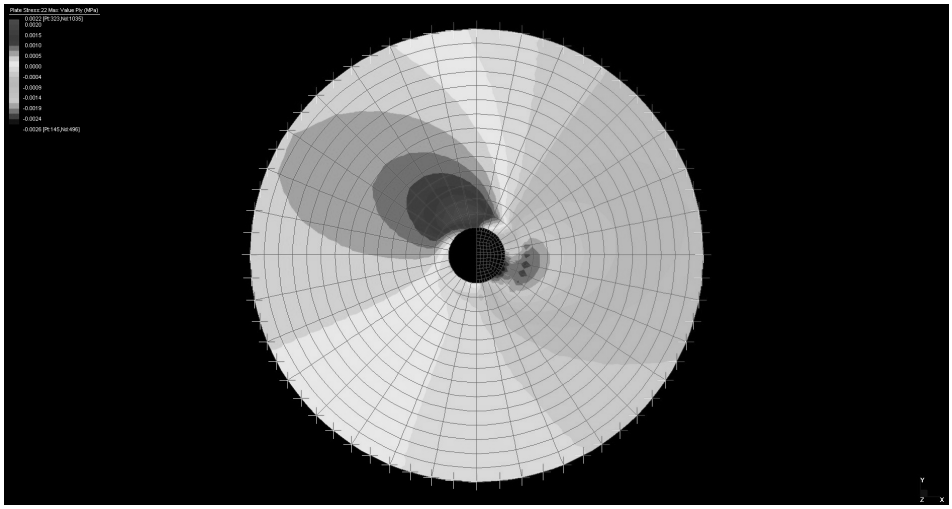

Figure 5.30. Diagram of stress σ_{22} – α = 60°– D_w = 30mm – p_w = 7.2 MPa.

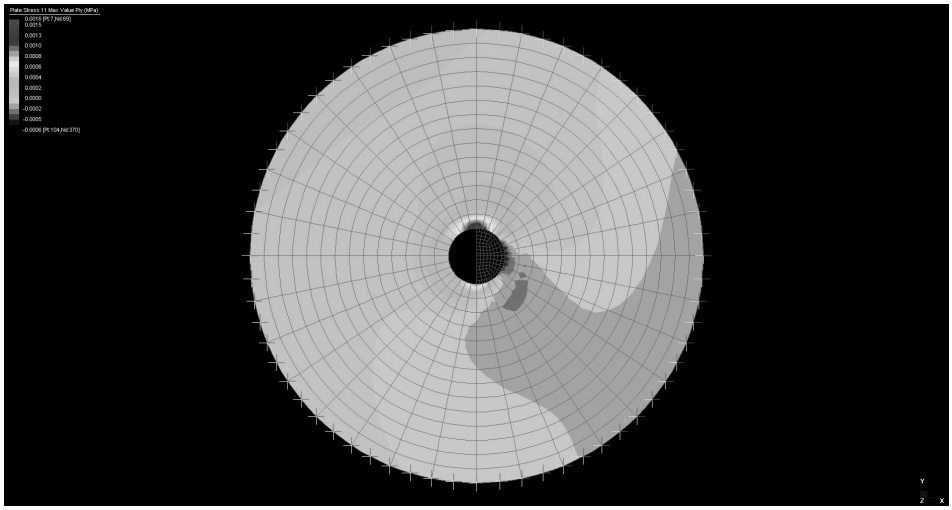

Figure 5.31. Diagram of stress σ_{11} – α = 75°– D_w = 30mm – p_w = 7.2 MPa.

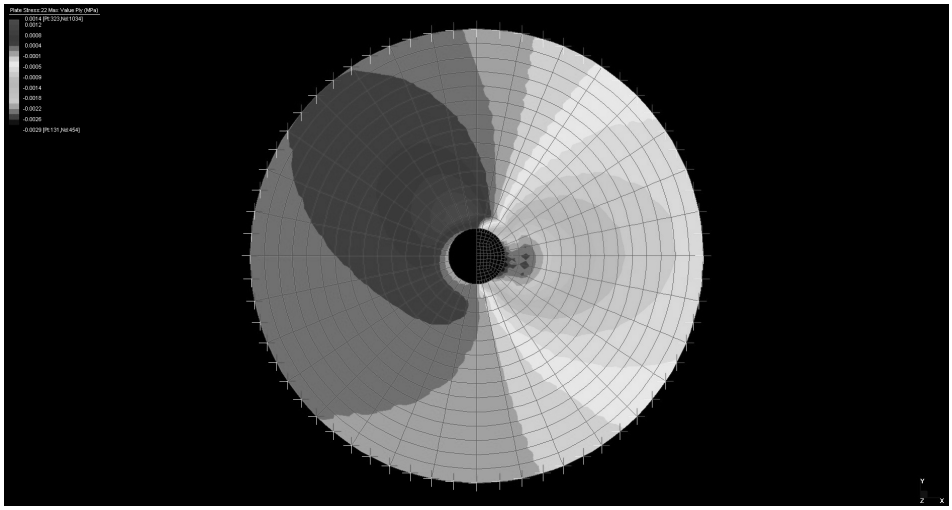

Figure 5.32. Diagram of stress σ_{22} – α = 75°– D_w = 30mm – p_w = 7.2 MPa.

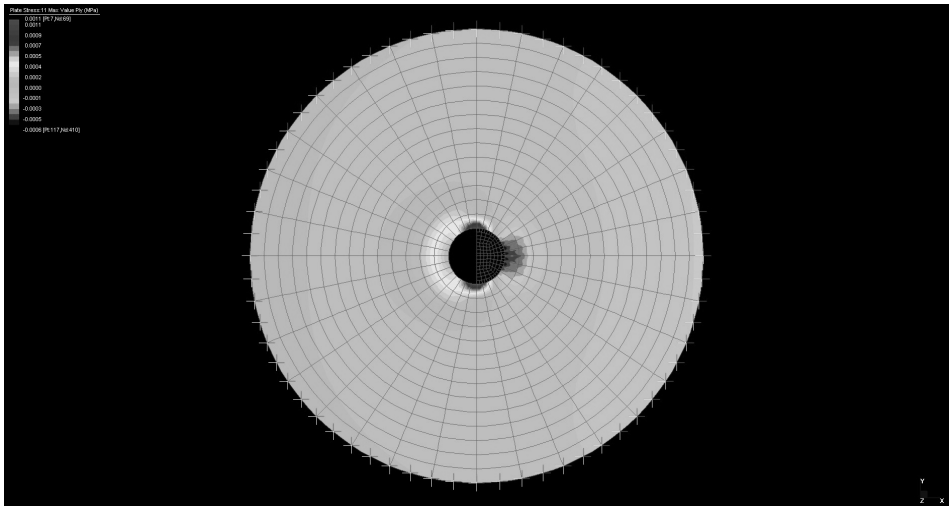

Figure 5.33. Diagram of stress σ_{11} – α = 90°– D_w = 30mm – p_w = 7.2 MPa.

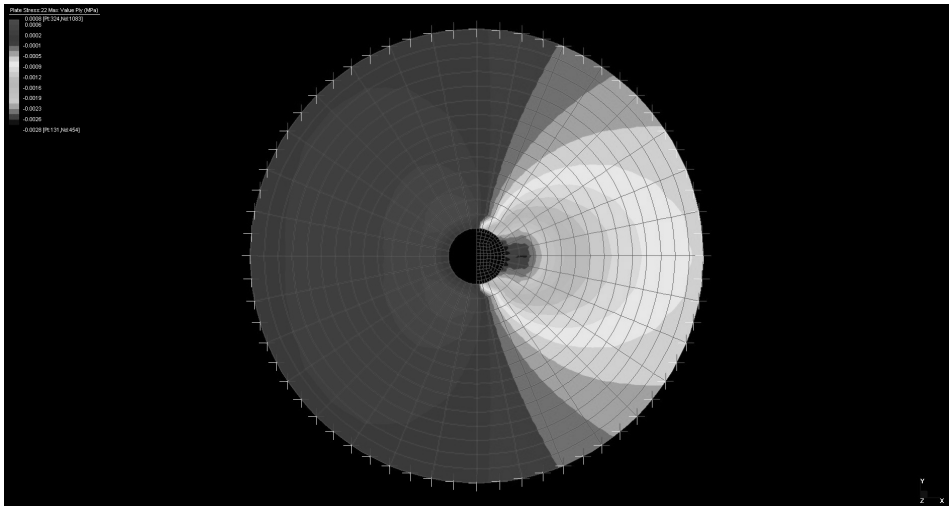

Figure 5.34. Diagram of stress σ_{22} – α = 90°– D_w = 30mm – p_w = 7.2 MPa.

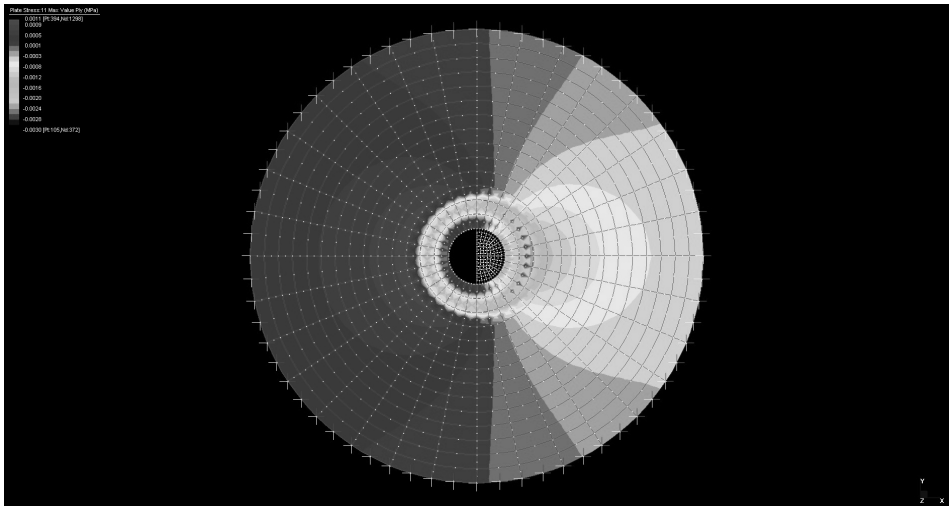

Figure 5.35. Diagram of stress σ_{11} – α = 0°– D_w = 40mm – p_w = 7.2 MPa.

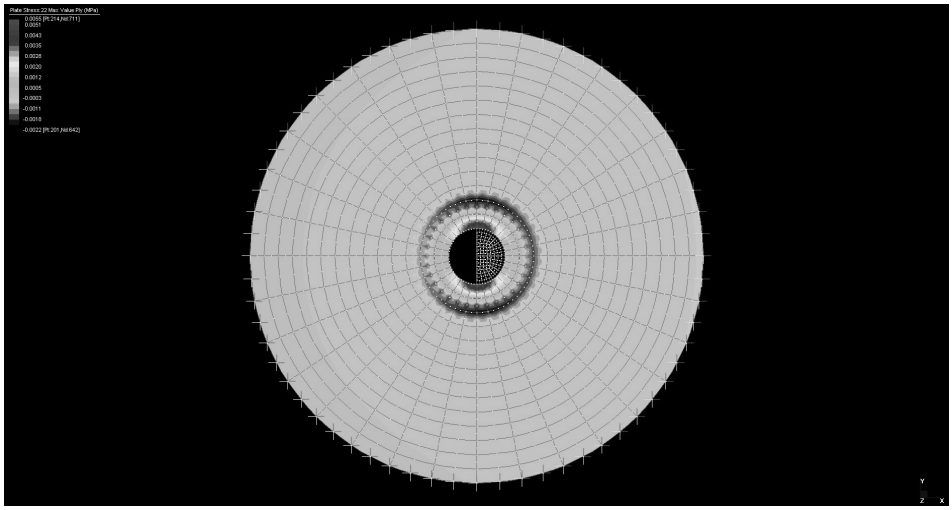

Figure 5.36. Diagram of stress σ_{22} – α = 0°– D_w = 40mm – p_w = 7.2 MPa.

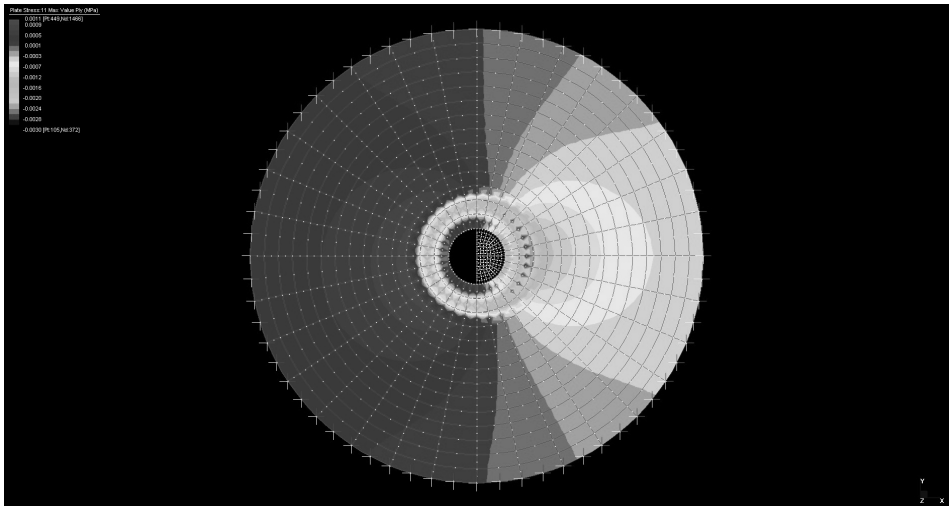

Figure 5.37. Diagram of stress σ_{11} – α = 5°– D_w = 40mm – p_w = 7.2 MPa.

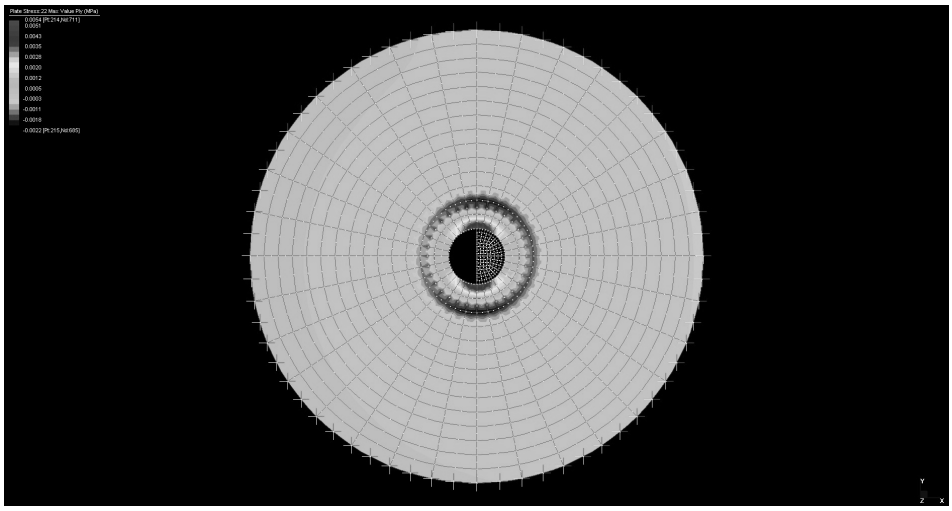

Figure 5.38. Diagram of stress σ_{22} – α = 5°– D_w = 40mm – p_w = 7.2 MPa.

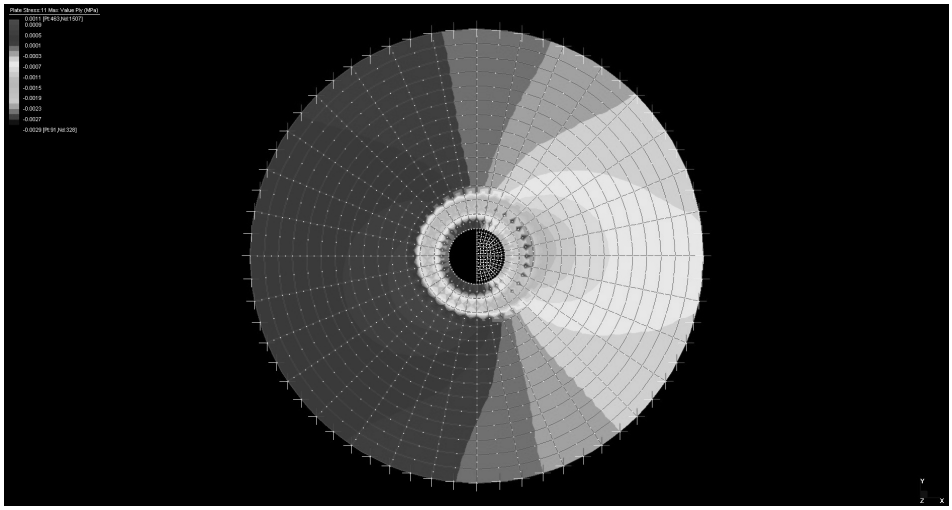

Figure 5.39. Diagram of stress σ_{11} – α = 15°– D_w = 40mm – p_w = 7.2 MPa.

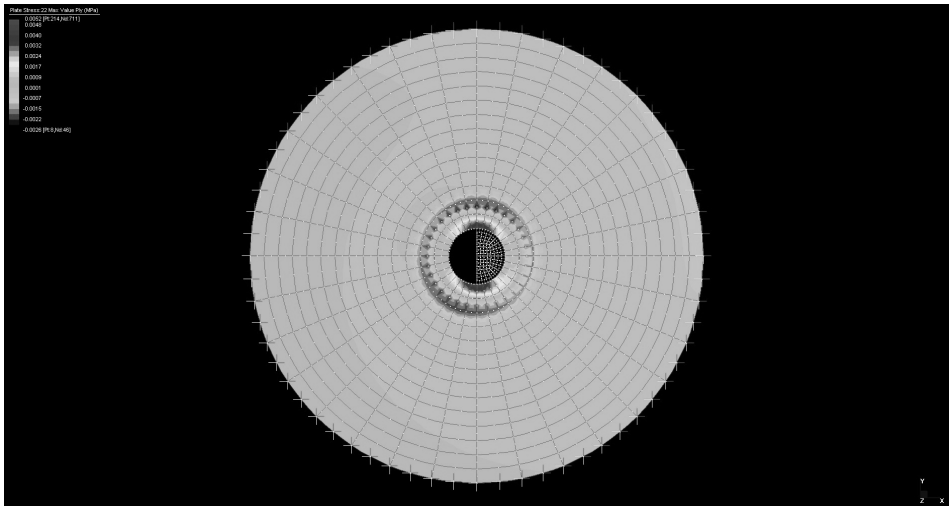

Figure 5.40. Diagram of stress σ_{22} – α = 15°– D_w = 40mm – p_w = 7.2 MPa.

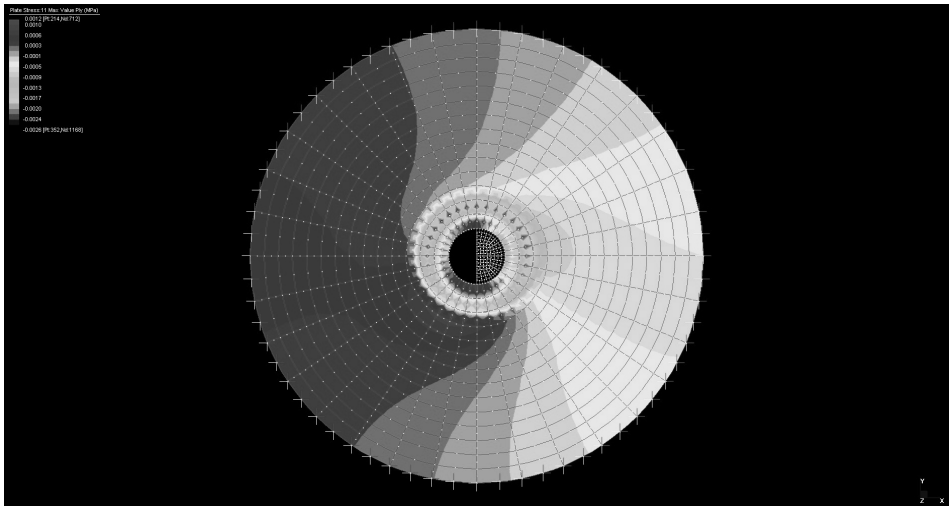

Figure 5.41. Diagram of stress σ_{11} – α = 30°– D_w = 40mm – p_w = 7.2 MPa.

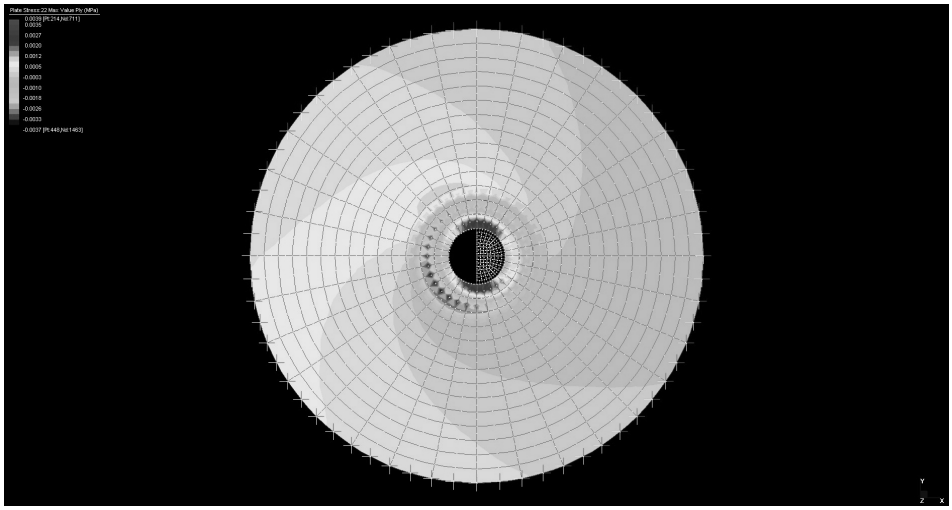

Figure 5.42. Diagram of stress σ_{22} – α = 30°– D_w = 40mm – p_w = 7.2 MPa.

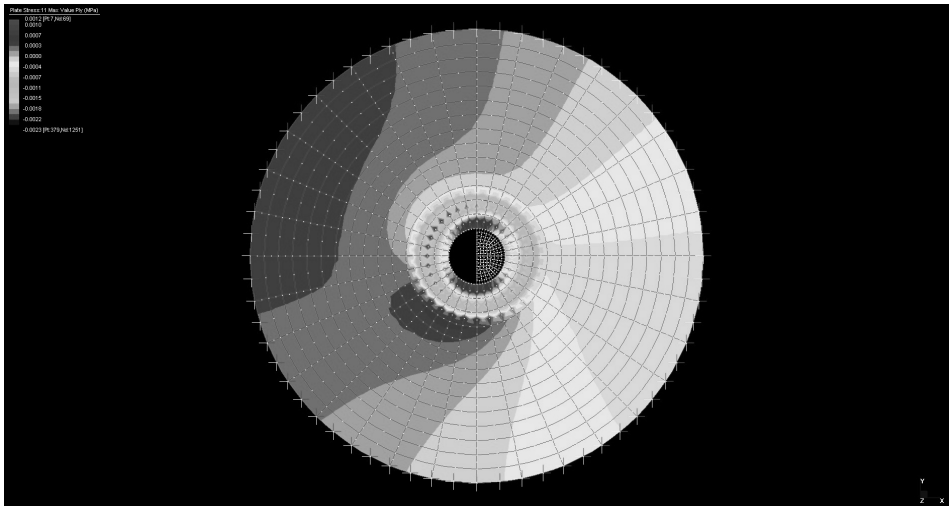

Figure 5.43. Diagram of stress σ_{11} – α = 45°– D_w = 40mm – p_w = 7.2 MPa.

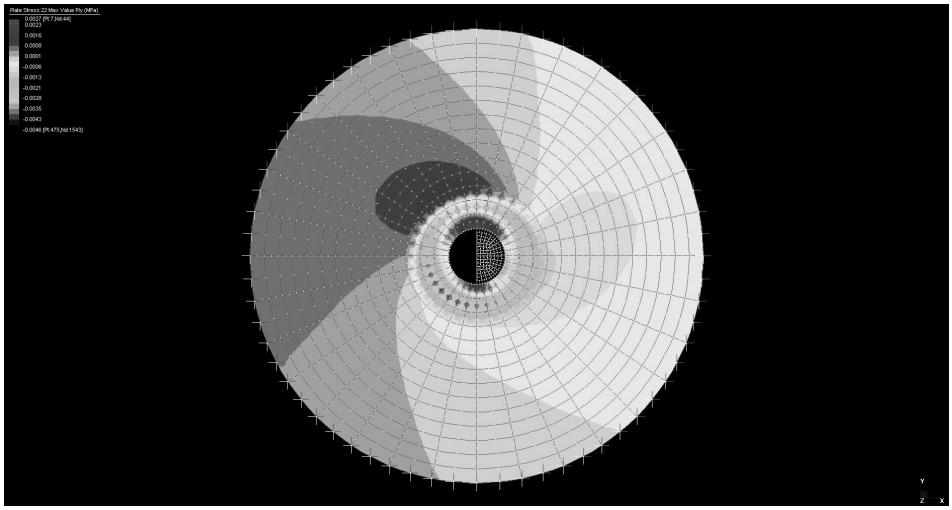

Figure 5.44. Diagram of stress σ_{22} – α = 45°– D_w = 40mm – p_w = 7.2 MPa.

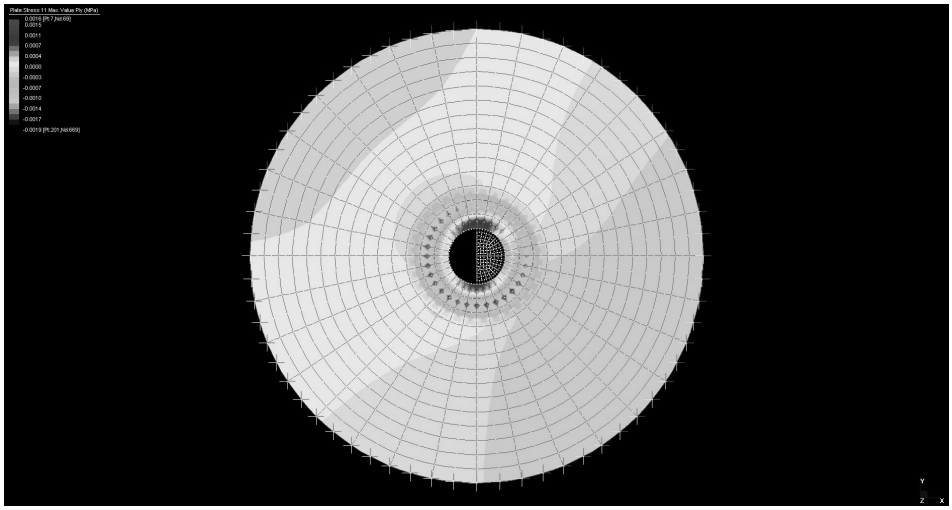

Figure 5.45. Diagram of stress σ_{11} – α = 60°– D_w = 40mm – p_w = 7.2 MPa.

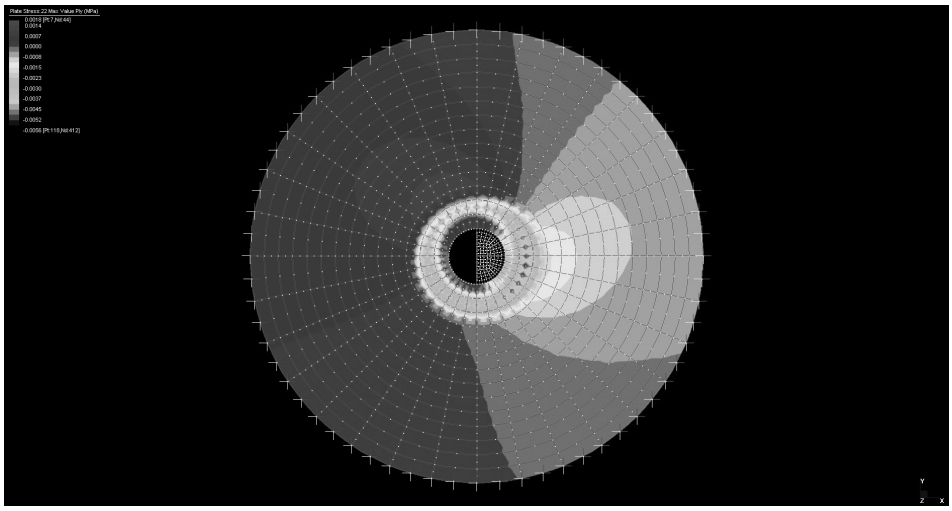

Figure 5.46. Diagram of stress σ_{22} – α = 60°– D_w = 40mm – p_w = 7.2 MPa.

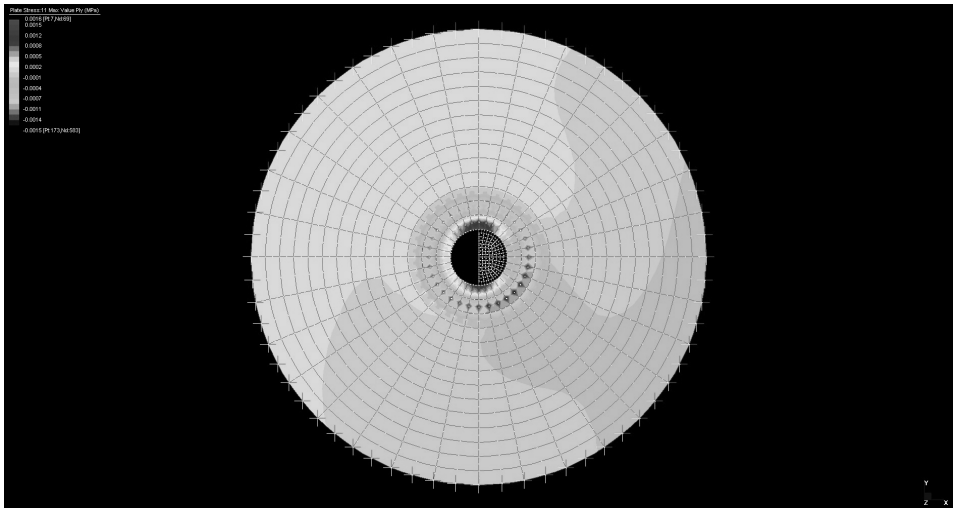

Figure 5.47. Diagram of stress σ_{11} – α = 75°– D_w = 40mm – p_w = 7.2 MPa.

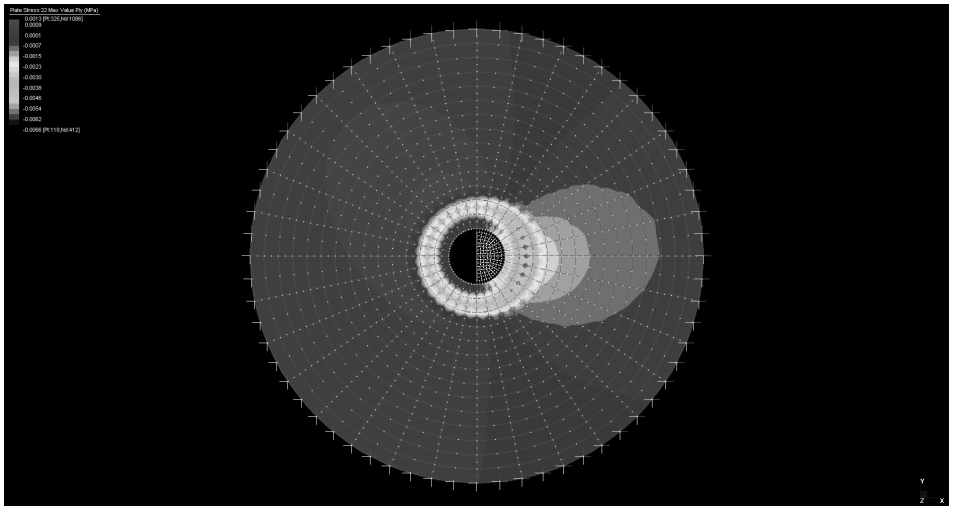

Figure 5.48. Diagram of stress σ_{22} – α = 75°– D_w = 40mm – p_w = 7.2 MPa.

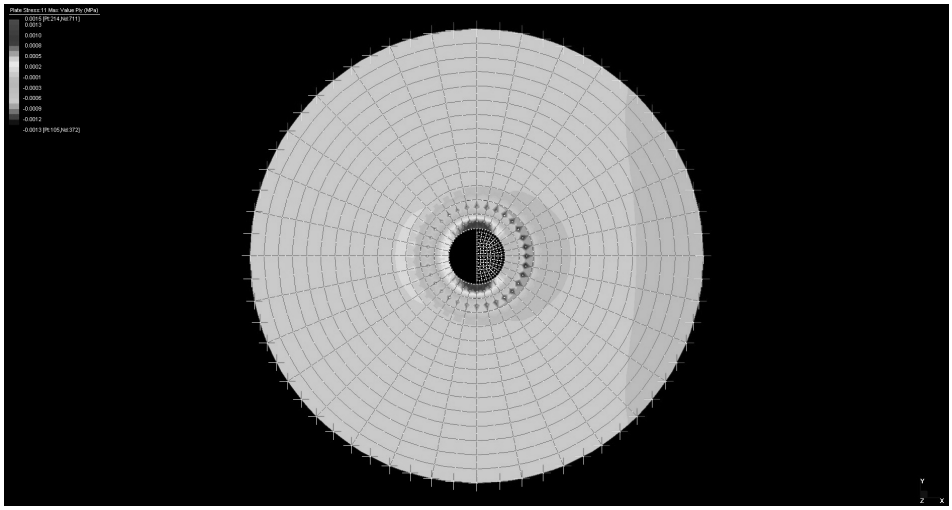

Figure 5.49. Diagram of stress σ_{11} – α = 90°– D_w = 40mm – p_w = 7.2 MPa.

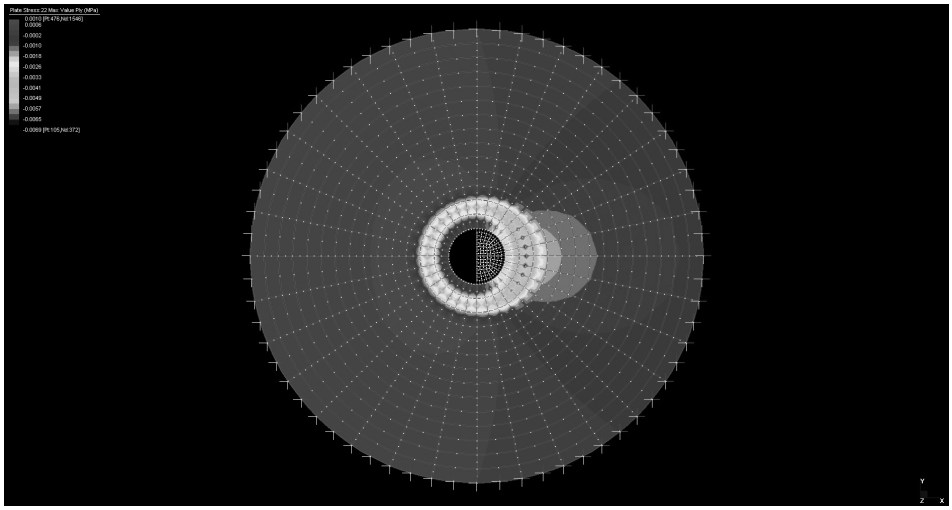

Figure 5.50. Diagram of stress σ_{22} – α = 90°– D_w = 40mm – p_w = 7.2 MPa.

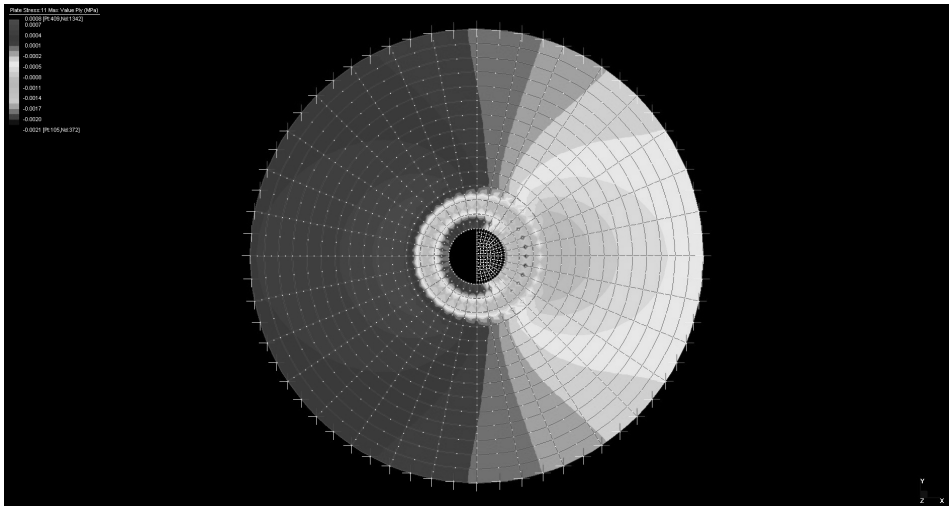

Figure 5.51. Diagram of stress σ_{11} – α = 0°– D_w = 50mm – p_w = 7.2 MPa.

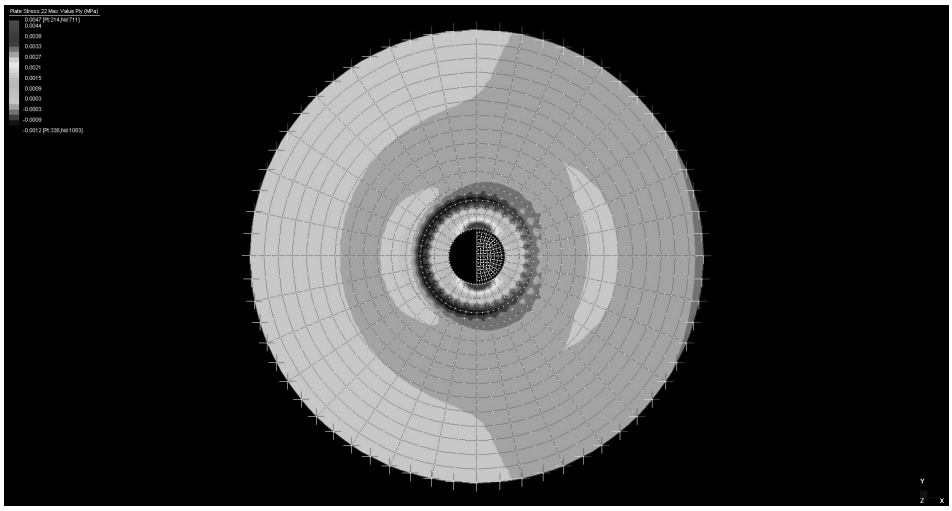

Figure 5.52. Diagram of stress σ_{22} – α = 0°– D_w = 50mm – p_w = 7.2 MPa.

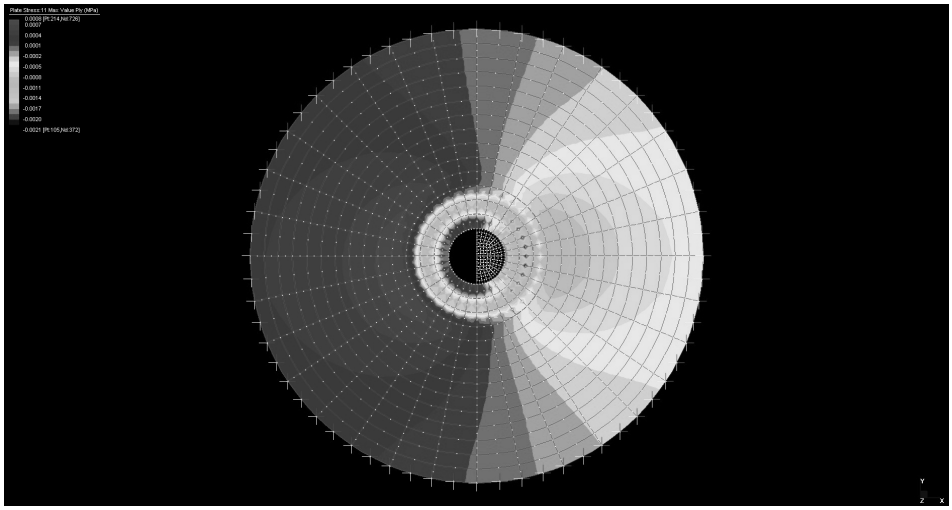

Figure 5.53. Diagram of stress σ_{11} – α = 5°– D_w = 50mm – p_w = 7.2 MPa.

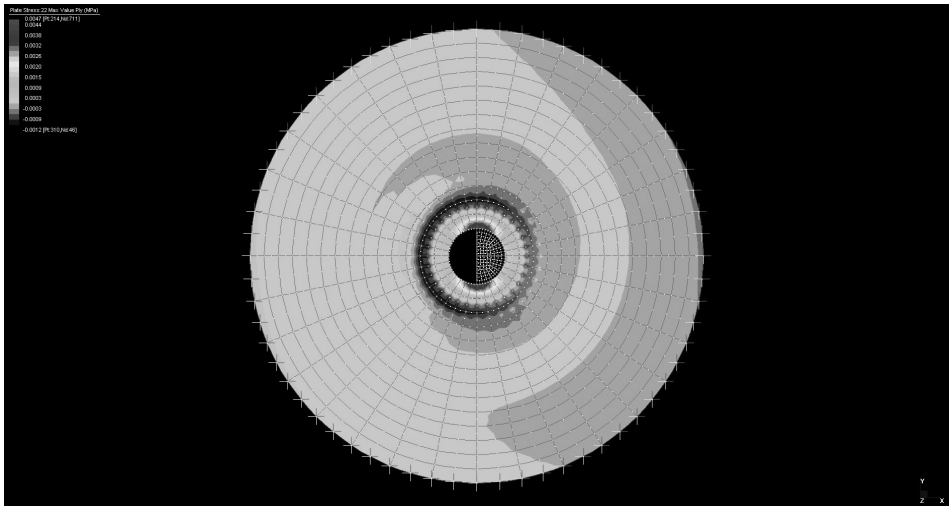

Figure 5.54. Diagram of stress σ_{22} – α = 5°– D_w = 50mm – p_w = 7.2 MPa.

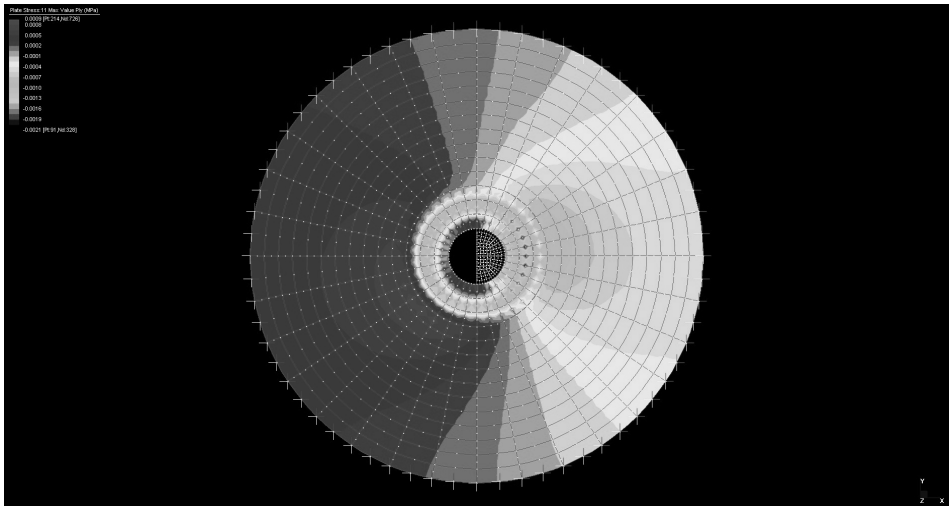

Figure 5.55. Diagram of stress σ_{11} – α = 15°– D_w = 50mm – p_w = 7.2 MPa.

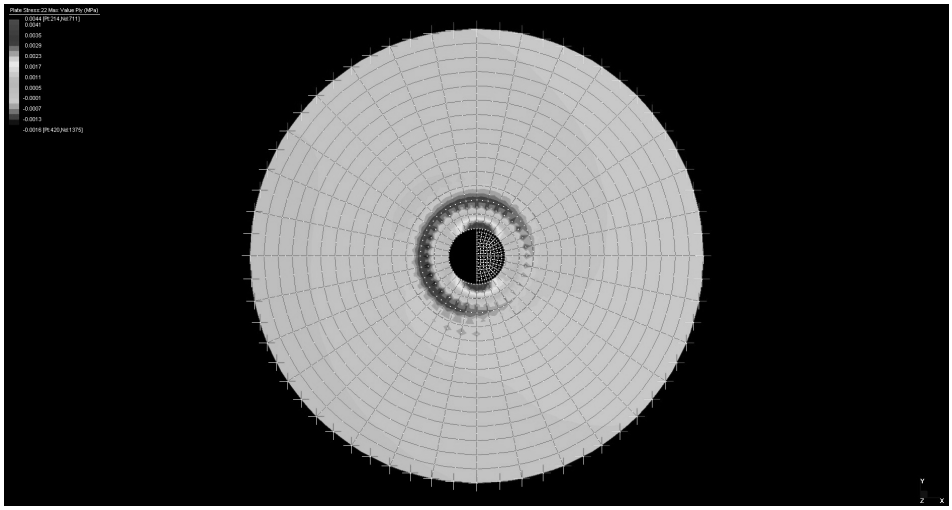

Figure 5.56. Diagram of stress σ_{22} – α = 15°– D_w = 50mm – p_w = 7.2 MPa.

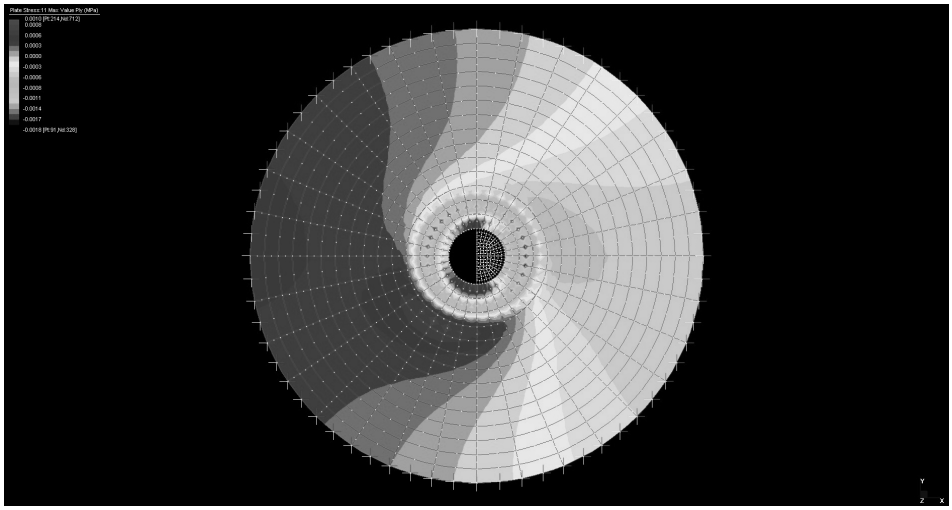

Figure 5.57. Diagram of stress σ_{11} – α = 30°– D_w = 50mm – p_w = 7.2 MPa.

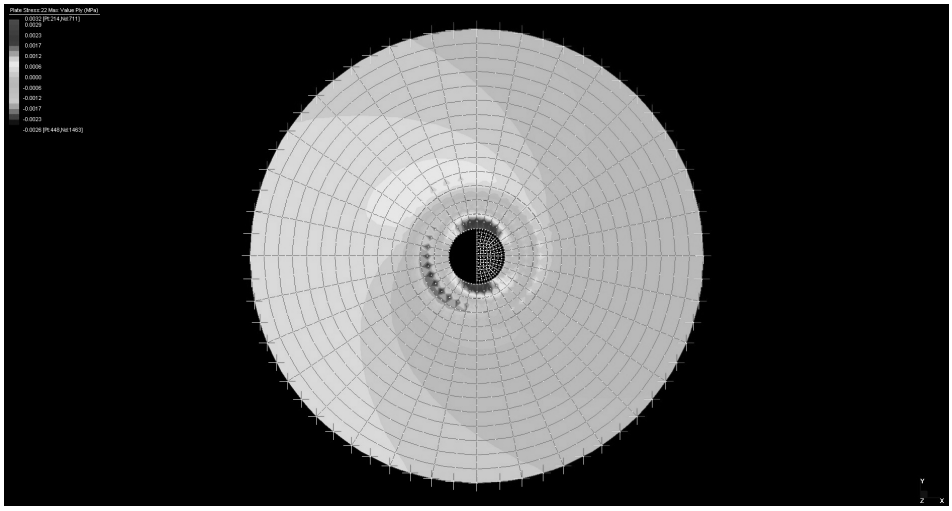

Figure 5.58. Diagram of stress σ_{22} – α = 30°– D_w = 50mm – p_w = 7.2 MPa.

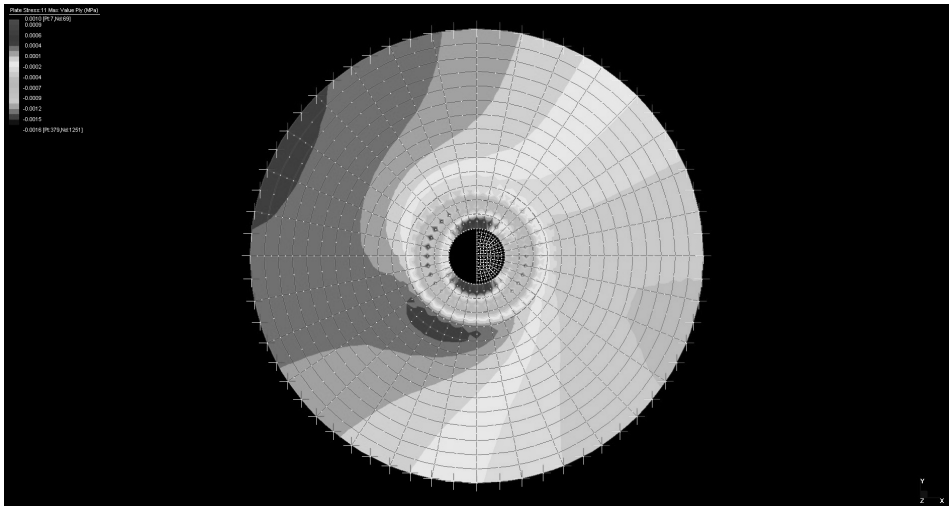

Figure 5.59. Diagram of stress σ_{11} – α = 45°– D_w = 50mm – p_w = 7.2 MPa.

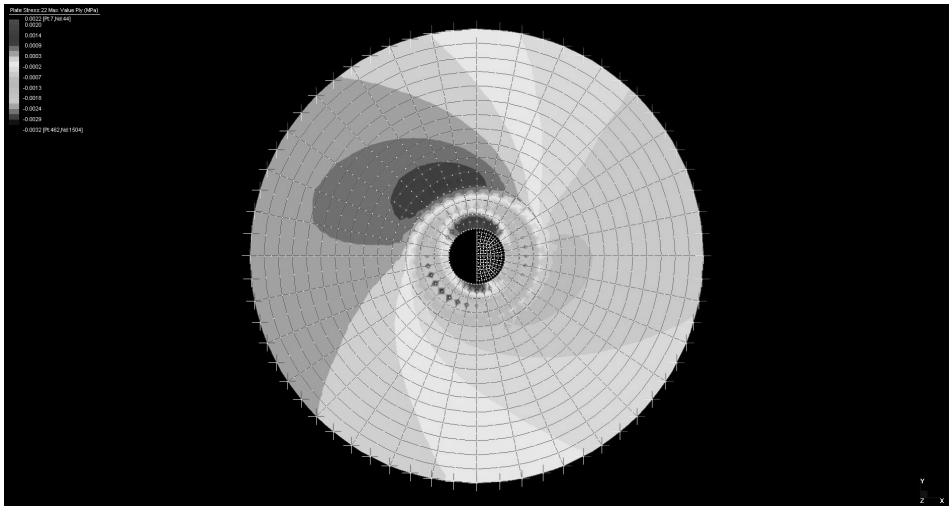

Figure 5.60. Diagram of stress σ_{22} – α = 45°– D_w = 50mm – p_w = 7.2 MPa.

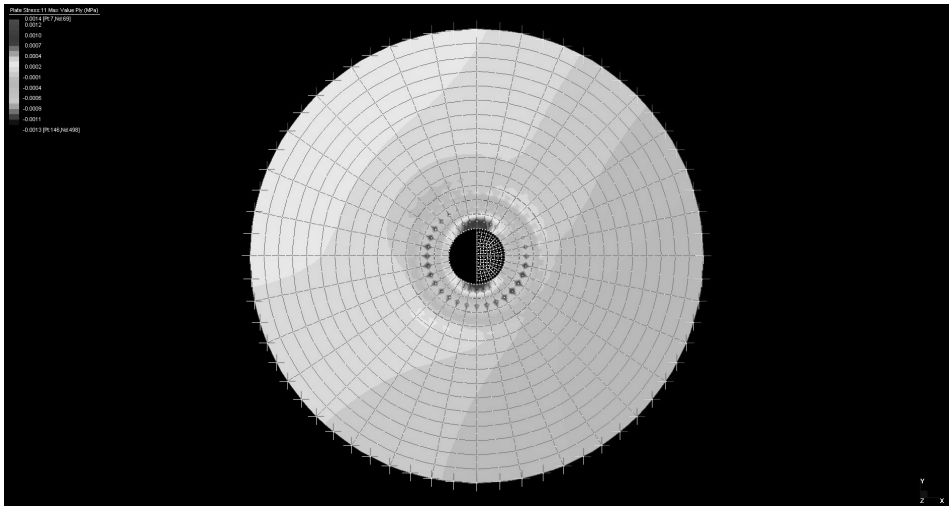

Figure 5.61. Diagram of stress σ_{11} – α = 60°– D_w = 50mm – p_w = 7.2 MPa.

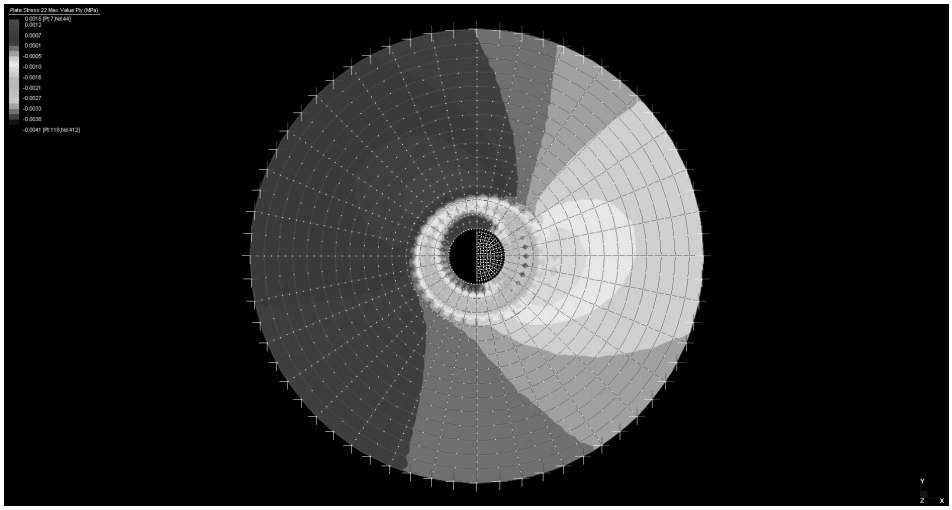

Figure 5.62. Diagram of stress σ_{22} – α = 60°– D_w = 50mm – p_w = 7.2 MPa.

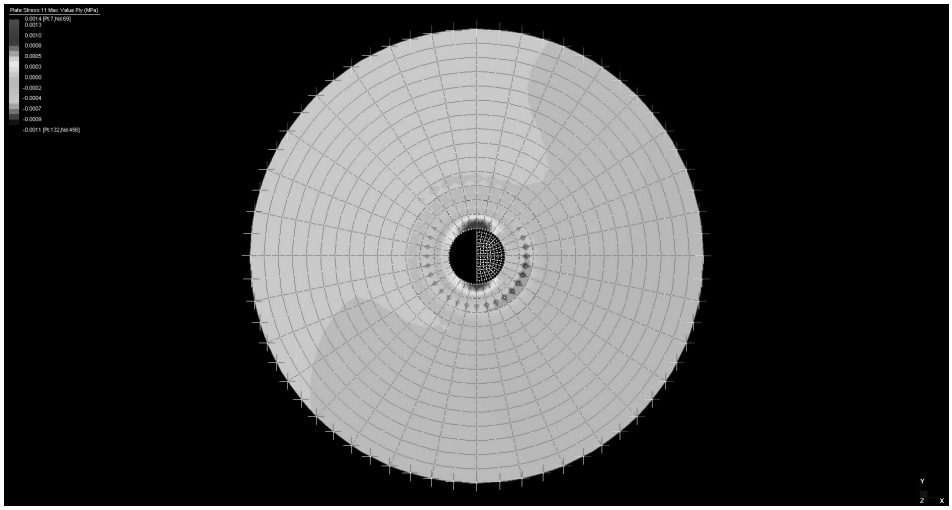

Figure 5.63. Diagram of stress σ_{11} – α = 75°– D_w = 50mm – p_w = 7.2 MPa.

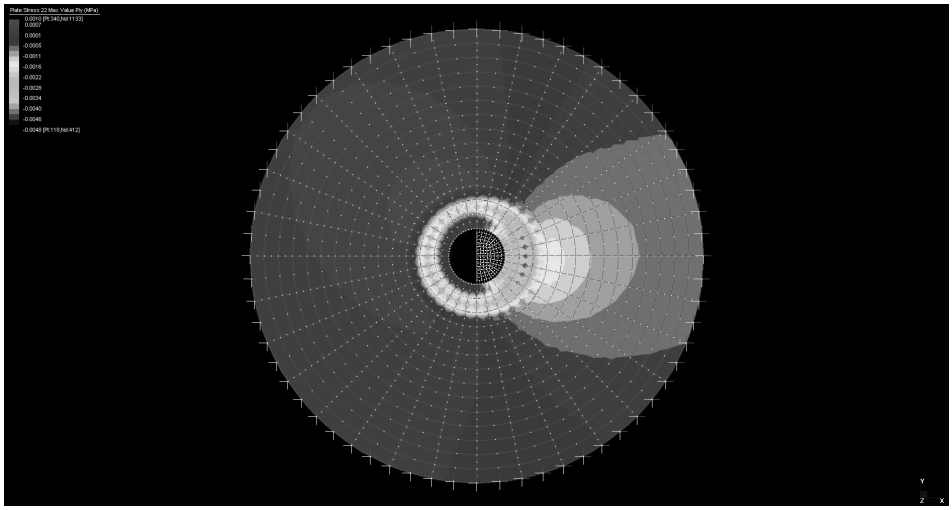

Figure 5.64. Diagram of stress σ_{22} – α = 75°– D_w = 50mm – p_w = 7.2 MPa.

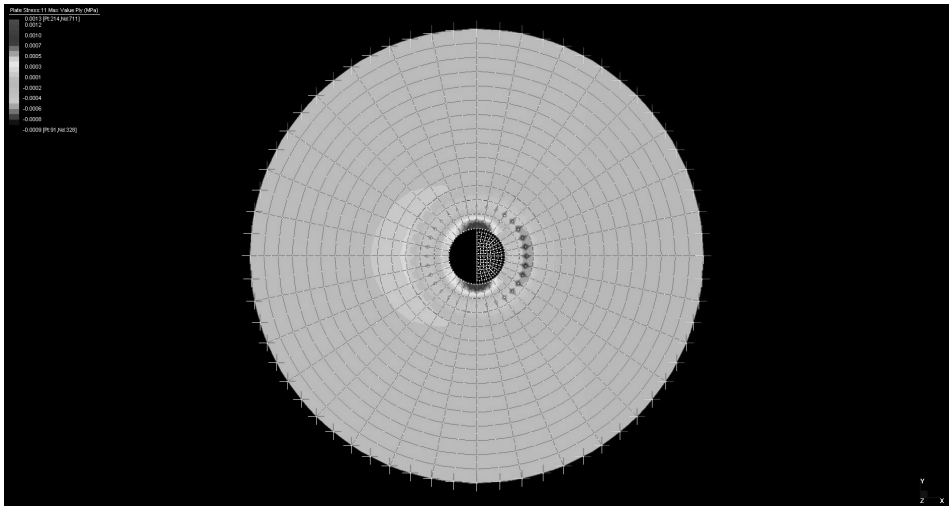

Figure 5.65. Diagram of stress σ_{11} – α = 90°– D_w = 50mm – p_w = 7.2 MPa.

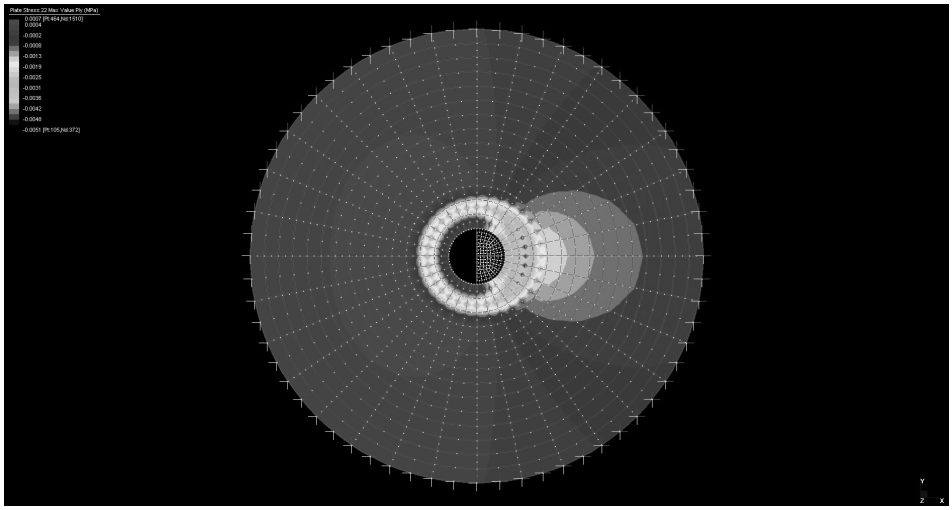

Figure 5.66. Diagram of stress σ_{22} – α = 90°– D_w = 50mm – p_w = 7.2 MPa.

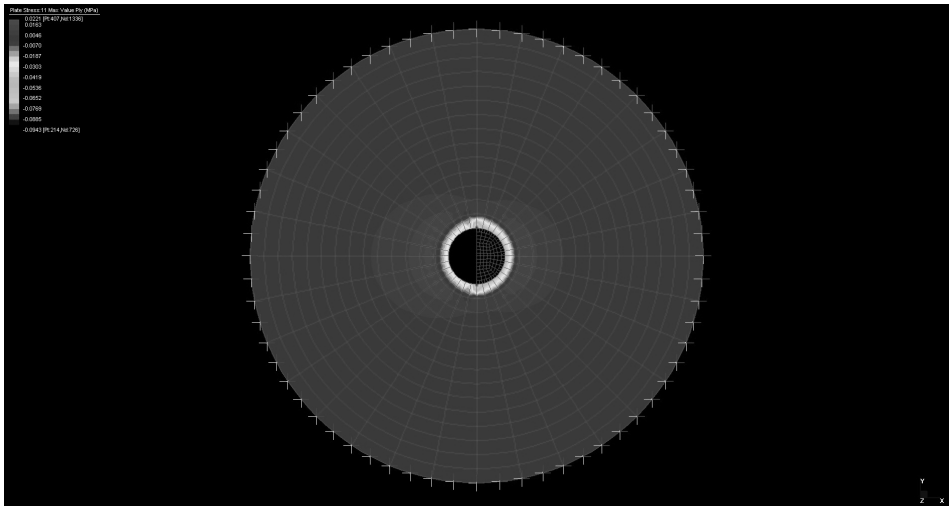

Figure 5.67. Diagram of stress σ_{11} – α = 0°– D_w = 30mm – p_w = 216 MPa.

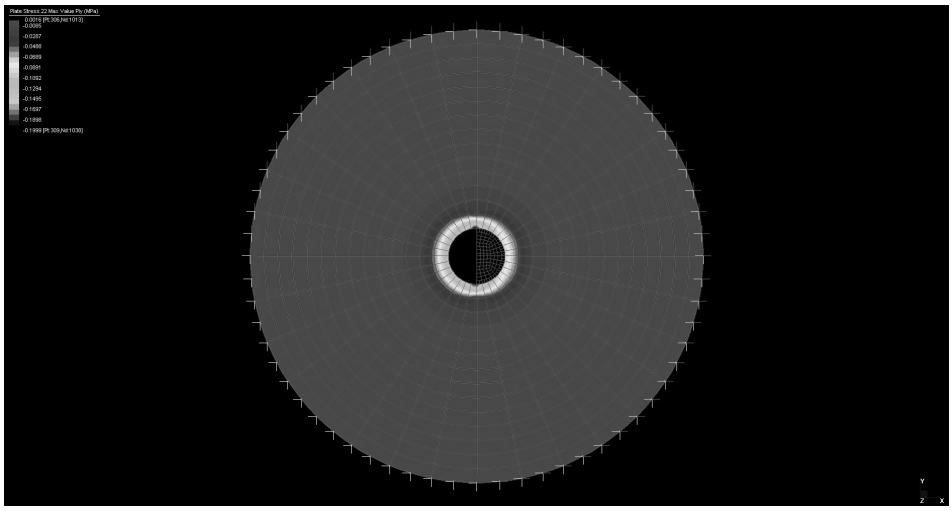

Figure 5.68. Diagram of stress σ_{22} – α = 0°– D_w = 30mm – p_w = 216 MPa.

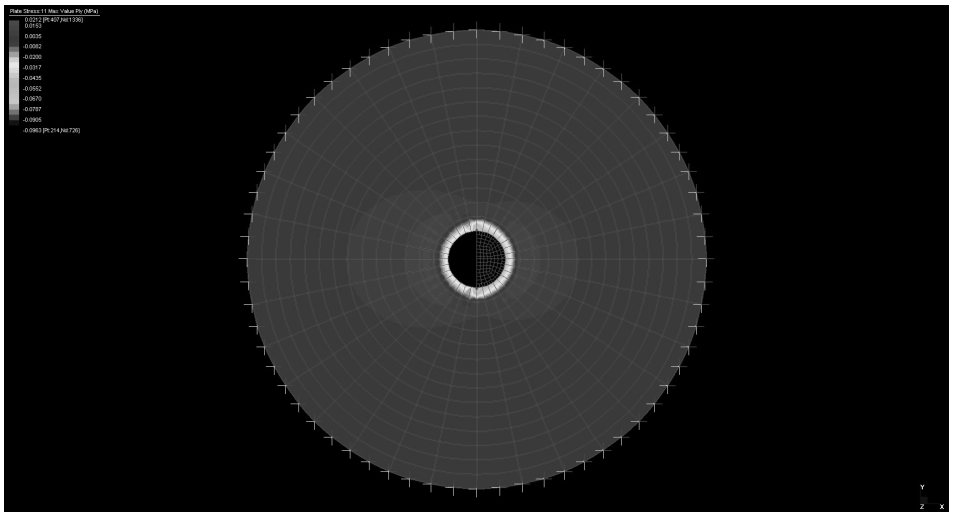

Figure 5.69. Diagram of stress σ_{11} – α = 5°– D_w = 30mm – p_w = 216 MPa.

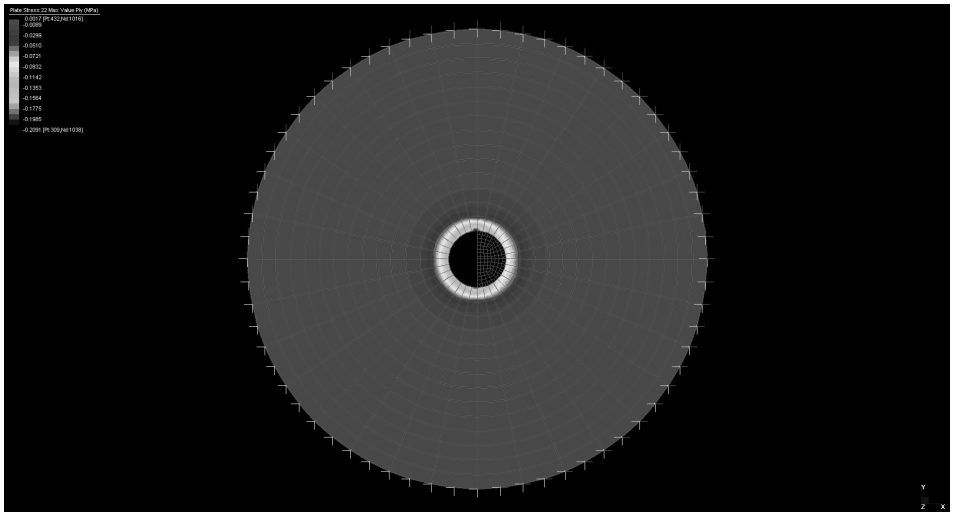

Figure 5.70. Diagram of stress σ_{22} – α = 5°– D_w = 30mm – p_w = 216 MPa.

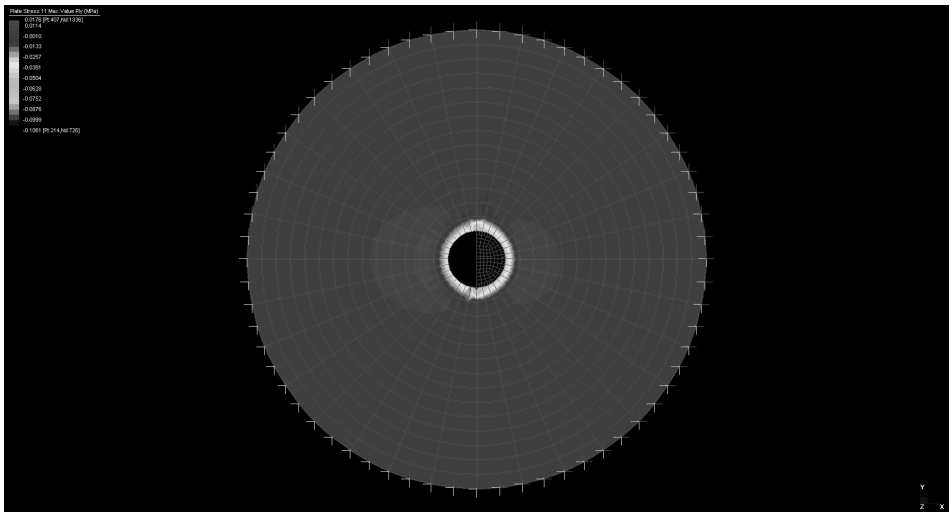

Figure 5.71. Diagram of stress σ_{11} – α = 15°– D_w = 30mm – p_w = 216 MPa.

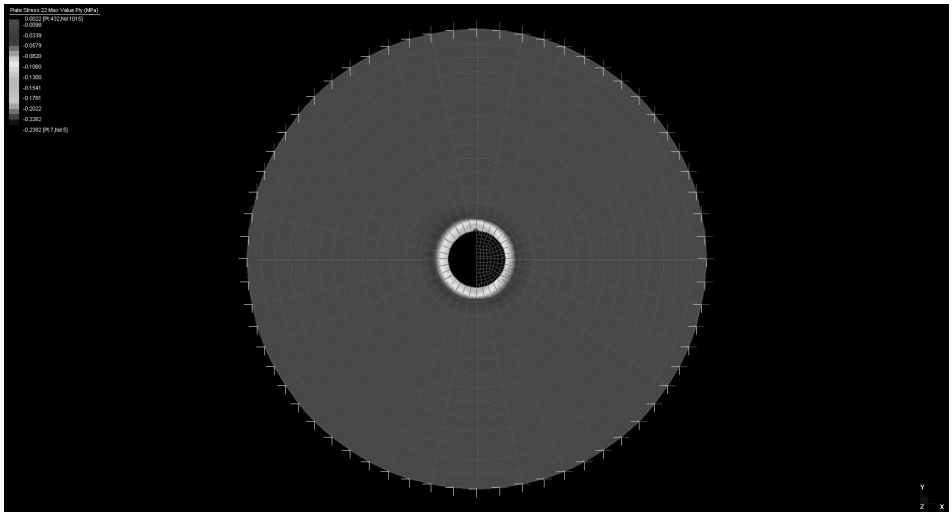

Figure 5.72. Diagram of stress σ_{22} – α = 15°– D_w = 30mm – p_w = 216 MPa.

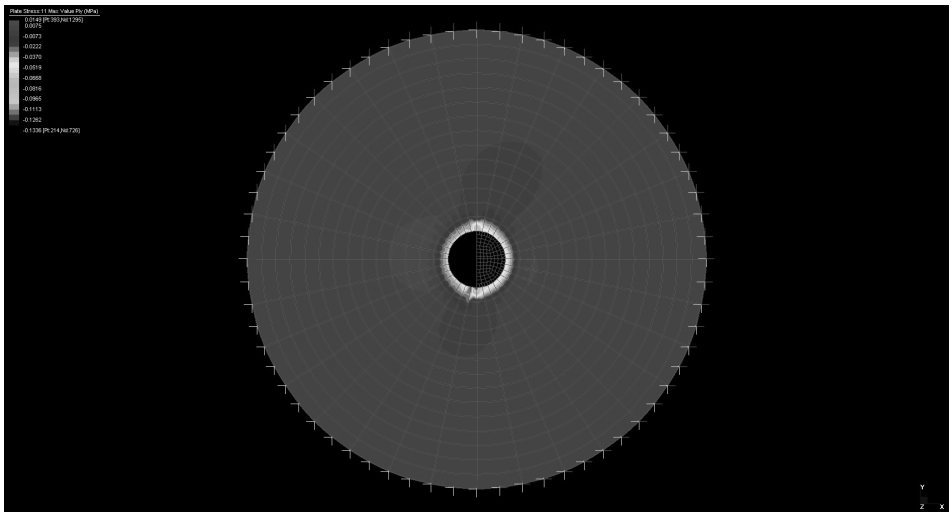

Figure 5.73. Diagram of stress σ_{11} – α = 30°– D_w = 30mm – p_w = 216 MPa.

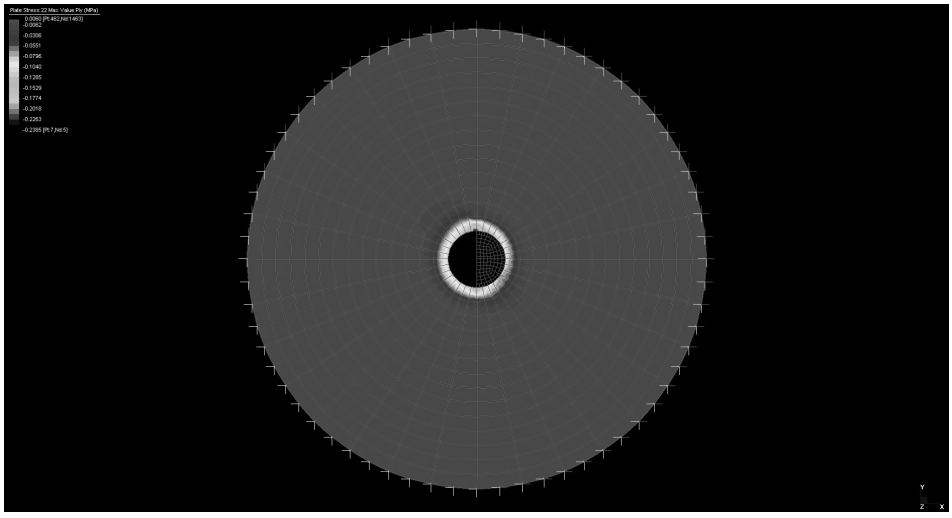

Figure 5.74. Diagram of stress σ_{22} – α = 30°– D_w = 30mm – p_w = 216 MPa.

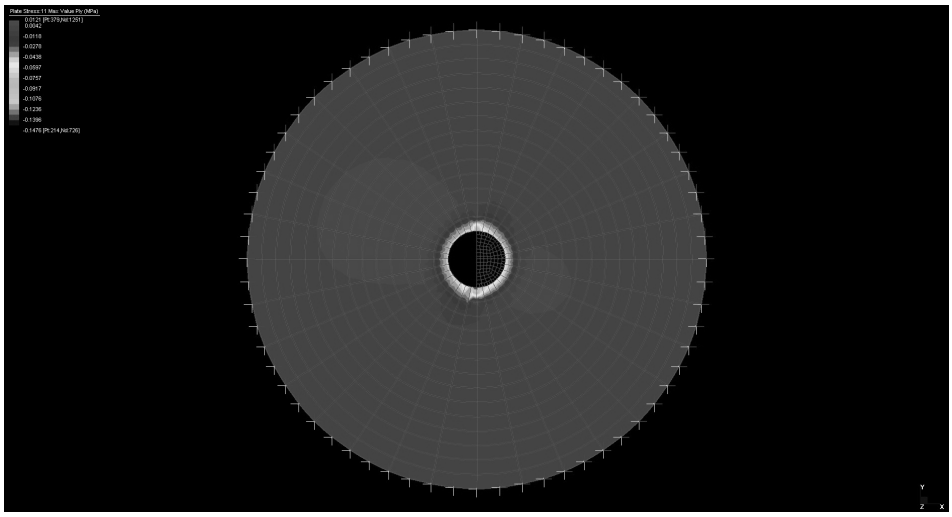

Figure 5.75. Diagram of stress σ_{11} – α = 45°– D_w = 30mm – p_w = 216 MPa.

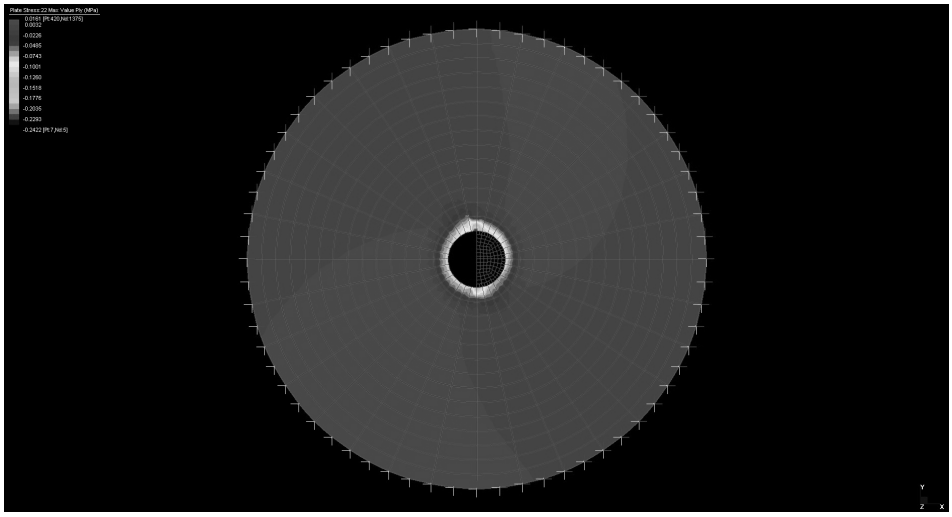

Figure 5.76. Diagram of stress σ_{22} – α = 45°– D_w = 30mm – p_w = 216 MPa.

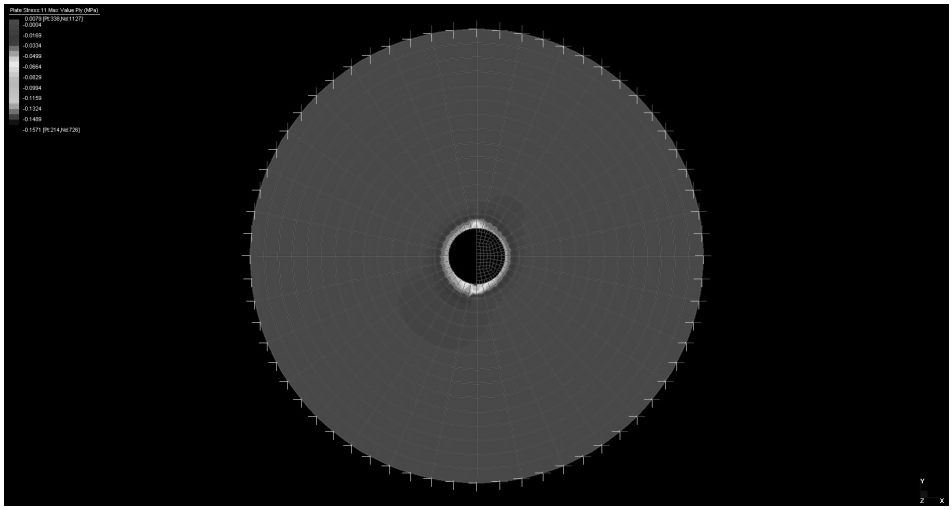

Figure 5.77. Diagram of stress σ_{11} – α = 60°– D_w = 30mm – p_w = 216 MPa.

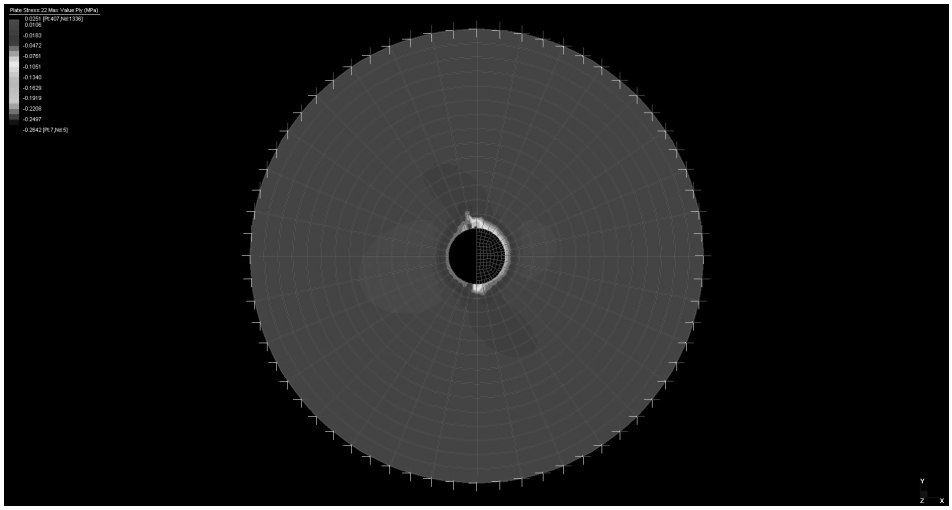

Figure 5.78. Diagram of stress σ_{22} – α = 60°– D_w = 30mm – p_w = 216 MPa.

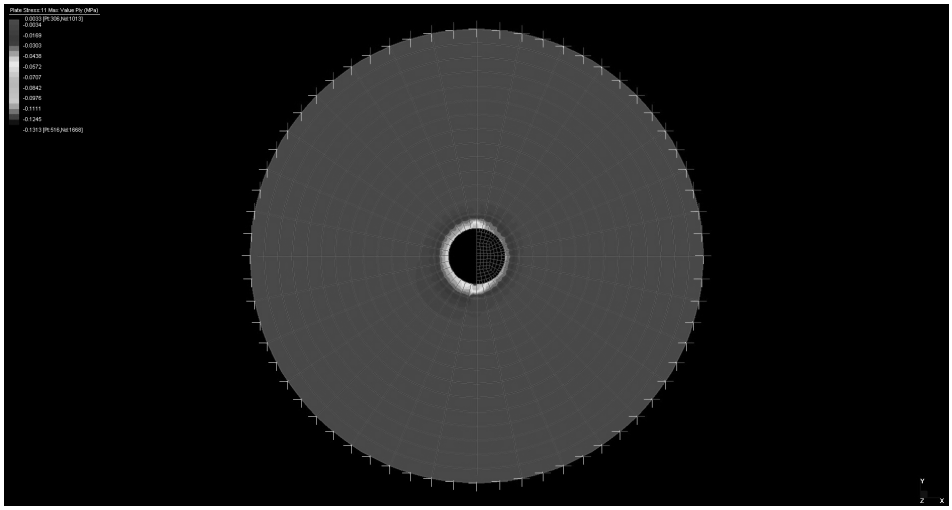

Figure 5.79. Diagram of stress σ_{11} – α = 75°– D_w = 30mm – p_w = 216 MPa.

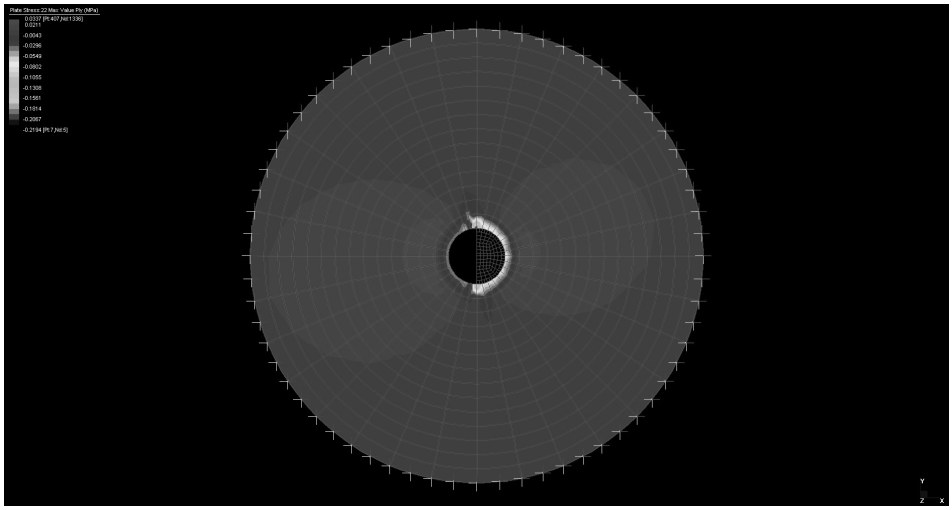

Figure 5.80. Diagram of stress σ_{22} – α = 75°– D_w = 30mm – p_w = 216 MPa.

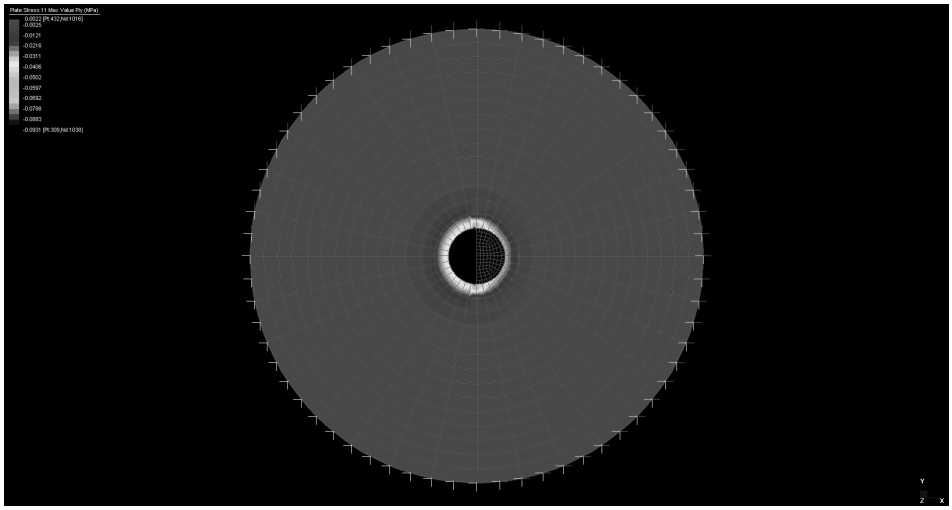

Figure 5.81. Diagram of stress σ_{11} – α = 90°– D_w = 30mm – p_w = 216 MPa.

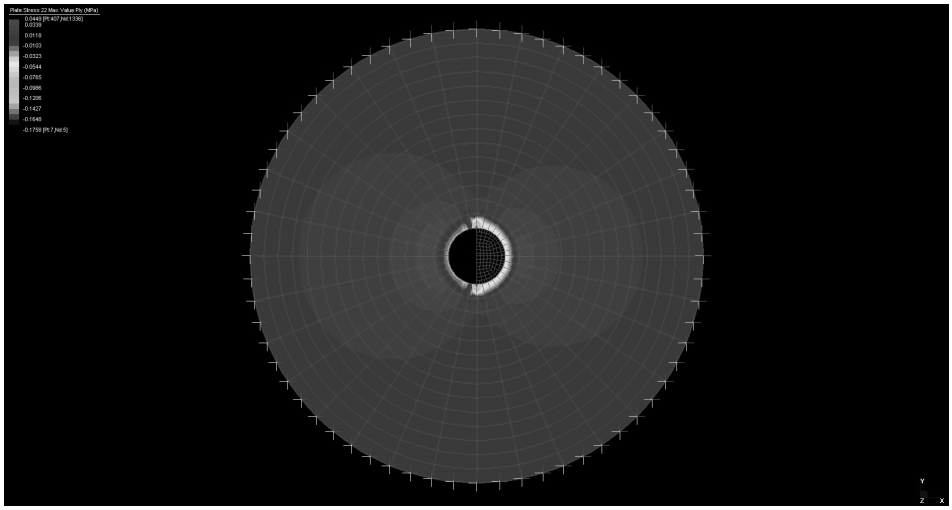

Figure 5.82. Diagram of stress σ_{22} – α = 90°– D_w = 30mm – p_w = 216 MPa.

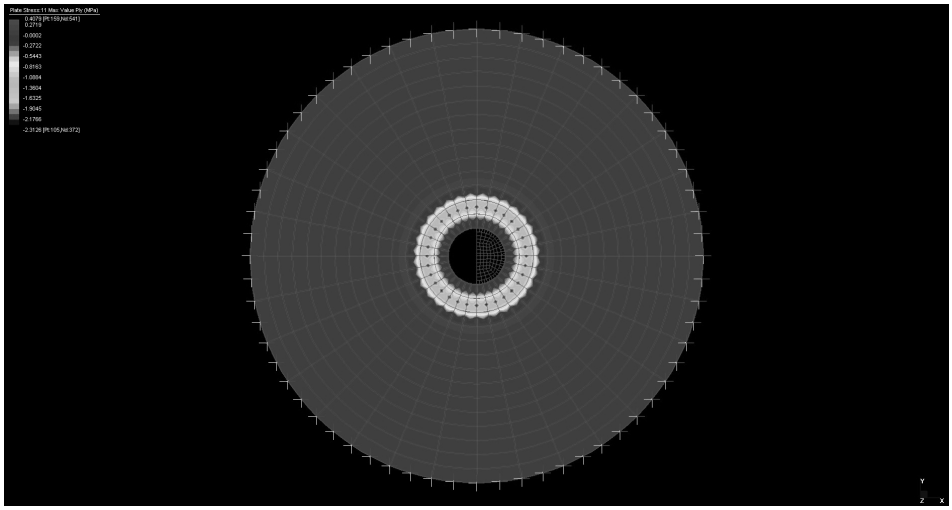

Figure 5.83. Diagram of stress σ_{11} – α = 0°– D_w = 40mm – p_w = 216 MPa.

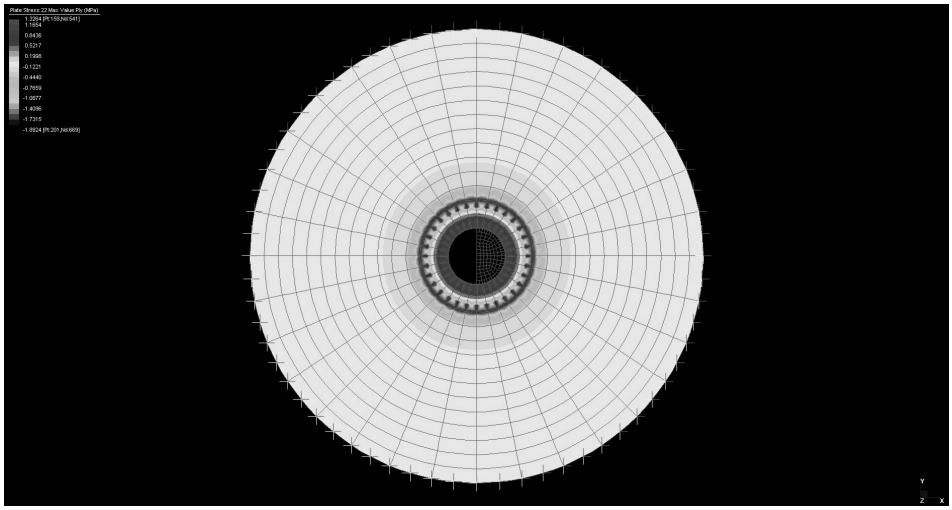

Figure 5.84. Diagram of stress σ_{22} – α = 0°– D_w = 40mm – p_w = 216 MPa.

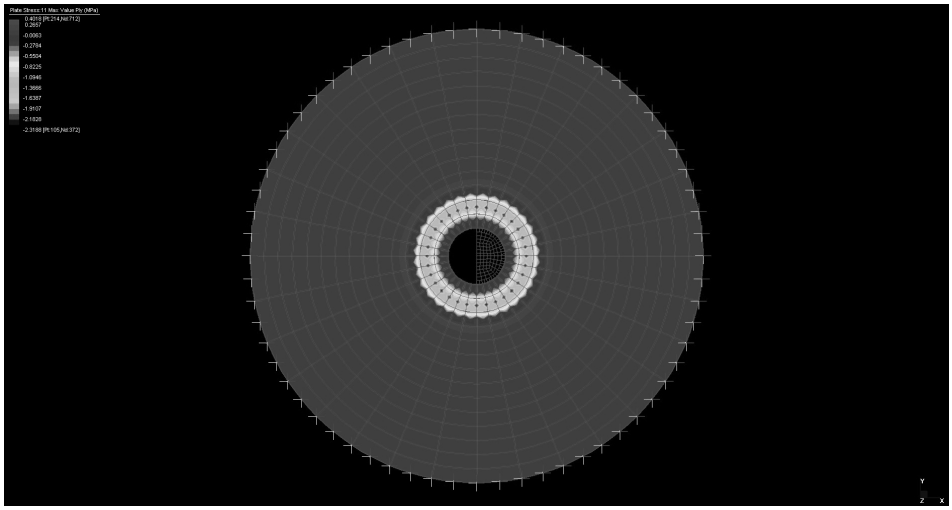

Figure 5.85. Diagram of stress σ_{11} – α = 5°– D_w = 40mm – p_w = 216 MPa.

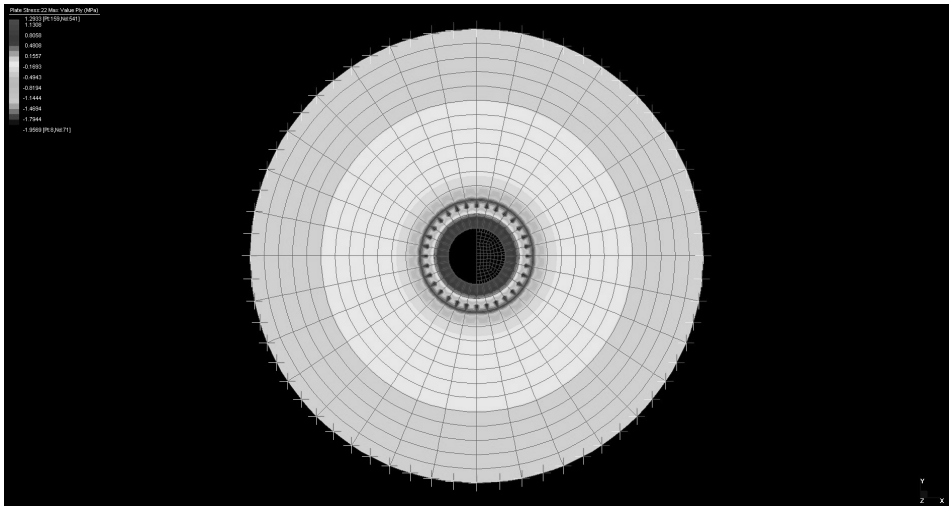

Figure 5.86. Diagram of stress σ_{22} – α = 5°– D_w = 40mm – p_w = 216 MPa.

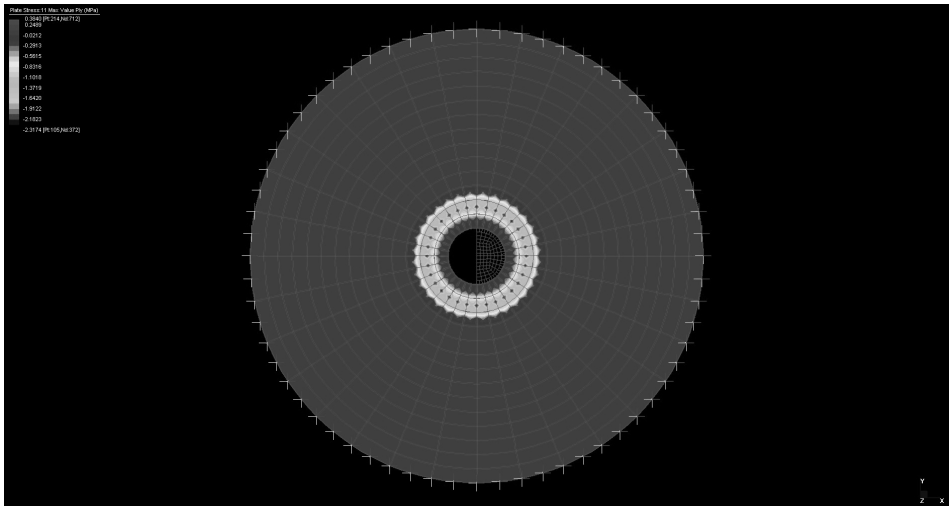

Figure 5.87. Diagram of stress σ_{11} – α = 15°– D_w = 40mm – p_w = 216 MPa.

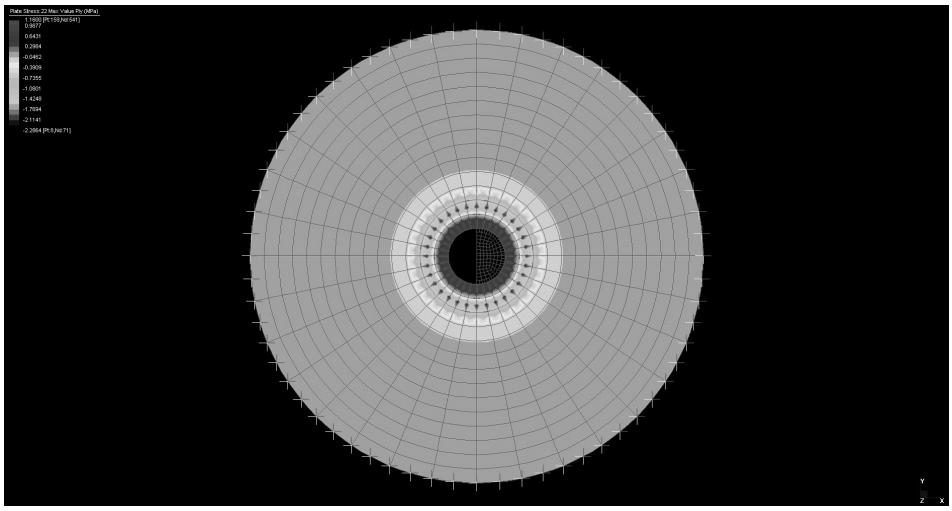

Figure 5.88. Diagram of stress σ_{22} – α = 15°– D_w = 40mm – p_w = 216 MPa.

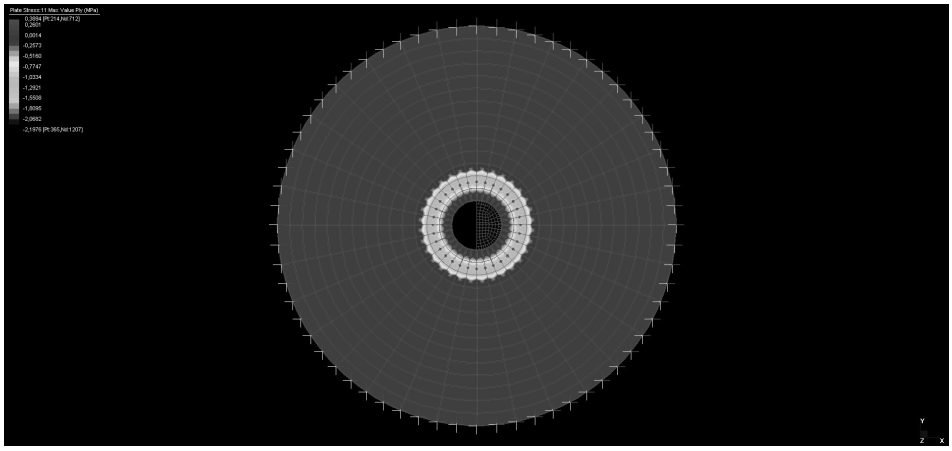

Figure 5.89. Diagram of stress σ_{11} – α = 30°– D_w = 40mm – p_w = 216 MPa.

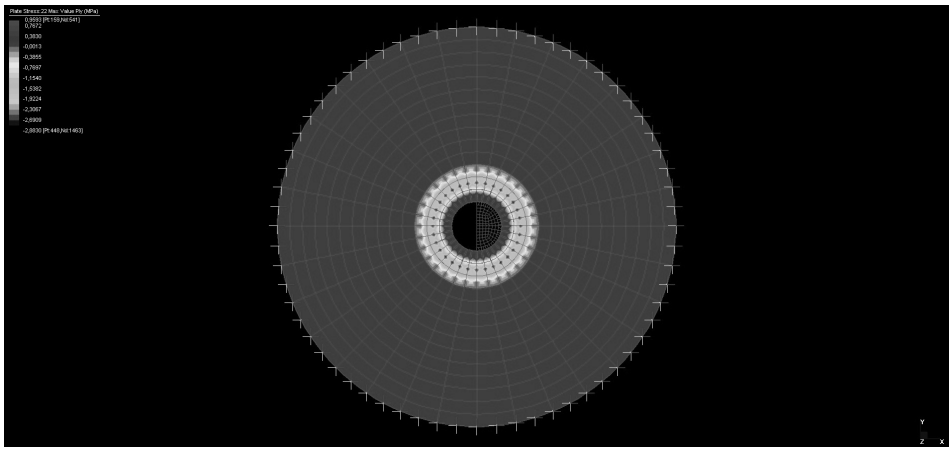

Figure 5.90. Diagram of stress σ_{22} – α = 30°– D_w = 40mm – p_w = 216 MPa.

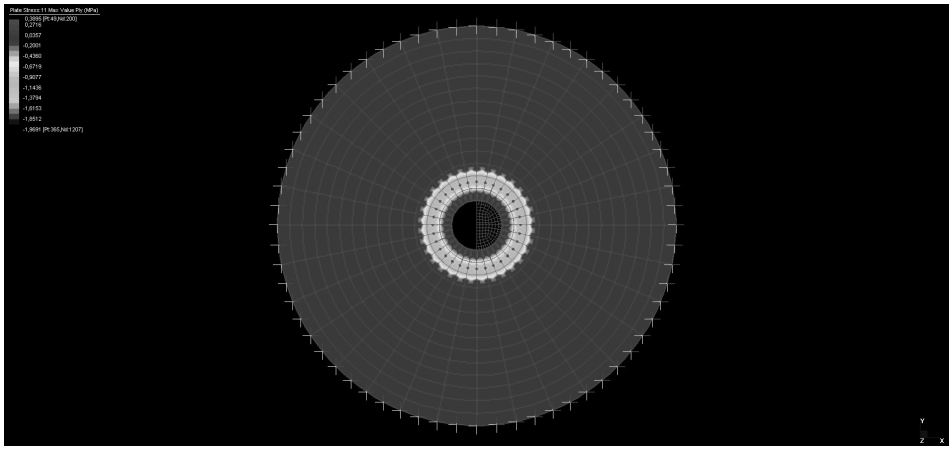

Figure 5.91. Diagram of stress σ_{11} – α = 45°– D_w = 40mm – p_w = 216 MPa.

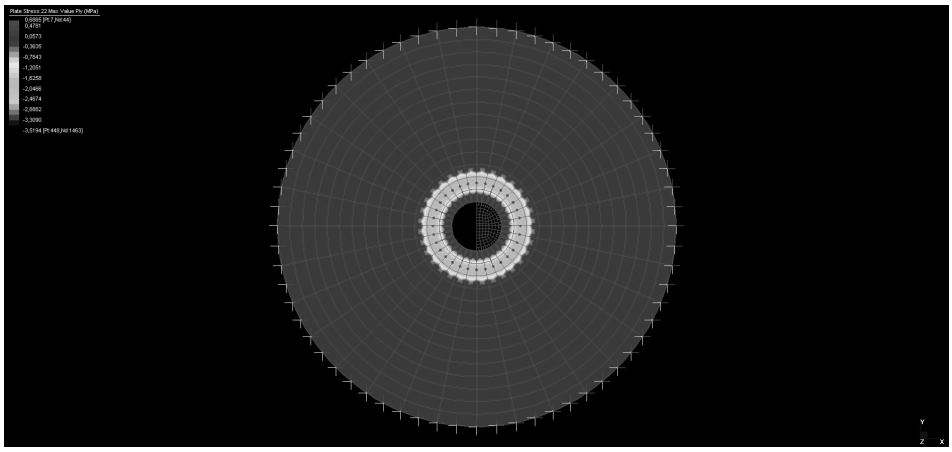

Figure 5.92. Diagram of stress σ_{22} – α = 45°– D_w = 40mm – p_w = 216 MPa.

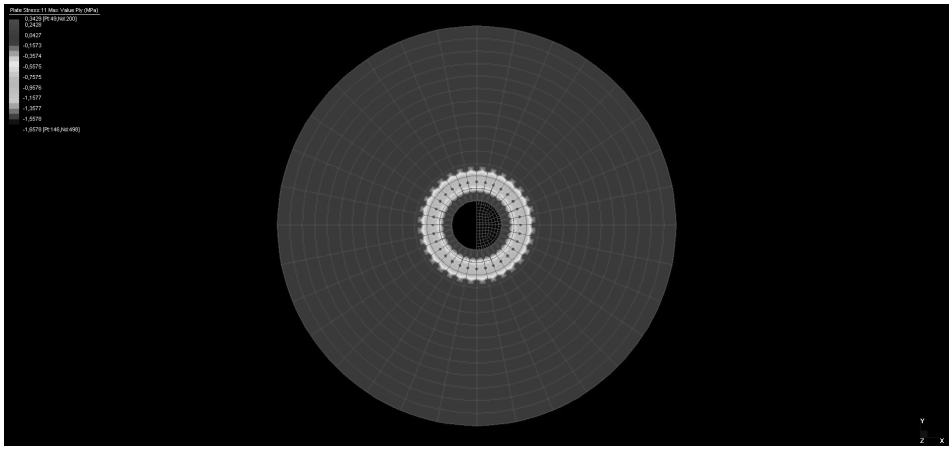

Figure 5.93. Diagram of stress σ_{11} – α = 60°– D_w = 40mm – p_w = 216 MPa.

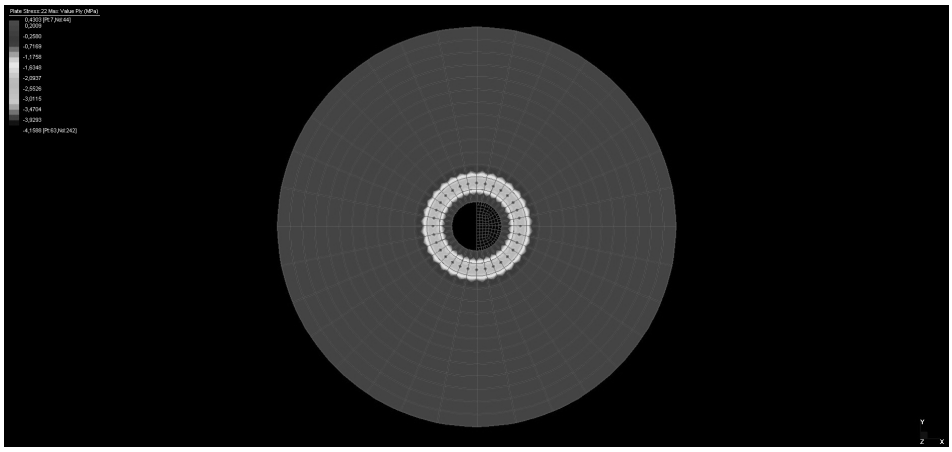

Figure 5.94. Diagram of stress σ_{22} – α = 60°– D_w = 40mm – p_w = 216 MPa.

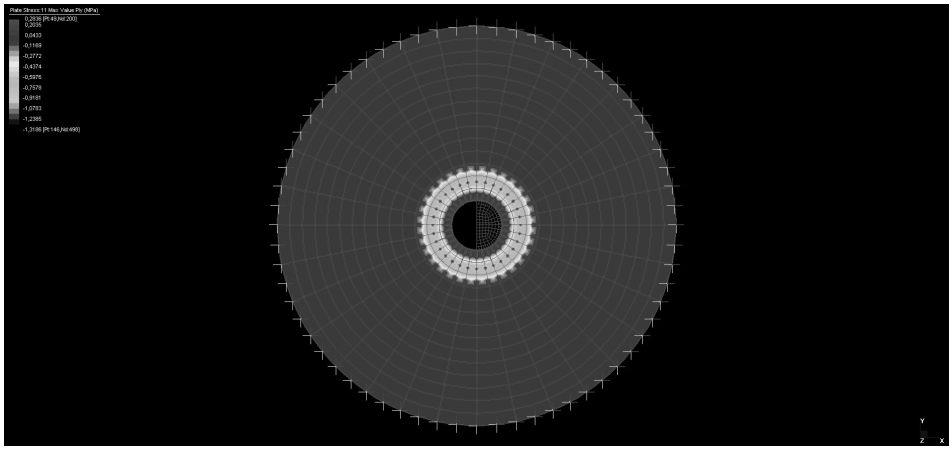

Figure 5.95. Diagram of stress σ_{11} – α = 75°– D_w = 40mm – p_w = 216 MPa.

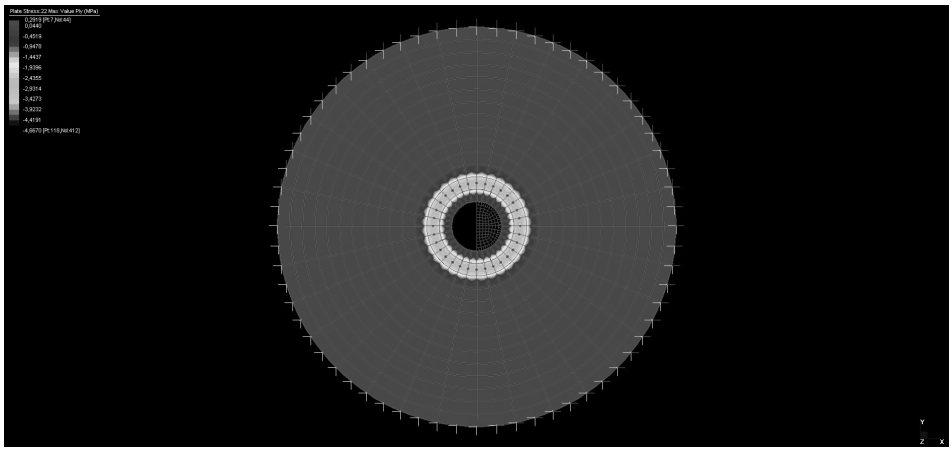

Figure 5.96. Diagram of stress σ_{22} – α = 75°– D_w = 40mm – p_w = 216 MPa.

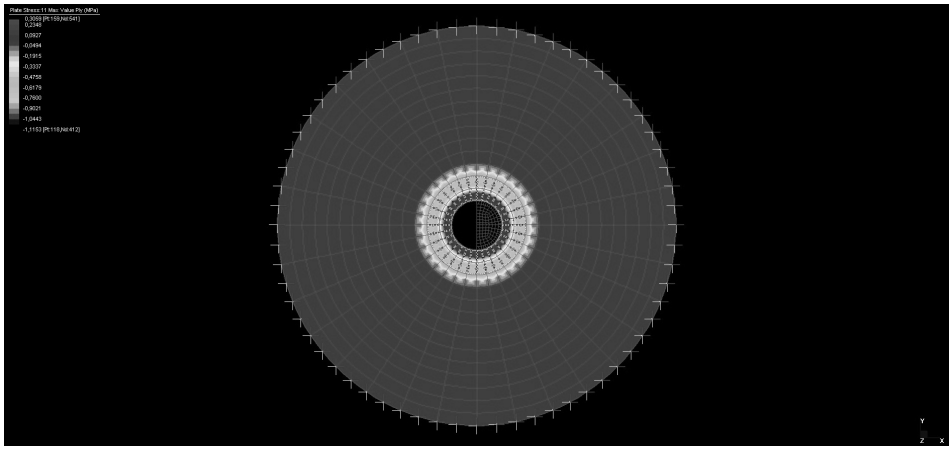

Figure 5.97. Diagram of stress σ_{11} – α = 90°– D_w = 40mm – p_w = 216 MPa.

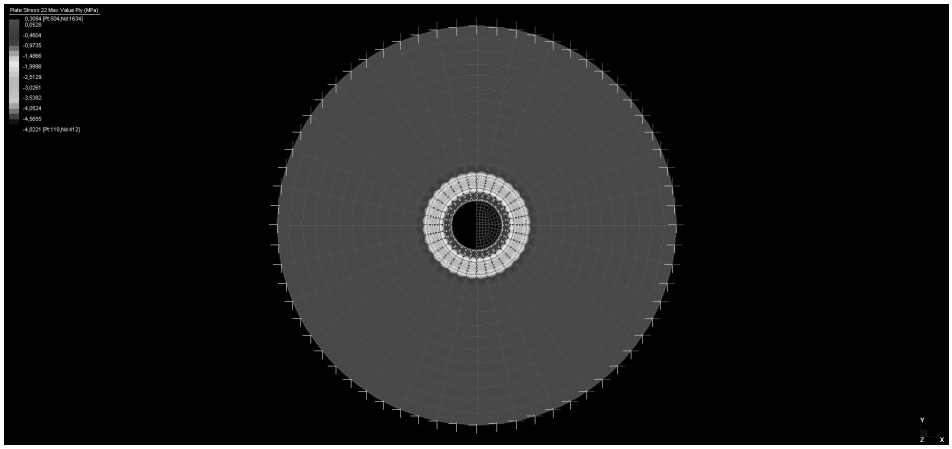

Figure 5.98. Diagram of stress σ_{22} – α = 90°– D_w = 40mm – p_w = 216 MPa.

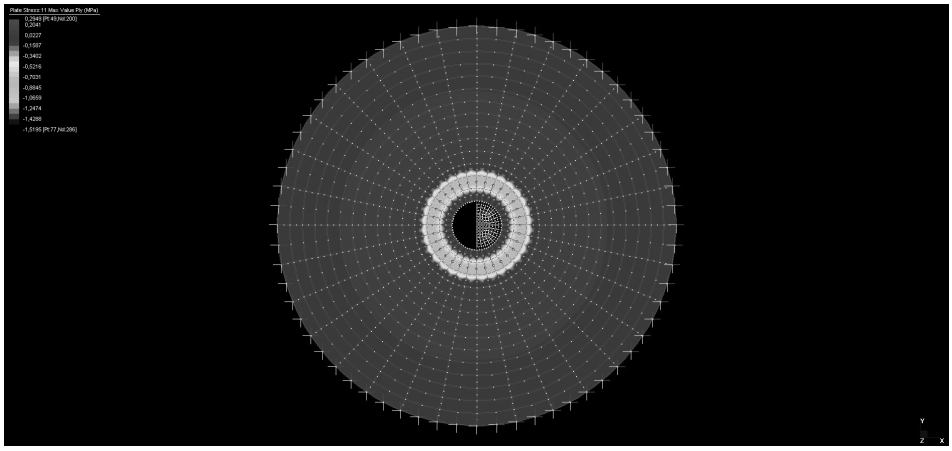

Figure 5.99. Diagram of stress σ_{11} – α = 0°– D_w = 50mm – p_w = 216 MPa.

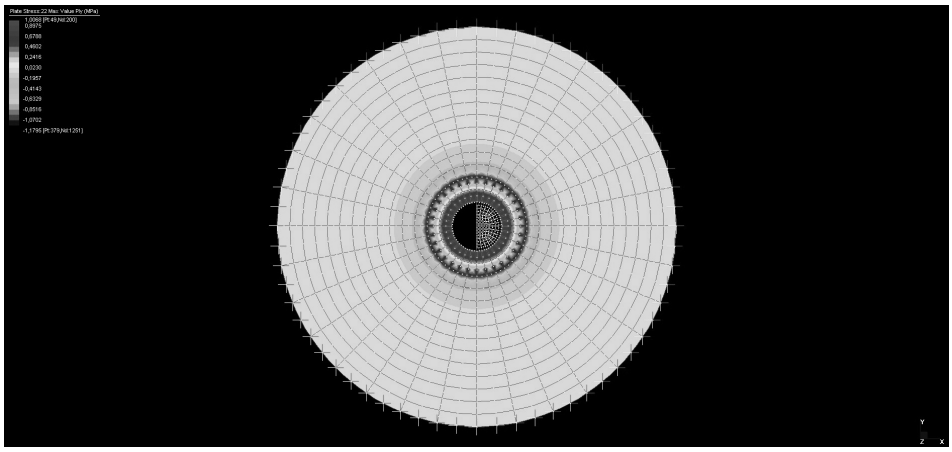

Figure 5.100. Diagram of stress σ_{22} – α = 0°– D_w = 50mm – p_w = 216 MPa.

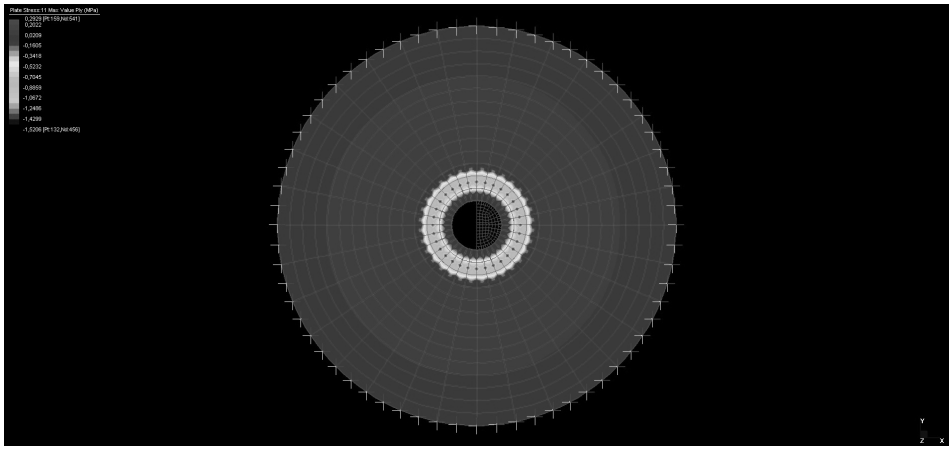

Figure 5.101. Diagram of stress σ_{11} – α = 5°– D_w = 50mm – p_w = 216 MPa.

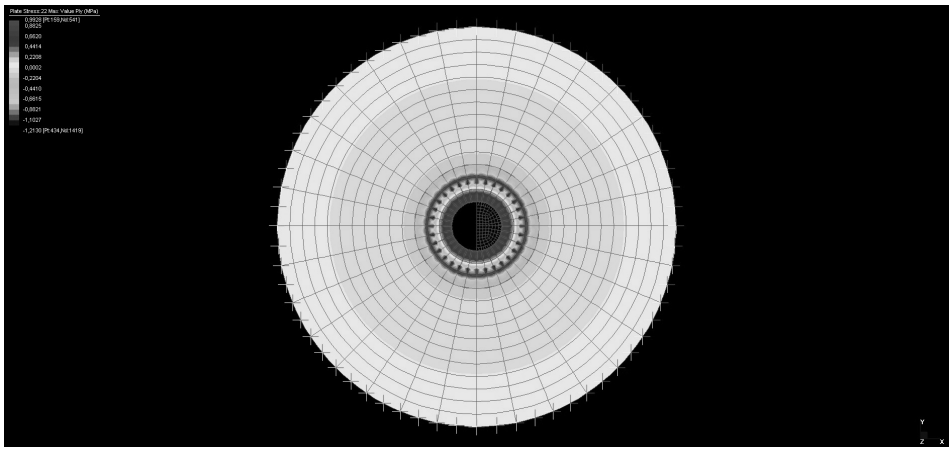

Figure 5.102. Diagram of stress σ_{22} – α = 5°– D_w = 50mm – p_w = 216 MPa.

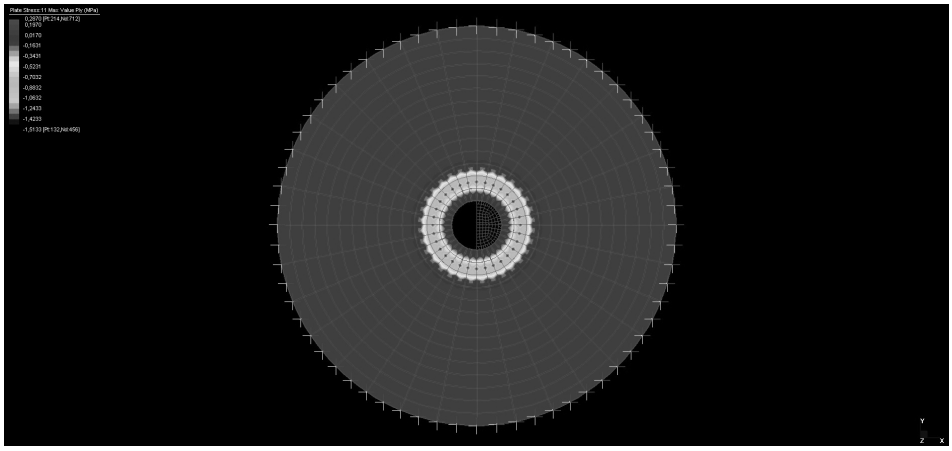

Figure 5.103. Diagram of stress σ_{11} – α = 15°– D_w = 50mm – p_w = 216 MPa.

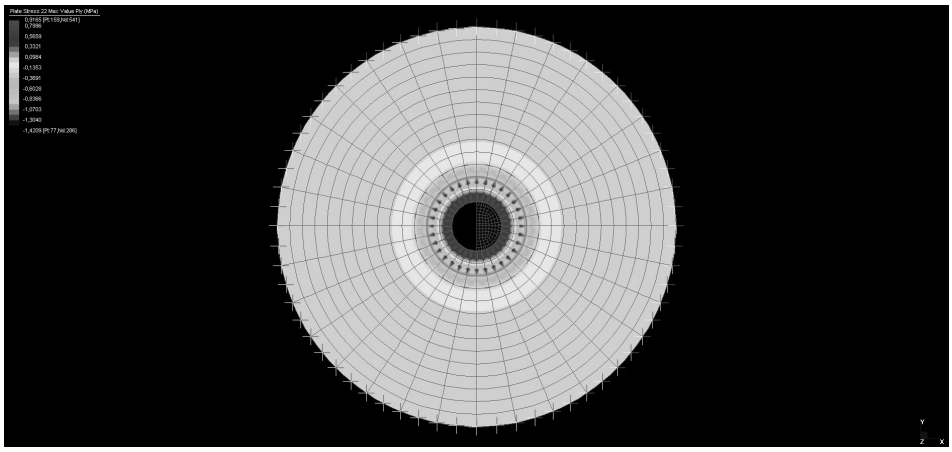

Figure 5.104. Diagram of stress σ_{22} – α = 15°– D_w = 50mm – p_w = 216 MPa.

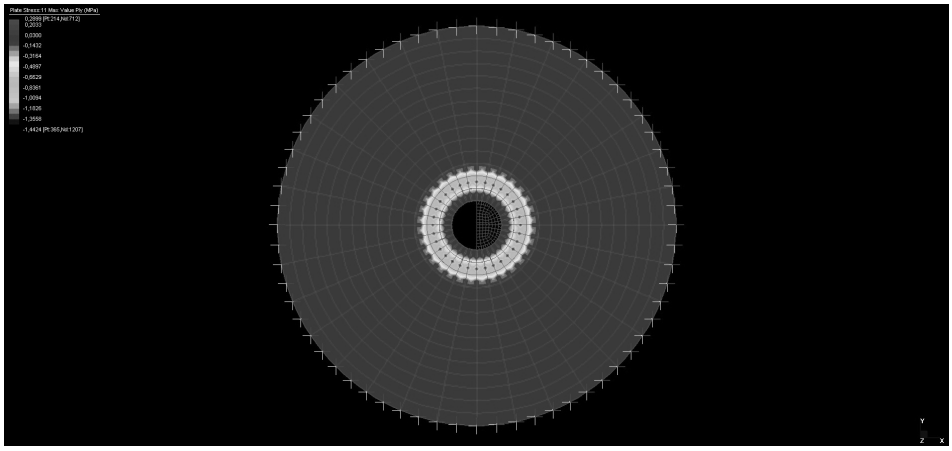

Figure 5.105. Diagram of stress σ_{11} – α = 30°– D_w = 50mm – p_w = 216 MPa.

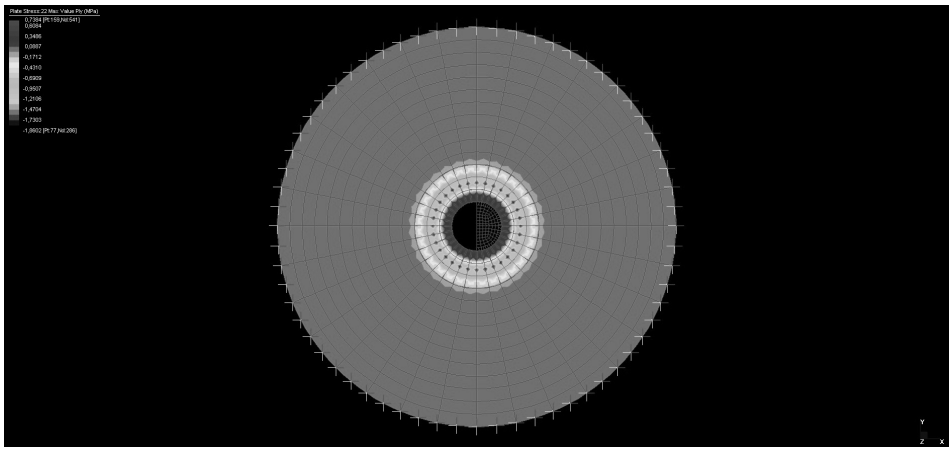

Figure 5.106. Diagram of stress σ_{22} – α = 30°– D_w = 50mm – p_w = 216 MPa.

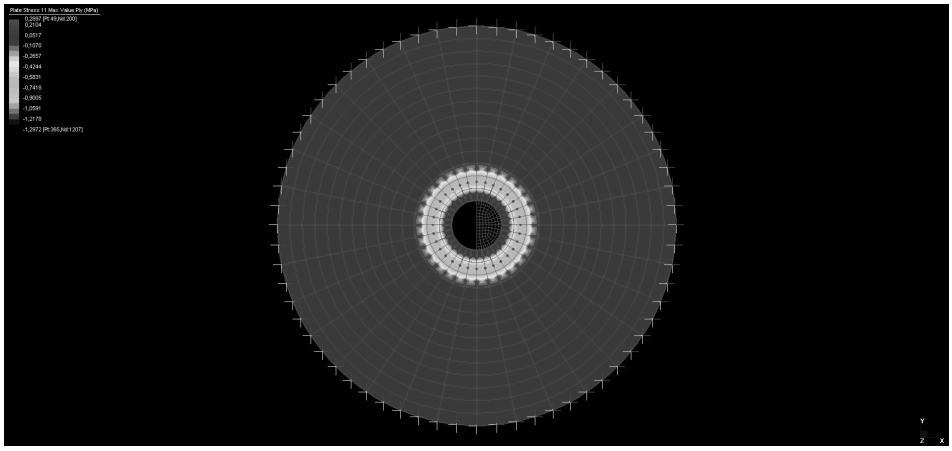

Figure 5.107. Diagram of stress σ_{11} – α = 45°– D_w = 50mm – p_w = 216 MPa.

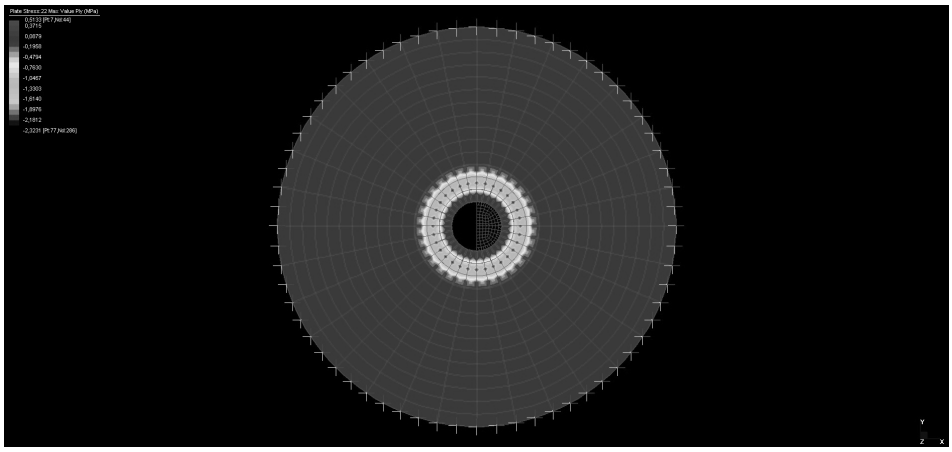

Figure 5.108. Diagram of stress σ_{22} – α = 45°– D_w = 50mm – p_w = 216 MPa.

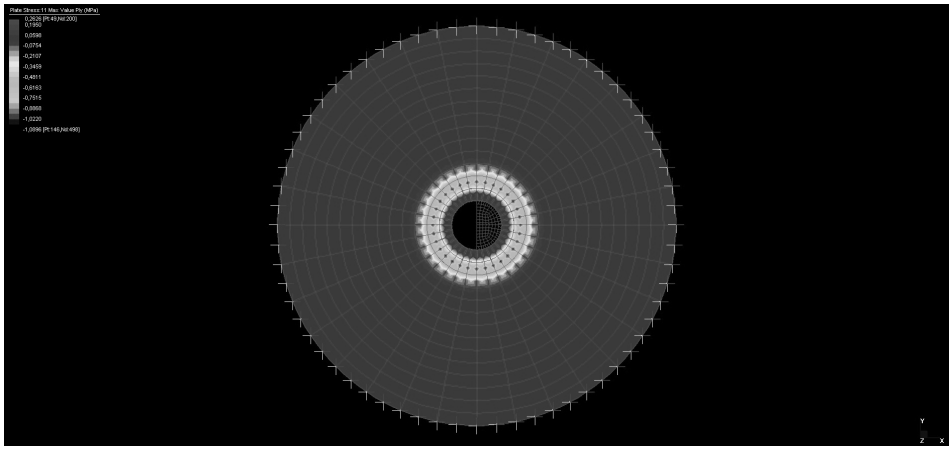

Figure 5.109. Diagram of stress σ_{11} – α = 60°– D_w = 50mm – p_w = 216 MPa.

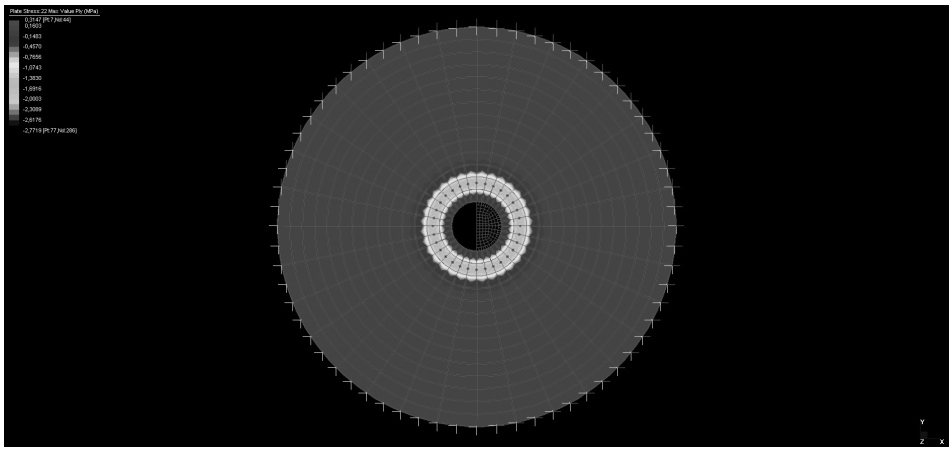

Figure 5.110. Diagram of stress σ_{22} – α = 60°– D_w = 50mm – p_w = 216 MPa.

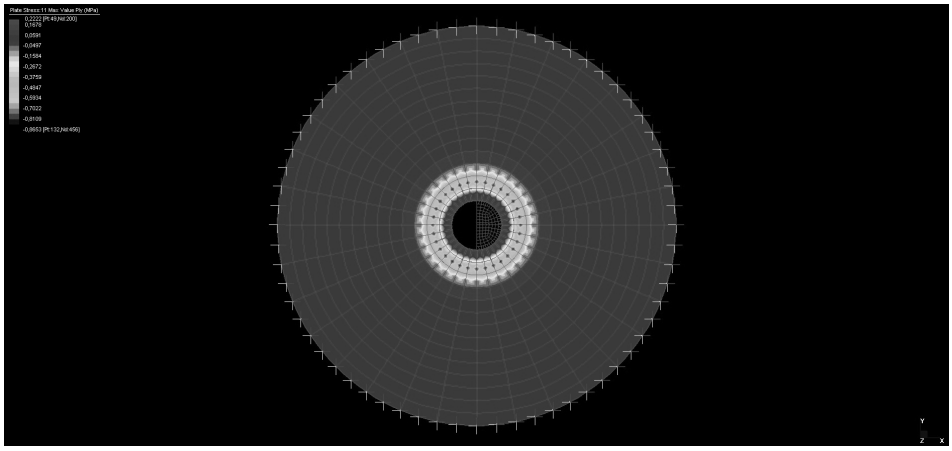

Figure 5.111. Diagram of stress σ_{11} – α = 75°– D_w = 50mm – p_w = 216 MPa.

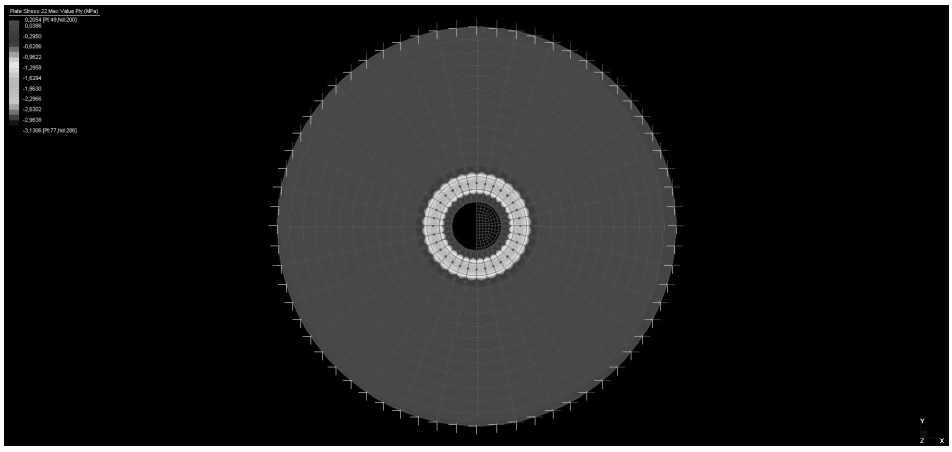

Figure 5.112. Diagram of stress σ_{22} – α = 75°– D_w = 50mm – p_w = 216 MPa.

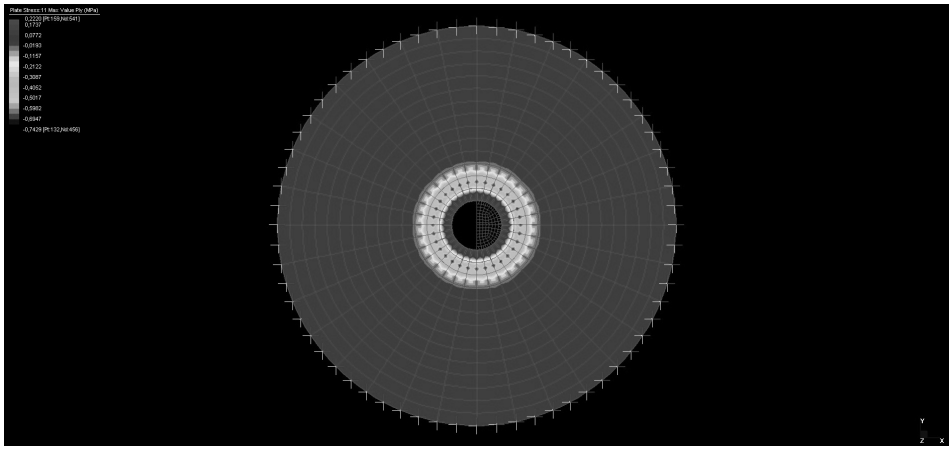

Figure 5.113. Diagram of stress σ_{11} – α = 90°– D_w = 50mm – p_w = 216 MPa.

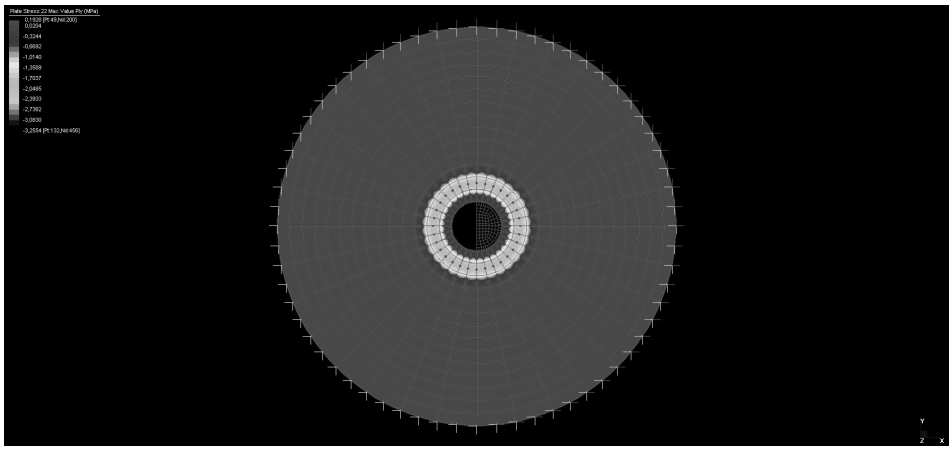

Figure 5.114. Diagram of stress σ_{22} – α = 90°– D_w = 50mm – p_w = 216 MPa.

Stress diagram σ_{11} and σ_{22}, around the hole of bolt, for sixteen values α of fiber inclination angle [14-15] are shown in **Figure 5.115** and **Figure 5.116**.

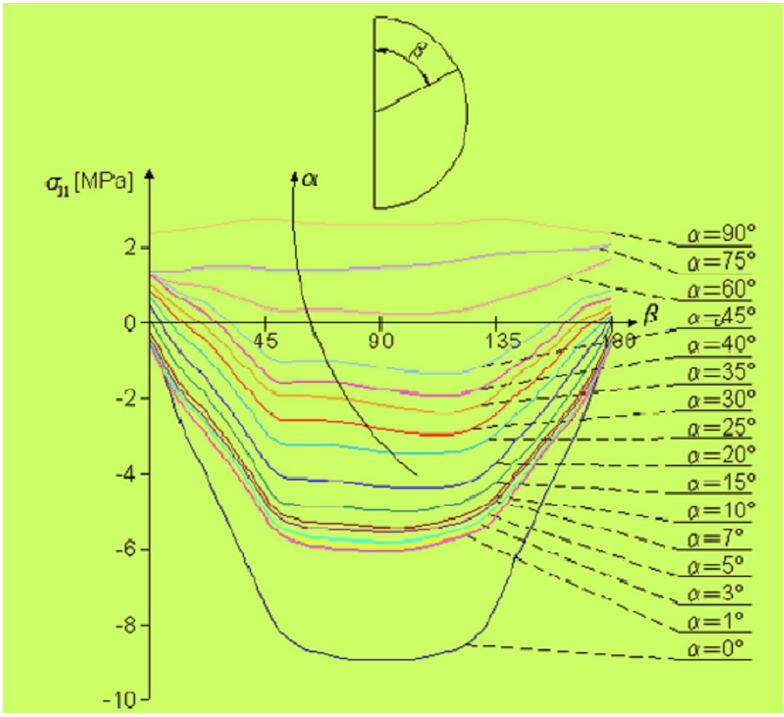

Figure 5.115. Diagram of stress σ_{11} around the hole (β).

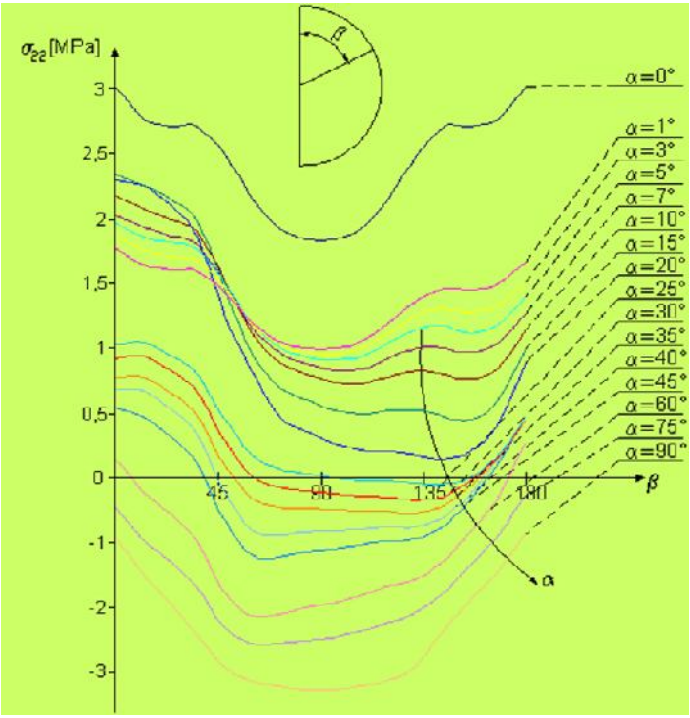

Figure 5.116. Diagram of stress σ_{22} around the hole (β).

The figures below (**Figure 5.117** and **Figure 5.118**) show that these stress distributions (σ11-fibre direction), varying fibre inclination, are almost all decreasing for each value of p_w. In particular, the effects of the presence of washers are more evident for high values of p_w than for low values. In fact, the main effect is that the bearing stresses σ_{11} show, for each value of α, a minimum value for $D_w=2d_b=40$mm (optimal washer diameter).

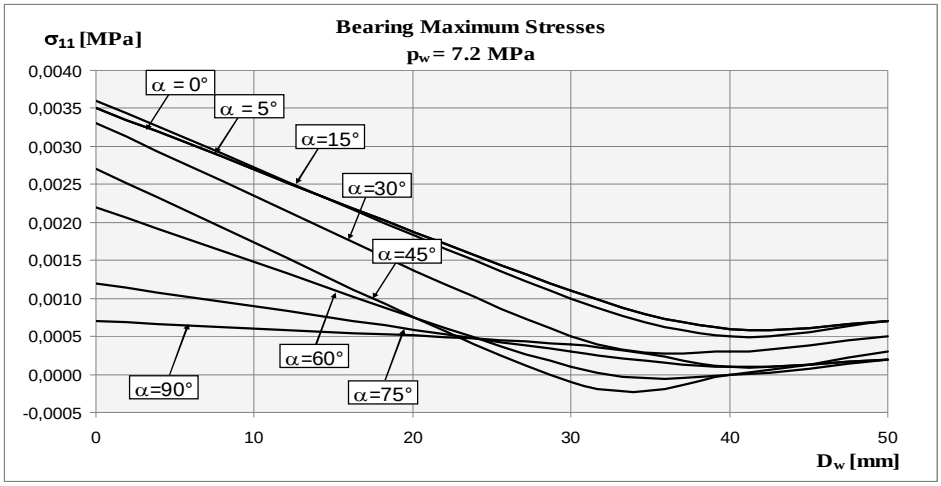

Figure 5.117. Bearing maximum stresses - p_w = 7.2 MPa.

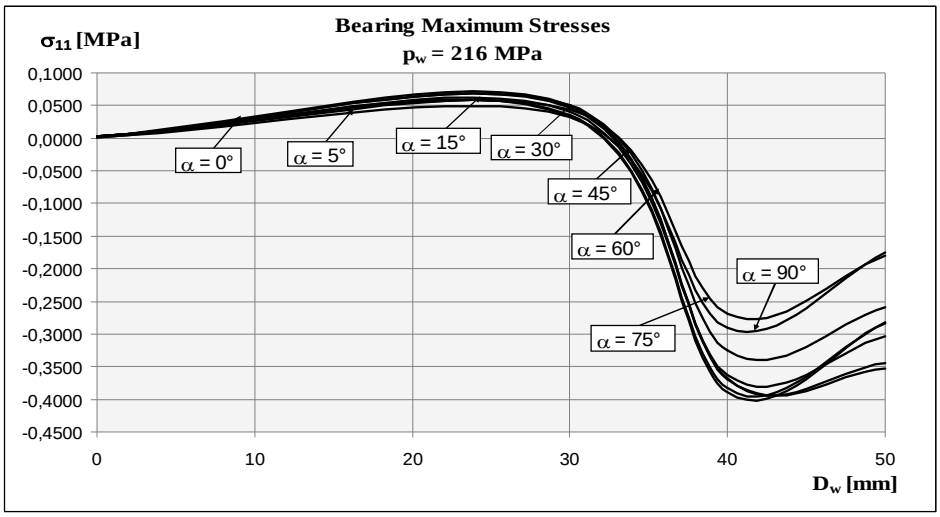

Figure 5.118. Bearing maximum stresses - p_w = 216 MPa.

The presence of the washers allows that bearing stresses decrease but, at a distance equal to $d_b/2$ from the hole edge, for the same value of optimal washer diameter, the stresses acting in the fibre direction increase as shown in **Figure 5.119** and in **Figure 5.120**.

The presence of washers determines, for low values of p_w, a ***shift of the peak stress***, comparing bearing maximum stress diagram with maximum stress [21-27].

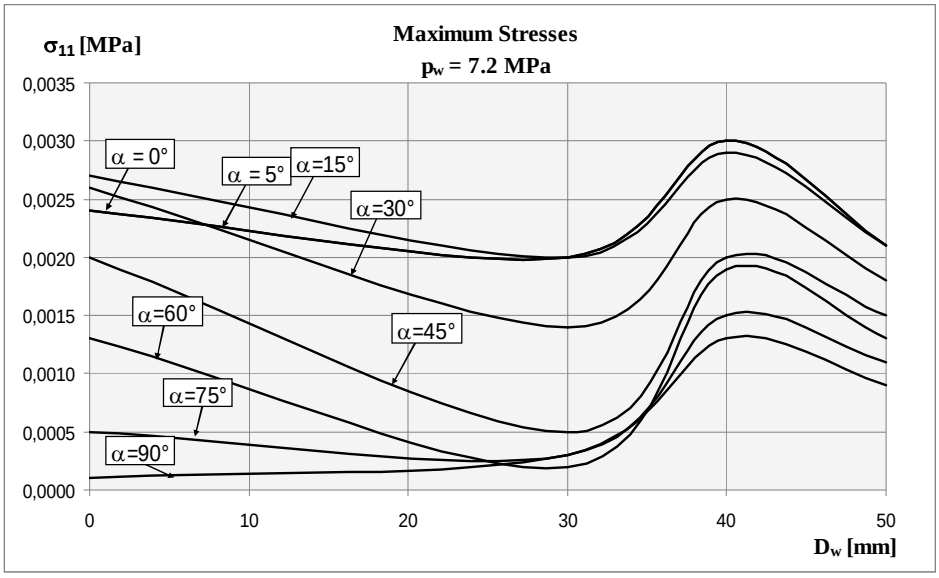

Figure 5.119. Maximum stresses - p_w = 7.2 MPa.

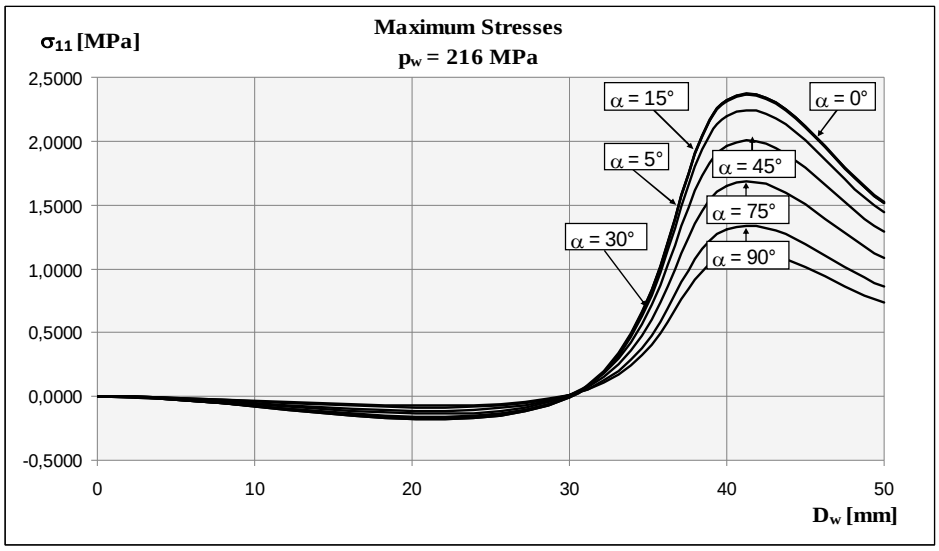

Figure 5.120. Maximum stresses - p_w = 216 MPa.

This ***shift*** is almost equal to $d_b/2$ from the hole edge for each value of α. The same shift occurs for high values of p_w.

However, in this case, there is also a significant increase of the stress peak, which is almost equal to five times higher than the same one near the hole edge.

The washers also influence the failure modes of bolted joints. In fact, the most probable failure mode of this type of joint is bearing failure when the presence of washers has little effect.

However, in the presence of washers, the main failure mode can be due to compression stresses σ_{yy} around the washer when its diameter is equal to $1.5d_b$ or just under the washer when its diameter is equal to $2d_b$.

For values higher of the diameter ($2.5d_b$, $3d_b$, etc.), the compression stresses decrease and the failure can be due to compression or tensile

stresses acting in a direction transverse (s_{22}) to fibre direction or due to shear stresses (t_{12}).

Looking at the stress diagram of σ_{11}, by varying the ***distance from the hole*** and considering a variable washer diameter (D_w) and pressure (p_w), you can observe the shift of the peak for some value of α as for example, 0°, 45° and 90°.

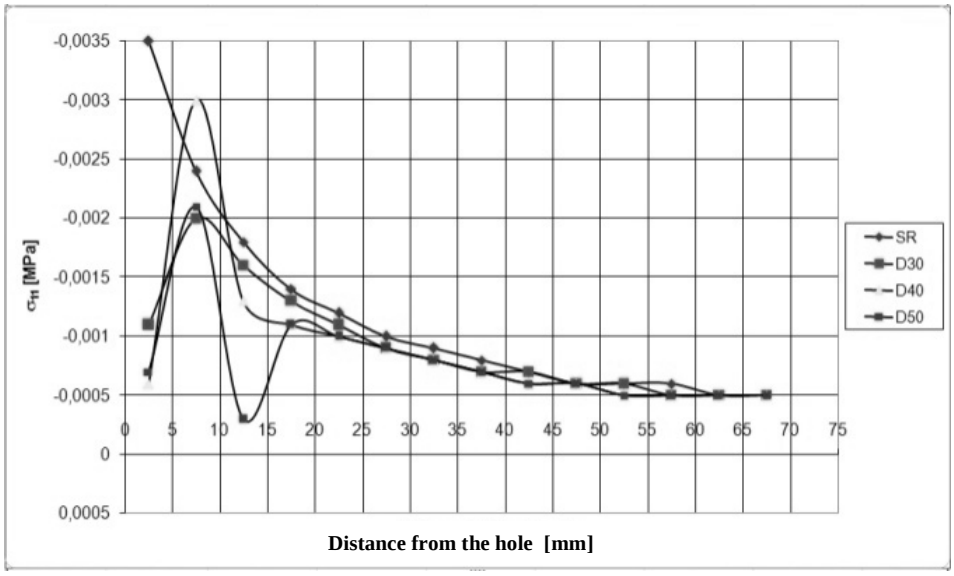

Figure 5.121. Stress σ_{11} diagram varying the distance from the hole $\alpha = 0°$- $p_w = 7.2$ MPa.

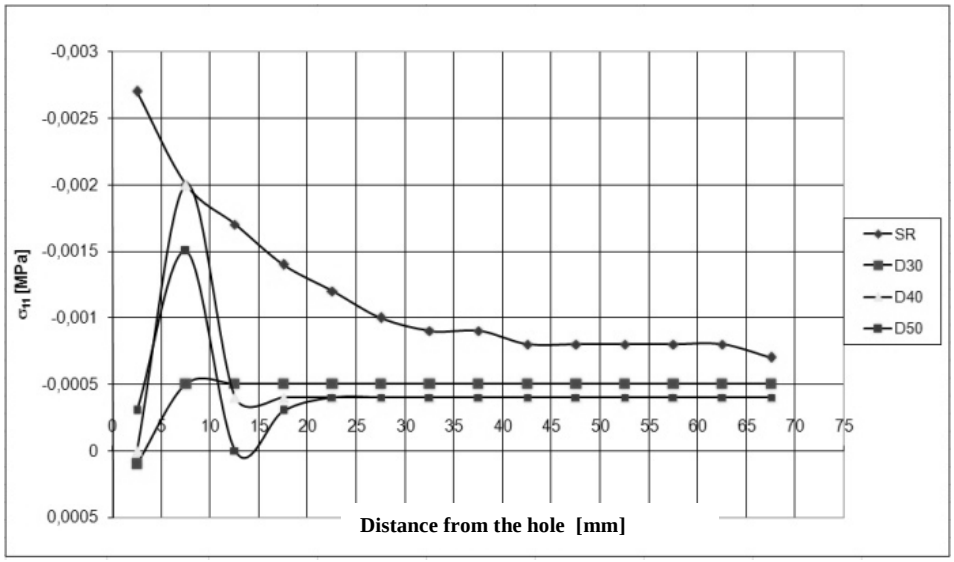

Figure 5.122. Stress σ_{11} diagram varying the distance from the hole $\alpha = 45°$- $p_w = 7.2$ MPa.

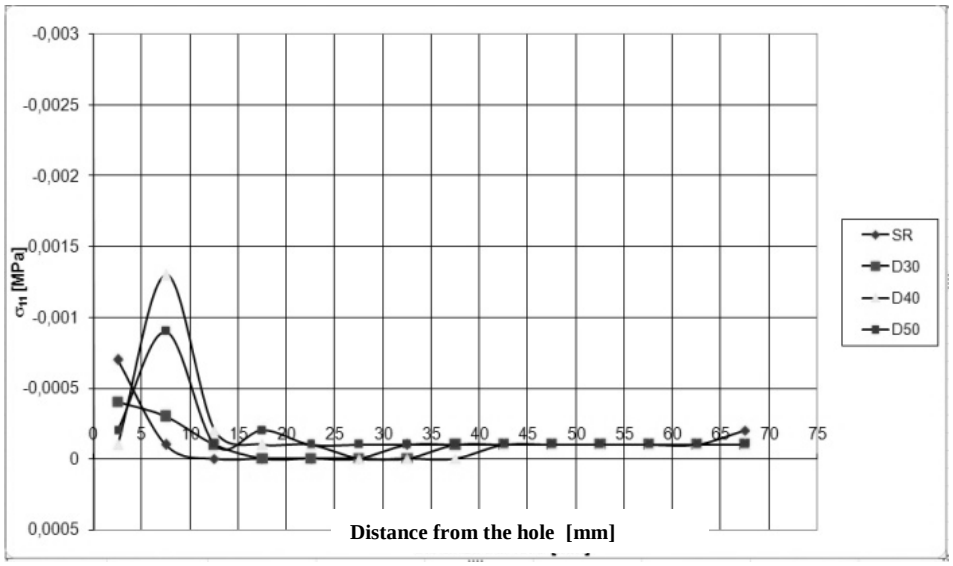

Figure 5.123. Stress σ_{11} diagram varying the distance from the hole $\alpha = 90°$- $p_w = 7.2$ MPa.

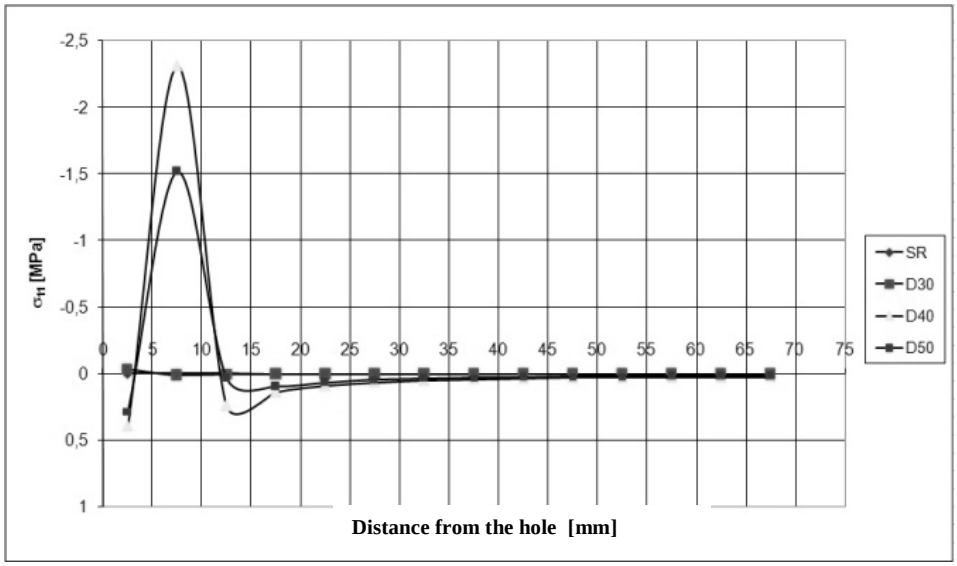

Figure 5.124. Stress σ_{11} diagram varying the distance from the hole $\alpha = 0°$- $p_w = 216$ MPa.

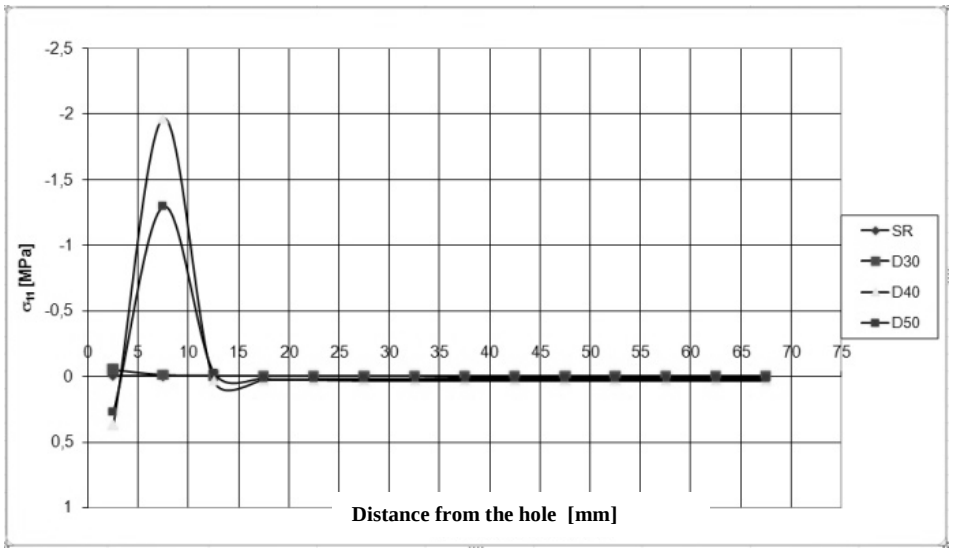

Figure 5.125. Stress σ_{11} diagram varying the distance from the hole $\alpha = 45°$- $p_w = 216$ MPa.

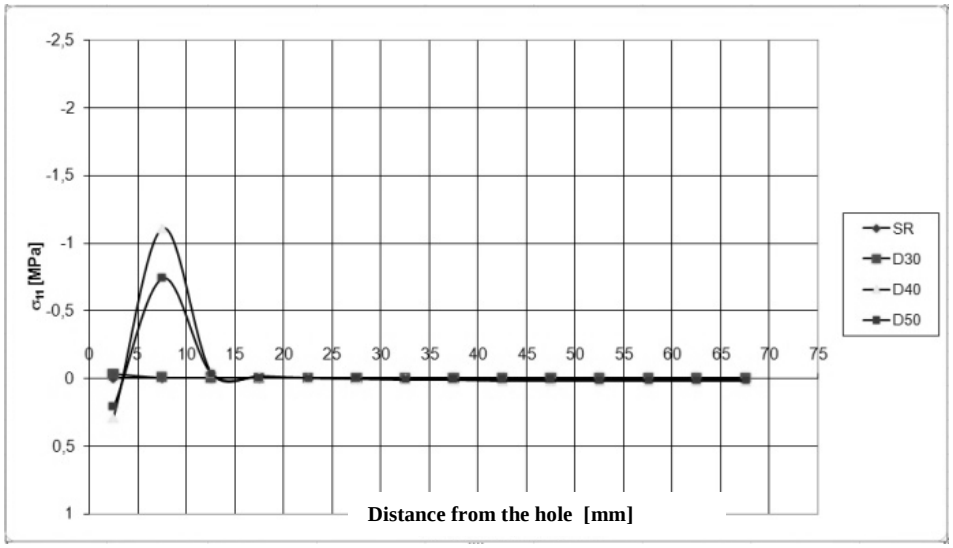

Figure 5.126. Stress σ_{11} diagram varying the distance from the hole $\alpha = 90°$- p_w = 216 MPa.

Using ***Tsai-Hill*** and ***Maximum stress*** criteria around the hole (β), for example for fiber inclination α=0° and p_w=7.2 MPa, the presence of washers determines a real benefit with respect of ***RF*** that is resistance/stress ratio around the hole (**Figure 5.127** and **Figure 5.128**).

This is true if washer diameter is lower than $2d_b$. This is due to stress σ_{22} that are higher for $D_w \geq 2d_b$ than for $D_w \leq 2d_b$.

Criteria used are:

- Tsai Hill: $$\frac{1}{RF^2} = \left(\frac{\sigma_1}{\sigma_{1u}}\right)^2 + \left(\frac{\sigma_2}{\sigma_{2u}}\right)^2 + \frac{\sigma_1\sigma_2}{\sigma_{1u}^2} + \left(\frac{\tau_{12}}{\tau_{12u}}\right)^2 \leq 1,$$

- Maximum stress: $$RF = \min\left(\frac{\sigma_{1u}}{\sigma_1}; \frac{\sigma_{2u}}{\sigma_2}; \frac{\tau_{12u}}{\tau_{12}}\right).$$

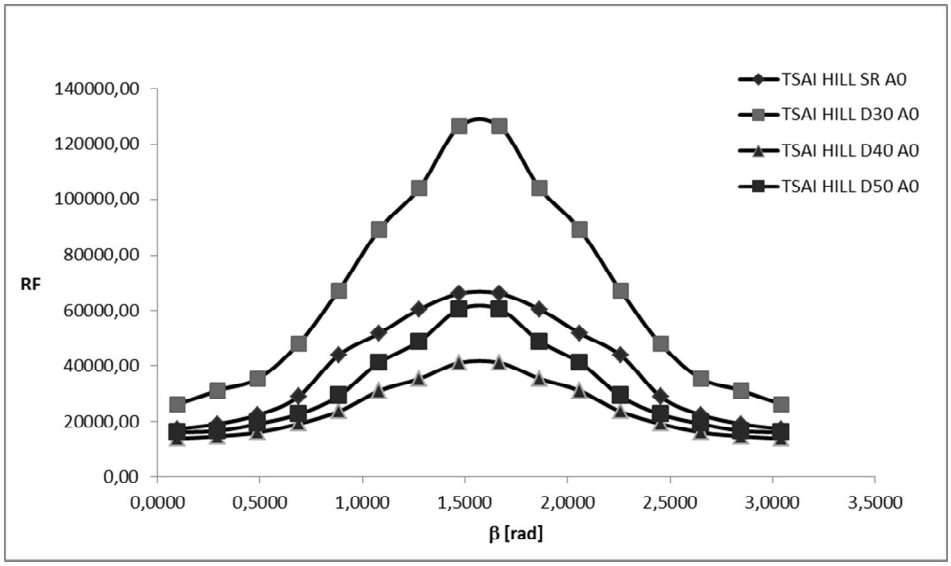

Figure 5.127. Tsai-Hill criterion.

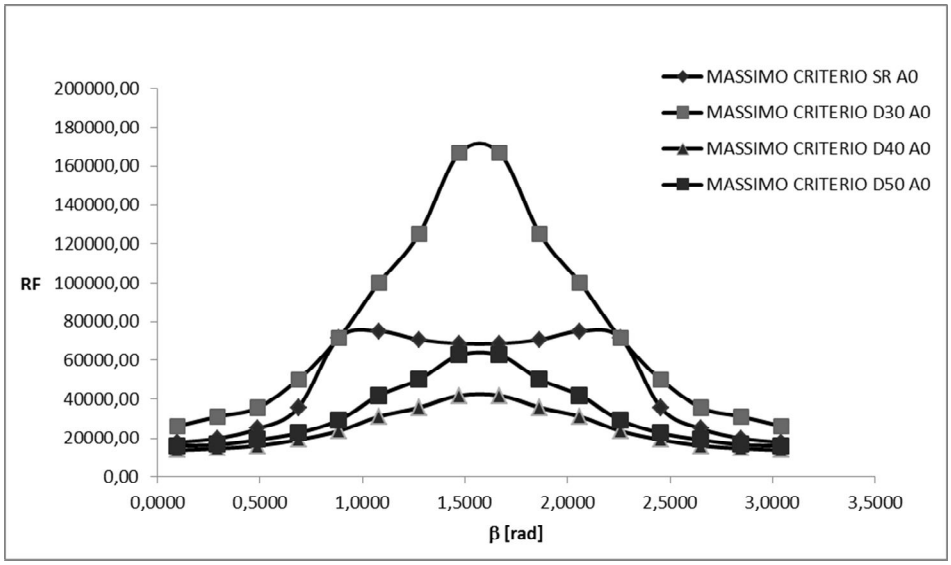

Figure 5.128. Maximum stress criterion.

The diagram of σ_{11} and of σ_{22}, for $\alpha = 0°$, $p_w = 7.2$ MPa and at varying of washer diameter, is shown in **Figure 5.129** and in **Figure 5.130**.

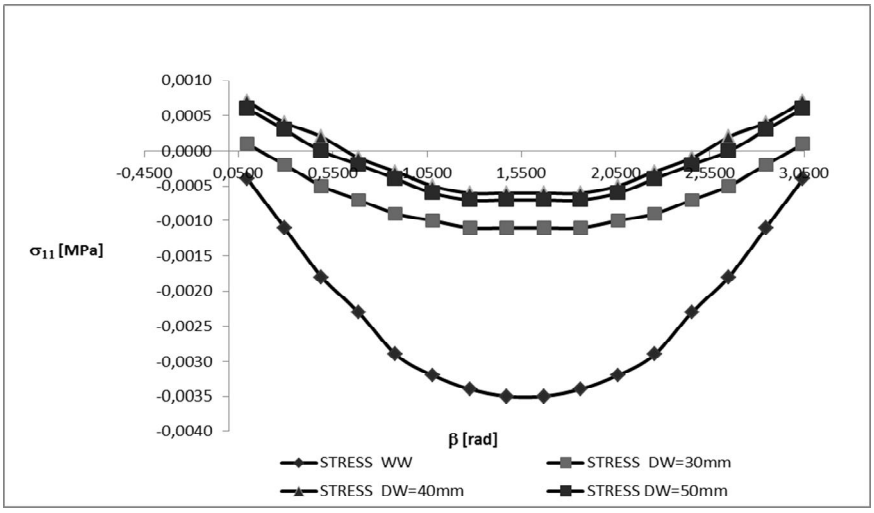

Figure 5.129. Stress σ_{11} around the hole.

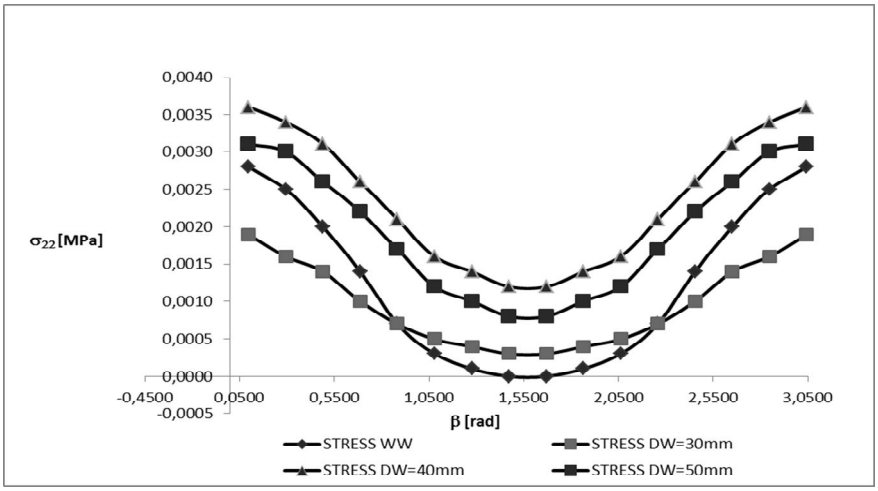

Figure 5.130. Stress σ_{22} around the hole.

CHAPTER VI
EXPERIMENTAL ANALYSIS OF BOLTED JOINTS WITH WASHERS

The GFRP specimens have a rectangular shape with dimensions 300mm x 160mm in plan, and thickness equal to 10 mm (**Figure 6.1**).

They were obtained by vacuum lamination of eight layers of fabric unidirectional GFRP and two outer layers of chopped strand mat impregnated with epoxy resin: the lamination is [CSM/04] S. The volume fractions of fibers and matrix were 60% and 40% respectively.

In particular, three specimens were made for each of the following values of the angle of inclination of the fiber α: 0 °, 15 °, 30 °, 45 °, 75 ° and 90 °.

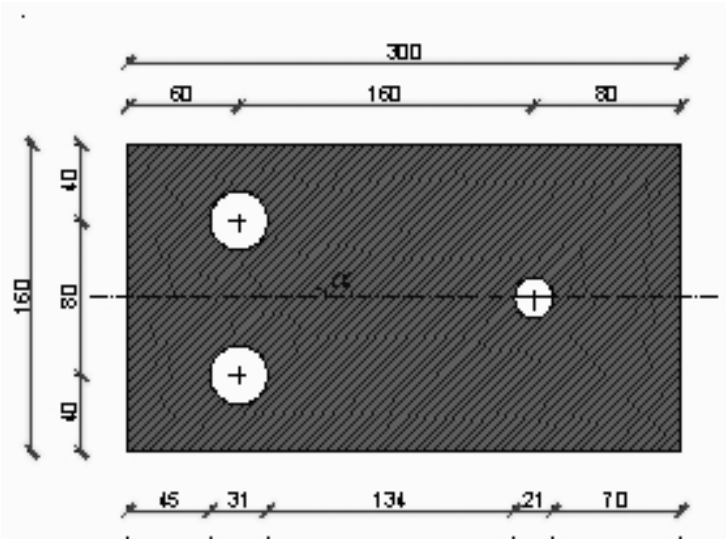

Figure 6.1. Geometry of GFRP specimens.

For the experimental tests, an universal machine SCHENCK Hydropolus S56 was used (**Figure 6.2**). This machine consists of a hydraulic piston with a loading capacity of +/- 630 kN, stroke of +/- 125 mm and a self-balanced steel frame used to counteract the axial loadings. The machine works both under displacement and load control.

In order to measure displacements, the testing machine is equipped with an LVDT, while the tension/compression loads are controlled by means of a load cell [21-27].

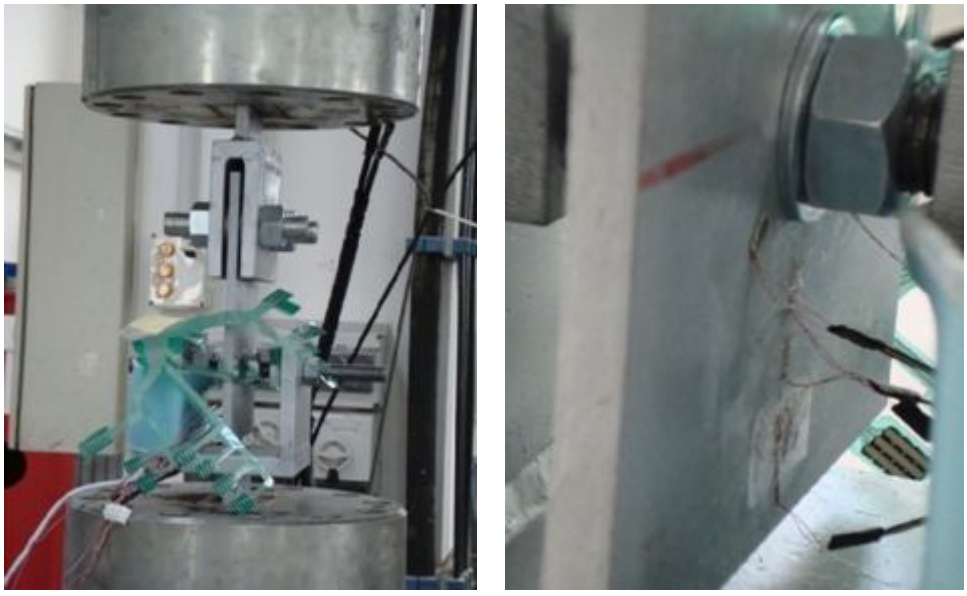

Figure 6.2. GFRP specimens in the machine test.

An experimental system was set up in order to carry out all the tests, made up of a test device as well as a sophisticated automatic data

acquisition system with three ‘‘System 5100 Vishay MM" switchboards, set out in parallel with 60 extensometric channels.

Furthermore, a pressure mapping system is used to measure bearing stresses at bolt-hole interface.

In fact this system has flexible sensors , ***GRIP*™ 4255N** of **Tekscan** that have been placed in the holes on the edge where the action of bearing stress is expected (**Figure 6.3**).

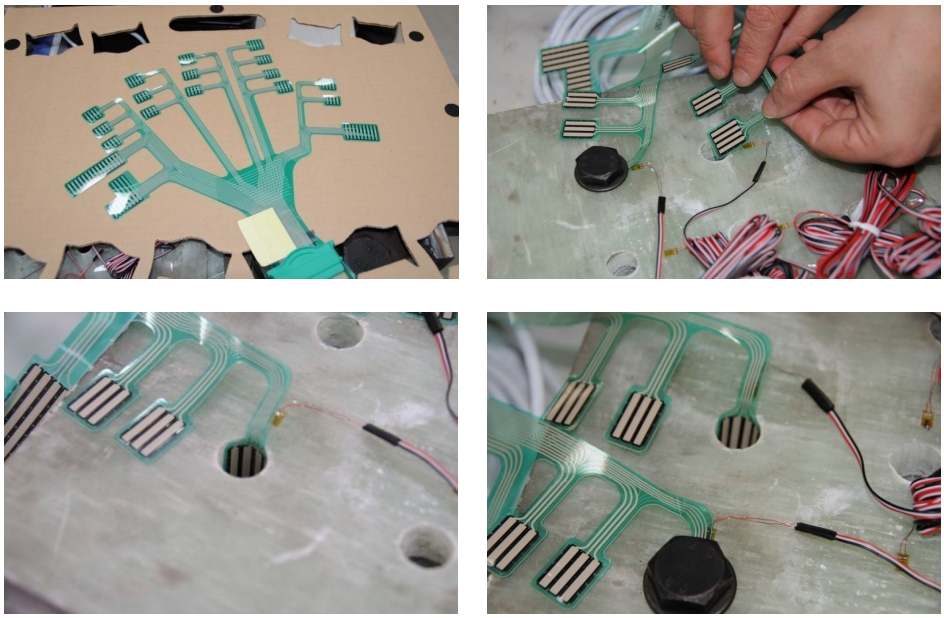

Figure 6.3. Glass composite plate (GFRP) with washer.

The mechanical properties of the GFRP plate are illustrated respectively in **Table 6.1**.

Table 6.1. Mechanical properties of the glass FRP.

Property	Value [MPa]
Tensile limit strength, 0°	222
Tensile limit strength, 90°	71
Compressive limit strength, 0°	201
Compressive limit strength, 90°	81
Modulus of elasticity, 0°	28431
Modulus of elasticity, 90°	11210

6.1. Discussion and results

In this paragraph the first results of the experimental investigation of tensile strength values for bearing failure $F_u^{(\alpha)}$, for each fiber inclination α, are presented.

The value of this tensile strength was obtained from the diagram and corresponds to the load-displacement curve peak (**Figure 6.4**).

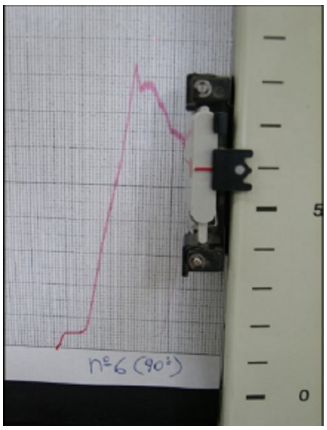

Figure 6.4. Load-displacement curve.

In **Figure 6.5** ratio $F_u^{(\alpha)} / F_u^{(0)}$ is shown for each value of α and considering the value of $F_u^{(0)}$ obtained for $\alpha = 0°$ both with washers and without washers [21-27].

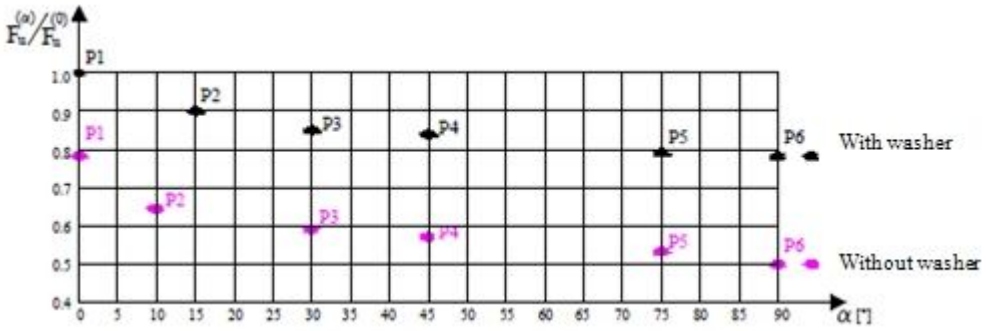

Figure 6.5. Diagram of $F_u^{(\alpha)} / F_u^{(0)}$ both with washers and without washers.

Results plotted in **Figure 6.5** are reported in **Table 6.2**.

Table 6.2. Mechanical properties of the glass FRP.

Specimen	$\alpha \pm 0.2$	$F_u^{(\alpha)*}$	$F_u^{(\alpha)}$
n°	[°]	[kN]	[kN]
1 (P1)	0	30.25	23.85
2 (P2)	15	27.20	19.50
3 (P3)	30	25.80	17.90
4 (P4)	45	25.40	17.35
5 (P5)	75	23.85	16.15
6 (P6)	90	23.35	16.00

(*) Case with washers

Bearing resistance shows minimum value for $\alpha = 90°$, both with washers and without.

In this case, the decrease of bearing resistance is equal to 33% with respect of the case where $\alpha = 0°$, without washer, while, in presence of washers, this decrease is equal to 23%.

For each value of α, the increase of bearing resistance is constant and equal to 25% of $F_u^{(0)}$ (**Figure 6.5**).

In particular specimens with fiber inclination equal to 45° show the best behavior with respect of bearing failure.

The experimental study regards the analysis of the influence of fuber inclination and washers on the ultimate load bearing strength for GFRP material .

The first results obtained allow to conclude that:

1) the value of tensile strength for bearing strength depends sensitively on the angle of inclination fibers compared to the load direction, both in presence and absence of washers;

2) the washers, while exerting pressure on the edges of the hole that remains constant during the test, results in an increased load bearing strength of 25% of $F_u^{(0)}$. This increase is not affected by the angle of grain

3) the lamination of the composite does not influence significantly the tensile strength forbearing failure.

CHAPTER VII
3D NUMERICAL ANALYSIS OF T-STUBS OF GLASS FIBER REINFORCED POLYMER

In this study a numerical analysis on the mechanical behavior of ***T-Stubs of GFRP pultruded profiles*** is presented.

The bolted node, shown in **Figure 7.1**, is modeled by using ***Straus7***.

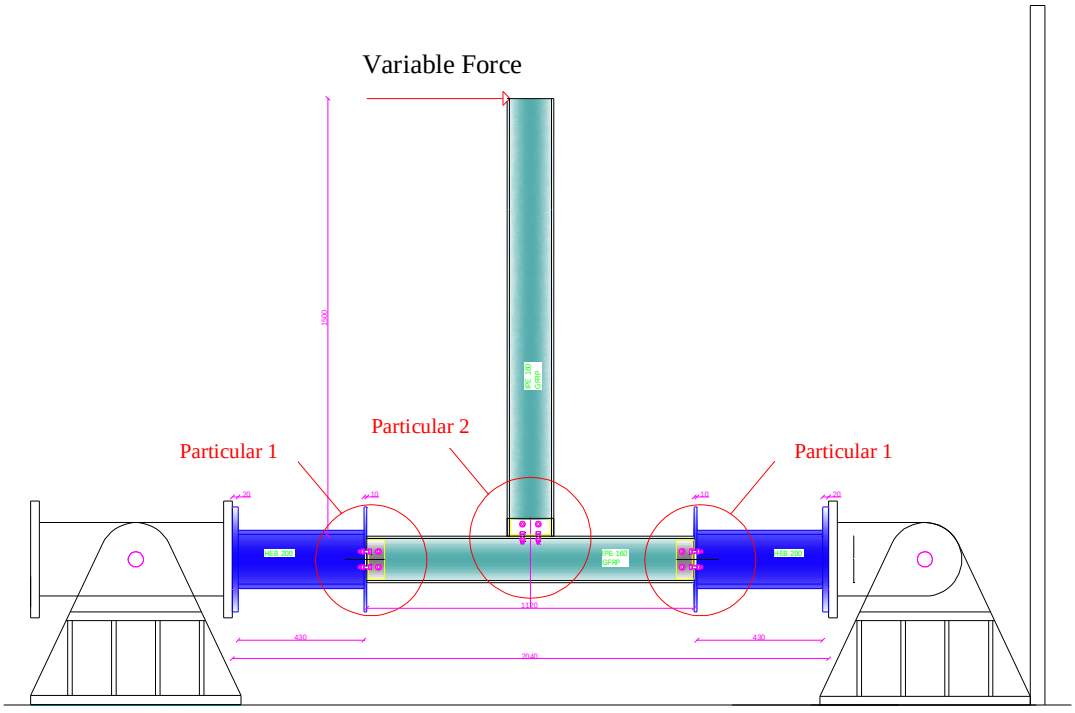

Figure 7.1. Geometry of the node.

The details of the node are illustrated in **Figure 7.2**.

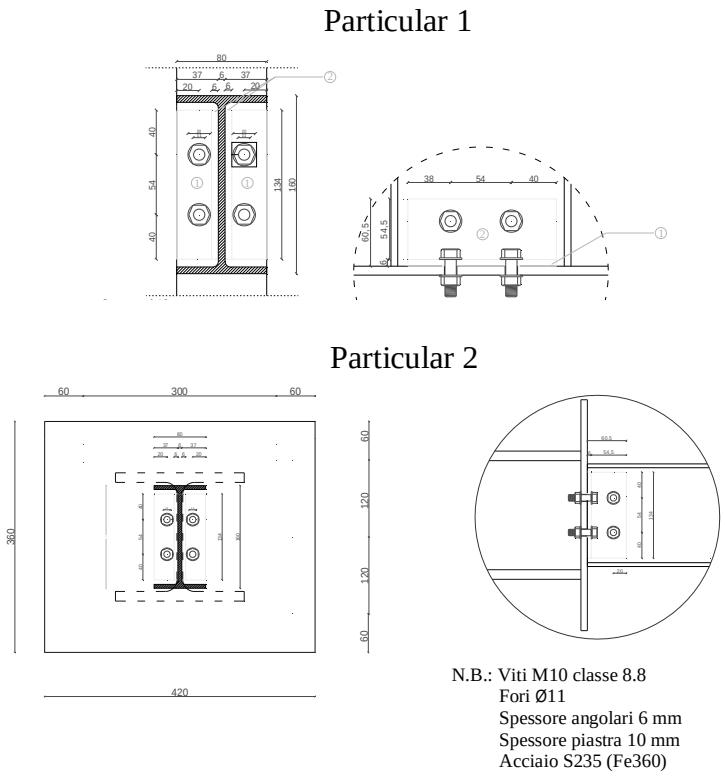

Figure 7.2. Details of the node.

Geometrical parameters of cross section, illustrated in **Figure 7.3**, are reported in **Table 7.1**.

Table 7.1. Geometrical parameters of cross section of GFRP.

B	H	s_{flange}	s_{web}	A
[mm]	[mm]	[mm]	[mm]	[mm^2]
80	160	6	6	1869.46

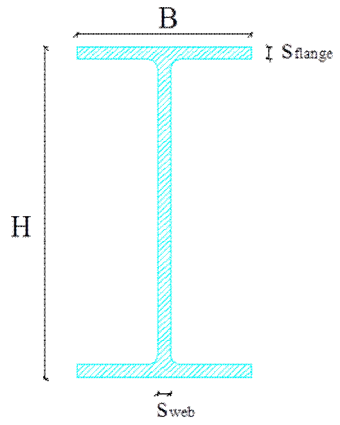

Figure 7.3. Cross section of column and beam.

Mechanical parameters are reported in **Table 7.2**.

Table 7.2. Mechanical parameters of cross section of GFRP.

E_1 [MPa]	E_2 [MPa]	E_3 [MPa]	G_{12} [MPa]	G_{13} [MPa]	G_{23} [MPa]
20000	9000	9000	6000	6000	6000
ν_{12}	ν_{13}	ν_{23}	ν_{21}	ν_{31}	ν_{32}
0.23	0.23	0.23	0.104	0.104	0.23

The node is bolted using stainless bolts, class 8.8, whose mechanical parameters are shown in **Table 7.3**.

Table 7.3. Mechanical parameters of steel bolt.

E [Mpa]	ν	G [MPa]
210000	0.2	87500

These values of mechanical parameters of GFRP satisfy the following equations “a priori” for orthotropic material:

$E_1 > 0$, $G_{12} > 0$, $(1-\nu_{23}\nu_{32}) = 0.95 > 0$,
$E_2 > 0$, $G_{13} > 0$, $(1-\nu_{13}\nu_{31}) = 0.98 > 0$,
$E_3 > 0$, $G_{23} > 0$, $(1-\nu_{12}\nu_{21}) = 0.98 > 0$,

$(1-\nu_{12}\nu_{21}-\nu_{23}\nu_{32}-\nu_{31}\nu_{13}-\nu_{21}\nu_{32}\nu_{13}-\nu_{31}\nu_{12}\nu_{23}) = 0.89 > 0$,

$|\nu_{21}| < (E_2/E_1)^{1/2} = 0.67$, $|\nu_{12}| < (E_1/E_2)^{1/2} = 1.49$,
$|\nu_{32}| < (E_3/E_2)^{1/2} = 1$, $|\nu_{23}| < (E_2/E_3)^{1/2} = 1$,
$|\nu_{13}| < (E_1/E_3)^{1/2} = 1.49$, $|\nu_{31}| < (E_3/E_1)^{1/2}$ 0.67,

$\nu_{21}\nu_{32}\nu_{13} < (1-\nu_{21}^2(E_1/E_2)- \nu_{32}^2(E_2/E_3)- \nu_{13}^2(E_3/E_1)) / 2 < 1/2$

$0.0055 < 0.45 < 0.5$.

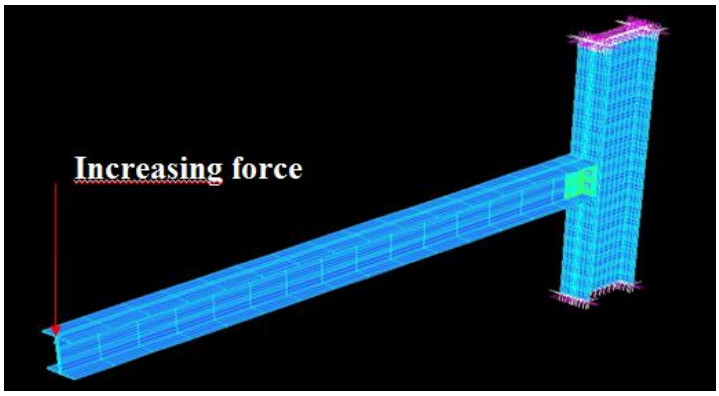

Figure 7.4. Beam-column node.

The non-linear analysis studies the mechanical behavior of beam-column node, with respect of failure mode for concentrated bending increasing load applied on the end section of the GFRP beam (**Figure 7.4**).

The failure expected, observing the strength class of the bolts, is the detachment of flange from the web due to normal stresses acting in this zone exclusively on the matrix of the cross section.

7.1. Results and discussion

Applying an increasing load on the end section of the GFRP beam (**Figure 7.4**) and adopting an orthotropic mesh for the discretization of the model (**Figure 7.5**), you can observe the normal stress map in **Figure 7.6**.

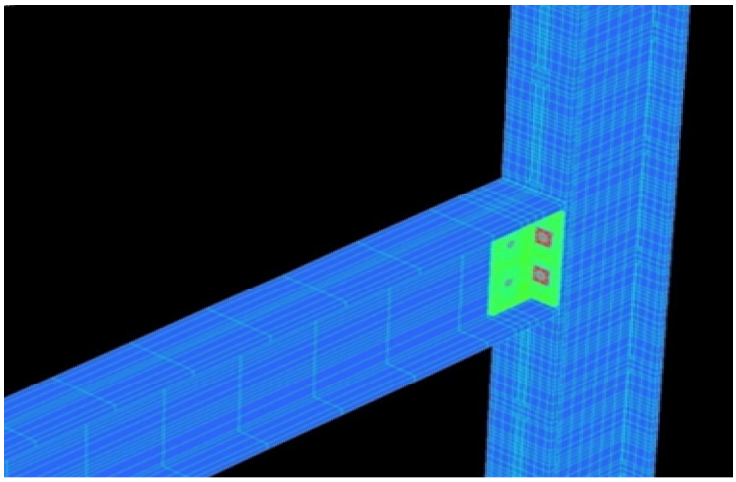

Figure 7.5. Beam-column node.

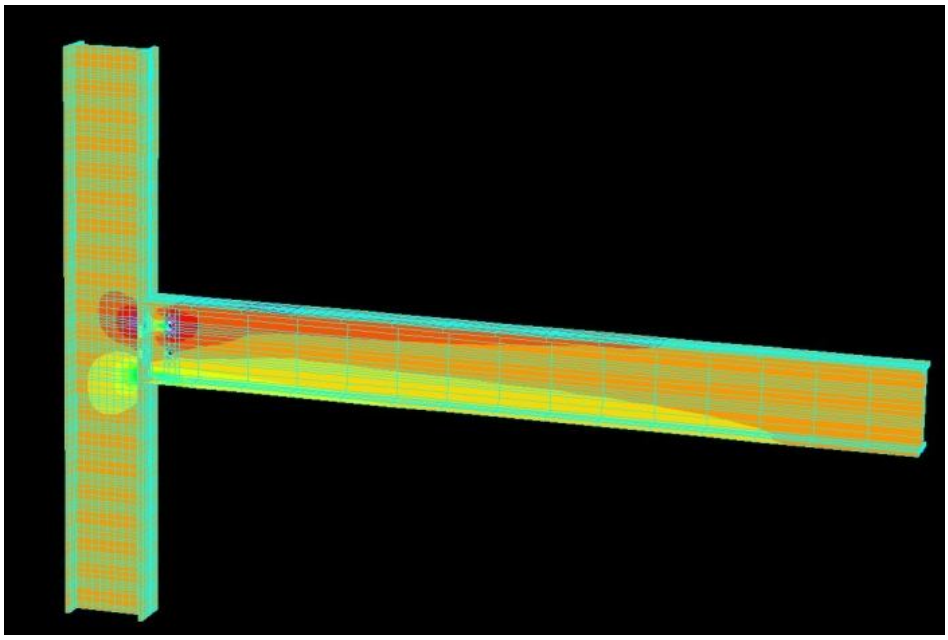

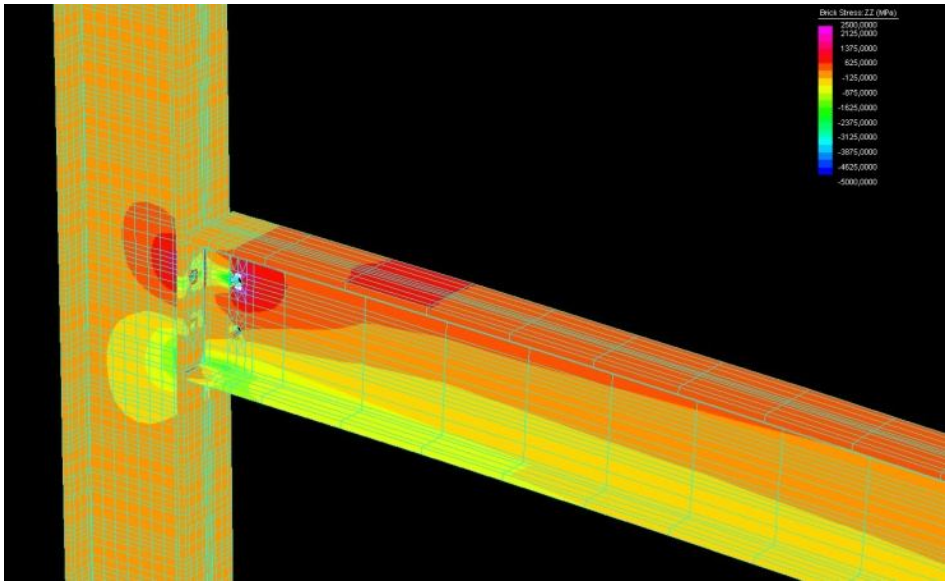
Brick Stress: ZZ (MPa)
2500,0000
2125,0000
1375,0000
625,0000
-125,0000
-875,0000
-1625,0000
-2375,0000
-3125,0000
-3875,0000
-4625,0000
-5000,0000

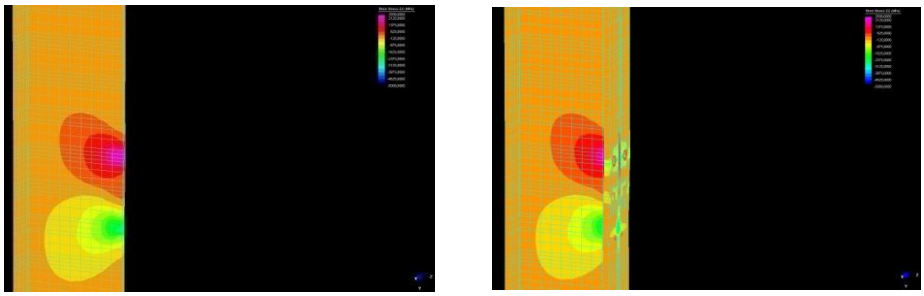

Figure 7.6. Normal stress at beam-column interface.

Results confirm expected failure. In fact maximum stresses act in correspondence of bolt hole, in the steel joint, between beam and column.

In **Figure 7.7** normal stresses at beam-column interface section are shown for different levels of load.

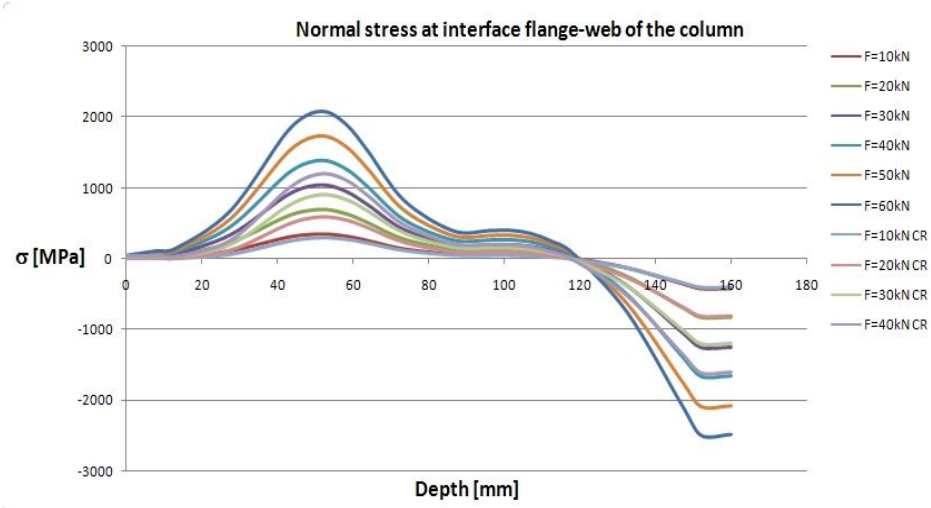

Figure 7.7. Normal stress at beam-column interface.

In detail, maximum stresses occur near the upper bolt hole of the GFRP column.

Shear stresses are illustrated in **Figure 7.8**, for different levels of load.

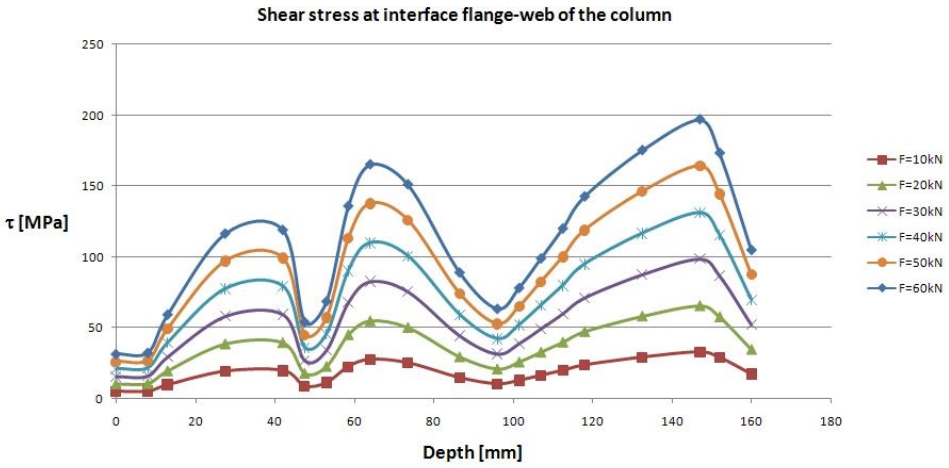

Figure 7.8. Normal stress at beam-column interface.

The node deformation is reported in **Figure 7.9**.

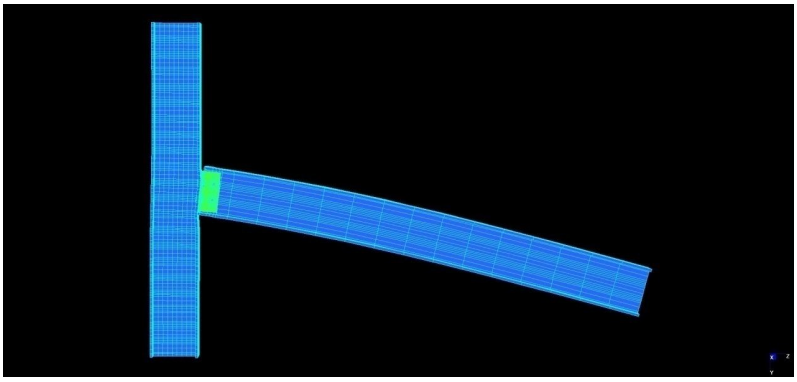

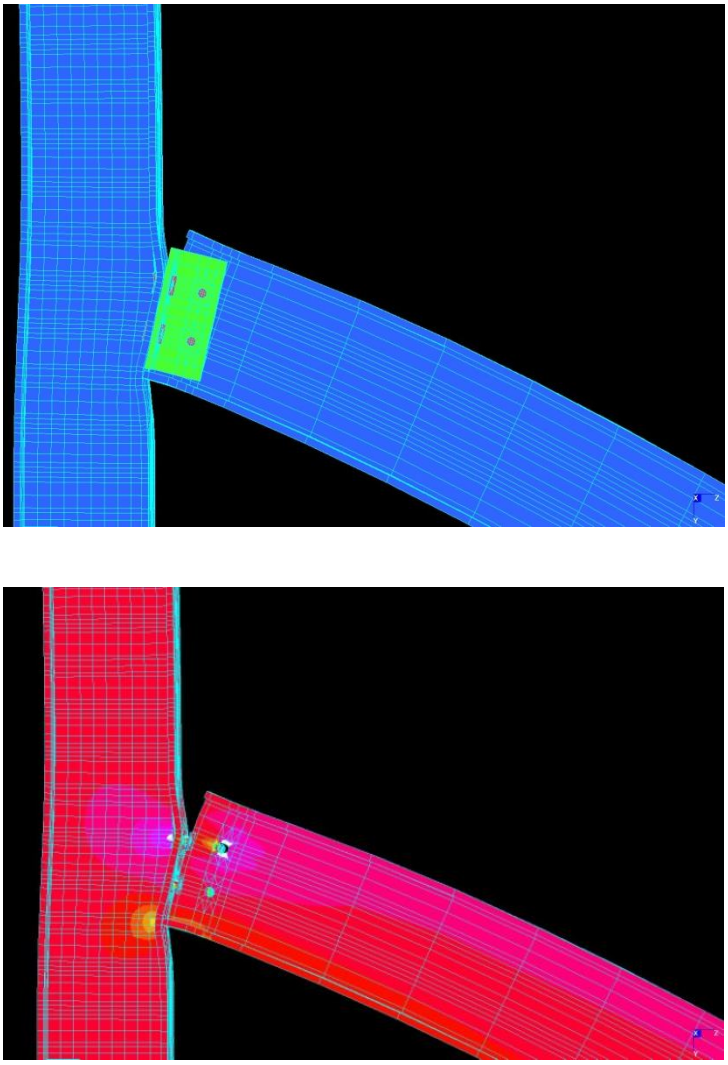

Figure 7.9. Node deformation.

To avoid this type of failure, one solution is connecting the opposite flange of the column by using steel profile.

References

[1] **R. Starikov**, **J. Schön** (2001): "Quasi-static behaviour of composite joints with protruding-head bolts". Composites Structures, Vol. 51, 411-425.

[2] **R. Prabhakaran, Z. Razzaq, S. Devara** (1996): "Load and resistance factor design (LRFD) approach for bolted joints in pultruded composites". Composites: Part B, Vol. 27 B, 351-360.

[3] **E. Persson**, **I. Eriksson** (1999): "Fatigue of multiple-row bolted joints in carbon/epoxy laminates: ranking of factors affecting strength and fatigue life". International Journal of Fatigue, Vol. 21, 337-353.

[4] **V.P. Lawlor**, **M.A. McCarthy**, **W.F. Stanley** (2005): "An experimental study of bolt–hole clearance effects in double-lap, multi-bolt composite joints". Composite Structures, Vol. 71, 176-190.

[5] **Y. Yan**, **W.-D. Wen**, **F.-K. Chang**, **P. Shyprykevich** (1999): "Experimental study on clamping effects on the tensile strength of composite plates with a bolt-filled hole". Composites Part A: Applied Science and Manufacturing, Vol. 30, 1215-1229.

[6] **N.K. Hassan**, **M.A. Mohamedien**, **S.H. Rizkalla** (1996): "Finite element analysis of bolted connections for PFRP composites". Composites Part B: Engineering, Vol. 27 (3-4), 339-349.

[7] **P.P. Camanho**, **F.L. Matthews** (1997): "Stress analysis and strength prediction of mechanically fastened joints in FRP: a review". Composites Part A: Applied Science and Manufacturing, Vol. 28 (6), 529-547.

[8] **J. Ekh**, **J. Schön** (2006): "Load transfer in multirow, single shear, composite-to-aluminium lap joints". Composites Science and Technology, Vol. 66, 875-885.

[9] **R. Starikov**, **J. Schön** (2002): "Experimental study on fatigue resistance of composite joints with protruding-head bolts". Composites Structures, Vol. 55, 1-11.

[10] **Y. Xiao**, **T. Ishikawa** (2005): "Bearing strength and failure behaviour of bolted composite joints (part II: modelling and

simulation)". Composites Science and Technology: Engineering, Vol. 65, 1032-1043.

[11] **G. Kelly**, **S. Hallström** (2004): "Bearing strength of carbon fibre/epoxy laminates: effects of bolt-hole clearance". Composites Part B: Engineering, Vol. 35, 331-343.

[12] **B. Vangrimde**, **R. Boukhili** (2003): "Descriptive relationships between bearing response and macroscopic damage in GFRP bolted joints". Composites Part B: Engineering, Vol. 34 (8), 593-605.

[13] **T. Ireman** (1998): "Three-dimensional stress analysis of bolted single-lap composite joints". Composites Structures, Vol. 43, 195-216.

[14] **F. Ascione**, **L. Feo**, **F. Maceri** (2006): "Un'analisi numerica preliminare ed un dispositivo sperimentale per lo studio del comportamento di collegamenti bullonati in strutture composite laminate". XXXV Convegno Nazionale dell'Associazione Italiana per l'Analisi delle Sollecitazioni (AIAS 2006), Ancona.

[15] **F. Ascione**, **L. Feo**, **F. Maceri** (2009): "An experimental investigation on the bearing failure load of glass fibre/epoxy laminates". Composites Part B: Engineering. Vol. 40 (3), 197-205.

[16] **Ever J. Barbero**: "Introduction to Composite Materials Design", Taylor & Francis.

[17] **J. N. Reddy**: "An Introduction to the Finite Element Method", Mc Graw-Hill, New York.

[18] **K. J. Bathe**, **E. L. Wilson**: "Numerical Methods in Finite Element Analysis", Prentice-Hall, Englewood Cliffs.

[19] **Documento Tecnico CNR-DT 200/2004** (2004): "Istruzioni per la Progettazione, l'Esecuzione ed il Controllo di Interventi di Consolidamento Statico mediante l'utilizzo di Compositi Fibrorinforzati". Consiglio Nazionale delle Ricerche, Roma.

[20] **Documento Tecnico CNR-DT 205/2007** (2008): "Istruzioni per la Progettazione, l'Esecuzione ed il Controllo di Strutture realizzate con Profili Pultrusi di Materiale Composito Fibrorinforzato (FRP)". Consiglio Nazionale delle Ricerche, Roma.

[21] **F. Ascione**, **V. Cerenza**, **L. Feo**, **G. Marra**: "Analisi delle tensioni in giunzioni bullonate tra profili pultrusi di FRP". In: AIAS XXXVIII Convegno Nazionale, 9-11 settembre 2009, Politecnico di Torino.

[22] **F. Ascione**, **V. Cerenza**, **L. Feo**, **G. Marra**: "A numerical and experimantal investigation on the shear forces distribution among the bolts of GFRP bolted joints". In: XIX Congresso AIMETA, 14-17 settembre 2009, Ancona.

[23] **F. Ascione**, **V. Cerenza**, **L. Feo**, **G. Marra**: " Stress analysis of bolted joints between FRP pultruded profiles". In: ICCE-17, 26 july – 1 august 2009, Hawaii, USA.

[24] **F. Ascione**, **V. Cerenza**, **L. Feo**, **G. Marra**: " Influenza della pressione esercitata da rondelle rigide sulla rottura per rifollamento di connessioni bullonate tra laminati compositi fibrorinforzati: primi risultati". In: AIAS XXXIX Convegno Nazionale, 7-10 settembre 2010, Maratea (PZ).

[25] **L. Feo**, **G. Marra**, **R. Penna**: "A numerical analysis on the pin-bearing failure load of glass fibre reinforced polymer laminates". In: ICCE-18, 04-10 july, Anchorage, Alaska, USA.

[26] **L. Feo**, **G. Marra**, **A. S. Mosallam**: "Stress Analysis of Bolted Joints for FRP pultruded structures" in press on Composite Engineering: Part B.

[27] **G. Marra** Thesis: "Analisi sperimentale sulle modalità di rottura di collegamenti bullonati tra profili sottili pultrusi in materiale composito fibrorinforzato (FRP)".